

NUMERICAL SOLUTIONS OF BOUNDARY VALUE PROBLEMS;
APPLICATIONS IN FERROHYDRODYNAMICS AND
MAGNETOHYDRODYNAMICS

A THESIS SUBMITTED TO
THE GRADUATE SCHOOL OF NATURAL AND APPLIED SCIENCES
OF
MIDDLE EAST TECHNICAL UNIVERSITY

BY

PELİN ŞENEL

IN PARTIAL FULFILLMENT OF THE REQUIREMENTS
FOR
THE DEGREE OF DOCTOR OF PHILOSOPHY
IN
MATHEMATICS

OCTOBER 2017

Approval of the thesis:

**NUMERICAL SOLUTIONS OF BOUNDARY VALUE PROBLEMS;
APPLICATIONS IN FERROHYDRODYNAMICS AND
MAGNETOHYDRODYNAMICS**

submitted by **PELİN ŞENEL** in partial fulfillment of the requirements for the degree of **Doctor of Philosophy in Mathematics Department, Middle East Technical University** by,

Prof. Dr. Gülbin Dural Ünver
Dean, Graduate School of **Natural and Applied Sciences**

Prof. Dr. Mustafa Korkmaz
Head of Department, **Mathematics**

Prof. Dr. Münevver Tezer
Supervisor, **Mathematics Dept., METU**

Examining Committee Members:

Prof. Dr. Bülent Karasözen
Mathematics Dept., METU

Prof. Dr. Münevver Tezer
Mathematics Dept., METU

Prof. Dr. Nevzat Güneri Gençer
Electrical and Electronics Engineering Dept., METU

Prof. Dr. Mustafa Türkyılmazoğlu
Mathematics Dept., Hacettepe University

Assoc. Prof. Dr. Gülnihal Meral
Mathematics-Computer Science Dept.,
Ankara Yıldırım Beyazıt University

Date: _____



I hereby declare that all information in this document has been obtained and presented in accordance with academic rules and ethical conduct. I also declare that, as required by these rules and conduct, I have fully cited and referenced all material and results that are not original to this work.

Name, Last Name: PELİN ŞENEL

Signature :

ABSTRACT

NUMERICAL SOLUTIONS OF BOUNDARY VALUE PROBLEMS; APPLICATIONS IN FERROHYDRODYNAMICS AND MAGNETOHYDRODYNAMICS

ŞENEL, PELİN

Ph.D., Department of Mathematics

Supervisor : Prof. Dr. Münevver Tezer

OCTOBER 2017, 195 pages

In this thesis, steady, laminar, fully developed flows in pipes subjected to a point magnetic source or uniform magnetic field are simulated by the dual reciprocity boundary element method (DRBEM). The Navier-Stokes and energy equations are solved in terms of the velocity, pressure and the temperature of the fluid which are all of the original variables of the problem. The missing pressure equation is derived and pressure boundary conditions are generated by a finite difference approximation and the DRBEM coordinate matrix. Fundamental solution of Laplace equation is made use of to convert the nonlinear partial differential equations into the boundary integral equations. The terms other than Laplacian are approximated by a series of radial basis functions. The nonlinearities in the governing equations are easily handled by the use of the DRBEM coordinate matrix. The influence of the point source magnetic field on the Ferrohydrodynamics (FHD) Stokes, incompressible, and forced convection flows are investigated first. The interaction between the buoyancy force,

magnetization force and the viscous dissipation is discussed. Then, the effect of multiple point magnetic sources on the FHD incompressible flow is studied. DRBEM simulations of Magneto hydrodynamics (MHD) pipe flow and the flow between parallel infinite plates with slip velocity conditions are also presented. The coupled momentum and magnetic induction equations are combined and solved without an iteration. This process provides the nodal solutions in one stroke both on the boundary and inside the problem domain. The importance of the thesis study is in the fact that it is the first DRBEM application to FHD flow under point magnetic source and MHD flow with slip walls.

Keywords: Fluid Mechanics, Ferrohydrodynamics, Magneto hydrodynamics, Dual Reciprocity Boundary Element Method, Slip Boundary Condition

ÖZ

SINIR DEĞER PROBLEMLERİNİN NÜMERİK ÇÖZÜMÜ; FERROHİDRODİNAMİK VE MAGNETOHİDRODİNAMİKTE UYGULAMALAR

ŞENEL, PELİN

Doktora, Matematik Bölümü

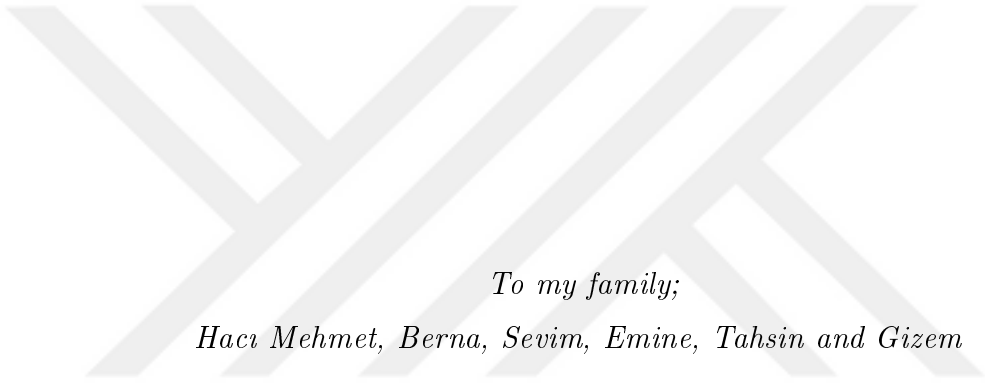
Tez Yöneticisi : Prof. Dr. Münevver Tezer

Ekim 2017 , 195 sayfa

Bu tezde, kanallardaki zamandan bağımsız, laminer, tam gelişmiş, noktasal manyetik kaynak veya düzgün manyetik alan etkisi altındaki akışın karşılıklı sınır elemanları metodu (DRBEM) kullanılarak simülasyonu yapılmıştır. Navier-Stokes ve enerji denklemleri hız, basınç ve sıcaklık cinsinden çözülmüş ve böylece tüm orijinal problem bilinmeyenleri elde edilmiştir. Fiziksel olarak kayıp basınç denklemi elde edilmiş ve sonlu fark yöntemi ile DRBEM koordinat matrisi kullanılarak basınç için sınır koşulları üretilmiştir. Lineer olmayan kısmi türevli denklemler, Laplace denkleminin temel çözümü kullanılarak sınır integral denklemlerine dönüştürülmüştür. Laplace dışındaki terimlere bir dizi radyal baz fonksiyonu ile yaklaşmıştır. Temel denklemlerdeki lineer olmayan terimler DRBEM koordinat matrisi ile kolaylıkla ele alınmıştır. İlk olarak, noktasal manyetik kaynağın Ferrohidrodinamik (FHD) Stokes, sıkıştırılmayan ve zorlanmış konveksiyon akışları üzerindeki etkisi incelenmiştir. Kaldırma kuvveti, manyetik kuvvet ve viskoz dissipasyon arasındaki etkileşim tartışılmıştır. Daha sonra, birden fazla noktasal

manyetik kaynağın FHD sıkıştırılmaz akış üzerindeki etkisi çalışılmıştır. Duvarlarda kayma koşulu olması durumunda, Magnetohidrodinamik (MHD) kanal akışının ve paralel sonsuz plakalar arasındaki akışın DRBEM ile simülasyonu da yapılmıştır. Momentum ve manyetik indüksiyon denklemlerinden oluşan sistem, birleştirilmiş ve iterasyon olmadan çözülmüştür. Bu yöntem problemin tanım bölgesinde ve sınırında noktasal çözümlerin bir seferde elde edilmesine olanak sağlamıştır. Tez çalışmasının önemi, sınır elemanları yöntemi ile manyetik kaynak etkisindeki Ferrohidrodinamik akış ve kayma sınır koşulu ile Magnetohidrodinamik akış problemlerinin ilk defa çözülmüş olmasıdır.

Anahtar Kelimeler: Akışkanlar Dinamiği, Ferrohidrodinamik, Magnetohidrodinamik, Karşılıklı Sınır Elemanları Metodu, Kayma Sınır Koşulu



To my family;

Hacı Mehmet, Berna, Sevim, Emine, Tahsin and Gizem

ACKNOWLEDGMENTS

Firstly, I would like to express my sincere gratitude to my supervisor Prof. Dr. Münevver Tezer for her precious guidance, continuous support, encouragement and patience during the development and preparation of this thesis.

Besides my supervisor, I would like to thank the rest of my defense committee: Prof. Dr. Bülent Karasözen, Prof. Dr. Nevzat Güneri Gençer, Prof. Dr. Mustafa Türkyılmazođlu and Assoc. Prof. Dr. Gülnihal Meral for their valuable suggestions, comments and reviews.

I gratefully thank to Middle East Technical University for the financial support under the Scientific Research Project BAP-01-01-2015-004.

I would also like to thank the members of the Department of Mathematics for their support both as academicians and coworkers. I present special thanks to Assoc. Prof. Dr. Canan Bozkaya for her help in coding at the beginning of my studies.

Lastly, sincerest thanks to my family, Hacı Mehmet, Berna, Sevim, Tahsin, Emine and Gizem Şenel, for supporting and believing in me all the way through my life. Their unrequited love and patience can not be paid.

TABLE OF CONTENTS

ABSTRACT	v
ÖZ	vii
ACKNOWLEDGMENTS	x
TABLE OF CONTENTS	xi
LIST OF TABLES	xvi
LIST OF FIGURES	xvii
NOMENCLATURE	xxvii
CHAPTERS	
1 INTRODUCTION	1
1.1 Fluid Dynamics Equations	3
1.1.1 Continuity Equation	3
1.1.2 Momentum Equations	4
1.1.3 Energy Equation	4
1.1.4 Magnetic Induction Equations	5
1.2 FHD Stokes Flow	5
1.3 FHD Incompressible Flow	9
1.4 FHD Forced Convection Flow	10

1.5	MHD Duct Flow with Slipping Velocity Condition . . .	14
1.6	MHD Flow Between Parallel Infinite Plates with Slipping Velocity Condition	15
1.7	Helpful Identities and Numerical Techniques	17
1.7.1	Green's First Identity	17
1.7.2	Gauss-Legendre Quadrature Method	17
1.7.3	Gaussian Elimination with Pivoting	18
1.8	Literature Survey	18
1.9	Originality of the Thesis	26
1.10	Plan of the Thesis	28
2	THE BEM AND THE DRBEM FORMULATIONS FOR FHD AND MHD FLOW PROBLEMS	31
2.1	The Boundary Element Method for the Laplace Equation	32
2.1.1	Fundamental Solution	33
2.1.2	Constant Element Discretization	35
2.1.3	Linear Element Discretization	37
2.1.4	Solution at the interior nodes	40
2.2	The Dual Reciprocity Boundary Element Method for Poisson's type Equations $\nabla^2\phi = b(x, y, \phi, \phi_x, \phi_y)$	41
2.3	Application of the DRBEM to the FHD Stokes flow problems	45
2.4	Application of the DRBEM to the FHD incompressible fluid flow problems	47

2.5	Application of the DRBEM to the FHD forced convection biomagnetic flow problems with viscous dissipation . . .	48
2.6	Application of the DRBEM to the MHD Duct Flow with Slipping Velocity Condition	50
2.7	Application of the DRBEM to the MHD Flow Between Parallel Infinite Plates with Slipping Velocity Condition	52
3	DRBEM SOLUTIONS OF STOKES, INCOMPRESSIBLE AND FORCED CONVECTION FLOWS UNDER THE EFFECT OF POINT MAGNETIC SOURCE	57
3.1	Stokes Flow in Cavities with Point Magnetic Source . .	59
3.1.1	Stokes flow in a lid-driven cavity with point magnetic source	61
3.1.2	Stokes flow in a square cavity with point magnetic source	68
3.1.3	Stokes flow in a lid-driven circular cavity with point magnetic source	71
3.2	Incompressible Flow in Cavities with Point Magnetic Source	75
3.2.1	Incompressible flow in a square cavity with point magnetic source	78
3.2.2	Incompressible flow in a lid-driven square cavity with point magnetic source	83
3.2.3	Incompressible flow in a circular cavity with point magnetic source	87
3.2.4	Incompressible flow in a square cavity with an obstacle (annular pipes) under point magnetic source	91
3.3	Incompressible Flow in Rectangular Cavities with Multiple Point Magnetic Sources	99

3.3.1	Square cavity with two or three sources below the bottom wall	101
3.3.2	Rectangular cavity with two or three sources below the bottom wall	105
3.3.3	Square and rectangular cavities with sources on opposite walls	107
3.4	Forced Convection Flow of Biomagnetic Fluid in Square, Lid-driven and Circular Cavities with Point Magnetic Source	110
3.4.1	Forced convection flow in a square cavity with horizontal adiabatic walls and point magnetic source	113
3.4.2	Forced convection flow in a lid-driven square cavity with horizontal adiabatic walls and point magnetic source	122
3.4.3	Forced convection flow in a square cavity with vertical adiabatic walls and point magnetic source	125
3.4.4	Forced convection flow in a circular cavity with point magnetic source	133
4	MHD FLOW IN DUCTS AND BETWEEN PARALLEL PLATES WITH SLIP CONDITIONS	141
4.1	MHD Duct Flow with Slipping Walls	143
4.1.1	MHD duct flow - Problem 1	144
4.1.2	MHD duct flow - Problem 2	148
4.1.3	MHD duct flow - Problem 3	151
4.1.4	MHD duct flow - Problem 4	154
4.2	MHD Flow in Ducts with Partly Insulated Partly Perfectly Conducting Slipping Walls	158

4.2.1	Problem 1, $d = 0$ Case	159
4.2.2	Problem 1, $d = 1$ Case	161
4.2.3	Problem 2, $d = 0$ Case	163
4.2.4	Problem 2, $d = 1$ Case	165
4.3	MHD Flow Driven by Electrodes Between Parallel Infinite Slipping Plates	167
4.3.1	Case 1: $s_2 = 0, l = 0, Ha$ increases	169
4.3.2	Case 2: $l = 0, Ha = 10, s_2$ varies as $s_2 < 1, s_2 = 1, s_2 > 1$	170
4.3.3	Case 3: $s_2 = 0, Ha = 50, l$ varies as $l = 0.1, 0.3, 0.5$	171
4.3.4	Case 4: $Ha = 10, s_2$ varies as $s_2 < 1, s_2 = 1, s_2 > 1$ and l varies as $l = 0.3, l = 0.5$	172
4.3.5	Electric potential computations	173
5	CONCLUSION	179
	REFERENCES	183
	CURRICULUM VITAE	191

LIST OF TABLES

TABLES

Table 3.1	Problems considered in Chapter 3.	58
Table 3.2	Variation of the Reynolds number with magnetic field intensity.	83
Table 3.3	Average Nusselt numbers, $Mn = 0$, $Ra = 10^{-3}$	116
Table 4.1	Problems considered in Chapter 4.	142

LIST OF FIGURES

FIGURES

Figure 2.1 Problem domain	32
Figure 2.2 Boundary augmented by a small semicircle	34
Figure 2.3 Constant and linear element discretizations	35
Figure 2.4 Linear element	37
Figure 2.5 Element coordinate system	38
Figure 3.1 Flow configuration for a rectangular pipe subjected to a mag- netic field generated by a thin wire.	58
Figure 3.2 Magnetic field strength equilines for $(a_1, a_2) = (0.5, -0.05)$	60
Figure 3.3 Stokes flow in a lid-driven cavity.	62
Figure 3.4 Stokes flow in a square cavity: Derivation of pressure wall conditions.	63
Figure 3.5 Stokes flow in a lid-driven square cavity, $M = 0$, (a) constant element approximation (b) linear element approximation.	65
Figure 3.6 Stokes flow in a lid-driven square cavity, $M = 10$, (a) constant element approximation (b) linear element approximation.	65
Figure 3.7 Stokes flow in a lid-driven square cavity, $M = 150$	66
Figure 3.8 Stokes flow in a lid-driven square cavity, $M = 500$	66
Figure 3.9 Stokes flow in a lid-driven square cavity, $M = 5000$	67

Figure 3.10 Stokes flow in a lid-driven square cavity, $M = 10000$	67
Figure 3.11 Stokes flow in a square cavity.	68
Figure 3.12 Stokes flow in a square cavity, $M = 5$	69
Figure 3.13 Stokes flow in a square cavity, $M = 30$	69
Figure 3.14 Stokes flow in a square cavity, $M = 50$	70
Figure 3.15 Stokes flow in a square cavity, $M = 100$	70
Figure 3.16 Stokes flow in a lid-driven circular cavity.	71
Figure 3.17 Stokes flow in a unit circular cavity: Derivation of wall pressure values.	71
Figure 3.18 Stokes flow in a lid-driven circular cavity, $M = 0$	73
Figure 3.19 Stokes flow in a lid-driven circular cavity, $M = 10$	73
Figure 3.20 Stokes flow in a lid-driven circular cavity, $M = 300$	74
Figure 3.21 Stokes flow in a lid-driven circular cavity, $M = 1000$	75
Figure 3.22 Flow in a square cavity.	78
Figure 3.23 Flow in a square cavity, $Mn = 0$	80
Figure 3.24 Flow in a square cavity, $Mn = 500$	80
Figure 3.25 Flow in a square cavity, $Mn = 3000$	81
Figure 3.26 Flow in a square cavity, $Mn = 5000$	81
Figure 3.27 Flow in a square cavity, $Mn = 17000$	82
Figure 3.28 Flow in a square cavity, $Mn = 30000$	82
Figure 3.29 Flow in a lid-driven square cavity.	84
Figure 3.30 Flow in a lid-driven square cavity, $Mn = 0$	84

Figure 3.31 Flow in a lid-driven square cavity, $Mn = 100$	85
Figure 3.32 Flow in a lid-driven square cavity, $Mn = 500$	85
Figure 3.33 Flow in a lid-driven square cavity, $Mn = 1000$	86
Figure 3.34 Flow in a lid-driven square cavity, $Mn = 3000$	86
Figure 3.35 Flow in a lid-driven square cavity, $Mn = 5000$	87
Figure 3.36 Flow in a circular cavity.	87
Figure 3.37 Flow in a circular cavity, $Mn = 0$	89
Figure 3.38 Flow in a circular cavity, $Mn = 100$	89
Figure 3.39 Flow in a circular cavity, $Mn = 500$	90
Figure 3.40 Flow in a circular cavity, $Mn = 1000$	90
Figure 3.41 Flow in a cavity with an obstacle.	91
Figure 3.42 Flow in a cavity with an obstacle: Derivation of pressure wall conditions.	91
Figure 3.43 Flow in a square cavity with a medium obstacle at the center, $d = 1/3$, $Mn = 0$	93
Figure 3.44 Flow in a square cavity with a medium obstacle at the center, $d = 1/3$, $Mn = 30$	94
Figure 3.45 Flow in a square cavity with a medium obstacle at the center, $d = 1/3$, $Mn = 500$	94
Figure 3.46 Flow in a square cavity with a medium obstacle at the center, $d = 1/3$, $Mn = 14000$	95
Figure 3.47 Flow in a square cavity with a small obstacle at the center, $d = 1/5$, $Mn = 5000$	96

Figure 3.48 Flow in a square cavity with a medium obstacle at the center, $d = 1/3, Mn = 5000$	96
Figure 3.49 Flow in a square cavity with a large obstacle at the center, $d = 1/2, Mn = 5000$	97
Figure 3.50 Flow in a square cavity with a small obstacle, left bottom corner placed at $(2/5, 3/5), d = 1/5, Mn = 5000$	98
Figure 3.51 Flow in a square cavity with a small obstacle, left bottom corner placed at $(3/5, 2/5), d = 1/5, Mn = 5000$	98
Figure 3.52 The flow configuration- two wires below the bottom wall. . .	99
Figure 3.53 Problem geometry and the boundary conditions for square cavity with one, two and three sources.	101
Figure 3.54 Planar velocity profiles on $y = 0.1$ line for two sources case $Mn = 10$ with $N = 60, 80, 100, 120$	102
Figure 3.55 Square cavity, (a) two sources (b) three sources, $Mn = 10$. .	103
Figure 3.56 Square cavity, two sources, (a) $Mn = 10$, (b) $Mn = 50$	104
Figure 3.57 Problem geometry and the boundary conditions for the rect- angular cavity with two and three sources.	105
Figure 3.58 Rectangular cavity, (a) two sources $Mn = 10$, (b) three sources $Mn = 10$, (c) three sources $Mn = 1000$	106
Figure 3.59 Problem geometry and boundary conditions for oppositely lo- cated sources (a) square cavity-two sources, (b) rectangular cavity- four sources.	107
Figure 3.60 Square cavity, two opposite sources, (a) $Mn=10$, (b) $Mn = 2000$.	108
Figure 3.61 Rectangular cavity, four opposite sources, (a) $Mn = 10$, (b) $Mn = 300$	109

Figure 3.62 Forced convection flow in a square cavity with horizontal adiabatic walls.	114
Figure 3.63 Natural convection flow of air, $Mn = 0$, $Ra = 10^3$	115
Figure 3.64 Forced convection flow in a square cavity with horizontal adiabatic walls, viscous dissipation is neglected. $Ra = 0$, $Mn = 5$	116
Figure 3.65 Forced convection flow in a square cavity with horizontal adiabatic walls, viscous dissipation is neglected. $Ra = 0$, $Mn = 200$	117
Figure 3.66 Forced convection flow in a square cavity with horizontal adiabatic walls, viscous dissipation is neglected. $Mn = 10$, $Ra = 10^2$	118
Figure 3.67 Forced convection flow in a square cavity with horizontal adiabatic walls, viscous dissipation is neglected. $Mn = 10$, $Ra = 10^3$	118
Figure 3.68 Forced convection flow in a square cavity with horizontal adiabatic walls, viscous dissipation is neglected. $Mn = 10$, $Ra = 10^5$	119
Figure 3.69 Linear elements-forced convection flow in a square cavity with horizontal adiabatic walls, viscous dissipation is neglected. $Mn = 10$, $Ra = 10^2$	119
Figure 3.70 Forced convection flow in a square cavity with horizontal adiabatic walls, viscous dissipation is neglected. $Mn = 80$, $Ra = 10^2$	120
Figure 3.71 Forced convection flow in a square cavity with horizontal adiabatic walls, viscous dissipation is neglected. $Mn = 80$, $Ra = 10^5$	120
Figure 3.72 Forced convection flow in a square cavity with horizontal adiabatic walls, viscous dissipation is included. $Mn = 10$, $Ra = 10^5$	121
Figure 3.73 Forced convection flow in a square cavity with horizontal adiabatic walls, viscous dissipation is included. $Mn = 80$, $Ra = 10^5$	122
Figure 3.74 Forced convection flow in a lid-driven square cavity with horizontal adiabatic walls.	122

Figure 3.75 Forced convection flow in a lid-driven square cavity with horizontal adiabatic walls, viscous dissipation is neglected. $Mn = 10$, $Ra = 10^2$	123
Figure 3.76 Forced convection flow in a lid-driven square cavity with horizontal adiabatic walls, viscous dissipation is included. $Mn = 80$, $Ra = 10^5$	124
Figure 3.77 Forced convection flow in a square cavity with vertical adiabatic walls.	125
Figure 3.78 Forced convection flow in a square cavity with vertical adiabatic walls, viscous dissipation is neglected. $Ra = 10^3$, $Mn = 0$	126
Figure 3.79 Forced convection flow in a square cavity with vertical adiabatic walls, viscous dissipation is neglected. $Ra = 10^4$, $Mn = 0$	126
Figure 3.80 Forced convection flow in a square cavity with vertical adiabatic walls, viscous dissipation is neglected. $Ra = 10^5$, $Mn = 0$	127
Figure 3.81 Forced convection flow in a square cavity with vertical adiabatic walls, viscous dissipation is neglected. $Ra = 0$, $Mn = 5$	128
Figure 3.82 Forced convection flow in a square cavity with vertical adiabatic walls, viscous dissipation is neglected. $Ra = 0$, $Mn = 80$	128
Figure 3.83 Forced convection flow in a square cavity with vertical adiabatic walls, viscous dissipation is neglected. $Ra = 0$, $Mn = 200$	129
Figure 3.84 Forced convection flow in a square cavity with vertical adiabatic walls, viscous dissipation is neglected. $Mn = 10$, $Ra = 10^3$	129
Figure 3.85 Forced convection flow in a square cavity with vertical adiabatic walls, viscous dissipation is neglected. $Mn = 10$, $Ra = 10^5$	130
Figure 3.86 Forced convection flow in a square cavity with vertical adiabatic walls, viscous dissipation is neglected. $Mn = 80$, $Ra = 10^4$	130

Figure 3.87 Forced convection flow in a square cavity with vertical adiabatic walls, viscous dissipation is neglected. $Mn = 80$, $Ra = 10^5$. . .	131
Figure 3.88 Forced convection flow in a square cavity with vertical adiabatic walls, viscous dissipation is added. $Mn = 10$, $Ra = 10^5$	132
Figure 3.89 Forced convection flow in a square cavity with vertical adiabatic walls, viscous dissipation is added. $Mn = 80$, $Ra = 10^5$	132
Figure 3.90 Forced convection flow in a circular cavity.	133
Figure 3.91 Forced convection flow in a circular cavity, viscous dissipation is neglected. $Mn = 0$, $Ra = 10^3$	134
Figure 3.92 Forced convection flow in a circular cavity, viscous dissipation is neglected. $Mn = 0$, $Ra = 10^4$	134
Figure 3.93 Forced convection flow in a circular cavity, viscous dissipation is neglected. $Mn = 10$, $Ra = 0$	135
Figure 3.94 Forced convection flow in a circular cavity, viscous dissipation is neglected. $Mn = 30$, $Ra = 0$	135
Figure 3.95 Forced convection flow in a circular cavity, viscous dissipation is neglected. $Mn = 10$, $Ra = 10^4$	136
Figure 3.96 Forced convection flow in a circular cavity, viscous dissipation is neglected. $Mn = 50$, $Ra = 10^4$	136
Figure 4.1 Flow configuration of MHD duct flow subjected to a horizontally applied uniform magnetic field.	143
Figure 4.2 MHD duct flow - Problem 1	144
Figure 4.3 MHD duct flow -Problem 1; Velocity profiles on $x = 0$, $x = 0.2$, $x = 0.5$, $x = 0.7$	145

Figure 4.4 MHD duct flow-Problem 1; Velocity and induced magnetic field profiles for varying Hartmann numbers. $\alpha = 0$ ($s_1 = 0$) left, $\alpha = 0.04$ ($s_1 < 1$) center, $\alpha = 0.4$ ($s_1 > 1$) right.	146
Figure 4.5 MHD duct flow -Problem 1; Velocity level curves for varying Hartmann numbers. $\alpha = 0.04$ ($s_1 < 1$) left, $\alpha = 0.4$ ($s_1 > 1$) right.	147
Figure 4.6 MHD duct flow - Problem 2	148
Figure 4.7 MHD duct flow -Problem 2; Velocity and induced magnetic field profiles for varying Hartmann numbers. $\alpha = 0$ ($s_2 = 0$) left, $\alpha = 0.001$ ($s_2 < 1$) center, $\alpha = 0.2$ ($s_2 > 1$) right.	149
Figure 4.8 MHD duct flow - Problem 2; Velocity level curves for varying Hartmann numbers. $\alpha = 0.001$ ($s_2 < 1$) left, $\alpha = 0.2$ ($s_2 > 1$) right.	150
Figure 4.9 MHD duct flow - Problem 3	151
Figure 4.10 MHD duct flow -Problem 3; Velocity and induced magnetic field profiles for varying Hartmann numbers. $\alpha = 0$ ($s_2 = 0$) left, $\alpha = 0.001$ $s_2 < 1$ center, $\alpha = 0.4$ $s_2 > 1$ right.	152
Figure 4.11 MHD duct flow-Problem 3; Velocity level curves for varying Hartmann numbers. $\alpha = 0.001$ ($s_2 < 1$) left, $\alpha = 0.4$ ($s_2 > 1$) right.	153
Figure 4.12 MHD duct flow - Problem 4	154
Figure 4.13 MHD duct flow -Problem 4; Velocity and induced magnetic field profiles for $Ha = 1, 5, 10$. Left: $\alpha = 0$ ($s_1 = s_2 = 0$). Center: from top to bottom $\alpha = 0.4$, $\alpha = 0.08$, $\alpha = 0.04$ ($s_1 < 1$, $s_2 < 1$), Right: from top to bottom $\alpha = 1.1$, $\alpha = 0.5$, $\alpha = 0.4$ ($s_1 > 1$, $s_2 > 1$).	155
Figure 4.14 MHD duct flow -Problem 4; Velocity and induced magnetic field profiles for $Ha = 50, 100$. Left: $\alpha = 0$ ($s_1 = s_2 = 0$). Center: from top to bottom $\alpha = 0.01$, $\alpha = 0.001$ ($s_1 < 1$, $s_2 < 1$), Right: from top to bottom $\alpha = 0.4$ ($s_1 > 1$, $s_2 > 1$).	156

Figure 4.15 MHD duct flow -Problem 4; Velocity level curves for varying Ha numbers. Left: from top to bottom $\alpha = 0.4, \alpha = 0.08, \alpha = 0.04, \alpha = 0.01, \alpha = 0.001$ ($s_1 < 1, s_2 < 1$), Right: from top to bottom $\alpha = 1.1, \alpha = 0.5, \alpha = 0.4, \alpha = 0.4, \alpha = 0.4$ ($s_1 > 1, s_2 > 1$).	157
Figure 4.16 MHD flow with partly insulated partly perfectly conducting walls	159
Figure 4.17 Problem 1, $d = 0$ case; velocity and induced magnetic field profiles for $Ha = 10, 30, 50$. $\alpha = 0$ ($s_2 = 0$) left, $\alpha = 0.01$ ($s_2 < 1$) center, $\alpha = 0.2$ ($s_2 > 1$) right.	160
Figure 4.18 Problem 1, $d = 0$ case; velocity level curves for $Ha = 10, 30, 50$. $\alpha = 0$ ($s_2 = 0$) left, $\alpha = 0.01$ ($s_2 < 1$) center, $\alpha = 0.2$ ($s_2 > 1$) right.	161
Figure 4.19 Problem 1, $d = 1$ case; velocity and induced magnetic field profiles for $Ha = 10, 30, 50$. $\alpha = 0$ ($s_2 = 0$) left, $\alpha = 0.01$ ($s_2 < 1$) center, $\alpha = 0.2$ ($s_2 > 1$) right.	162
Figure 4.20 Problem 1, $d = 1$ case; velocity level curves for $Ha = 10, 30, 50$. $\alpha = 0$ ($s_2 = 0$) left, $\alpha = 0.01$ ($s_2 < 1$) center, $\alpha = 0.2$ ($s_2 > 1$) right.	163
Figure 4.21 Problem 2, $d = 0$ case; velocity and induced magnetic field profiles for $Ha = 10, 30, 50$. $\alpha = 0$ ($s_2 = 0$) left, $\alpha = 0.01$ ($s_2 < 1$) center, $\alpha = 0.2$ ($s_2 > 1$) right.	164
Figure 4.22 Problem 2, $d = 0$ case; velocity level curves for $Ha = 10, 30, 50$. $\alpha = 0$ ($s_2 = 0$) left, $\alpha = 0.01$ ($s_2 < 1$) center, $\alpha = 0.2$ ($s_2 > 1$) right.	165
Figure 4.23 Problem 2, $d = 1$ case; velocity and induced magnetic field profiles for $Ha = 10, 30, 50$. $\alpha = 0$ ($s_2 = 0$) left, $\alpha = 0.01$ ($s_2 < 1$) center, $\alpha = 0.2$ ($s_2 > 1$) right.	166
Figure 4.24 Problem 2, $d = 1$ case; velocity level curves for $Ha = 10, 30, 50$. $\alpha = 0$ ($s_2 = 0$) left, $\alpha = 0.01$ ($s_2 < 1$) center, $\alpha = 0.2$ ($s_2 > 1$) right.	167
Figure 4.25 Problem geometry and the boundary conditions.	168

Figure 4.26 $s_2 = 0, l = 0$ from left to right $Ha = 10, 50, 100$	169
Figure 4.27 $s_2 = 0, l = 0$ from left to right $Ha = 10, 50, 100$, velocity profile on the bottom half of the channel.	170
Figure 4.28 $l = 0, Ha = 10$ from left to right $s_2 < 1$ ($\alpha = 0.001$), $s_2 =$ 1 ($\alpha = 0.1$), $s_2 > 1$ ($\alpha = 0.2$)	170
Figure 4.29 $s_2 = 0, Ha = 50$ from left to right $l = 0.1, l = 0.3, l = 0.5$. .	171
Figure 4.30 $Ha = 10, l = 0.3$ from left to right $s_2 < 1$ ($\alpha = 0.001$), $s_2 = 1$ ($\alpha = 0.1$), $s_2 > 1$ ($\alpha = 0.2$)	172
Figure 4.31 $Ha = 10, l = 0.5$ from left to right $s_2 < 1$ ($\alpha = 0.001$), $s_2 = 1$ ($\alpha = 0.1$), $s_2 > 1$ ($\alpha = 0.2$)	172
Figure 4.32 Electric potential boundary conditions.	173
Figure 4.33 Validation case. The bottom wall is on $y = 0$ line, $Ha = 0$, $s_2 = 0, l = 0.3, \Phi = 1$ on the top and $\Phi = -1$ on the bottom electrodes.174	174
Figure 4.34 $Ha = 10, s_2 = 0$ from left to right $l = 0.1, 0.3, 0.5$	174
Figure 4.35 $Ha = 50, s_2 = 0$ from left to right $l = 0.1, 0.3, 0.5$	175
Figure 4.36 $Ha = 10, l = 0.3$ from left to right $s_2 < 1$ ($\alpha = 0.001$), $s_2 = 1$ ($\alpha = 0.1$), $s_2 > 1$ ($\alpha = 0.2$).	175

NOMENCLATURE

BEM	Boundary element method
DRBEM	Dual reciprocity boundary element method
MHD	Magnetohydrodynamics
FHD	Ferrohydrodynamics
BFD	Biomagnetic fluid dynamics
CFD	Computational fluid dynamics
MEMS	Micromechanical systems
\mathbf{n}	unit outward normal to the boundary
$\mathbf{V} = (u, v, w)$	velocity field
\mathbf{g}	gravitational field
\mathbf{B}	induced magnetic field
\mathbf{H}	magnetic field
\mathbf{E}	electric field
\mathbf{j}	electric current density
Φ	electric potential
Ω	problem domain
Γ	boundary of the problem domain
Ψ	stream function
T	temperature
P	pressure
Mn	magnetic number
Re	Reynolds number
Pr	Prandtl number
Ec	Eckert number
Ra	Rayleigh number
Nu_{avg}	average Nusselt number
ϵ	temperature number
ρ	density
μ	dynamic viscosity

ν	kinematic viscosity
c_p	specific heat
k	thermal conductivity
σ	electrical conductivity
μ_0	magnetic permeability of vacuum
χ	magnetic susceptibility
β	thermal expansion coefficient
H	magnetic field intensity
M	magnetization
M_T	magnetization depending on the temperature
I	electric current
h, L	characteristic length
U	characteristic velocity
t	time
x, y, z	Cartesian coordinates

CHAPTER 1

INTRODUCTION

A boundary value problem is a coupled system, consisting of differential equations together with boundary conditions for the unknowns. Many problems arising in fluid dynamics, magnetohydrodynamics, ferrohydrodynamics and thermodynamics are modeled in terms of boundary value problems.

Fluid dynamics is a discipline concerned with motion of fluids. Fluid is a material that deforms continuously when influenced by a shear stress (force per unit area) of any magnitude such as gases, plasmas and liquids [1]. It is possible to find an application of fluid dynamics almost every area in our daily lives, such as blood flow through arteries, water flow through rivers, hurricanes, air flow over planes or cars. All engineering disciplines require some expertise in the area of fluid mechanics [2]. The analysis of fluid motion is considerable in the designs of airplanes, turbines, valves and in transport systems.

The interaction of the fluid with the magnetic field or electromagnetic field is made use of in nuclear fusion, high speed noiseless printing and transformer cooling. Magnetohydrodynamics (MHD) theory deals with the influence of the applied magnetic field on the flow of electrically conducting fluids (water, liquid metals). The interaction of the fluid with the magnetic field takes place and the investigation of the fluid motion stands the simultaneous consideration of the fluid mechanics and the electromagnetic field equations. Ferrohydrodynamics (FHD) is an area dealing with the mechanics of electrically nonconducting fluids subjected to magnetic effect. The body force acting on the fluid is due to the polarization force. There are several types of magnetic fluids in FHD. In general, a ferrofluid is homogeneous fluid composed of magnetic nanoparticles (e.g. iron, nickel) coated by a molecular layer of a dispersant and a carrier fluid

[3]. Blood, mineral oil or paint flows are also investigated under the FHD theory. Micromechanical system (MEMS) devices are one of the most important applications of ferrofluids where the flow control is a critical factor. The use of ferrofluids in electronic packing, aerospace and microscaled heat exchangers makes it a novel technology branch.

Fluid motion and its thermal characteristics under the influence of magnetic field are described by continuity, momentum, energy and magnetic induction (if the fluid is electrically conducting) equations which are coupled, nonlinear partial differential equations. The solution of full system of equations requires a numerical approach. Computational fluid dynamics (CFD) is a field using the data structures or numerical analysis to solve fluid dynamics problems. There are quite a number of numerical methods that are used to simulate the flow behavior such as finite difference method (FDM), finite element method (FEM), boundary element method (BEM) and finite volume method (FVM). Among these the BEM is the one which requires only the boundary discretization. It transforms the partial differential equations into the boundary integral equations by the use of fundamental solutions. Hence, the resultant matrix-vector equation is small in size when compared to other domain type discretization methods. The dual reciprocity boundary element method (DRBEM) is used to approximate the inhomogeneities in the equations by a series of radial basis functions. It is the most suitable boundary nature method when the partial differential equation involves time derivative, convection and some nonlinear terms. The DRBEM coordinate matrix, consisting of the radial basis functions, is established once and easily handles the nonlinearities in the equations. It is made use of in the approximation of the spatial derivatives of the unknowns and even in the approximation of the pressure boundary conditions.

In this chapter, fundamental equations of the fluid dynamics and magnetohydrodynamics are introduced. The governing equations for the FHD and MHD flows are presented in terms of the primitive variables (velocity-pressure formulation). The derivation of the pressure equation is given. Previous studies on the thesis subject and the originality of the thesis are discussed. Then, the plan of the thesis is explained.

1.1 Fluid Dynamics Equations

In this section, momentum equations describing the fluid motion, energy equation allowing the temperature difference in the fluid and the magnetic induction equations introducing the induced magnetic field in the fluid environment are presented.

1.1.1 Continuity Equation

The differential continuity equation is derived from the conservation of mass law. To derive the equation an infinitesimal volume element is taken from the flow region. The total change of the mass in this volume element must be equal to the difference between the mass flows in and the mass flows out from the element. This is expressed as [2]

$$\frac{\partial \rho}{\partial t} + u \frac{\partial \rho}{\partial x} + v \frac{\partial \rho}{\partial y} + w \frac{\partial \rho}{\partial z} + \rho \left(\frac{\partial u}{\partial x} + \frac{\partial v}{\partial y} + \frac{\partial w}{\partial z} \right) = 0 \quad (1.1)$$

where $\mathbf{V} = (u, v, w)$ is the fluid velocity field, t denotes the time and ρ is the density of the fluid.

To simplify the notation define the material derivative (corresponds to the rate of change at instantaneous time)

$$\frac{D}{Dt} = \frac{\partial}{\partial t} + u \frac{\partial}{\partial x} + v \frac{\partial}{\partial y} + w \frac{\partial}{\partial z} \quad (1.2)$$

and the divergence operator

$$\nabla = \frac{\partial}{\partial x} \mathbf{i} + \frac{\partial}{\partial y} \mathbf{j} + \frac{\partial}{\partial z} \mathbf{k} \quad (1.3)$$

with unit coordinate vectors \mathbf{i} , \mathbf{j} and \mathbf{k} . Then, the continuity equation becomes

$$\frac{D\rho}{Dt} + \rho \nabla \cdot \mathbf{V} = 0 \quad (1.4)$$

which reduces to

$$\nabla \cdot \mathbf{V} = 0 \quad (1.5)$$

for an incompressible (constant density) fluid.

1.1.2 Momentum Equations

The continuity equation is not enough to determine the velocity and the pressure of a fluid motion. Momentum equations together with initial and boundary conditions are required for a well-defined fluid flow. The momentum equation is derived from the conservation of momentum law as [2, 4]

$$\rho \frac{D\mathbf{V}}{Dt} = -\nabla P + \mu \nabla^2 \mathbf{V} + \rho \mathbf{g} + \mathbf{f} \quad (1.6)$$

for an incompressible flow. Here, P , μ and \mathbf{g} denote pressure, dynamic viscosity and the gravitational field; respectively. The viscosity is the internal stickiness of the fluid and results in shear stress within the flow. The left-hand side of the momentum equation presents the momentum of the fluid and the right-hand side contains, respectively, the pressure gradient, the viscous forces, the gravitational force and an additional force. In this thesis, magnetization force $\mathbf{f} = \mu_0 M \nabla H$, and the Lorentz force $\mathbf{f} = \mathbf{j} \times \mathbf{B}$ are considered as additional forces. Here, \mathbf{j} and \mathbf{B} are the electric current density and the induced magnetic field, and M and H are the magnetization and magnetic field strengths, respectively. μ_0 is the magnetic permeability of vacuum. In electrically conducting fluids Lorentz force dominates the magnetization force whereas in electrically nonconducting fluids the leading additional force is the magnetization force. The operator

$$\nabla^2 = \frac{\partial^2}{\partial x^2} + \frac{\partial^2}{\partial y^2} + \frac{\partial^2}{\partial z^2} \quad (1.7)$$

is the Laplacian. The differential momentum equations are called the Navier-Stokes equations.

1.1.3 Energy Equation

The differential energy equation for an incompressible fluid is obtained by the application of the conservation of energy and the Fourier laws in a control volume [5]

$$\rho c_p \frac{DT}{Dt} = k \nabla^2 T \quad (1.8)$$

where c_p and k are the specific heat and the thermal conductivity of the fluid. Energy equation may attain some additional terms when the temperature of the fluid is influenced by external forces.

1.1.4 Magnetic Induction Equations

The magnetic induction equation describes the temporal alternation of the induced magnetic field \mathbf{B} owing to diffusion $\nabla^2\mathbf{B}$, advection $(\mathbf{V} \cdot \nabla)\mathbf{B}$ and field intensity sources $(\mathbf{B} \cdot \nabla)\mathbf{V}$. The magnetic induction equation is derived through Ohm's law and Maxwell equations using the fact that fluid is incompressible and \mathbf{B} is solenoidal (i.e. $\nabla \cdot \mathbf{B} = 0$).

Ohm's law represents the current density in a moving conductor [6]

$$\mathbf{j} = \sigma(\mathbf{E} + \mathbf{V} \times \mathbf{B}) . \quad (1.9)$$

The combination of Ampere's and Faraday's laws gives the Maxwell equations

$$\nabla \times \mathbf{H} = \mathbf{j} \quad (1.10)$$

$$\nabla \times \mathbf{E} = -\frac{\partial}{\partial t}(\mu_0\mathbf{H}) \quad (1.11)$$

where displacement currents are negligible and \mathbf{E} , \mathbf{H} are the electric field and the magnetic field, respectively. $\mathbf{B} = \mu_0\mathbf{H}$ and σ is the electrical conductivity of the fluid.

Applying curl operator $(\nabla \times .)$ on Ohm's law, substituting \mathbf{E} and \mathbf{j} from the Maxwell equations and assuming \mathbf{B} is solenoidal the magnetic induction equation is obtained for the incompressible fluids as [6]

$$\frac{\partial \mathbf{B}}{\partial t} + (\mathbf{V} \cdot \nabla)\mathbf{B} = \frac{1}{\mu_0\sigma} \nabla^2\mathbf{B} + (\mathbf{B} \cdot \nabla)\mathbf{V} . \quad (1.12)$$

1.2 FHD Stokes Flow

Stokes flow is an incompressible viscous flow in slow motion. Study of slow and viscous flow in a pipe with moving boundaries provides useful information on flow behavior in distributive mixing, which has many industrial and engineering applications [7, 8]. A flow containing very small particles moving in the fluid, for example settling of dust particles and the swimming of microorganisms are considered as Stokes flow. Fluid flow through small cracks or channels (ground water or oil) such as in hydrodynamic lubrication or the seepage in sand or rock formations are other examples of Stokes flow. The flow of high-viscosity fluids

may also be described as Stokes flow, for example, the extrusion of melts, transport of paints, heavy oils or food-processing materials. Stokes flow equations are a subset of incompressible flow equations whose nonlinear convective terms are negligibly small. For the solution of Stokes flow three formulations are well known: these are in terms of primitive variables as velocity-pressure, stream function-vorticity and velocity-vorticity forms. In this thesis, Stokes flow equations are considered together with the magnetization force terms coming from the FHD theory. A pressure equation is derived and an approximation for the pressure boundary conditions is generated through the DRBEM coordinate matrix.

We consider the two-dimensional, steady (time independent), laminar flow of an incompressible, electrically non-conducting, magnetizable fluid in a long impermeable pipe with square or circular cross-section (cavity). The fluid is pumped within the pipe due to a constant pressure gradient in the pipe-axis direction. The flow is fully developed, in other words, the flow behavior remains the same in each cross-section perpendicular to the axial direction. The flow is under the influence of the magnetic field generated by a thin wire carrying electric current. The governing equations of the fluid flow are from the case of ferrohydrodynamics [3]. Continuity and momentum equations defining the two-dimensional flow in terms of dimensional velocity $\vec{V} = (\bar{u}, \bar{v}, \bar{w})$ and pressure \bar{P} are given by

$$\frac{\partial \bar{u}}{\partial \bar{x}} + \frac{\partial \bar{v}}{\partial \bar{y}} = 0 \quad (1.13)$$

$$\bar{u} \frac{\partial \bar{u}}{\partial \bar{x}} + \bar{v} \frac{\partial \bar{u}}{\partial \bar{y}} = -\frac{1}{\rho} \frac{\partial \bar{P}}{\partial \bar{x}} + \nu \left(\frac{\partial^2 \bar{u}}{\partial \bar{x}^2} + \frac{\partial^2 \bar{u}}{\partial \bar{y}^2} \right) + \frac{\mu_0 \bar{M}}{\rho} \frac{\partial \bar{H}}{\partial \bar{x}} \quad (1.14)$$

$$\bar{u} \frac{\partial \bar{v}}{\partial \bar{x}} + \bar{v} \frac{\partial \bar{v}}{\partial \bar{y}} = -\frac{1}{\rho} \frac{\partial \bar{P}}{\partial \bar{y}} + \nu \left(\frac{\partial^2 \bar{v}}{\partial \bar{x}^2} + \frac{\partial^2 \bar{v}}{\partial \bar{y}^2} \right) + \frac{\mu_0 \bar{M}}{\rho} \frac{\partial \bar{H}}{\partial \bar{y}} \quad (1.15)$$

$$\bar{u} \frac{\partial \bar{w}}{\partial \bar{x}} + \bar{v} \frac{\partial \bar{w}}{\partial \bar{y}} = -\frac{1}{\rho} \frac{\partial \bar{P}}{\partial \bar{z}} + \nu \left(\frac{\partial^2 \bar{w}}{\partial \bar{x}^2} + \frac{\partial^2 \bar{w}}{\partial \bar{y}^2} \right) \quad (1.16)$$

where ν , \bar{H} and \bar{M} are the kinematic viscosity, the magnetic field strength and the magnetization, respectively. $\bar{M} = \chi \bar{H}$ where χ is the magnetic susceptibility of the fluid. The additional force terms in the momentum equations are the components of the magnetization force. The magnetization force in the z - (axial) direction vanishes due to the problem configuration. On the cross-section

of the pipe the wire acts as a point magnetic source.

In fully developed flows pressure is split as [9]

$$\bar{P}(\bar{x}, \bar{y}, \bar{z}) = \bar{P}_1(\bar{z}) + \bar{p}(\bar{x}, \bar{y}) \quad (1.17)$$

and

$$\frac{\partial \bar{P}}{\partial \bar{z}} = \frac{\partial \bar{P}_1}{\partial \bar{z}} = \bar{P}_z = \text{constant} . \quad (1.18)$$

The components of the magnetic field $\bar{\mathbf{H}}$ are [10]

$$\bar{H}_x = -\frac{I}{2\pi} \frac{\bar{y} - \bar{a}_2}{(\bar{x} - \bar{a}_1)^2 + (\bar{y} - \bar{a}_2)^2}, \quad \bar{H}_y = \frac{I}{2\pi} \frac{\bar{x} - \bar{a}_1}{(\bar{x} - \bar{a}_1)^2 + (\bar{y} - \bar{a}_2)^2} \quad (1.19)$$

where (\bar{a}_1, \bar{a}_2) denotes the place of the point source, (\bar{x}, \bar{y}) is any point inside the cavity and I is the current carried by the wire. For square cavity $(\bar{a}_1, \bar{a}_2) = (h/2, -\bar{c})$ and for circular cavity $(\bar{a}_1, \bar{a}_2) = (0, -h - \bar{c})$ with \bar{c} being the closest distance from the point source to the cavity. The magnitude of the magnetic field (magnetic field strength) is given by

$$\bar{H}(\bar{x}, \bar{y}) = \sqrt{\bar{H}_x^2 + \bar{H}_y^2} = \frac{I}{2\pi} \frac{1}{\sqrt{(\bar{x} - \bar{a}_1)^2 + (\bar{y} - \bar{a}_2)^2}} . \quad (1.20)$$

Introducing non-dimensional variables $H = \bar{H}/H_0$, $x = \bar{x}/h$ and $y = \bar{y}/h$, the magnetic field strength in non-dimensional form is obtained for a square cavity as

$$H(x, y) = \frac{|a_2|}{\sqrt{(x - a_1)^2 + (y - a_2)^2}} \quad (1.21)$$

and for a circular cavity as

$$H(x, y) = \frac{|c|}{\sqrt{(x - a_1)^2 + (y - a_2)^2}} \quad (1.22)$$

where $(a_1, a_2) = (\bar{a}_1/h, \bar{a}_2/h)$, h is the height of the square cavity and the radius of the circular cavity, H_0 is the magnetic field strength at $(h/2, 0)$ for square and $(0, -h)$ for circular cavity. $c = \bar{c}/h$.

When the flow is slow or the fluid is highly viscous, Reynolds number depending on the axial velocity of the fluid is very small. Introducing non-dimensional variables

$$x = \frac{\bar{x}}{h}, \quad y = \frac{\bar{y}}{h}, \quad z = \frac{\bar{z}}{h}, \quad u = \frac{\bar{u}}{U}, \quad v = \frac{\bar{v}}{U}, \quad w = \frac{\bar{w}}{U}, \quad P = \frac{\bar{P}h}{\mu U}, \quad H = \frac{\bar{H}}{H_0} \quad (1.23)$$

where U is the characteristic velocity, the non-dimensional governing equations in terms of velocity (u, v, w) and the pressure $p(x, y)$ are obtained

$$\frac{\partial u}{\partial x} + \frac{\partial v}{\partial y} = 0 \quad (1.24)$$

$$Re(u \frac{\partial u}{\partial x} + v \frac{\partial u}{\partial y}) = -\frac{\partial p}{\partial x} + (\frac{\partial^2 u}{\partial x^2} + \frac{\partial^2 u}{\partial y^2}) + \frac{Mn}{Re} H \frac{\partial H}{\partial x} \quad (1.25)$$

$$Re(u \frac{\partial v}{\partial x} + v \frac{\partial v}{\partial y}) = -\frac{\partial p}{\partial y} + (\frac{\partial^2 v}{\partial x^2} + \frac{\partial^2 v}{\partial y^2}) + \frac{Mn}{Re} H \frac{\partial H}{\partial y} \quad (1.26)$$

$$Re(u \frac{\partial w}{\partial x} + v \frac{\partial w}{\partial y}) = -P_z + (\frac{\partial^2 w}{\partial x^2} + \frac{\partial^2 w}{\partial y^2}) \quad (1.27)$$

where non-dimensional parameters Re and Mn are the Reynolds number and the magnetic number, respectively, defined as

$$Re = \frac{Uh}{\nu}, \quad Mn = \frac{\mu_0 \chi H_0^2 h^2}{\nu^2 \rho}. \quad (1.28)$$

In the case of Stokes flow, $Re \ll 1$ and convection terms in the momentum equations are neglected. Then, we have

$$\frac{\partial u}{\partial x} + \frac{\partial v}{\partial y} = 0 \quad (1.29)$$

$$\nabla^2 u = \frac{\partial p}{\partial x} - MH \frac{\partial H}{\partial x} \quad (1.30)$$

$$\nabla^2 v = \frac{\partial p}{\partial y} - MH \frac{\partial H}{\partial y} \quad (1.31)$$

$$\nabla^2 w = P_z \quad (1.32)$$

where $M = Mn/Re$.

The z - momentum equation is not coupled with the others and depends on the pressure gradient P_z only for the Stokes flow. Thus, the axial velocity is not affected by the magnetization force and this equation will not be considered in the Stokes flow.

In this thesis, our aim is to simulate the flow in terms of original variables; velocity and the pressure. The equation for pressure $p(x, y)$ is obtained by taking the derivative of equation (1.30) with respect to x and the derivative of equation (1.31) with respect to y , and adding them. Then, using the continuity equation pressure Poisson equation becomes

$$\nabla^2 p = M \left(\left(\frac{\partial H}{\partial x} \right)^2 + \left(\frac{\partial H}{\partial y} \right)^2 + H \nabla^2 H \right). \quad (1.33)$$

In order to visualize the flow patterns in the cavity, stream function for two-dimensional flow is introduced

$$u = \frac{\partial \Psi}{\partial y}, \quad v = -\frac{\partial \Psi}{\partial x} \quad (1.34)$$

which satisfies the continuity equation automatically. Then, the stream function equation is obtained as

$$\nabla^2 \Psi = \frac{\partial u}{\partial y} - \frac{\partial v}{\partial x} . \quad (1.35)$$

Equations (1.30)-(1.33) and (1.35) together with the Dirichlet type no-slip boundary conditions (the velocity of the fluid is equal to the velocity of the boundary at the fluid-solid interface)

$$u(x, y) = u_b, \quad v(x, y) = v_b, \quad p(x, y) = p_b, \quad \Psi(x, y) = \Psi_b \quad (1.36)$$

define the FHD Stokes flow problem. The equations are discretized with BEM or the DRBEM and solved iteratively. The test problems, the numerical solution procedure and the derivation of the pressure boundary conditions are explained in detail in Chapter 3, Section 3.1.

1.3 FHD Incompressible Flow

This problem is a generalization of FHD Stokes flow case. Incompressible fluid flow subjected to a uniform or non-uniform (e.g. point magnetic source) magnetic field has wide range of applications in engineering and medicine. Flow in cooling and insulating systems, ferrofluid seals, audio speakers, material separation, solenoids, domain detection systems, sensors and switches are some examples of FHD incompressible flow.

In this thesis, the FHD incompressible, steady flow is considered in pipes with square and circular cross-sections and in annular pipes. The influence of a magnetic field generated by multiple point magnetic sources is also studied. In these studies velocity-pressure formulation is used for modeling the problem.

Introduce the following non-dimensional variables for the equations (1.13)-(1.16)

$$x = \frac{\bar{x}}{h}, \quad y = \frac{\bar{y}}{h}, \quad z = \frac{\bar{z}}{h}, \quad u = \frac{\bar{u}h}{\nu}, \quad v = \frac{\bar{v}h}{\nu}, \quad w = \frac{\bar{w}h}{\nu}, \quad P = \frac{\bar{P}h^2}{\rho\nu^2}, \quad H = \frac{\bar{H}}{H_0} \quad (1.37)$$

and split the pressure as in (1.17) and (1.18). Then, non-dimensional equations modeling the incompressible flow under the influence of point magnetic source(s) are

$$\frac{\partial u}{\partial x} + \frac{\partial v}{\partial y} = 0 \quad (1.38)$$

$$\nabla^2 u = \frac{\partial p}{\partial x} + u \frac{\partial u}{\partial x} + v \frac{\partial u}{\partial y} - MnH \frac{\partial H}{\partial x} \quad (1.39)$$

$$\nabla^2 v = \frac{\partial p}{\partial y} + u \frac{\partial v}{\partial x} + v \frac{\partial v}{\partial y} - MnH \frac{\partial H}{\partial y} \quad (1.40)$$

$$\nabla^2 w = P_z + u \frac{\partial w}{\partial x} + v \frac{\partial w}{\partial y} \quad (1.41)$$

where Mn is the magnetic number as defined in equation (1.28). In this problem, the axial velocity profile changes according to the magnetization force. Thus, the influence of the magnetization force on the axial velocity profile is also taken into account. Pressure and the stream function equations are found similarly to the Stokes flow case including the convection terms

$$\nabla^2 p = Mn \left(\left(\frac{\partial H}{\partial x} \right)^2 + \left(\frac{\partial H}{\partial y} \right)^2 + H \nabla^2 H \right) - \left(\frac{\partial u}{\partial x} \right)^2 - \left(\frac{\partial v}{\partial y} \right)^2 - 2 \frac{\partial v}{\partial x} \frac{\partial u}{\partial y} \quad (1.42)$$

$$\nabla^2 \Psi = \frac{\partial u}{\partial y} - \frac{\partial v}{\partial x} . \quad (1.43)$$

The FHD incompressible flow problem is considered with the no-slip boundary conditions

$$u(x, y) = u_b, \quad v(x, y) = v_b, \quad w(x, y) = w_b, \quad p(x, y) = p_b, \quad \Psi(x, y) = \Psi_b . \quad (1.44)$$

Numerical solution procedure of the FHD incompressible flow problem is more complicated than the FHD Stokes flow problem due to the nonlinear convection terms. Section 3.2 and Section 3.3 of Chapter 3 express the approximation of the pressure boundary conditions and the iterative solution procedure as well as the numerical results for various flow configurations.

1.4 FHD Forced Convection Flow

A forced convection flow occurs in the presence of an external forcing condition. For example, when the fluid is driven by a fan or pump, or a solid is dragged

through the fluid [5]. Biomagnetic fluid dynamics (BFD) is the area, investigating the biological fluid dynamics in the presence of magnetic fields. Biomagnetic fluid is a living material which is influenced by an applied magnetic field such as blood. The magnetization property of blood comes from the cell membrane and the hemoglobin molecule, iron-based protein, carried by the red blood cells [11]. An externally applied magnetic field change the flow and the heat transfer characteristics of blood significantly. The mathematical formulation of BFD is similar to the case of FHD. There are various applications of magnetic fields in medicine and bioengineering. For example, cell separation devices [12], drug targeting [13], magnet therapies [14], hypothermia treatment of cancer tumors [15] and reduction of bleeding during surgeries.

Consider a fully developed, steady flow of biomagnetic fluid in a long impermeable pipe with square or circular cross-section. The fluid is driven by a constant pressure gradient \bar{P}_z along the axial direction. The flow and the heat transfer in the pipe are affected by magnetization and buoyancy forces. Magnetization force is generated by a long wire carrying electric current placed \bar{c} units below and parallel to the axis of the pipe. Buoyancy force occurs due to the temperature differences between the walls of the pipe and the gravitational acceleration. Being a fully developed flow the problem is considered in the two-dimensional cross-section of the pipe and in this case the electric wire serves as a point magnetic source as in FHD incompressible and Stokes flows. There is a longitudinal heat transport, but isotherms have the same profile on each cross-section of the pipe [16]. Magnetization, buoyancy forces and the constant pressure gradient in the axial direction develop a forced convection flow in the cavity. The axial velocity can be separately obtained with the computed plane velocity components. The governing equations in dimensional form are given by continuity, momentum and the energy equations in terms of pressure \bar{P} , velocity $(\bar{u}, \bar{v}, \bar{w})$ and the temperature \bar{T} of the fluid which are two-dimensional in the cross-section of the pipe [17]

$$\frac{\partial \bar{u}}{\partial \bar{x}} + \frac{\partial \bar{v}}{\partial \bar{y}} = 0 \quad (1.45)$$

$$\bar{u} \frac{\partial \bar{u}}{\partial \bar{x}} + \bar{v} \frac{\partial \bar{u}}{\partial \bar{y}} = -\frac{1}{\rho} \frac{\partial \bar{P}}{\partial \bar{x}} + \nu \left(\frac{\partial^2 \bar{u}}{\partial \bar{x}^2} + \frac{\partial^2 \bar{u}}{\partial \bar{y}^2} \right) + \frac{\mu_0 \bar{M}_T}{\rho} \frac{\partial \bar{H}}{\partial \bar{x}} \quad (1.46)$$

$$\bar{u} \frac{\partial \bar{v}}{\partial \bar{x}} + \bar{v} \frac{\partial \bar{v}}{\partial \bar{y}} = -\frac{1}{\rho} \frac{\partial \bar{P}}{\partial \bar{y}} + \nu \left(\frac{\partial^2 \bar{v}}{\partial \bar{x}^2} + \frac{\partial^2 \bar{v}}{\partial \bar{y}^2} \right) + \frac{\mu_0 \bar{M}_T}{\rho} \frac{\partial \bar{H}}{\partial \bar{y}} + g\beta(\bar{T} - T_{cold}) \quad (1.47)$$

$$\bar{u} \frac{\partial \bar{w}}{\partial \bar{x}} + \bar{v} \frac{\partial \bar{w}}{\partial \bar{y}} = -\frac{1}{\rho} \frac{\partial \bar{P}}{\partial \bar{z}} + \nu \left(\frac{\partial^2 \bar{w}}{\partial \bar{x}^2} + \frac{\partial^2 \bar{w}}{\partial \bar{y}^2} \right) \quad (1.48)$$

$$\begin{aligned} \rho c_p \left(\bar{u} \frac{\partial \bar{T}}{\partial \bar{x}} + \bar{v} \frac{\partial \bar{T}}{\partial \bar{y}} \right) &= -\mu_0 \bar{T} \frac{\partial \bar{M}_T}{\partial \bar{T}} \left(\bar{u} \frac{\partial \bar{H}}{\partial \bar{x}} + \bar{v} \frac{\partial \bar{H}}{\partial \bar{y}} \right) + k \left(\frac{\partial^2 \bar{T}}{\partial \bar{x}^2} + \frac{\partial^2 \bar{T}}{\partial \bar{y}^2} \right) \\ &+ \mu \left[2 \left(\frac{\partial \bar{u}}{\partial \bar{x}} \right)^2 + 2 \left(\frac{\partial \bar{v}}{\partial \bar{y}} \right)^2 + \left(\frac{\partial \bar{v}}{\partial \bar{x}} + \frac{\partial \bar{u}}{\partial \bar{y}} \right)^2 \right]. \end{aligned} \quad (1.49)$$

where β is the thermal expansion coefficient of the fluid, and g is the magnitude of the gravitational acceleration. $\bar{M}_T = \chi \bar{H}(T_c - \bar{T})$ is the magnetization depending on the temperature this time and T_c is the Curie temperature of iron. The terms $\frac{\mu_0 \bar{M}_T}{\rho} \frac{\partial \bar{H}}{\partial \bar{x}}$ and $\frac{\mu_0 \bar{M}_T}{\rho} \frac{\partial \bar{H}}{\partial \bar{y}}$ are the components of the magnetization force so called Kelvin force. $g\beta(\bar{T} - T_{cold})$ is the buoyancy force, where T_{cold} is the temperature of the cold wall. The second term in the energy equation is the heating due to magnetization and the last term is the viscous dissipation which is a heat source caused by the friction between the fluid particles.

Splitting the pressure as in (1.17) and (1.18) and introducing the non-dimensional variables

$$\begin{aligned} x &= \frac{\bar{x}}{h}, & y &= \frac{\bar{y}}{h}, & z &= \frac{\bar{z}}{h}, & u &= \frac{\bar{u}h}{\nu}, & v &= \frac{\bar{v}h}{\nu}, & w &= \frac{\bar{w}h}{\nu}, \\ P &= \frac{\bar{P}h^2}{\rho\nu^2}, & H &= \frac{\bar{H}}{H_0}, & T &= \frac{\bar{T} - T_{cold}}{T_{hot} - T_{cold}} \end{aligned} \quad (1.50)$$

the governing equations in non-dimensional form are obtained as

$$\frac{\partial u}{\partial x} + \frac{\partial v}{\partial y} = 0 \quad (1.51)$$

$$\nabla^2 u = \frac{\partial p}{\partial x} + u \frac{\partial u}{\partial x} + v \frac{\partial u}{\partial y} - Mn(T_c - T)H \frac{\partial H}{\partial x} \quad (1.52)$$

$$\nabla^2 v = \frac{\partial p}{\partial y} + u \frac{\partial v}{\partial x} + v \frac{\partial v}{\partial y} - Mn(T_c - T)H \frac{\partial H}{\partial y} - \frac{Ra}{Pr} T \quad (1.53)$$

$$\nabla^2 w = P_z + u \frac{\partial w}{\partial x} + v \frac{\partial w}{\partial y} \quad (1.54)$$

$$\begin{aligned} \nabla^2 T &= Pr \left(u \frac{\partial T}{\partial x} + v \frac{\partial T}{\partial y} \right) - MnEcPr(\epsilon + T)H \left(u \frac{\partial H}{\partial x} + v \frac{\partial H}{\partial y} \right) \\ &- EcPr \left(2 \left(\frac{\partial u}{\partial x} \right)^2 + 2 \left(\frac{\partial v}{\partial y} \right)^2 + \left(\frac{\partial v}{\partial x} + \frac{\partial u}{\partial y} \right)^2 \right). \end{aligned} \quad (1.55)$$

The pressure equation is derived using a similar procedure to the FHD Stokes flow problem

$$\begin{aligned}\nabla^2 p = & \frac{Ra}{Pr} \frac{\partial T}{\partial y} - \left(\frac{\partial u}{\partial x}\right)^2 - \left(\frac{\partial v}{\partial y}\right)^2 - 2\frac{\partial v}{\partial x} \frac{\partial u}{\partial y} \\ & - Mn \left(\frac{\partial T}{\partial x} H \frac{\partial H}{\partial x} + \frac{\partial T}{\partial y} H \frac{\partial H}{\partial y} \right) \\ & + Mn(T_c - T) \left(\left(\frac{\partial H}{\partial x}\right)^2 + \left(\frac{\partial H}{\partial y}\right)^2 + H \nabla^2 H \right).\end{aligned}\quad (1.56)$$

The stream function equation is also added to the system of equations and solved

$$\nabla^2 \Psi = \frac{\partial u}{\partial y} - \frac{\partial v}{\partial x} . \quad (1.57)$$

The non-dimensional parameters entering the problem are

$$Mn = \frac{\mu_0 \chi H_0^2 (T_{hot} - T_{cold}) h^2}{\nu^2 \rho} \quad (\text{Magnetic number}) \quad (1.58)$$

$$Pr = \frac{\rho c_p \nu}{k} \quad (\text{Prandtl number}) \quad (1.59)$$

$$Ra = \frac{g \rho c_p \beta (T_{hot} - T_{cold}) h^3}{\nu k} \quad (\text{Rayleigh number}) \quad (1.60)$$

$$\epsilon = \frac{T_{cold}}{T_{hot} - T_{cold}} \quad (\text{Temperature number}) \quad (1.61)$$

$$Ec = \frac{\nu^2}{h^2 c_p (T_{hot} - T_{cold})} \quad (\text{Eckert number}) . \quad (1.62)$$

Magnetic number expresses the ratio of the magnetic forces and the inertia forces. Prandtl number is the ratio of the momentum and thermal diffusivities. Rayleigh number is the product of the Grashof number and the Prandtl number where Grashof number denotes the ratio of the buoyancy forces to viscous forces. Eckert number defines the kinetic energy of the flow relative to the boundary layer enthalpy difference.

Dirichlet type boundary conditions are valid for the velocity, pressure and stream function

$$u(x, y) = u_b, \quad v(x, y) = v_b, \quad w(x, y) = w_b, \quad p(x, y) = p_b, \quad \Psi(x, y) = \Psi_b \quad (1.63)$$

for the temperature Neumann or Dirichlet type boundary conditions are used

$$T(x, y) = T_b \quad \text{or} \quad \frac{\partial T}{\partial n} = T_n \quad (1.64)$$

where $\partial/\partial n$ is the derivative in the direction of unit outward normal \mathbf{n} to the boundary. Physically, if $T_n = 0$, then the corresponding boundary is called the adiabatic wall (i.e., the wall is thermally insulated). The flow configurations for the test problems, the numerical solution procedure and results are presented in Section 3.4 of Chapter 3.

1.5 MHD Duct Flow with Slipping Velocity Condition

The analysis of MHD flow behavior in pipes has considerable importance due to its wide range of applications in engineering and industrial processes such as pumps, cooling systems in nuclear reactors, generators, flow meters and transport control. Finding the exact solution of the problem is possible only for some special cases with no-slip boundary conditions [18].

We consider a fully developed, steady, pressure driven flow of an electrically conducting fluid in a rectangular pipe (duct). The flow is subjected to a horizontally applied uniform magnetic field $\mathbf{B}_0 = B_0 \mathbf{e}_x$. The problem is governed by the momentum and the magnetic induction equations. Being a fully developed flow both the velocity and the induced magnetic field vary only on the cross-section of the pipe (xy -plane). The dimensional form of the equations in terms of the velocity $\mathbf{V} = (0, 0, \bar{V}(\bar{x}, \bar{y}))$ and the induced magnetic field $\mathbf{B} = (B_0, 0, \bar{B}(\bar{x}, \bar{y}))$ are obtained through momentum and magnetic induction equations and Ampere's law (equation (1.10)) [6]

$$\rho\nu\left(\frac{\partial^2 \bar{V}}{\partial \bar{x}^2} + \frac{\partial^2 \bar{V}}{\partial \bar{y}^2}\right) + \frac{B_0}{\mu_0} \frac{\partial \bar{B}}{\partial \bar{x}} = \frac{\partial \bar{P}}{\partial \bar{z}} \quad (1.65)$$

$$\frac{1}{\mu_0 \sigma} \left(\frac{\partial^2 \bar{B}}{\partial \bar{x}^2} + \frac{\partial^2 \bar{B}}{\partial \bar{y}^2} \right) + B_0 \frac{\partial \bar{V}}{\partial \bar{x}} = 0. \quad (1.66)$$

The system of equations consists of only the third components of the momentum and the magnetic induction equations. The last term on the left-hand side of the momentum equation (1.65) is the Lorentz force which occurs due to the electrical conductivity of the fluid.

Introducing non-dimensional variables

$$x = \frac{\bar{x}}{L}, \quad y = \frac{\bar{y}}{L}, \quad V = \frac{\bar{V}}{V_0}, \quad B = \frac{\bar{B}}{V_0 \mu_0 \sqrt{\sigma \mu}} \quad (1.67)$$

where L is the half-height of the duct and $V_0 = -L^2(\frac{\partial \bar{P}}{\partial \bar{z}})/\mu$, one gets the dimensionless form of the MHD equations describing the MHD pressure driven flow

$$\nabla^2 V + Ha \frac{\partial B}{\partial x} = -1 \quad (1.68)$$

$$\nabla^2 B + Ha \frac{\partial V}{\partial x} = 0 . \quad (1.69)$$

In the system of equations Ha is the Hartmann number defined as

$$Ha = \frac{B_0 L \sqrt{\sigma}}{\sqrt{\rho \nu}} \quad (1.70)$$

and corresponds to the ratio of electromagnetic force to viscous force.

Mixed (Robin) type boundary condition is valid for the velocity in the case of slip at the walls

$$V + \alpha \frac{\partial V}{\partial n} = 0 \quad (1.71)$$

where α is the dimensionless slip length. The physical details of the slip boundary condition are given in Chapter 4.

Either Dirichlet or Neumann type boundary conditions are employed for the induced magnetic field

$$B(x, y) = B_b, \quad \text{or} \quad \frac{\partial B}{\partial n} = B_n . \quad (1.72)$$

If $B_b = 0$, then the pipe wall is electrically insulated. If $B_n = 0$, then the wall is perfectly conducting.

1.6 MHD Flow Between Parallel Infinite Plates with Slipping Velocity Condition

The flow of electrically conducting fluid between two parallel infinite conducting plates is called the Hartmann flow. The simulation of Hartmann flow provides practical information for the designs of space propulsion, liquid metal mixing and MHD generators.

In this problem, the MHD flow between two parallel infinite plates is considered under the effect of vertically applied magnetic field ($\mathbf{B}_0 = B_0 \mathbf{e}_y$). The fluid is viscous, incompressible, electrically conducting and the flow is laminar and

steady. The equations describing such flows are the same as those of MHD duct flow with zero pressure gradient and with its horizontal walls tending to infinity [6]

$$\rho\nu\left(\frac{\partial^2\bar{V}}{\partial\bar{x}^2} + \frac{\partial^2\bar{V}}{\partial\bar{y}^2}\right) + \frac{B_0}{\mu_0}\frac{\partial\bar{B}}{\partial\bar{y}} = 0 \quad (1.73)$$

$$\frac{1}{\mu_0\sigma}\left(\frac{\partial^2\bar{B}}{\partial\bar{x}^2} + \frac{\partial^2\bar{B}}{\partial\bar{y}^2}\right) + B_0\frac{\partial\bar{V}}{\partial\bar{y}} = 0 . \quad (1.74)$$

where $\bar{V}(\bar{x}, \bar{y})$ and $\bar{B}(\bar{x}, \bar{y})$ are the third components of the velocity and the magnetic induction fields. The plates contain either point or line electrodes symmetrically placed at the center of the plates. The fluid motion is generated from the interaction of the electrically conducting fluid with the imposed electric current travelling between the plates and the external magnetic field.

In this problem, electric potential between the infinite plates is also computed. Since the electric field is irrotational ($\nabla \times \mathbf{E} = 0$), it is expressed in terms of a scalar electric potential $\bar{\Phi}(\bar{x}, \bar{y})$ as

$$\mathbf{E} = -\nabla\bar{\Phi} . \quad (1.75)$$

Then, by the equation (1.9) (i.e. $\mathbf{j} = \sigma(\mathbf{E} + \mathbf{V} \times \mathbf{B})$) one gets

$$\mathbf{j} = \sigma(-\nabla\bar{\Phi} + \mathbf{V} \times \mathbf{B}) . \quad (1.76)$$

Taking divergence of both sides and using equation (1.10) (i.e. $\nabla \times \mathbf{H} = \mathbf{j}$) the electric potential equation is obtained

$$\frac{\partial^2\bar{\Phi}}{\partial\bar{x}^2} + \frac{\partial^2\bar{\Phi}}{\partial\bar{y}^2} + B_0\frac{\partial\bar{V}}{\partial\bar{x}} = 0 . \quad (1.77)$$

The variables defined in the equation (1.67) and $\Phi = \frac{\bar{\Phi}}{\Phi_0}$ where $\Phi_0 = LV_0B_0$ are used to obtain the non-dimensional form of the equations (1.73), (1.74) and (1.77) as

$$\nabla^2V + Ha\frac{\partial B}{\partial y} = 0 \quad (1.78)$$

$$\nabla^2B + Ha\frac{\partial V}{\partial y} = 0 \quad (1.79)$$

$$\nabla^2\Phi + \frac{\partial V}{\partial x} = 0 . \quad (1.80)$$

The boundary conditions for the slipping velocity and the induced magnetic field are similarly imposed as in the case of MHD duct flow with slipping velocity (Section 1.5). Neumann type boundary condition is valid for the electric potential

$$\frac{\partial \Phi}{\partial n} = \Phi_n . \quad (1.81)$$

where $\Phi_n = \pm 1$ at $y = \pm 1$ on the electrodes placed in the middle of the plates and $\Phi_n = 0$ outside the electrodes.

1.7 Helpful Identities and Numerical Techniques

In this section, some mathematical identities and the numerical techniques that are mentioned throughout the thesis are recalled.

1.7.1 Green's First Identity

Let u and v be scalar functions defined on some region $U \in \mathbb{R}^2$ and suppose that u is twice and v is once continuously differentiable. Then,

$$\int_U (v \nabla^2 u + \nabla v \nabla u) dA = \int_{\partial U} v \frac{\partial u}{\partial n} dl \quad (1.82)$$

where ∂U is the boundary of the region U and \mathbf{n} is the outward unit normal.

1.7.2 Gauss-Legendre Quadrature Method

If f is $2n$ times continuously differentiable the Gaussian formula on $[-1, 1]$ is given by [19]

$$\int_{-1}^1 f(x) dx \approx \sum_{j=1}^n w_j f(x_j) \quad (1.83)$$

where the nodes x_j 's are the zeros of the n -th degree Legendre polynomial P_n on $[-1, 1]$ and

$$w_j = \frac{-2}{(n+1)P_n'(x_j)P_{n+1}(x_j)} \quad \text{for } j = 1, 2, \dots, n . \quad (1.84)$$

The degree of precision for the integration formula is $2n - 1$ and the error is given by

$$E_n(f) = \int_{-1}^1 f(x)dx - \sum_{j=1}^n w_j f(x_j) = \frac{2^{(2n+1)}(n!)^4}{(2n+1)[(2n)!]^2} \cdot \frac{f^{(2n)}(\eta)}{(2n)!} \quad (1.85)$$

for some $-1 < \eta < 1$. The integrals on some finite interval $[a, b]$ can be reduced to an integral on $[-1, 1]$ by using a linear change of variables.

1.7.3 Gaussian Elimination with Pivoting

Gaussian elimination is the basic algorithm for solving linear equations of type $\mathbf{Ax} = \mathbf{c}$, [20].

In this algorithm first the matrix \mathbf{A} is factorized as $\mathbf{A} = \mathbf{PLU}$ where \mathbf{P} , \mathbf{L} and \mathbf{U} are permutation, unit lower triangular (with the ones on the diagonal) and nonsingular upper triangular matrices, respectively. Then, \mathbf{x} is solved as $\mathbf{x} = \mathbf{U}^{-1}(\mathbf{L}^{-1}\mathbf{P}^{-1}\mathbf{c})$.

If \mathbf{A} is nonsingular, then there exist permutations \mathbf{P}_1 and \mathbf{P}_2 , a unit lower triangular matrix \mathbf{L} and a nonsingular upper triangular matrix \mathbf{U} such that $\mathbf{P}_1\mathbf{A}\mathbf{P}_2 = \mathbf{LU}$. Only one of \mathbf{P}_1 and \mathbf{P}_2 are necessary. ($\mathbf{P}_1\mathbf{A}$ reorders the rows of \mathbf{A} and $\mathbf{A}\mathbf{P}_2$ reorders the columns of \mathbf{A} .)

If at the step i of Gaussian elimination, where the i -th column of \mathbf{L} is computed, the rows are reordered such that the largest entry in the column is on the diagonal, then this is called the Gaussian elimination with partial pivoting.

If at the step i , the rows and the columns are reordered such that the largest entry in the matrix is on the diagonal, then this is called the Gaussian elimination with complete pivoting.

1.8 Literature Survey

The study of the flow under the effect of a magnetic field has many industrial and medical applications such as food-processing, hydrodynamic lubrication, cell-separation devices, reduction of bleeding during surgeries, cooling and insulating systems. Application of a uniform or point source magnetic field on the

incompressible flows in pipes changes the flow behavior and induces magnetic field inside the fluid. Thus, it is possible to extract usable electrical energy and heat outside which is the basis of MHD generators, pumps and some medical instruments in bioengineering.

The flow of fluids are modeled by the continuity and the momentum equations resulting from the conservation of mass and momentum laws, respectively. If the fluid is highly viscous or the flow is in slow motion, Stokes flow, the assumption $Re \ll 1$ is valid and the momentum equations are simplified. 2D and 3D Stokes flows were considered by Young et al. [21] in a lid-driven square and cubical cavities using the method of fundamental solutions (MFS). They discussed also the effect of the number of source points and their locations on the numerical accuracy. Kutanaei et al. [22] investigated Stokes flow in a circular cavity using mesh-free local radial basis function-based differential quadrature method (RBF-DQ) which enables to approximate derivatives also at irregularly distributed points. Chen et al. [23] developed a new method for the Stokes flow in pipes with circular boundaries. They expanded the boundary densities in the boundary integrals in terms of Fourier series, and kernel functions to degenerate kernels. Thus, the improper integrals were transformed into series sum and were easily calculated. The method of approximate particular solutions using integrated radial basis functions was used for solving the 2D Stokes cavity and step flows by Bustamante et al. [24]. Kreeft and Gerritsma [25] applied mimetic discretization spectral element method to the mixed formulation of the Stokes problem in terms of vorticity, velocity and pressure. Stokes flow in a rectangular cavity with moving lids and a (rotating) cylinder at the center were investigated by Galaktionov et al. [26]. They implemented a general analytical method of superposition. Applications were in 2D and 3D lid-driven rectangular and triangular cavities and flow around a cylinder with a pointwise divergence free solution.

The first investigations on the fluid flow under the magnetic field are due to Faraday in 1836. MHD is an area combining classical fluid mechanics and electrodynamics. It deals with flows of electrically conducting fluids which are sub-

jected to a magnetic field and/or an electric current driven by external voltage [6]. In MHD, the magnetic field influences the fluid motion and the fluid flow changes in turn (through Ohm's law) the magnetic field [18]. MHD has wide range of application areas in engineering and industry such as generators, pumps, stirring and transport control. 2D Stokes flow of an electrically conducting fluid past a cylinder in a uniform magnetic field was solved by Yosinobu and Kakutani [27]. Sellier et al. [28] gave an analytical approach for solving 2D MHD Stokes flow produced by the rigid body motion of a solid particle. Hunt and Williams [29] investigated the flow motion between parallel plates subjected to an applied magnetic field perpendicular to the planes theoretically and asymptotically. Analytical solutions for the magnetohydrodynamic steady flow in an infinite channel and on a half-plane was developed by Sezgin [30, 31] by reducing the problem to the solution of a Fredholm integral equation of the second kind. The electric current within the fluid induces an electric field. Since $\nabla \times \mathbf{E} = 0$, the electric field \mathbf{E} can be expressed as $\mathbf{E} = -\nabla\Phi$ (negative of the gradient of an electric potential). Then, $\nabla \cdot \mathbf{j} = 0$ follows a Laplace equation $\nabla^2\Phi = 0$ or a Poisson's equation $\nabla^2\Phi = -\frac{\partial V}{\partial x}$ when the flow is two-dimensional with the velocity $\mathbf{V} = (u, v, 0)$ or $\mathbf{V} = (0, 0, V)$, respectively. James et al. [32] investigated the electric potential distribution in the cross-section of an MHD generator by a finite difference method. They found that, the potential drop at the electrodes are increasing with higher current densities. Asymptotic and experimental studies are carried by Hunt and Malcolm [33] to examine velocity, electric current and electric potential distributions between two circular electrodes of finite diameter when a current is passed between them. Chowdhury et al. [34] detected electric potential behavior to investigate flow instabilities in liquid metal MHD duct flows experimentally. Nerguizian et al. [35] derived Fourier series expressions for the electric potential, electric field and dielectric forces between two electrodes with opposite potentials in a bio-microfluidic channel.

In the case of non-conducting fluid (FHD) no electric current is generated and the flow is affected only by the magnetization of the fluid under the magnetic field. The arising force in the equations is due to the magnetization and depends on the existence of a spatially varying magnetic field (e.g. point magnetic

source). Ferrofluids are suspensions of magnetic nanoparticles coated by a surfactant layer and a carrier fluid. The flow of ferrofluids are highly affected by the non-uniform magnetic fields. Aminfar et al. [36] investigated the hydrothermal characteristics of a ferrofluid in a vertical rectangular pipe under the influence of a point magnetic source using two-phase mixture model and the control volume technique. A semi-implicit finite element solution of magnetic gradient and thermal buoyancy induced cavity ferrofluid flow was given by Jue [37]. Sheikholeslami et al. [38] were studied ferrofluid flow and heat transfer in a semi annulus enclosure considering thermal radiation. They used control volume based finite element method (CVFEM) for the numerical simulations.

In some applications, rather than a unique point magnetic source, multiple point magnetic sources are used to control the flow in pipes. Kenjeres [39] considered both Lorentz and magnetization forces generated by multiple wires and the flow simulations were presented for different test cases ranging from a simple cylindrical geometry to real-life right-coronary arteries in humans by the use of finite volume method. He reported that an imposed non-uniform magnetic field could have created significant changes in the secondary flow patterns which made it possible to optimize the targeted drug delivery. The flow characteristics and heat transfer on the ferrofluid flow in channels were investigated using a control volume technique by Goharkhah and Ashjaee [40] and Sheikholeslami and Rashidi [41] considering eight line source dipoles and two magnetic sources, respectively.

BFD investigates fluid dynamics of biological fluids in the presence of a magnetic field and the most characteristic biomagnetic fluid is blood. Many scientist have studied the effect of magnetic field on blood flow. Tzirtzilakis et al. [42] investigated the fully developed blood flow in a square cavity. They solved the governing equations with a pressure-linked pseudotransient method. Biomagnetic fluid flow model is extended by taking into account both magnetization and Lorentz forces by Tzirtzilakis [4]. Tzirtzilakis and Xenos [43] considered electrically conducting fluid which also exhibits magnetization in a lid-driven cavity. They used the semi-implicit method for pressure linked equations (SIMPLE) for

the numerical solution of the problem. The effect of gravitational acceleration on unsteady biomagnetic fluid flow in a channel under the influence of a spatially varying magnetic field is investigated by Idris et al. [44] by using pressure correction method with SIMPLE algorithm. A finite element study of biomagnetic fluid flow between two parallel plates is given by Morega and Four [45]. Khassan and Haik [46] studied the biomagnetic fluid downstream an eccentric stenotic using the finite volume method. They found that based on the location of the magnetic field the reattachment point downstream the stenotic orifice changes. A finite element study of nonlinear two-dimensional deoxygenated biomagnetic micropolar flow is given by Bhargava et al. [47]. Khashan et al. [48] presented a numerical simulation for magnetically mediated separation of labeled biospecies from a native fluid flowing through a two-dimensional channel using finite volume method. The influence of a dipole like field and a magnetic field generated by a thin electric wire on the flow of biomagnetic fluid flow in a circular pipe with stenosis is studied by Tzirakis et al. [49]. They used a method based on pressure correction scheme combining discontinuous and continuous Galerkin approximations. Mousavi et al. [50] numerically simulated the three dimensional channel flow of biomagnetic fluid with a commercial software. They found that the magnetization force effect has dominated the Lorentz force and the fluid flow has been affected by the magnetization force.

The heat transfer through the blood flow in the presence of magnetic field can be used in hypothermic sessions, thermal simulation and thermal therapy applications [51]. The temperature differences within the fluid cause heat transfer and the fluid flow is effected by a force so called buoyancy force. Convection in rectangular enclosures with partially heated or partially cooled vertical walls while the other two walls are kept adiabatic is of special interest in many engineering applications such as solar receivers, solar passive design, and cooling of electronic equipment. Laminar mixed convection flow and double diffusive natural convection flow in a square cavity with a heated square blockage inside were investigated by Islam et al. [52] and Nazari et al. [53] by using the finite volume method and Lattice Boltzmann method, respectively. Selimefendigil and Oztop [54] studied natural convection flow in a nano-fluid filled cavity having

different shaped obstacles installed under the influence of a uniform heat generation and magnetic field by using Galerkin weighted residual finite element formulation. The heat transfer to individual blood vessels studied by Chato [55] in a single vessel, two vessels in counter flow and a single vessel near the skin. The stretching disk flow of a heated biomagnetic fluid is investigated as a special case by Tzirtzilakis and Kafoussias [56]. They transformed the nonlinear system of equations to ordinary differential equations by introducing appropriate non-dimensional variables. The blood flow between two parallel plates is numerically simulated by Loukopoulos and Tzirtzilakis [17] using a finite difference scheme. They reported that the rate of heat transfer increases at the area where the magnetic source is placed. Alimohamadi et al. [57] investigated the influence of numerous numbers of magnetic dipoles on the heat transfer in a rectangular pipe. They compared MHD and FHD cases of the flow which are obtained by a commercial software.

In most of the applications containing interaction between a solid and a fluid, no-slip boundary condition is set under the assumption of good wettability at the solid-fluid interface. In this case, the velocity of the fluid adjacent to the boundary is equal to the solid boundary velocity. However, in thin film dynamics, flow over hydrophobic surfaces, problems involving multiple interfaces and the flow of rheological fluids, the hydrodynamic slip condition is needed, as first proposed by Navier. The strength of the slip is quantified by the slip length which is the distance from the liquid to the surface within the solid phase, where the extrapolated flow velocity vanishes. The consequences of the slip at the wall on the flow of a linearly viscous fluid in a channel was investigated by Rao and Rajagopal [58] using the finite volume method (FVM). They considered both shear and normal stress dependence of the slip velocity and found that if the slip velocity strongly depends on the normal stress then the flow is not fully developed. Martini et al. [59] presented evidence for the molecular mechanisms by which slip occurs in nano- and micro- liquid flows by experimental and computational studies. They found that at extremely large values of forcing, the slip length approaches to a constant value. The behavior of the slip length in Newtonian liquids subject to planar shear in a Couette cell with mixed surface

boundary conditions was investigated numerically by Priezjev et al. [60]. They computed velocity fields and effective slip lengths both from molecular dynamics (MD) simulations and solution of Stokes equation for the flow configurations. Closed form analytical solutions for the flows of Navier-Stokes fluid, power-law fluid and the second grade fluid subject to Navier's slip on the boundary were established by Hron et al. [61].

Due to the coupling of the governing equations in MHD flows in pipes, analytical solutions can be obtained only for special boundary conditions such as insulated walls or perfectly conducting walls or two opposite insulated walls with the other two conducting. The velocity has no-slip boundary condition in these analytical studies [18]. Smolentsev [62] and Ligere et al. [63] presented analytical solutions in terms of infinite series for the fully developed MHD pipe flows admitting slip only at the Hartmann and the side walls, respectively. They observed that the influence of the slip on the flow is more advanced when the slip length is greater than the boundary layer thickness. It is reported that, the case of completely slipping duct walls requires an asymptotic approach or a numerical solution. Bhatti et al. [64] obtained analytical solution to the Ree-Eyring fluid for blood flow with partial slip under the low wavelength and low Reynolds number assumptions. Rivero and Cuevas [65] considered the wall slip in MHD micropumps by neglecting the induced magnetic field. They simulated the flow rate with respect to the slip length for small Hartmann numbers. A numerical study based on finite difference for the steady flow through a square duct with the slip at the Hartmann walls under the action of an external magnetic field is presented by Sarma and Deka [66]. Rashad et al. [67] and Ismael et al. [68] investigated the MHD mixed convection flow in a nanofluid-filled lid-driven square cavity with partial slip using the FVM.

In most of the studies simulating the fluid flow, finite difference, finite volume or finite element methods are used. The requirement of the discretization of the domain in these methods bring huge and sparse linear systems to solve and increase the computational cost. BEM is a well established method for solving elasticity and fluid flow problems [69]. BEM provides accurate results in prob-

lems such as stress concentration or where the domain extends to infinity [70]. It requires the fundamental solution of the original partial differential equation in order to obtain the corresponding boundary integral equation by the use of the Green's first identity which enables one to discretize only the boundary of the problem domain. The inhomogeneities (the terms other than the dominating partial differential operator) are collected under a domain integral. The dual reciprocity boundary element method approximates the inhomogeneities by a series expansion using global approximating functions as radial basis functions and converts the remaining domain integral to a boundary integral through the Green's first identity. It also allows one to approximate the space derivatives of the unknowns easily which helps in the treatment of nonlinear terms in partial differential equations. The method is an efficient tool for the numerical solutions of fluid flow problems in the cross-section of the pipes due to its easy implementation and low computational cost. DRBEM applications for the Stokes equation in velocity-vorticity formulation were presented in [71, 72]. Young et al. [71] used compactly-supported, positive-definite radial basis functions in the approximation of inhomogeneities and Eldho and Young [72] took $Re = 1$ as Stokes approximation in the Navier-Stokes equations. Biomagnetic fluid flow between parallel plates imposed to a magnetic source was investigated by Tezer-Sezgin et al. [73]. They used both finite element and dual reciprocity boundary element method for solving momentum and energy equations in terms of stream function and vorticity. There are quite a number of studies on MHD flows with no-slip boundary conditions using the BEM or the DRBEM. Tezer-Sezgin et al. [74, 75] presented BEM solutions of MHD flow in ducts with different cross-sections. Liu and Zhu [76] studied MHD flow through a channel with an arbitrary wall conductivity by the DRBEM. Bozkaya and Tezer-Sezgin [77] derived a fundamental solution for the coupled convection-diffusion type equations and studied MHD flow in a rectangular duct in the presence of an external oblique magnetic field. Nishad et al. [78] investigated the pressure driven two-dimensional flow of Newtonian fluid through slip patterned rectangular channels in the low Reynolds number limit using the BEM. BEM solutions of MHD flow in an infinite region and between infinite strips were obtained by Bozkaya and Tezer-Sezgin [79, 80].

The DRBEM has been used for all the ferrohydrodynamic and magnetohydrodynamic fluid flow problems considered in this thesis. The advantage of the DRBEM is made use of treating the nonlinearities in all the problems easily with the help of DRBEM coordinate matrix. Also, in the slip-wall MHD problems, both the velocity and its normal derivative are unknowns and they are obtained with the property of DRBEM which provides both of them on the boundary.

1.9 Originality of the Thesis

In this thesis, first of all the application of DRBEM to the fully developed FHD pipe flow problems under the influence of point source magnetic field are established. The three-dimensional pipe flow problems are also considered in the two-dimensional cross-sections of the pipe (cavity) being a fully developed flow. In the literature, for most of the cavity flow problems simulated by the DRBEM, the stream function-vorticity formulation were used to eliminate the pressure gradient from the momentum equations. In this thesis, the governing equations are considered in primitive variables (velocity-pressure-temperature form). Pressure equation is derived and a numerical technique, based on finite difference approximation and the DRBEM, is presented for the approximation of the Dirichlet type pressure boundary conditions. Hence, numerical solutions are obtained in terms of the original variables as the velocity, pressure and the temperature which possess the physics of the fluid.

The governing equations are converted to the boundary integral equations with the use of the fundamental solution of the Laplace equation. All the terms other than diffusion (Laplacian) are considered as inhomogeneity and approximated by linear radial basis functions. In most of the test problems the boundaries are discretized by constant elements giving also a comparison between constant and linear element discretizations in two problems. Since the accuracy gain in using linear elements is not considerable much, the rest of the problems in the thesis are solved by using constant elements. An iterative solution technique

based on the pressure equation is proposed. To the best of our knowledge, as a first application in the literature, a mathematical formulation of the FHD Stokes cavity flow subjected to a point source magnetic field is established and velocity, pressure profiles are presented for increasing values of magnetic field intensity [Senel and Tezer-Sezgin, 2015(2.7)]. DRBEM simulations are carried for the FHD incompressible flow in cavities and annular pipes [Senel and Tezer-Sezgin, 2015(2.6)], [Senel and Tezer-Sezgin, 2016(1.3)] and [Senel and Tezer-Sezgin, 2016(2.4)]. The influences of the unique or multiple point magnetic sources on the pressure of the fluid are discussed constituting a contribution to the literature [Senel and Tezer-Sezgin, 2017(1.1)]. The DRBEM formulation in terms of velocity, pressure and the temperature of the fluid is also presented for the forced convection cavity flow of biomagnetic fluids. The interaction between the magnetization and buoyancy forces on the flow is discussed [Senel and Tezer-Sezgin, 2016(2.5)], [Senel and Tezer-Sezgin, 2017(1.2)].

The study of MHD duct flow is very popular among scientist due to its wide range of engineering and industrial applications. A big majority of these studies consider the no-slip boundary conditions for the velocities. In this thesis, a DRBEM formulation is established for the MHD duct flow with slip velocity condition on the boundary which constitutes another part of the originality of the thesis. The coupled system of equations in terms of velocity and the induced magnetic field in the axial direction are discretized by the DRBEM and combined into a large system. After a rearrangement according to the slip wall conditions, the obtained linear system of equations are solved in one stroke. This process offers nodal solutions on the boundary and in the domain at once and saves computational time when compared to other iterative procedures. The slip wall condition is considered in the Hartmann flow (flow between infinite plates) as well, and the numerical results are presented which can be considered a new contribution to the Hartmann flow problems.

It can be concluded that, the mathematical formulations and the proposed numerical schemes presented in this thesis will provide practical information for the numerical solutions of some other FHD and MHD cavity flow problems in

the velocity-pressure-temperature form. The numerical solution idea based on the DRBEM for the MHD flow problems with slip boundary conditions can be generalized to some more MHD and FHD duct or parallel plates problems. The obtained numerical results in this thesis especially for the pressure and the axial velocity may be used to increase the efficiency of the engineering and medical instruments based on the FHD and MHD cavity flows.

1.10 Plan of the Thesis

In this chapter, fundamental equations of fluid dynamics including the magnetization or Lorentz forces are described. The equations modeling the FHD Stokes, FHD incompressible, FHD forced convection flows in primitive variables are presented. The derivation of the pressure equation is given. Governing equations for MHD pipe and Hartmann flows are introduced. Non-dimensional forms of the equations are obtained. In Section 1.8, a general literature survey is presented on the thesis subject. In Section 1.9 contribution of the thesis to the literature is explained.

In Chapter 2, BEM formulation for the Laplace equation and the DRBEM formulation for the Poisson's type equations using the fundamental solution of the Laplace equation are provided using linear and constant elements for boundary discretizations. Then, the applications of BEM and DRBEM on the FHD and MHD flow problems are provided. The numerical solution process without an iteration is described for the MHD duct flow problem with slipping velocity also.

In Chapter 3, the DRBEM analysis is presented for the FHD Stokes, incompressible and forced convection flows in pipes subjected to point magnetic source(s) generated by thin wire(s). The numerical solution processes and the generation of the pressure boundary conditions are described for each test problem. Then, the obtained numerical results are analyzed and the discussions are given according to the physics of the problems.

Chapter 4 is devoted to the DRBEM solutions of MHD flow in pipes and between parallel infinite plates with slip velocity condition. In this chapter, the physical meaning of the slip wall condition is explained and the numerical results are discussed for various flow configurations.

In Chapter 5, the studies carried in the thesis and the most important numerical findings are summarized.





CHAPTER 2

THE BEM AND THE DRBEM FORMULATIONS FOR FHD AND MHD FLOW PROBLEMS

In this thesis, all the numerical results are obtained by using the Boundary Element Method (BEM) and the Dual Reciprocity Boundary Element Method (DRBEM). The BEM is an efficient technique for the numerical solutions of initial and boundary value problems. In BEM, the fundamental solution of the dominant differential operator is made use of to convert the partial differential equations into the boundary integral equations. The idea of the DRBEM is the approximation of all the terms other than the leading differential operator by the radial basis functions and generate a series of particular solutions. This process enables one to discretize only the boundary of the problem domain which reduces the size of the linear systems achieved after the discretization. Thus, the computational cost will be considerably small compared to domain discretization type methods. Another advantage of the DRBEM is the treatment of the nonlinear terms in the differential equations by using the radial basis functions. This chapter is going to provide the BEM formulation on the Laplace equation and the DRBEM formulation on the Poisson's type equations using the fundamental solution of the Laplace equation.

2.1 The Boundary Element Method for the Laplace Equation

Consider a two-dimensional boundary value problem

$$\begin{aligned} \nabla^2 \phi &= 0 && \text{in } \Omega \\ \phi &= \bar{\phi} && \text{on } \Gamma_1 \\ q &= \frac{\partial \phi}{\partial n} = \bar{q} && \text{on } \Gamma_2 \end{aligned} \quad (2.1)$$

where \mathbf{n} is the outward normal to the boundary $\Gamma = \Gamma_1 + \Gamma_2$, and the bars indicate the known values. (Figure 2.1)

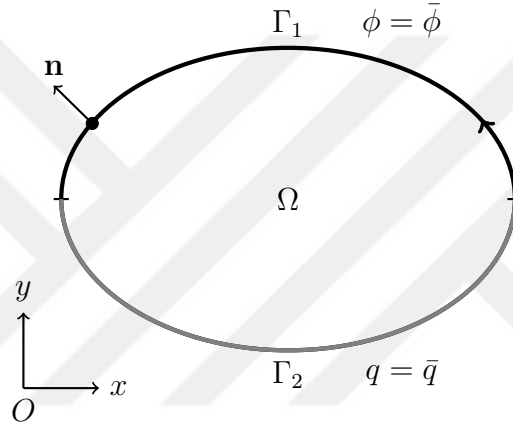


Figure 2.1: Problem domain

Multiplication of the Laplace equation by a weight function ϕ^* and integrating over the domain Ω brings the weighted residual statement

$$\int_{\Omega} (\nabla^2 \phi) \phi^* d\Omega = 0. \quad (2.2)$$

Applying Green's first identity once gives

$$- \int_{\Omega} \nabla \phi \nabla \phi^* d\Omega + \int_{\Gamma} q \phi^* d\Gamma = 0, \quad (2.3)$$

and the second application results in boundary integrals containing ϕ and q

$$\int_{\Omega} (\nabla^2 \phi^*) \phi d\Omega - \int_{\Gamma} \phi q^* d\Gamma + \int_{\Gamma} q \phi^* d\Gamma = 0 \quad (2.4)$$

where $q^* = \frac{\partial \phi^*}{\partial n}$.

The domain integral on the left-hand side of equation (2.4) is evaluated with the

special choice of the weight function ϕ^* which is the solution of the Poisson's equation with negative Dirac delta function on the right-hand side and called the fundamental solution of Laplace equation.

2.1.1 Fundamental Solution

The fundamental solution ϕ^* represents the field generated by a concentrated unit source acting at a point i and it satisfies [69]

$$\nabla^2 \phi^* + \Delta_i = 0 \quad (2.5)$$

where Δ_i is the Dirac delta function which goes to infinity at the point $i = (x_i, y_i)$ and is equal to zero elsewhere. The integral of Δ_i over the domain is equal to one and the integral of the Dirac delta function multiplied by any other function is equal to the value of the latter at the point i . Then,

$$\int_{\Omega} (\nabla^2 \phi^*) \phi d\Omega = \int_{\Omega} (-\Delta_i) \phi = -\phi_i \quad (2.6)$$

now, Equation (2.4) is rewritten as

$$\phi_i + \int_{\Gamma} \phi q^* d\Gamma = \int_{\Gamma} q \phi^* d\Gamma . \quad (2.7)$$

For a two-dimensional isotropic medium [69]

$$\phi^* = \frac{1}{2\pi} \ln\left(\frac{1}{|\mathbf{r} - \mathbf{r}_i|}\right) \quad (2.8)$$

where \mathbf{r}_i and \mathbf{r} are the position vectors of the source point i and the field point (any other point), respectively.

Then,

$$q^* = -\frac{1}{2\pi} \frac{(\mathbf{r} - \mathbf{r}_i) \cdot \mathbf{n}}{|\mathbf{r} - \mathbf{r}_i|^2} \quad (2.9)$$

where \mathbf{n} is the outward unit normal vector to the boundary Γ .

The boundary integral equation (2.7) is valid for any point i within the domain Ω .

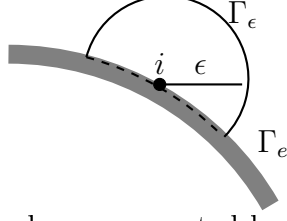


Figure 2.2: Boundary augmented by a small semicircle

If the source point i is on the boundary Γ , it is assumed that the boundary is augmented by a semi circle with radius ϵ , centered at the point i (Figure 2.2). In this case, equation (2.7) is valid for the region bounded by $\Gamma' = \Gamma_e + \Gamma_\epsilon$.

$$\phi_i + \int_{\Gamma_e + \Gamma_\epsilon} \phi q^* d\Gamma = \int_{\Gamma_e + \Gamma_\epsilon} q \phi^* d\Gamma \quad (2.10)$$

Then, as the radius of the semi circle tends to zero, the point i becomes a boundary point of Γ .

$$\phi_i + \lim_{\epsilon \rightarrow 0^+} \int_{\Gamma_e} \phi q^* d\Gamma + \lim_{\epsilon \rightarrow 0^+} \int_{\Gamma_\epsilon} \phi q^* d\Gamma = \lim_{\epsilon \rightarrow 0^+} \int_{\Gamma_e} q \phi^* d\Gamma + \lim_{\epsilon \rightarrow 0^+} \int_{\Gamma_\epsilon} q \phi^* d\Gamma \quad (2.11)$$

where

$$\lim_{\epsilon \rightarrow 0^+} \int_{\Gamma_e} \phi q^* d\Gamma = \int_{\Gamma} \phi q^* d\Gamma \quad \text{and} \quad \lim_{\epsilon \rightarrow 0^+} \int_{\Gamma_\epsilon} q \phi^* d\Gamma = \int_{\Gamma} q \phi^* d\Gamma \quad (2.12)$$

$$\begin{aligned} \lim_{\epsilon \rightarrow 0^+} \int_{\Gamma_\epsilon} \phi q^* d\Gamma &= - \lim_{\epsilon \rightarrow 0^+} \int_{\Gamma_\epsilon} \phi \frac{1}{2\pi} \frac{(\mathbf{r} - \mathbf{r}_i) \cdot \mathbf{n}}{|\mathbf{r} - \mathbf{r}_i|^2} d\Gamma \\ &= - \lim_{\epsilon \rightarrow 0^+} \int_{\Gamma_\epsilon} \phi \frac{1}{2\pi} \frac{|\mathbf{n}| \cos(0)}{|\mathbf{r} - \mathbf{r}_i|} d\Gamma \\ &= - \lim_{\epsilon \rightarrow 0^+} \int_{\Gamma_\epsilon} \phi \frac{1}{2\pi\epsilon} d\Gamma \\ &= - \lim_{\epsilon \rightarrow 0^+} \phi \frac{\pi\epsilon}{2\pi\epsilon} \\ &= -\frac{1}{2} \phi_i . \end{aligned} \quad (2.13)$$

Similarly,

$$\begin{aligned} \lim_{\epsilon \rightarrow 0^+} \int_{\Gamma_\epsilon} q \phi^* d\Gamma &= \lim_{\epsilon \rightarrow 0^+} \int_{\Gamma_\epsilon} q \frac{1}{2\pi} \ln\left(\frac{1}{|\mathbf{r} - \mathbf{r}_i|}\right) d\Gamma \\ &= -\frac{1}{2\pi} \lim_{\epsilon \rightarrow 0^+} q \ln \epsilon \int_{\Gamma_\epsilon} d\Gamma \\ &= -\frac{1}{2} \lim_{\epsilon \rightarrow 0^+} q \epsilon \ln \epsilon = 0 . \end{aligned} \quad (2.14)$$

Using equations (2.12)-(2.14) one can write the boundary integral equation (2.7) valid for any source point i on the boundary

$$\frac{1}{2} \phi_i + \int_{\Gamma} \phi q^* d\Gamma = \int_{\Gamma} q \phi^* d\Gamma . \quad (2.15)$$

If the source point i is in the domain Ω , a small circle with radius ϵ is taken around the point i and the same analysis is carried for the boundary integrals in (2.7) in the limit sense which result in zero. Thus, the coefficient of ϕ_i becomes 1 if i is an interior point.

The two cases can be combined as

$$c_i \phi_i + \int_{\Gamma} \phi q^* d\Gamma = \int_{\Gamma} q \phi^* d\Gamma \quad (2.16)$$

where

$$c_i = \frac{\theta}{2\pi}, \quad (2.17)$$

with θ being the internal angle at i measured in radians.

Let us assume the boundary is discretized into N number of elements. Figure 2.3 displays the discretization with constant and linear elements for the boundary of the domain Ω . In constant element case, the values of ϕ and q are assumed to be constant over each element and equal to the nodal value at the center of the element. In using linear elements, the values of ϕ and q are a linear combination of extreme points nodal values of each element.

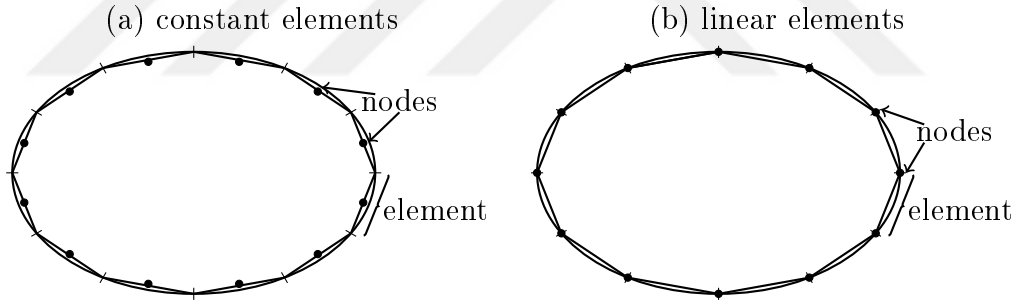


Figure 2.3: Constant and linear element discretizations

Discretizing the boundary Γ with N elements gives the discretized form of equation (2.16)

$$c_i \phi_i + \sum_{j=1}^N \int_{\Gamma_j} \phi q^* d\Gamma = \sum_{j=1}^N \int_{\Gamma_j} q \phi^* d\Gamma . \quad (2.18)$$

2.1.2 Constant Element Discretization

In the case of constant elements, ϕ and q are constants on the element j and take the values ϕ_j and q_j , respectively. Hence, equation (2.16) written for the

source point i on the boundary turns into

$$\frac{1}{2}\phi_i + \sum_{j=1}^N \phi_j \int_{\Gamma_j} q^* d\Gamma = \sum_{j=1}^N q_j \int_{\Gamma_j} \phi^* d\Gamma, \quad i = 1, 2, \dots, N. \quad (2.19)$$

The integrals in equation (2.19) relate the source point i to any other field point j . Defining

$$\bar{H}_{ij} = \int_{\Gamma_j} q^* d\Gamma, \quad G_{ij} = \int_{\Gamma_j} \phi^* d\Gamma \quad (2.20)$$

for a particular node i on the boundary, equation (2.19) can be written in discretized form

$$\frac{1}{2}\phi_i + \sum_{j=1}^N \bar{H}_{ij}\phi_j = \sum_{j=1}^N G_{ij}q_j, \quad i = 1, 2, \dots, N. \quad (2.21)$$

Using

$$H_{ij} = \bar{H}_{ij} + \frac{1}{2}\delta_{ij} \quad (2.22)$$

where δ_{ij} is the Kronecker delta (i.e., if $i = j$ then $\delta_{ij} = 1$, otherwise $\delta_{ij} = 0$) one writes

$$\sum_{j=1}^N H_{ij}\phi_j = \sum_{j=1}^N G_{ij}q_j, \quad i = 1, 2, \dots, N. \quad (2.23)$$

This results in a matrix-vector equation

$$\mathbf{H}\boldsymbol{\phi} = \mathbf{G}\mathbf{q} \quad (2.24)$$

where \mathbf{H} and \mathbf{G} are $N \times N$ matrices with entries given in equation (2.20) and (2.22), and $\boldsymbol{\phi}$ and \mathbf{q} are vectors of length N containing the solution and its normal derivative at all the boundary nodes, respectively.

The entries of matrices $\bar{\mathbf{H}}$ and \mathbf{G} may be computed either analytically or numerically (e.g. using Gaussian quadrature, Section 1.7.2) for $i \neq j$ in the case of constant elements. The diagonal entries of $\bar{\mathbf{H}}$ are

$$\bar{H}_{ii} = \int_{\Gamma_i} q^* d\Gamma = \frac{1}{2\pi} \int_{\Gamma_i} \frac{(\mathbf{r} - \mathbf{r}_i) \cdot \mathbf{n}}{|\mathbf{r} - \mathbf{r}_i|^2} d\Gamma \equiv 0 \quad (2.25)$$

since the vector $(\mathbf{r} - \mathbf{r}_i)$ is always perpendicular to the normal \mathbf{n} on the i -th element.

When $i = j$ due to the singularity of the fundamental solution, the diagonal entries of \mathbf{G} have to be computed using exact integration.

$$G_{ii} = \int_{\Gamma_i} \phi^* d\Gamma = \frac{1}{2\pi} \int_{\Gamma_i} \ln\left(\frac{1}{|\mathbf{r} - \mathbf{r}_i|}\right) d\Gamma. \quad (2.26)$$

Let

$$|\mathbf{r} - \mathbf{r}_i| = \left| \frac{l}{2}\xi \right| \quad d\Gamma = \frac{l}{2}d\xi \quad (2.27)$$

where l is the length of the i -th element. Then, taking into account the symmetry,

$$G_{ii} = \frac{1}{2\pi} \int_{\text{Point 1}}^{\text{Point 2}} \ln\left(\frac{1}{|\mathbf{r} - \mathbf{r}_i|}\right) d\Gamma \quad (2.28)$$

$$= \frac{1}{\pi} \int_{\text{node } i}^{\text{Point 2}} \ln\left(\frac{1}{|\mathbf{r} - \mathbf{r}_i|}\right) d\Gamma \quad (2.29)$$

$$= \frac{l}{2\pi} \int_0^1 \ln\left(\frac{2}{l\xi}\right) d\xi \quad (2.30)$$

$$= \frac{l}{2\pi} \left\{ \ln\left(\frac{2}{l}\right) + \int_0^1 \ln\left(\frac{1}{\xi}\right) d\xi \right\} \quad (2.31)$$

$$= \frac{l}{2\pi} \left\{ \ln\left(\frac{2}{l}\right) + 1 \right\} \quad (2.32)$$

where Point 1 and Point 2 are the extreme points, and node i lies at the center of the element i .

2.1.3 Linear Element Discretization

In the case of linear elements, the variables are the linear combinations of the values at the extreme points of the element. That is,

$$\phi(\xi) = N_1\phi_1 + N_2\phi_2 \quad (2.33)$$

$$q(\xi) = N_1q_1 + N_2q_2 .$$

Here, ϕ_1, ϕ_2 are the nodal values of the extreme points (Figure 2.4), $-1 \leq \xi \leq 1$ is the variable on the element coordinate system (Figure 2.5) and N_1, N_2 are linear interpolation functions given by

$$\begin{aligned} N_1 &= \frac{1}{2}(1 - \xi) \\ N_2 &= \frac{1}{2}(1 + \xi) \end{aligned} \quad (2.34)$$

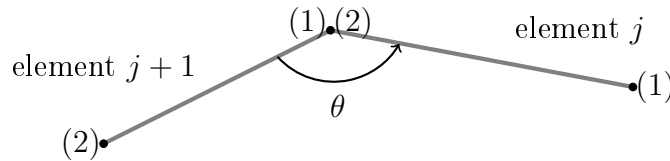


Figure 2.4: Linear element

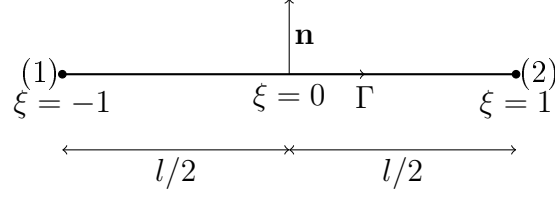


Figure 2.5: Element coordinate system

Dividing the boundary into N linear elements in equation (2.16) we still have N equations

$$c_i \phi_i + \sum_{j=1}^N \int_{\Gamma_j} \phi q^* d\Gamma = \sum_{j=1}^N \int_{\Gamma_j} q \phi^* d\Gamma, \quad i = 1, 2, \dots, N. \quad (2.35)$$

The integrals in equation (2.35) are not easy to evaluate and a special treatment is needed. Inserting the approximations of ϕ and q from (2.33) one gets,

$$c_i \phi_i + \sum_{j=1}^N \int_{\Gamma_j} (N_1 \phi_1 + N_2 \phi_2) q^* d\Gamma = \sum_{j=1}^N \int_{\Gamma_j} (N_1 q_1 + N_2 q_2) \phi^* d\Gamma, \quad i = 1, 2, \dots, N \quad (2.36)$$

and then,

$$c_i \phi_i + \sum_{j=1}^N \int_{\Gamma_j} \begin{bmatrix} N_1 & N_2 \end{bmatrix} q^* d\Gamma \begin{bmatrix} \phi_1 \\ \phi_2 \end{bmatrix} = \sum_{j=1}^N \int_{\Gamma_j} \begin{bmatrix} N_1 & N_2 \end{bmatrix} \phi^* d\Gamma \begin{bmatrix} q_1 \\ q_2 \end{bmatrix}, \quad i = 1, 2, \dots, N. \quad (2.37)$$

Introducing

$$h_{ij}^1 = \int_{\Gamma_j} N_1 q^* d\Gamma \quad h_{ij}^2 = \int_{\Gamma_j} N_2 q^* d\Gamma \quad (2.38)$$

and

$$g_{ij}^1 = \int_{\Gamma_j} N_1 \phi^* d\Gamma \quad g_{ij}^2 = \int_{\Gamma_j} N_2 \phi^* d\Gamma \quad (2.39)$$

the boundary integral equation for the source point i on the boundary becomes

$$c_i \phi_i + \sum_{j=1}^N \begin{bmatrix} h_{ij}^1 & h_{ij}^2 \end{bmatrix} \begin{bmatrix} \phi_1 \\ \phi_2 \end{bmatrix} = \sum_{j=1}^N \begin{bmatrix} g_{ij}^1 & g_{ij}^2 \end{bmatrix} \begin{bmatrix} q_1 \\ q_2 \end{bmatrix}, \quad i = 1, 2, \dots, N. \quad (2.40)$$

In the linear element discretization, the second node of the element j coincides with the first node of the element $j+1$. Hence, the sum in the boundary integral equation needs a special arrangement. This arrangement is called the assembly procedure.

For a bounded region defining

$$\bar{H}_{ij} = \begin{cases} h_{i(j-1)}^2 + h_{ij}^1 & \text{if } j \neq 1 \\ h_{iN}^2 + h_{ij}^1 & \text{if } j = 1 \end{cases} \quad G_{ij} = \begin{cases} g_{i(j-1)}^2 + g_{ij}^1 & \text{if } j \neq 1 \\ g_{iN}^2 + g_{ij}^1 & \text{if } j = 1 \end{cases} \quad (2.41)$$

one obtains the system

$$c_i \phi_i + \begin{bmatrix} \bar{H}_{i1} & \bar{H}_{i2} & \dots & \bar{H}_{iN} \end{bmatrix} \begin{bmatrix} \phi_1 \\ \phi_2 \\ \vdots \\ \phi_N \end{bmatrix} = \begin{bmatrix} G_{i1} & G_{i2} & \dots & G_{iN} \end{bmatrix} \begin{bmatrix} q_1 \\ q_2 \\ \vdots \\ q_N \end{bmatrix}. \quad (2.42)$$

Similar to the constant element case this formula can be written for boundary nodes i as

$$c_i \phi_i + \sum_{j=1}^N \bar{H}_{ij} \phi_j = \sum_{j=1}^N G_{ij} q_j, \quad i = 1, 2, \dots, N \quad (2.43)$$

which results in a matrix-vector equation

$$\mathbf{H}\boldsymbol{\phi} = \mathbf{G}\mathbf{q} \quad (2.44)$$

where \mathbf{H} ($H_{ij} = c_i \delta_{ij} + \bar{H}_{ij}$) and \mathbf{G} are $N \times N$ matrices with entries given in equation (2.41), $\boldsymbol{\phi}$ and \mathbf{q} are $N \times 1$ vectors consisting of the values of the solution and its normal derivative at the boundary nodes, respectively.

The constant c_i can be computed by using the definition (2.17) explicitly. If the successive boundary elements connect smoothly, then $c_i = 1/2$ as in the case of constant elements. If the node lies at a corner, then the computation of the internal angle θ may not be practical. If this is the case, a numerical approximation is generally used.

When a uniform potential is applied over a bounded region, all the derivatives (including q values) must be zero [69]. So, equation (2.44) becomes

$$\mathbf{H}\boldsymbol{\phi} = \mathbf{0}. \quad (2.45)$$

Thus, the sum of all the elements of any row of \mathbf{H} should be zero. This approximation leads another way to compute the diagonal elements of the matrix \mathbf{H} in

terms of the off-diagonal elements.

$$H_{ii} = - \sum_{j=1(j \neq i)}^N H_{ij} . \quad (2.46)$$

For each problem studied in this thesis whether the solution or its normal derivative is known on the boundary. After the boundary conditions are inserted to the matrix-vector equations (2.24) (for the constant elements) (2.44) (for the linear elements), the unknown values have to be collected on one side of the equation. If the k -th element of the vector \mathbf{q} is unknown, then the k -th columns of the matrices \mathbf{H} and \mathbf{G} are interchanged negating the sign. This process is called the shuffling. Once all the unknowns are passed to the left-hand side a linear system is achieved

$$\mathbf{A}\mathbf{x} = \mathbf{c} . \quad (2.47)$$

The matrix \mathbf{A} is full but containing scattered zeros showing no special form which forces one to use Gaussian elimination scheme with pivoting (Section 1.7.3) or an iterative solver for the numerical solution.

2.1.4 Solution at the interior nodes

As the solution at all of the boundary nodes are calculated, equation (2.16) with $c_i = 1$ is used to find the solution ϕ_i and the derivatives $(q_x)_i, (q_y)_i$ at the interior nodes. Now,

$$\phi_i = \sum_{j=1}^N \int_{\Gamma_j} q \phi^* d\Gamma - \sum_{j=1}^N \int_{\Gamma_j} \phi q^* d\Gamma = \sum_{j=1}^N G_{ij} q_j - \sum_{j=1}^N \bar{H}_{ij} \phi_j, \quad (2.48)$$

$$(q_x)_i = \left. \frac{\partial \phi}{\partial x} \right|_i = \sum_{j=1}^N \int_{\Gamma_j} q \frac{\partial \phi^*}{\partial x} d\Gamma - \sum_{j=1}^N \int_{\Gamma_j} \phi \frac{\partial q^*}{\partial x} d\Gamma, \quad (2.49)$$

$$(q_y)_i = \left. \frac{\partial \phi}{\partial y} \right|_i = \sum_{j=1}^N \int_{\Gamma_j} q \frac{\partial \phi^*}{\partial y} d\Gamma - \sum_{j=1}^N \int_{\Gamma_j} \phi \frac{\partial q^*}{\partial y} d\Gamma \quad (2.50)$$

where ϕ and q are the known values on the boundary j . The entries G_{ij} and \bar{H}_{ij} are computed from equations (2.20) for constant elements and (2.41) for linear

elements, now by using the distance r_{ij} from an interior point to a boundary point for each internal source point i .

2.2 The Dual Reciprocity Boundary Element Method for Poisson's type Equations $\nabla^2\phi = b(x, y, \phi, \phi_x, \phi_y)$

Consider a two-dimensional boundary value problem with the inhomogeneity

$$\begin{aligned}\nabla^2\phi &= b(x, y, \phi, \phi_x, \phi_y) && \text{in } \Omega \\ \phi &= \bar{\phi} && \text{on } \Gamma_1 \\ q &= \frac{\partial\phi}{\partial n} = \bar{q} && \text{on } \Gamma_2 .\end{aligned}\tag{2.51}$$

The solution of the problem (2.51) can be expressed as the sum of the homogeneous solution ($\nabla^2\phi = 0$) and a particular solution $\hat{\phi}$, such that

$$\nabla^2\hat{\phi} = b .\tag{2.52}$$

It is generally difficult to find a solution $\hat{\phi}$ that satisfies the above equation, particularly in the case of nonlinear or time dependent problems. DRBEM proposes the use of a series of particular solutions $\hat{\phi}_j$ instead of a single function $\hat{\phi}$. The number of $\hat{\phi}_j$ used is equal to the total number of nodes in the closed domain [69].

Let N and L be the number of boundary and interior nodes, respectively, in which the solution is needed. The inhomogeneity part b is approximated by the use of radial basis functions $f(r)$. Examples of radial basis functions are:

$$\begin{aligned}f(r) &= 1 + r + r^2 + .. + r^n && \text{(polynomial)} \\ f(r) &= e^{-r^2/(2c^2)} && \text{(Gaussian)} \\ f(r) &= (r^2 + c^2)^{1/2} && \text{(multiquadrics)} \\ f(r) &= \frac{1}{(r^2 + c^2)^{1/2}} && \text{(inverse multiquadrics)}\end{aligned}\tag{2.53}$$

where r is the distance between the source i and the field point j and $c > 0$. Then, the following approximation is taken [69]

$$b(x, y, \phi, \phi_x, \phi_y) \approx \sum_{j=1}^{N+L} \alpha_j f_j\tag{2.54}$$

with α_j 's being the unknown coefficients that will be determined by collocating b at $N + L$ points and $f_j = f(r_j)$. Writing the equation (2.54) for all the source points, a matrix-vector equation is obtained

$$\mathbf{b} = \mathbf{F}\boldsymbol{\alpha} . \quad (2.55)$$

Here, \mathbf{F} (DRBEM coordinate matrix) is a symmetric, non-singular [81, 82] $(N + L) \times (N + L)$ matrix with entries $\mathbf{F}_{ij} = f_i(r_j)$, and \mathbf{b} and $\boldsymbol{\alpha}$ are vectors of size $N + L$. Then,

$$\boldsymbol{\alpha} = \mathbf{F}^{-1}\mathbf{b} . \quad (2.56)$$

The radial basis functions f_j 's are related to the particular solutions $\hat{\phi}_j$'s with the Laplace operator

$$\nabla^2 \hat{\phi}_j = f_j . \quad (2.57)$$

Substituting equation (2.57) into equation (2.54) gives

$$b(x, y, \phi, \phi_x, \phi_y) \approx \sum_{j=1}^{N+L} \alpha_j (\nabla^2 \hat{\phi}_j) \quad (2.58)$$

and hence, the Poisson's equation in (2.51) turns into

$$\nabla^2 \phi = \sum_{j=1}^{N+L} \alpha_j (\nabla^2 \hat{\phi}_j) . \quad (2.59)$$

As in the case of BEM, we weight both sides of the equation (2.59) with the fundamental solution ϕ^* and apply Green's first identity two times to obtain the boundary integral equation for the source point i on the boundary or inside the region

$$c_i \phi_i + \int_{\Gamma} \phi q^* d\Gamma - \int_{\Gamma} q \phi^* d\Gamma = \sum_{j=1}^{N+L} \alpha_j (c_i \hat{\phi}_{ij} + \int_{\Gamma} \hat{\phi}_j q^* d\Gamma - \int_{\Gamma} \hat{q}_j \phi^* d\Gamma) \quad (2.60)$$

$i = 1, 2, \dots, N + L$ where

$$q = \frac{\partial \phi}{\partial n}, \quad q^* = \frac{\partial \phi^*}{\partial n}, \quad \hat{q}_j = \frac{\partial \hat{\phi}_j}{\partial n} . \quad (2.61)$$

Discretizing the boundary with N constant or linear elements in (2.60) gives

$$\begin{aligned} c_i \phi_i + \sum_{k=1}^N \int_{\Gamma_k} \phi q^* d\Gamma - \sum_{k=1}^N \int_{\Gamma_k} q \phi^* d\Gamma = \\ = \sum_{j=1}^{N+L} \alpha_j (c_i \hat{\phi}_{ij} + \sum_{k=1}^N \int_{\Gamma_k} \hat{\phi}_j q^* d\Gamma - \sum_{k=1}^N \int_{\Gamma_k} \hat{q}_j \phi^* d\Gamma) \quad i = 1, 2, \dots, N + L . \end{aligned} \quad (2.62)$$

Once the radial basis function is determined the values of $\hat{\phi}_j$ and \hat{q}_j are found through (2.57) and (2.61). However, in order to use the same \mathbf{H} and \mathbf{G} matrices on both sides of the equation (2.62), the same constant or linear element treatment, as done for ϕ and q , is applied also for $\hat{\phi}_j$ and \hat{q}_j .

After introducing the interpolation functions one gets

$$c_i \phi_i + \sum_{k=1}^N \bar{H}_{ik} \phi_k - \sum_{k=1}^N G_{ik} q_k = \sum_{j=1}^{N+L} \alpha_j (c_i \hat{\phi}_{ij} + \sum_{k=1}^N \bar{H}_{ik} \hat{\phi}_{kj} - \sum_{k=1}^N G_{ik} \hat{q}_{kj}) \quad (2.63)$$

$i = 1, 2, \dots, N + L$ where the entries of \bar{H}_{ik} and G_{ik} are the same as given in the equations (2.20) (for constant elements) and (2.41) (for linear elements). Writing equation (2.63) for all the source points i on the boundary and interior nodes gives

$$\mathbf{H}\phi - \mathbf{G}\mathbf{q} = \sum_{j=1}^{N+L} \alpha_j (\mathbf{H}\hat{\phi}_j - \mathbf{G}\hat{\mathbf{q}}_j) . \quad (2.64)$$

In the equation (2.64) the value of c_i is incorporated to the diagonal elements of the matrix \mathbf{H} for the boundary nodes. Constructing matrices $\hat{\mathbf{U}}$ and $\hat{\mathbf{Q}}$ by taking the vectors $\hat{\phi}_j$ and $\hat{\mathbf{q}}_j$ as columns, respectively, equation (2.64) becomes using (2.56)

$$\mathbf{H}\phi - \mathbf{G}\mathbf{q} = (\mathbf{H}\hat{\mathbf{U}} - \mathbf{G}\hat{\mathbf{Q}})\alpha = (\mathbf{H}\hat{\mathbf{U}} - \mathbf{G}\hat{\mathbf{Q}})\mathbf{F}^{-1}\mathbf{b} . \quad (2.65)$$

Here,

$$\mathbf{H} = \begin{bmatrix} \mathbf{H}_B & \mathbf{0} \\ \mathbf{H}_I & \mathbf{I} \end{bmatrix} \quad \mathbf{G} = \begin{bmatrix} \mathbf{G}_B & \mathbf{0} \\ \mathbf{G}_I & \mathbf{0} \end{bmatrix} \quad (2.66)$$

$$\hat{\mathbf{U}} = \begin{bmatrix} \hat{\mathbf{U}}_B \\ \hat{\mathbf{U}}_I \end{bmatrix} \quad \hat{\mathbf{Q}} = \begin{bmatrix} \hat{\mathbf{Q}}_B \\ \mathbf{0} \end{bmatrix} \quad (2.67)$$

and

$$\phi = \begin{bmatrix} \phi_B \\ \phi_I \end{bmatrix} \quad \mathbf{q} = \begin{bmatrix} \mathbf{q}_B \\ \mathbf{0} \end{bmatrix} \quad \alpha = \begin{bmatrix} \alpha_B \\ \alpha_I \end{bmatrix} \quad (2.68)$$

where the subscripts B and I denote the boundary and interior solutions, respectively. \mathbf{H}_B and \mathbf{G}_B are $N \times N$, \mathbf{H}_I and \mathbf{G}_I are $L \times N$, $\hat{\mathbf{U}}_B$ and $\hat{\mathbf{Q}}_B$ are $N \times (N+L)$, $\hat{\mathbf{U}}_I$ is $L \times (N+L)$, \mathbf{H} , \mathbf{G} , $\hat{\mathbf{U}}$ and $\hat{\mathbf{Q}}$ are $(N+L) \times (N+L)$ matrices. ϕ_B , \mathbf{q}_B and α_B are $N \times 1$, ϕ_I and α_I are $L \times 1$, ϕ , \mathbf{q} and α are $(N+L) \times 1$ vectors. $\mathbf{0}$ and \mathbf{I} are zero and unit matrices, respectively. In the equation (2.65)

all the matrices have constant entries and they are constructed once.

In the case of polynomial radial basis functions of the form

$$f(r) = 1 + r + r^2 + \dots + r^n \quad (2.69)$$

the particular solution $\hat{\phi}$ and its normal derivative \hat{q} are given by (integrating the Laplace operator backwards)

$$\hat{\phi} = \frac{r^2}{4} + \frac{r^3}{9} + \dots + \frac{r^{n+2}}{(n+2)^2} \quad (2.70)$$

$$\hat{q} = (r_x \frac{\partial x}{\partial n} + r_y \frac{\partial y}{\partial n}) \left(\frac{1}{2} + \frac{r}{3} + \dots + \frac{r^n}{(n+2)} \right) \quad (2.71)$$

where r_x, r_y are the x - and y - components of the distance vector \mathbf{r} .

The vector on the right-hand side of the equation (2.65) may include the unknown ϕ nodal values and its spatial derivatives ϕ_x and/or ϕ_y nodal values.

If the function $b(x, y, \phi, \phi_x, \phi_y)$ has the unknown ϕ , then the vector $\boldsymbol{\phi}$ also appears on the right-hand side of the equation (2.65) due to $\mathbf{F}^{-1}\mathbf{b}$ and it is carried to the left-hand side.

The convection terms in $b(x, y, \phi, \phi_x, \phi_y)$ need a special treatment by the use of the DRBEM coordinate matrix \mathbf{F} . In this case, the unknown ϕ is also assumed to be approximated as

$$\boldsymbol{\phi} = \mathbf{F}\boldsymbol{\beta} . \quad (2.72)$$

where $\boldsymbol{\beta}$ contains the undetermined coefficients and it is different from $\boldsymbol{\alpha}$ in (2.56). Then,

$$\frac{\partial \boldsymbol{\phi}}{\partial x} = \frac{\partial \mathbf{F}}{\partial x} \boldsymbol{\beta} \quad (2.73)$$

and

$$\frac{\partial \boldsymbol{\phi}}{\partial y} = \frac{\partial \mathbf{F}}{\partial y} \boldsymbol{\beta} . \quad (2.74)$$

Since the coordinate matrix \mathbf{F} is a function of nodal coordinates (r_x, r_y) one gets an approximation for the spatial derivatives of the unknown ϕ from (2.72),

$$\frac{\partial \boldsymbol{\phi}}{\partial x} = \frac{\partial \mathbf{F}}{\partial x} \mathbf{F}^{-1} \boldsymbol{\phi} \quad (2.75)$$

and

$$\frac{\partial \boldsymbol{\phi}}{\partial y} = \frac{\partial \mathbf{F}}{\partial y} \mathbf{F}^{-1} \boldsymbol{\phi} . \quad (2.76)$$

Here \mathbf{F}^{-1} , $\frac{\partial \mathbf{F}}{\partial x}$ and $\frac{\partial \mathbf{F}}{\partial y}$ are full $(N + L) \times (N + L)$ matrices. The entries of $\frac{\partial \mathbf{F}}{\partial x}$ and $\frac{\partial \mathbf{F}}{\partial y}$ are determined in terms of the partial derivatives of the radial basis function. For example in the case of polynomial radial basis functions, the derivatives are

$$\frac{\partial f}{\partial x} = \frac{\partial f}{\partial r} \frac{\partial r}{\partial x} = \frac{\partial f}{\partial r} \frac{r_x}{r} = r_x \left(\frac{1}{r} + 2 + \dots + nr^{(n-2)} \right) \quad (2.77)$$

and

$$\frac{\partial f}{\partial y} = \frac{\partial f}{\partial r} \frac{\partial r}{\partial y} = \frac{\partial f}{\partial r} \frac{r_y}{r} = r_y \left(\frac{1}{r} + 2 + \dots + nr^{(n-2)} \right) \quad (2.78)$$

where r_x and r_y are the x - and y -components of the distance vector \mathbf{r} .

After the construction of all the vectors and matrices in equation (2.65), inserting the boundary conditions and putting all the unknown values to the left-hand side, a linear discretized system is obtained to be solved numerically

$$\mathbf{Ax} = \mathbf{c} \quad (2.79)$$

in which the vector \mathbf{x} contains all the unknown boundary ϕ or $\frac{\partial \phi}{\partial n}$ values and interior ϕ values. Thus, the solution of the problem at all the boundary and interior nodes is computed at once. This is the main advantage of the DRBEM.

2.3 Application of the DRBEM to the FHD Stokes flow problems

The governing equations of the FHD Stokes flow problem were presented in Chapter 1 (equations (1.30)-(1.35)) as

$$\nabla^2 u = \frac{\partial p}{\partial x} - MH \frac{\partial H}{\partial x} \quad (2.80)$$

$$\nabla^2 v = \frac{\partial p}{\partial y} - MH \frac{\partial H}{\partial y} \quad (2.81)$$

$$\nabla^2 p = M \left(\left(\frac{\partial H}{\partial x} \right)^2 + \left(\frac{\partial H}{\partial y} \right)^2 + H \nabla^2 H \right) \quad (2.82)$$

$$\nabla^2 \Psi = \frac{\partial u}{\partial y} - \frac{\partial v}{\partial x} \quad (2.83)$$

where $M = Mn/Re$. The Dirichlet type boundary conditions are employed for all of the problem variables since the velocity is specified on the boundary and pressure boundary values are obtained through the coordinate matrix of

DRBEM and the finite difference method.

The corresponding $(N + L) \times (N + L)$ system of DRBEM discretized matrix-vector equations are obtained by treating the right-hand sides of each equation in (2.80)-(2.83) as a function b containing the unknown and its space derivatives and obtained from (2.65) as

$$\mathbf{H}u - \mathbf{G} \frac{\partial u}{\partial n} = (\mathbf{H}\hat{\mathbf{U}} - \mathbf{G}\hat{\mathbf{Q}})\mathbf{F}^{-1} \left\{ \frac{\partial p}{\partial x} - MH \frac{\partial H}{\partial x} \right\} \quad (2.84)$$

$$\mathbf{H}v - \mathbf{G} \frac{\partial v}{\partial n} = (\mathbf{H}\hat{\mathbf{U}} - \mathbf{G}\hat{\mathbf{Q}})\mathbf{F}^{-1} \left\{ \frac{\partial p}{\partial y} - MH \frac{\partial H}{\partial y} \right\} \quad (2.85)$$

$$\mathbf{H}p - \mathbf{G} \frac{\partial p}{\partial n} = M(\mathbf{H}\hat{\mathbf{U}} - \mathbf{G}\hat{\mathbf{Q}})\mathbf{F}^{-1} \left\{ \left(\frac{\partial H}{\partial x} \right)^2 + \left(\frac{\partial H}{\partial y} \right)^2 + H\nabla^2 H \right\} \quad (2.86)$$

$$\mathbf{H}\Psi - \mathbf{G} \frac{\partial \Psi}{\partial n} = (\mathbf{H}\hat{\mathbf{U}} - \mathbf{G}\hat{\mathbf{Q}})\mathbf{F}^{-1} \left\{ \frac{\partial u}{\partial y} - \frac{\partial v}{\partial x} \right\}. \quad (2.87)$$

Note that, the case $Mn = 0$ reduces the equation (2.86) to the BEM formulation of the Laplace equation for the pressure equation. After the spatial derivatives of the unknowns on the right-hand sides of the equations (2.84)-(2.87) are approximated in terms of the coordinate matrix \mathbf{F} one gets,

$$\mathbf{H}u - \mathbf{G} \frac{\partial u}{\partial n} = \mathbf{D} \{ \mathbf{S}_x p - MH \frac{\partial H}{\partial x} \} \quad (2.88)$$

$$\mathbf{H}v - \mathbf{G} \frac{\partial v}{\partial n} = \mathbf{D} \{ \mathbf{S}_y p - MH \frac{\partial H}{\partial y} \} \quad (2.89)$$

$$\mathbf{H}p - \mathbf{G} \frac{\partial p}{\partial n} = M\mathbf{D} \left\{ \left(\frac{\partial H}{\partial x} \right)^2 + \left(\frac{\partial H}{\partial y} \right)^2 + H\nabla^2 H \right\} \quad (2.90)$$

$$\mathbf{H}\Psi - \mathbf{G} \frac{\partial \Psi}{\partial n} = \mathbf{D} \{ \mathbf{S}_y u - \mathbf{S}_x v \} \quad (2.91)$$

where

$$\mathbf{D} = (\mathbf{H}\hat{\mathbf{U}} - \mathbf{G}\hat{\mathbf{Q}})\mathbf{F}^{-1} \quad \mathbf{S}_x = \frac{\partial \mathbf{F}}{\partial x} \mathbf{F}^{-1} \quad \mathbf{S}_y = \frac{\partial \mathbf{F}}{\partial y} \mathbf{F}^{-1}. \quad (2.92)$$

These system of equations are solved iteratively, hence the right-hand sides of the equations (2.88)-(2.91) can be evaluated from the previous or the same iteration level values for advancing the iteration. Once the appropriate boundary conditions are inserted and the shuffling process is applied, each matrix-vector equation turns into a linear system to be solved for the unknowns u , v , p and Ψ .

2.4 Application of the DRBEM to the FHD incompressible fluid flow problems

The system of equations to be solved were presented in Chapter 1 (equations (1.39)-(1.43)) as follows

$$\nabla^2 u = \frac{\partial p}{\partial x} + u \frac{\partial u}{\partial x} + v \frac{\partial u}{\partial y} - MnH \frac{\partial H}{\partial x} \quad (2.93)$$

$$\nabla^2 v = \frac{\partial p}{\partial y} + u \frac{\partial v}{\partial x} + v \frac{\partial v}{\partial y} - MnH \frac{\partial H}{\partial y} \quad (2.94)$$

$$\nabla^2 w = P_z + u \frac{\partial w}{\partial x} + v \frac{\partial w}{\partial y} \quad (2.95)$$

$$\nabla^2 p = Mn \left(\left(\frac{\partial H}{\partial x} \right)^2 + \left(\frac{\partial H}{\partial y} \right)^2 + H \left(\frac{\partial^2 H}{\partial x^2} + \frac{\partial^2 H}{\partial y^2} \right) \right) - \left(\frac{\partial u}{\partial x} \right)^2 - \left(\frac{\partial v}{\partial y} \right)^2 - 2 \frac{\partial v}{\partial x} \frac{\partial u}{\partial y} \quad (2.96)$$

$$\nabla^2 \Psi = \frac{\partial u}{\partial y} - \frac{\partial v}{\partial x} \quad (2.97)$$

for the velocity (u, v, w) , pressure p and the stream function Ψ where Mn is the magnetic number. The problem is solved in different geometries from circular cavity to a square cavity containing an obstacle in it. In all these problems Dirichlet type boundary conditions are used for all of the problem unknowns.

The corresponding DRBEM discretized matrix-vector equations are obtained by considering the inhomogeneities in (2.93)-(2.97) as the vector \mathbf{b} in the equation (2.65)

$$\mathbf{H}u - \mathbf{G} \frac{\partial u}{\partial n} = (\mathbf{H}\hat{\mathbf{U}} - \mathbf{G}\hat{\mathbf{Q}})\mathbf{F}^{-1} \left\{ \frac{\partial p}{\partial x} + u \frac{\partial u}{\partial x} + v \frac{\partial u}{\partial y} - MnH \frac{\partial H}{\partial x} \right\} \quad (2.98)$$

$$\mathbf{H}v - \mathbf{G} \frac{\partial v}{\partial n} = (\mathbf{H}\hat{\mathbf{U}} - \mathbf{G}\hat{\mathbf{Q}})\mathbf{F}^{-1} \left\{ \frac{\partial p}{\partial y} + u \frac{\partial v}{\partial x} + v \frac{\partial v}{\partial y} - MnH \frac{\partial H}{\partial y} \right\} \quad (2.99)$$

$$\mathbf{H}w - \mathbf{G} \frac{\partial w}{\partial n} = (\mathbf{H}\hat{\mathbf{U}} - \mathbf{G}\hat{\mathbf{Q}})\mathbf{F}^{-1} \left\{ P_z + u \frac{\partial w}{\partial x} + v \frac{\partial w}{\partial y} \right\} \quad (2.100)$$

$$\begin{aligned} \mathbf{H}p - \mathbf{G} \frac{\partial p}{\partial n} &= (\mathbf{H}\hat{\mathbf{U}} - \mathbf{G}\hat{\mathbf{Q}})\mathbf{F}^{-1} \left\{ Mn \left(\left(\frac{\partial H}{\partial x} \right)^2 + \left(\frac{\partial H}{\partial y} \right)^2 + H \nabla^2 H \right) \right. \\ &\quad \left. - \left(\frac{\partial u}{\partial x} \right)^2 - \left(\frac{\partial v}{\partial y} \right)^2 - 2 \frac{\partial v}{\partial x} \frac{\partial u}{\partial y} \right\} \end{aligned} \quad (2.101)$$

$$\mathbf{H}\Psi - \mathbf{G} \frac{\partial \Psi}{\partial n} = (\mathbf{H}\hat{\mathbf{U}} - \mathbf{G}\hat{\mathbf{Q}})\mathbf{F}^{-1} \left\{ \frac{\partial u}{\partial y} - \frac{\partial v}{\partial x} \right\}. \quad (2.102)$$

Different from the Stokes flow case, the equations for the u -, v - and w -velocity components have nonlinearities due to the convection terms. After approximating the spatial derivatives of the unknowns with the help of the coordinate matrix \mathbf{F} and combining them on the left-hand side of the equations (2.98)-(2.102) one gets

$$(\mathbf{H} - \mathbf{D}(u\mathbf{S}_x + v\mathbf{S}_y))u - \mathbf{G}\frac{\partial u}{\partial n} = \mathbf{D}\{\mathbf{S}_x p - MnH\frac{\partial H}{\partial x}\} \quad (2.103)$$

$$(\mathbf{H} - \mathbf{D}(u\mathbf{S}_x + v\mathbf{S}_y))v - \mathbf{G}\frac{\partial v}{\partial n} = \mathbf{D}\{\mathbf{S}_y p - MnH\frac{\partial H}{\partial y}\} \quad (2.104)$$

$$(\mathbf{H} - \mathbf{D}(u\mathbf{S}_x + v\mathbf{S}_y))w - \mathbf{G}\frac{\partial w}{\partial n} = \mathbf{D}\{P_z\} \quad (2.105)$$

$$\begin{aligned} \mathbf{H}p - \mathbf{G}\frac{\partial p}{\partial n} = & \mathbf{D}\{Mn((\frac{\partial H}{\partial x})^2 + (\frac{\partial H}{\partial y})^2 + H\nabla^2 H) \\ & - (\mathbf{S}_x u)^2 - (\mathbf{S}_y v)^2 - 2(\mathbf{S}_x v)(\mathbf{S}_y u)\} \end{aligned} \quad (2.106)$$

$$\mathbf{H}\Psi - \mathbf{G}\frac{\partial \Psi}{\partial n} = \mathbf{D}\{\mathbf{S}_y u - \mathbf{S}_x v\} . \quad (2.107)$$

The nonlinearities on the left-hand sides of the equations (2.103), (2.104) are handled by taking the velocities from the previous iteration level. The details of the numerical solution process will be given in the next chapter.

2.5 Application of the DRBEM to the FHD forced convection bio-magnetic flow problems with viscous dissipation

The equations defining the problem as presented in Chapter 1 (equations (1.52)-(1.57)) for the velocity (u, v, w) , the pressure p , the temperature T and the stream function Ψ are

$$\nabla^2 u = \frac{\partial p}{\partial x} + u\frac{\partial u}{\partial x} + v\frac{\partial u}{\partial y} - Mn(T_c - T)H\frac{\partial H}{\partial x} \quad (2.108)$$

$$\nabla^2 v = \frac{\partial p}{\partial y} + u\frac{\partial v}{\partial x} + v\frac{\partial v}{\partial y} - Mn(T_c - T)H\frac{\partial H}{\partial y} - \frac{Ra}{Pr}T \quad (2.109)$$

$$\nabla^2 w = P_z + u\frac{\partial w}{\partial x} + v\frac{\partial w}{\partial y} \quad (2.110)$$

$$\begin{aligned} \nabla^2 T = & Pr(u\frac{\partial T}{\partial x} + v\frac{\partial T}{\partial y}) - MnEcPr(\epsilon + T)H(u\frac{\partial H}{\partial x} + v\frac{\partial H}{\partial y}) \\ & - EcPr(2(\frac{\partial u}{\partial x})^2 + 2(\frac{\partial v}{\partial y})^2 + (\frac{\partial v}{\partial x} + \frac{\partial u}{\partial y})^2) \end{aligned} \quad (2.111)$$

$$\begin{aligned}
\nabla^2 p &= \frac{Ra}{Pr} \frac{\partial T}{\partial y} - \left(\frac{\partial u}{\partial x}\right)^2 - \left(\frac{\partial v}{\partial y}\right)^2 - 2 \frac{\partial v}{\partial x} \frac{\partial u}{\partial y} \\
&\quad - Mn \left(\frac{\partial T}{\partial x} H \frac{\partial H}{\partial x} + \frac{\partial T}{\partial y} H \frac{\partial H}{\partial y} \right) \\
&\quad + Mn(T_c - T) \left(\left(\frac{\partial H}{\partial x}\right)^2 + \left(\frac{\partial H}{\partial y}\right)^2 + H \nabla^2 H \right)
\end{aligned} \tag{2.112}$$

$$\nabla^2 \Psi = \frac{\partial u}{\partial y} - \frac{\partial v}{\partial x} \tag{2.113}$$

where Mn , Ec , Pr , Ra , ϵ are the magnetic, Eckert, Prandtl, Rayleigh and temperature numbers, respectively. The boundary conditions for the velocities, pressure and the stream function are Dirichlet type, where the temperature has Neumann type boundary conditions on the adiabatic walls.

The corresponding discretized system of matrix-vector equations using (2.65) for the inhomogeneities are

$$\mathbf{H}u - \mathbf{G} \frac{\partial u}{\partial n} = (\mathbf{H}\hat{\mathbf{U}} - \mathbf{G}\hat{\mathbf{Q}})\mathbf{F}^{-1} \left\{ \frac{\partial p}{\partial x} + u \frac{\partial u}{\partial x} + v \frac{\partial u}{\partial y} - Mn(T_c - T)H \frac{\partial H}{\partial x} \right\} \tag{2.114}$$

$$\mathbf{H}v - \mathbf{G} \frac{\partial v}{\partial n} = (\mathbf{H}\hat{\mathbf{U}} - \mathbf{G}\hat{\mathbf{Q}})\mathbf{F}^{-1} \left\{ \frac{\partial p}{\partial y} + u \frac{\partial v}{\partial x} + v \frac{\partial v}{\partial y} - Mn(T_c - T)H \frac{\partial H}{\partial y} - \frac{Ra}{Pr}T \right\} \tag{2.115}$$

$$\mathbf{H}w - \mathbf{G} \frac{\partial w}{\partial n} = (\mathbf{H}\hat{\mathbf{U}} - \mathbf{G}\hat{\mathbf{Q}})\mathbf{F}^{-1} \left\{ P_z + u \frac{\partial w}{\partial x} + v \frac{\partial w}{\partial y} \right\} \tag{2.116}$$

$$\begin{aligned}
\mathbf{H}T - \mathbf{G} \frac{\partial T}{\partial n} &= (\mathbf{H}\hat{\mathbf{U}} - \mathbf{G}\hat{\mathbf{Q}})\mathbf{F}^{-1} \left\{ Pr \left(u \frac{\partial T}{\partial x} + v \frac{\partial T}{\partial y} \right) \right. \\
&\quad - MnEcPr(\epsilon + T)H \left(u \frac{\partial H}{\partial x} + v \frac{\partial H}{\partial y} \right) \\
&\quad \left. - EcPr \left(2 \left(\frac{\partial u}{\partial x} \right)^2 + 2 \left(\frac{\partial v}{\partial y} \right)^2 + \left(\frac{\partial v}{\partial x} + \frac{\partial u}{\partial y} \right)^2 \right) \right\}
\end{aligned} \tag{2.117}$$

$$\begin{aligned}
\mathbf{H}p - \mathbf{G} \frac{\partial p}{\partial n} &= (\mathbf{H}\hat{\mathbf{U}} - \mathbf{G}\hat{\mathbf{Q}})\mathbf{F}^{-1} \left\{ \frac{Ra}{Pr} \frac{\partial T}{\partial y} - \left(\frac{\partial u}{\partial x}\right)^2 - \left(\frac{\partial v}{\partial y}\right)^2 - 2 \frac{\partial v}{\partial x} \frac{\partial u}{\partial y} \right. \\
&\quad - Mn \left(\frac{\partial T}{\partial x} H \frac{\partial H}{\partial x} + \frac{\partial T}{\partial y} H \frac{\partial H}{\partial y} \right) \\
&\quad \left. + Mn(T_c - T) \left(\left(\frac{\partial H}{\partial x}\right)^2 + \left(\frac{\partial H}{\partial y}\right)^2 + H \nabla^2 H \right) \right\}
\end{aligned} \tag{2.118}$$

$$\mathbf{H}\Psi - \mathbf{G} \frac{\partial \Psi}{\partial n} = (\mathbf{H}\hat{\mathbf{U}} - \mathbf{G}\hat{\mathbf{Q}})\mathbf{F}^{-1} \left\{ \frac{\partial u}{\partial y} - \frac{\partial v}{\partial x} \right\}. \tag{2.119}$$

As in the case of the FHD incompressible flow, after the treatment of the spatial derivatives and collection of the unknowns on the left-hand side bring the system

to be solved iteratively

$$(\mathbf{H} - \mathbf{D}(u\mathbf{S}_x + v\mathbf{S}_y))u - \mathbf{G}\frac{\partial u}{\partial n} = \mathbf{D}\{\mathbf{S}_x p - Mn(T_c - T)H\frac{\partial H}{\partial x}\} \quad (2.120)$$

$$(\mathbf{H} - \mathbf{D}(u\mathbf{S}_x + v\mathbf{S}_y))v - \mathbf{G}\frac{\partial v}{\partial n} = \mathbf{D}\{\mathbf{S}_y p - Mn(T_c - T)H\frac{\partial H}{\partial y} - \frac{Ra}{Pr}T\} \quad (2.121)$$

$$(\mathbf{H} - \mathbf{D}(u\mathbf{S}_x + v\mathbf{S}_y))w - \mathbf{G}\frac{\partial w}{\partial n} = \mathbf{D}\{P_z\} \quad (2.122)$$

$$\begin{aligned} & (\mathbf{H} - Pr\mathbf{D}(u\mathbf{S}_x + v\mathbf{S}_y - MnEcH(u\frac{\partial H}{\partial x} + v\frac{\partial H}{\partial y})))T - \mathbf{G}\frac{\partial T}{\partial n} = \\ & = \mathbf{D}\{-MnEcPr\epsilon H(u\frac{\partial H}{\partial x} + v\frac{\partial H}{\partial y}) - EcPr(2(\mathbf{S}_x u)^2 + 2(\mathbf{S}_y v)^2 \\ & + (\mathbf{S}_x v + \mathbf{S}_y u)^2)\} \end{aligned} \quad (2.123)$$

$$\begin{aligned} \mathbf{H}p - \mathbf{G}\frac{\partial p}{\partial n} & = \mathbf{D}\{\frac{Ra}{Pr}\mathbf{S}_y T - (\mathbf{S}_x u)^2 - (\mathbf{S}_y v)^2 - 2(\mathbf{S}_x v)(\mathbf{S}_y u) \\ & - Mn(\mathbf{S}_x T H\frac{\partial H}{\partial x} + \mathbf{S}_y T H\frac{\partial H}{\partial y}) \\ & + Mn(T_c - T)((\frac{\partial H}{\partial x})^2 + (\frac{\partial H}{\partial y})^2 + H\nabla^2 H)\} \end{aligned} \quad (2.124)$$

$$\mathbf{H}\Psi - \mathbf{G}\frac{\partial \Psi}{\partial n} = \mathbf{D}\{\mathbf{S}_y u - \mathbf{S}_x v\} . \quad (2.125)$$

2.6 Application of the DRBEM to the MHD Duct Flow with Slipping Velocity Condition

Governing equations of the MHD flow in a pipe of rectangular cross-section with horizontally applied magnetic field are (Chapter 1, equations (1.68) and (1.69))

$$\begin{aligned} \nabla^2 V & = -1 - Ha\frac{\partial B}{\partial x} \\ \nabla^2 B & = -Ha\frac{\partial V}{\partial x} \end{aligned} \quad (2.126)$$

where V and B are the velocity and the induced magnetic field and Ha is the Hartmann number. The problem is considered in several regions with slip-velocity condition on some boundaries and Dirichlet or Neumann type boundary conditions for the induced magnetic field B . Taking the right-hand sides in

(2.126) as the inhomogeneities in the equation (2.65), the DRBEM discretized matrix-vector equations become

$$\begin{aligned}\mathbf{H}V - \mathbf{G}\frac{\partial V}{\partial n} &= -(\mathbf{H}\hat{\mathbf{U}} - \mathbf{G}\hat{\mathbf{Q}})\mathbf{F}^{-1}\left\{Ha\frac{\partial B}{\partial x} + 1\right\} \\ \mathbf{H}B - \mathbf{G}\frac{\partial B}{\partial n} &= -(\mathbf{H}\hat{\mathbf{U}} - \mathbf{G}\hat{\mathbf{Q}})\mathbf{F}^{-1}\left\{Ha\frac{\partial V}{\partial x}\right\}.\end{aligned}\quad (2.127)$$

Instead of using an iterative procedure or decoupling the equations which introduces difficulties due to the slip velocity condition, the coupled matrix-vector equations (2.127) are combined to obtain a larger system and solved at once. Even the sizes of the matrices increase, the numerical solution is obtained with considerably less computational time. The combination of the equations (2.127) again by using the matrix \mathbf{F} for the approximation of the derivatives $\frac{\partial B}{\partial x}$ and $\frac{\partial V}{\partial x}$ gives

$$\begin{bmatrix} \mathbf{H} & \mathbf{0} \\ \mathbf{0} & \mathbf{H} \end{bmatrix} \begin{Bmatrix} V \\ B \end{Bmatrix} - \begin{bmatrix} \mathbf{G} & \mathbf{0} \\ \mathbf{0} & \mathbf{G} \end{bmatrix} \begin{Bmatrix} \frac{\partial V}{\partial n} \\ \frac{\partial B}{\partial n} \end{Bmatrix} = -Ha \begin{bmatrix} \mathbf{M} & \mathbf{0} \\ \mathbf{0} & \mathbf{M} \end{bmatrix} \begin{Bmatrix} B \\ V \end{Bmatrix} + \begin{bmatrix} \mathbf{D} & \mathbf{0} \\ \mathbf{0} & \mathbf{0} \end{bmatrix} \begin{Bmatrix} -1 \\ 0 \end{Bmatrix}\quad (2.128)$$

where $\mathbf{D} = (\mathbf{H}\hat{\mathbf{U}} - \mathbf{G}\hat{\mathbf{Q}})\mathbf{F}^{-1}$ and $\mathbf{M} = \mathbf{D}\frac{\partial \mathbf{F}}{\partial x}\mathbf{F}^{-1}$.

The first term on the right-hand side of the equation (2.128) is written as

$$\begin{bmatrix} \mathbf{H} & \mathbf{0} \\ \mathbf{0} & \mathbf{H} \end{bmatrix} \begin{Bmatrix} V \\ B \end{Bmatrix} - \begin{bmatrix} \mathbf{G} & \mathbf{0} \\ \mathbf{0} & \mathbf{G} \end{bmatrix} \begin{Bmatrix} \frac{\partial V}{\partial n} \\ \frac{\partial B}{\partial n} \end{Bmatrix} = -Ha \begin{bmatrix} \mathbf{0} & \mathbf{M} \\ \mathbf{M} & \mathbf{0} \end{bmatrix} \begin{Bmatrix} V \\ B \end{Bmatrix} + \begin{bmatrix} \mathbf{D} & \mathbf{0} \\ \mathbf{0} & \mathbf{0} \end{bmatrix} \begin{Bmatrix} -1 \\ 0 \end{Bmatrix}\quad (2.129)$$

Rearranging the right-hand side gives the system

$$\left(\begin{bmatrix} \mathbf{H} & \mathbf{0} \\ \mathbf{0} & \mathbf{H} \end{bmatrix} + Ha \begin{bmatrix} \mathbf{0} & \mathbf{M} \\ \mathbf{M} & \mathbf{0} \end{bmatrix} \right) \begin{Bmatrix} V \\ B \end{Bmatrix} - \begin{bmatrix} \mathbf{G} & \mathbf{0} \\ \mathbf{0} & \mathbf{G} \end{bmatrix} \begin{Bmatrix} \frac{\partial V}{\partial n} \\ \frac{\partial B}{\partial n} \end{Bmatrix} = \begin{bmatrix} \mathbf{D} & \mathbf{0} \\ \mathbf{0} & \mathbf{0} \end{bmatrix} \begin{Bmatrix} -1 \\ 0 \end{Bmatrix}.\quad (2.130)$$

Defining new matrices

$$\hat{\mathbf{H}} = \begin{bmatrix} \mathbf{H} & \mathbf{0} \\ \mathbf{0} & \mathbf{H} \end{bmatrix} + Ha \begin{bmatrix} \mathbf{0} & \mathbf{M} \\ \mathbf{M} & \mathbf{0} \end{bmatrix}, \quad \hat{\mathbf{G}} = \begin{bmatrix} \mathbf{G} & \mathbf{0} \\ \mathbf{0} & \mathbf{G} \end{bmatrix}, \quad \hat{\mathbf{D}} = \begin{bmatrix} \mathbf{D} & \mathbf{0} \\ \mathbf{0} & \mathbf{0} \end{bmatrix}\quad (2.131)$$

where $\hat{\mathbf{H}}$, $\hat{\mathbf{G}}$, $\hat{\mathbf{D}}$ are $2(N + L) \times 2(N + L)$ sized matrices, one gets the enlarged system,

$$\hat{\mathbf{H}} \begin{Bmatrix} V \\ B \end{Bmatrix} = \hat{\mathbf{G}} \begin{Bmatrix} \frac{\partial V}{\partial n} \\ \frac{\partial B}{\partial n} \end{Bmatrix} + \hat{\mathbf{D}} \begin{Bmatrix} -1 \\ 0 \end{Bmatrix}. \quad (2.132)$$

For each MHD flow problem presented in this thesis either the induced magnetic field or its normal derivative is known on one part of the boundary. If there is slip velocity condition on a boundary, the velocity is the unknown, and thus for the normal derivative the slip condition $\frac{\partial V}{\partial n} = -\frac{1}{\alpha}V$ is used. If there is no-slip on the boundary, then the velocity is known and the unknown is the normal derivative. The velocity and the induced magnetic field are the unknowns and their normal derivatives are zero for the interior nodes. Then, all the conditions for the boundary and interior nodes are inserted into the matrix vector equation (2.132). In this case, both vectors on the left and right-hand sides of equation (2.132) have some known and unknown values. In order to obtain a linear system of equations one needs to rearrange the system. Each unknown on the right-hand side of equation (2.132) is carried to the left-hand side by interchanging the corresponding columns of matrices $\hat{\mathbf{H}}$ and $\hat{\mathbf{G}}$. In the case of slip velocity condition, since the velocity is unknown, the corresponding columns of the matrices $\hat{\mathbf{H}}$ and $\frac{1}{\alpha}\hat{\mathbf{G}}$ are added and carried to the left-hand side, and the corresponding column on the right-hand side is left as zero. Once all the unknowns are passed to the left-hand side a linear system of equations

$$\mathbf{Ax} = \mathbf{c} \quad (2.133)$$

is obtained and solved. This process gives the velocity V and the induced magnetic field B both in the interior and on the boundary nodes in one stroke.

2.7 Application of the DRBEM to the MHD Flow Between Parallel Infinite Plates with Slipping Velocity Condition

The MHD flow between infinite parallel plates under the effect of vertically applied magnetic field and the electric potential are defined by the equations

(Chapter 1, equations (1.78)-(1.80)) in the absence of the pressure gradient.

$$\begin{aligned}\nabla^2 V &= -Ha \frac{\partial B}{\partial y} \\ \nabla^2 B &= -Ha \frac{\partial V}{\partial y} \\ \nabla^2 \Phi &= -\frac{\partial V}{\partial x}\end{aligned}\tag{2.134}$$

where V , B and Φ are the fluid velocity, induced magnetic field and the electric potential, and Ha is the Hartmann number. The flow is started with the interaction of the electrodes placed symmetrically at the centers of the plates and the electrically conducting fluid. The problem is considered in an infinite region $\Omega = \{(x, y) : -1 < y < 1, -\infty < x < \infty\}$ with slip-velocity conditions on the plates and Dirichlet or Neumann type boundary conditions for the induced magnetic field; i.e. on the electrodes $\frac{\partial B}{\partial n} = 0$, on the rest of the plates $B = \text{constant}$. Electric potential equation in (2.134) is solved after the velocity and the induced magnetic field are computed through the first two coupled equations. The corresponding DRBEM discretized matrix-vector equations for the velocity and the induced magnetic field are (by taking as the inhomogeneity b the right-hand sides of (2.134))

$$\begin{aligned}\mathbf{H}V - \mathbf{G} \frac{\partial V}{\partial n} &= -(\mathbf{H}\hat{\mathbf{U}} - \mathbf{G}\hat{\mathbf{Q}})\mathbf{F}^{-1}\left\{Ha \frac{\partial B}{\partial y}\right\} \\ \mathbf{H}B - \mathbf{G} \frac{\partial B}{\partial n} &= -(\mathbf{H}\hat{\mathbf{U}} - \mathbf{G}\hat{\mathbf{Q}})\mathbf{F}^{-1}\left\{Ha \frac{\partial V}{\partial y}\right\}.\end{aligned}\tag{2.135}$$

Then, similar to the case of Section 2.6, the matrix-vector systems in (2.135) are combined to a large system and rearranged as

$$\left(\left[\begin{array}{cc}\mathbf{H} & \mathbf{0} \\ \mathbf{0} & \mathbf{H}\end{array}\right] + Ha \left[\begin{array}{cc}\mathbf{0} & \mathbf{N} \\ \mathbf{N} & \mathbf{0}\end{array}\right]\right) \begin{Bmatrix} V \\ B \end{Bmatrix} - \begin{bmatrix} \mathbf{G} & \mathbf{0} \\ \mathbf{0} & \mathbf{G} \end{bmatrix} \begin{Bmatrix} \frac{\partial V}{\partial n} \\ \frac{\partial B}{\partial n} \end{Bmatrix} = \begin{Bmatrix} 0 \\ 0 \end{Bmatrix}\tag{2.136}$$

where $\mathbf{N} = \mathbf{D} \frac{\partial \mathbf{F}}{\partial y} \mathbf{F}^{-1}$. Defining new matrices

$$\tilde{\mathbf{H}} = \begin{bmatrix} \mathbf{H} & \mathbf{0} \\ \mathbf{0} & \mathbf{H} \end{bmatrix} + Ha \begin{bmatrix} \mathbf{0} & \mathbf{N} \\ \mathbf{N} & \mathbf{0} \end{bmatrix}, \quad \tilde{\mathbf{G}} = \begin{bmatrix} \mathbf{G} & \mathbf{0} \\ \mathbf{0} & \mathbf{G} \end{bmatrix}\tag{2.137}$$

one obtains the enlarged system

$$\tilde{\mathbf{H}} \begin{Bmatrix} V \\ B \end{Bmatrix} = \tilde{\mathbf{G}} \begin{Bmatrix} \frac{\partial V}{\partial n} \\ \frac{\partial B}{\partial n} \end{Bmatrix}. \quad (2.138)$$

where $\tilde{\mathbf{H}}$ and $\tilde{\mathbf{G}}$ are $2(N + L) \times 2(N + L)$ matrices.

In this problem, the portions of the plates with electrodes are perfectly conducting giving $\frac{\partial B}{\partial n} = 0$ whereas the rest of the walls are conducting meaning that induced magnetic field $B = \text{constant}$. If the no-slip condition is imposed for the velocity, then $V = 0$ on the boundary. If the infinite plates admit slip, then the velocity is also unknown and $\frac{\partial V}{\partial n} = -\frac{1}{\alpha}V$. For all of the interior nodes velocity and the induced magnetic field are unknowns and their normal derivatives are zero. When the boundary conditions are inserted, the unknown values on the right-hand side are carried to the left-hand side by interchanging corresponding columns of the $\tilde{\mathbf{H}}$ and $\tilde{\mathbf{G}}$ matrices as in Section 2.6. The obtained linear system is solved using Gaussian elimination with pivoting. This procedure gives the nodal solution of the velocity and the induced magnetic field in one stroke.

After the velocity of the fluid is obtained Poisson's type equation for the electric potential is discretized by the DRBEM as

$$\mathbf{H}\Phi - \mathbf{G} \frac{\partial \Phi}{\partial n} = -(\mathbf{H}\hat{\mathbf{U}} - \mathbf{G}\hat{\mathbf{Q}})\mathbf{F}^{-1} \left\{ \frac{\partial V}{\partial x} \right\} \quad (2.139)$$

and solved for the discretized values of Φ by using the Neumann type boundary conditions $\frac{\partial \Phi}{\partial n} = \Phi_n$ where $\Phi_n = \pm 1$ on $y = \pm 1$ on the electrodes and $\Phi_n = 0$ outside the electrodes.

In Chapter 2, the BEM formulation for the Laplace equation and the DRBEM formulation for the Poisson's type equations containing unknown itself and some of its space derivatives as inhomogeneity are presented. The applications of the methods to the FHD Stokes flow, incompressible and forced convection biomagnetic fluid flows, and MHD rectangular pipe flow, MHD flow between parallel plates with slipping velocity at the fluid-solid interface are given. In Chapter 3 and 4 the numerical solution procedures and the numerical results obtained

from the BEM and DRBEM discretized matrix-vector systems are going to be illustrated for each of these problems in several regions and for several values of problem parameters.





CHAPTER 3

DRBEM SOLUTIONS OF STOKES, INCOMPRESSIBLE AND FORCED CONVECTION FLOWS UNDER THE EFFECT OF POINT MAGNETIC SOURCE

In this chapter, the dual reciprocity boundary element method analysis is presented for FHD Stokes, incompressible and forced convection flows in pipes subjected to point magnetic source(s) generated by thin wire(s). The electrically non-conducting fluid is pumped within the pipe by a constant pressure gradient which results in a laminar, steady and fully developed flow (Figure 3.1). In fully developed flows, the velocity, pressure and the temperature disturbances repeat themselves in each cross-section of a long enough pipe taken perpendicular to the flow field. This means that, all the problem unknowns show variations only in the cross-section (cavity) which is perpendicular to the pipe axis and in this cross-section the magnetic wire(s) acts as point magnetic source(s). In most of the numerical studies in cavity flows, especially with the DRBEM, stream function-vorticity formulation is used to eliminate the pressure gradient terms in the momentum equations [17, 73]. This may be due to the absence of the pressure equation and the boundary conditions, and the difficulties in the convergence of the derived pressure equation in the iterative procedure. In practice, pipe flow problems mostly occur in the process of transportation of heat and mass, and the knowledge of the pressure in the cavity is important in the design of medical and engineering instruments. In this study, the aim is to develop an algorithm using the DRBEM to simulate all the problem unknowns (the velocity, pressure, and the temperature) of the FHD pipe flow problems presented in Chapter 1. For each problem studied in this chapter, the unknown pressure boundary conditions are approximated by a combination of finite difference and

the DRBEM coordinate matrix. Then, the discretized systems (2.88)-(2.91), (2.103)-(2.107) and (2.120)-(2.125) given in Chapter 2 are solved iteratively. The achieved numerical results are displayed in terms of the velocity, pressure and the temperature of the fluid and interpreted physically. All of the computer codes are written in Matlab R2014a using a 16GB RAM computer. Linear radial basis functions $f(r_j) = 1 + r_j$ for $j = 1, 2, \dots, N + L$ are used to approximate the inhomogeneous parts of each Poisson's type equation in (2.80)-(2.83), (2.93)-(2.97) and (2.108)-(2.113).

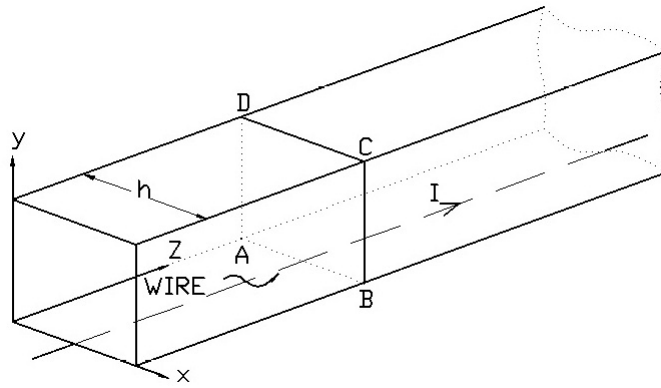


Figure 3.1: Flow configuration for a rectangular pipe subjected to a magnetic field generated by a thin wire.

The considered problems in this chapter are listed in Table 3.1.

Table 3.1: Problems considered in Chapter 3.

3.1.1	Stokes flow in a lid-driven cavity with point magnetic source
3.1.2	Stokes flow in a square cavity with point magnetic source
3.1.3	Stokes flow in a lid-driven circular cavity with point magnetic source
3.2.1	Incompressible flow in a square cavity with point magnetic source
3.2.2	Incompressible flow in a lid-driven square cavity with point magnetic source
3.2.3	Incompressible flow in a circular cavity with point magnetic source
3.2.4	Incompressible flow in a square cavity with an obstacle (annular pipes) under point magnetic source
3.3.1	Square cavity with two or three sources below the bottom wall
3.3.2	Rectangular cavity with two or three sources below the bottom wall
3.3.3	Square and rectangular cavities with sources on opposite walls
3.4.1	Forced convection flow in a square cavity with horizontal adiabatic walls and point magnetic source

3.4.2	Forced convection flow in a lid-driven square cavity with horizontal adiabatic walls and point magnetic source
3.4.3	Forced convection flow in a square cavity with vertical adiabatic walls and point magnetic source
3.4.4	Forced convection flow in a circular cavity with point magnetic source

3.1 Stokes Flow in Cavities with Point Magnetic Source

Stokes flows (creeping flows) are incompressible (highly) viscous flows in slow motion. Swimming of microorganisms, settling of dust particles, fluid flow in small channels or cracks (such as ground water or oil) and the seepage in rock or sand formations are considered as Stokes flow. Extrusion of melt, paint transportation, hydrodynamic lubrication, heavy-oils or food-processing materials are also interpreted by the Stokes flow phenomena. Stokes flow equations are simplified versions of Navier-Stokes equations by neglecting the non-linear convective acceleration terms. In this section, the DRBEM solutions of Stokes flow in lid-driven, square and circular cavities under the influence of the point source magnetic field placed below the bottom wall are presented.

The DRBEM discretized matrix-vector equations corresponding to the Stokes flow problem are given in Chapter 2 (equations (2.88)-(2.91)) as

$$\mathbf{H}u - \mathbf{G} \frac{\partial u}{\partial n} = \mathbf{D} \{ \mathbf{S}_x p - MH \frac{\partial H}{\partial x} \} \quad (3.1)$$

$$\mathbf{H}v - \mathbf{G} \frac{\partial v}{\partial n} = \mathbf{D} \{ \mathbf{S}_y p - MH \frac{\partial H}{\partial y} \} \quad (3.2)$$

$$\mathbf{H}p - \mathbf{G} \frac{\partial p}{\partial n} = M\mathbf{D} \left\{ \left(\frac{\partial H}{\partial x} \right)^2 + \left(\frac{\partial H}{\partial y} \right)^2 + H\nabla^2 H \right\} \quad (3.3)$$

$$\mathbf{H}\Psi - \mathbf{G} \frac{\partial \Psi}{\partial n} = \mathbf{D} \{ \mathbf{S}_y u - \mathbf{S}_x v \} \quad (3.4)$$

where

$$\mathbf{D} = (\mathbf{H}\hat{\mathbf{U}} - \mathbf{G}\hat{\mathbf{Q}})\mathbf{F}^{-1} \quad \mathbf{S}_x = \frac{\partial \mathbf{F}}{\partial x} \mathbf{F}^{-1} \quad \mathbf{S}_y = \frac{\partial \mathbf{F}}{\partial y} \mathbf{F}^{-1} . \quad (3.5)$$

The magnetic field strength $H(x, y)$ for a square cavity is given in terms of the position of the point magnetic source (a_1, a_2)

$$H(x, y) = \frac{|a_2|}{\sqrt{(x - a_1)^2 + (y - a_2)^2}}. \quad (3.6)$$

Figure 3.2 presents the magnetic field strength contour lines in a square cavity for $(a_1, a_2) = (0.5, -0.05)$.

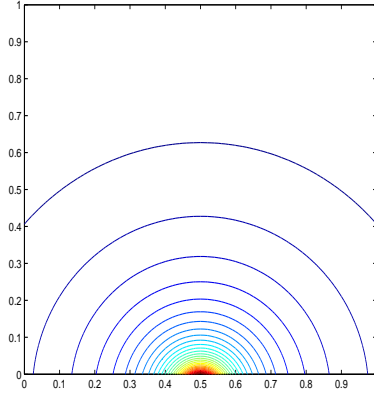


Figure 3.2: Magnetic field strength equilines for $(a_1, a_2) = (0.5, -0.05)$.

The system of equations (3.1)-(3.4) are solved iteratively as in the following algorithm:

S.1 Define the ratio $M = Mn/Re$, pre-assign a tolerance tol for the convergence criteria, and a relaxation parameter κ for accelerating pressure convergence.

S.2 Compute spatial derivatives $\frac{\partial H}{\partial x}$, $\frac{\partial H}{\partial y}$, $\frac{\partial^2 H}{\partial x^2}$, $\frac{\partial^2 H}{\partial y^2}$ of the magnetic field intensity function $H(x, y)$ from its definition (3.6).

S.3 Take an initial guess $p^{(0)}$ for pressure.

S.4 Solve the velocity components from the momentum equations

$$\mathbf{H}u^{(k+1)} - \mathbf{G} \frac{\partial u^{(k+1)}}{\partial n} = \mathbf{D}\{\mathbf{S}_x p^{(k)} - MH \frac{\partial H}{\partial x}\} \quad (3.7)$$

$$\mathbf{H}v^{(k+1)} - \mathbf{G} \frac{\partial v^{(k+1)}}{\partial n} = \mathbf{D}\{\mathbf{S}_y p^{(k)} - MH \frac{\partial H}{\partial y}\} \quad (3.8)$$

using the Dirichlet boundary conditions for the velocity.

S.5 Solve

$$\mathbf{H}\Psi^{(k+1)} - \mathbf{G} \frac{\partial \Psi^{(k+1)}}{\partial n} = \mathbf{D}\{\mathbf{S}_y u^{(k+1)} - \mathbf{S}_x v^{(k+1)}\} \quad (3.9)$$

using the natural boundary condition for the stream function.

S.6 Generate boundary conditions for pressure using the x - and y - components of the momentum equations and newly obtained solutions for the u - and the v -velocities. Approximate pressure gradients by a forward difference and the spatial derivatives of the velocities using the DRBEM coordinate matrix \mathbf{F} . The details are given in the following sections.

S.7 Solve pressure equation

$$\mathbf{H}p^{(k+1)} - \mathbf{G} \frac{\partial p^{(k+1)}}{\partial n} = MD\left\{\left(\frac{\partial H}{\partial x}\right)^2 + \left(\frac{\partial H}{\partial y}\right)^2 + H\nabla^2 H\right\} \quad (3.10)$$

using the obtained pressure boundary conditions in step **S.6**.

S.8 Relax the obtained pressure values

$$p^{(k+1)} = \kappa p^{(k+1)} + (1 - \kappa)p^{(k)}, \quad 0 < \kappa \leq 1 \quad (3.11)$$

S.9 Check the convergence criteria

$$\frac{\|z^{(k+1)} - z^{(k)}\|_\infty}{\|z^{(k)}\|_\infty} < tol \quad (3.12)$$

where $\|z\|_\infty = \max\{|z_1|, |z_2|, \dots, |z_{N+L}|\}$ for u , v , p and Ψ , and k denotes the iteration level.

S.10 If the criteria is satisfied for all of the problem unknowns stop.

S.11 If the criteria is not satisfied for one of the unknowns go to step **S.4**.

3.1.1 Stokes flow in a lid-driven cavity with point magnetic source

In this section, fully developed Stokes flow in a square cross-section of a rectangular pipe with a moving top-lid is studied. The cavity flow is subjected to a point source magnetic field. In the absence of the magnetic field ($M = 0$) the problem turns to the basic lid-driven cavity flow and the numerical solution of

this problem is available in the literature [21] and [71]. The problem geometry and the boundary conditions are presented in Figure 3.3.

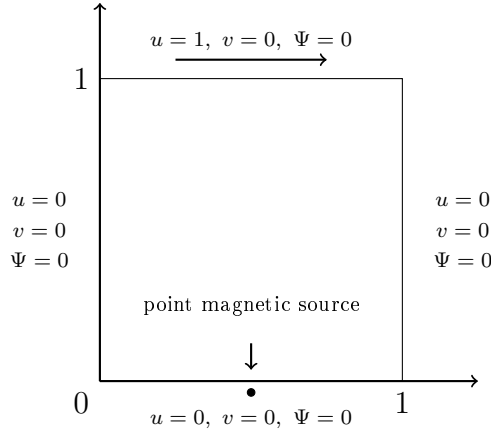


Figure 3.3: Stokes flow in a lid-driven cavity.

The pressure boundary conditions for each part of the boundary are found through the momentum equations

$$\frac{\partial p}{\partial x} = \nabla^2 u + MH \frac{\partial H}{\partial x} \quad (3.13)$$

$$\frac{\partial p}{\partial y} = \nabla^2 v + MH \frac{\partial H}{\partial y} . \quad (3.14)$$

The Taylor series expansion of the pressure $p(x, y)$ around a boundary point $bd = (x_{bd}, y_{bd})$ is given by

$$p(x_{bd} + \delta x, y_{bd} + \delta y) = p(x_{bd}, y_{bd}) + \left. \frac{\partial p}{\partial x} \right|_{bd} \delta x + \left. \frac{\partial p}{\partial y} \right|_{bd} \delta y + O((\delta x)^2 + (\delta y)^2) \quad (3.15)$$

under the assumption of infinitely many times differentiability of p in a sufficiently large neighborhood of the point bd where $\delta x = (x - x_{bd})$ and $\delta y = (y - y_{bd})$. Then, for the closest interior node $int = (x_{int}, y_{int})$ to the boundary point bd (Figure 3.4) one has

$$p(x_{int}, y_{int}) \approx p(x_{bd}, y_{bd}) + \left. \frac{\partial p}{\partial x} \right|_{bd} \Delta x + \left. \frac{\partial p}{\partial y} \right|_{bd} \Delta y \quad (3.16)$$

with $\Delta x = x_{int} - x_{bd}$ and $\Delta y = y_{int} - y_{bd}$.

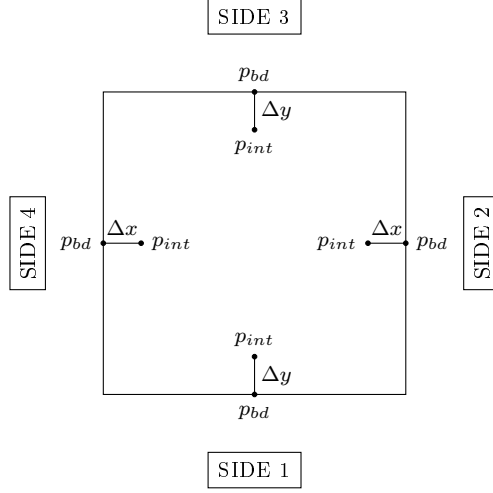


Figure 3.4: Stokes flow in a square cavity: Derivation of pressure wall conditions.

The approximation in (3.16) implies the following approaches for the spatial derivatives of pressure evaluated at the corresponding boundary node

$$\begin{aligned}
\text{SIDE 1:} & \quad \left. \frac{\partial p}{\partial y} \right|_{bd} \approx \frac{p_{int} - p_{bd}}{\Delta y} \\
\text{SIDE 2:} & \quad \left. \frac{\partial p}{\partial x} \right|_{bd} \approx \frac{p_{bd} - p_{int}}{\Delta x} \\
\text{SIDE 3:} & \quad \left. \frac{\partial p}{\partial y} \right|_{bd} \approx \frac{p_{bd} - p_{int}}{\Delta y} \\
\text{SIDE 4:} & \quad \left. \frac{\partial p}{\partial x} \right|_{bd} \approx \frac{p_{int} - p_{bd}}{\Delta x}.
\end{aligned} \tag{3.17}$$

Using equations (3.13) and (3.14)

$$\begin{aligned}
\text{SIDE 1:} & \quad \frac{p_{int}^{(k)} - p_{bd}^{(k+1)}}{\Delta y} = \nabla^2 v^{(k+1)} + MH \frac{\partial H}{\partial y} \\
\text{SIDE 2:} & \quad \frac{p_{bd}^{(k+1)} - p_{int}^{(k)}}{\Delta x} = \nabla^2 u^{(k+1)} + MH \frac{\partial H}{\partial x} \\
\text{SIDE 3:} & \quad \frac{p_{bd}^{(k+1)} - p_{int}^{(k)}}{\Delta y} = \nabla^2 v^{(k+1)} + MH \frac{\partial H}{\partial y} \\
\text{SIDE 4:} & \quad \frac{p_{int}^{(k)} - p_{bd}^{(k+1)}}{\Delta x} = \nabla^2 u^{(k+1)} + MH \frac{\partial H}{\partial x}.
\end{aligned} \tag{3.18}$$

The Laplacian terms on the right-hand sides of the equations (3.18) are approximated by the DRBEM coordinate matrix \mathbf{F} by taking

$$\nabla^2 \approx \mathbf{S}_{\nabla} = \frac{\partial \mathbf{F}}{\partial x} \mathbf{F}^{-1} \frac{\partial \mathbf{F}}{\partial x} \mathbf{F}^{-1} + \frac{\partial \mathbf{F}}{\partial y} \mathbf{F}^{-1} \frac{\partial \mathbf{F}}{\partial y} \mathbf{F}^{-1} \tag{3.19}$$

and writing

$$\nabla^2 u \approx \mathbf{S}_{\nabla} u, \quad \nabla^2 v \approx \mathbf{S}_{\nabla} v. \quad (3.20)$$

Then, pressure boundary condition approximation is obtained for each side of the cavity as

$$\begin{aligned} \text{SIDE 1:} \quad p_{bd}^{(k+1)} &= p_{int}^{(k)} - \Delta y (\mathbf{S}_{\nabla} v^{(k+1)} + MH \frac{\partial H}{\partial y}) \\ \text{SIDE 2:} \quad p_{bd}^{(k+1)} &= p_{int}^{(k)} + \Delta x (\mathbf{S}_{\nabla} u^{(k+1)} + MH \frac{\partial H}{\partial x}) \\ \text{SIDE 3:} \quad p_{bd}^{(k+1)} &= p_{int}^{(k)} + \Delta y (\mathbf{S}_{\nabla} v^{(k+1)} + MH \frac{\partial H}{\partial y}) \\ \text{SIDE 4:} \quad p_{bd}^{(k+1)} &= p_{int}^{(k)} - \Delta x (\mathbf{S}_{\nabla} u^{(k+1)} + MH \frac{\partial H}{\partial x}). \end{aligned} \quad (3.21)$$

The effect of the point magnetic source on the Stokes flow of electrically non-conducting fluid is studied for various ranges of M . The point source is placed at $(0.5, -0.05)$ below the bottom wall. The problem domain is discretized both with constant and linear elements for the $M = 0$ and $M = 10$ cases in order to compare the efficiency of the two approaches. $N = 160$ constant or linear elements are used. The relaxation parameter for pressure is found as $\kappa = 0.055$ by trial and error. 10^{-3} tolerance is taken for the stopping criteria and $p^{(0)} = 0$ initially. The numerical results are displayed in Figures 3.5-3.10 in terms of the equal lines of velocity (u, v) , stream function Ψ and pressure p of the fluid with increasing $M = Mn/Re$ values.

Figures 3.5 ($M = 0$) and 3.6 ($M = 10$) show the DRBEM solutions with constant and linear elements. It can be visualized that almost the same profiles are obtained with almost the same accuracy. Linear element discretization requires more iterations for convergence. Thus, the rest of the computations in Stokes and incompressible flow problems are carried by using constant elements due to its less computational time and space requirements.

When the fluid is free of magnetization ($M = 0$, Figure 3.5) the flow is under the control of the moving top lid and the obtained numerical results are in good agreement with the results in [21] and [71]. In the absence of the magnetic field, flow consist of one main vortex rotating in clockwise direction and pressure is high at the top corners. A secondary flow develops in u -velocity showing the effect of the moving lid. Pressure and v -velocity profiles are symmetric in magnitude with respect to $x = 0.5$ line.

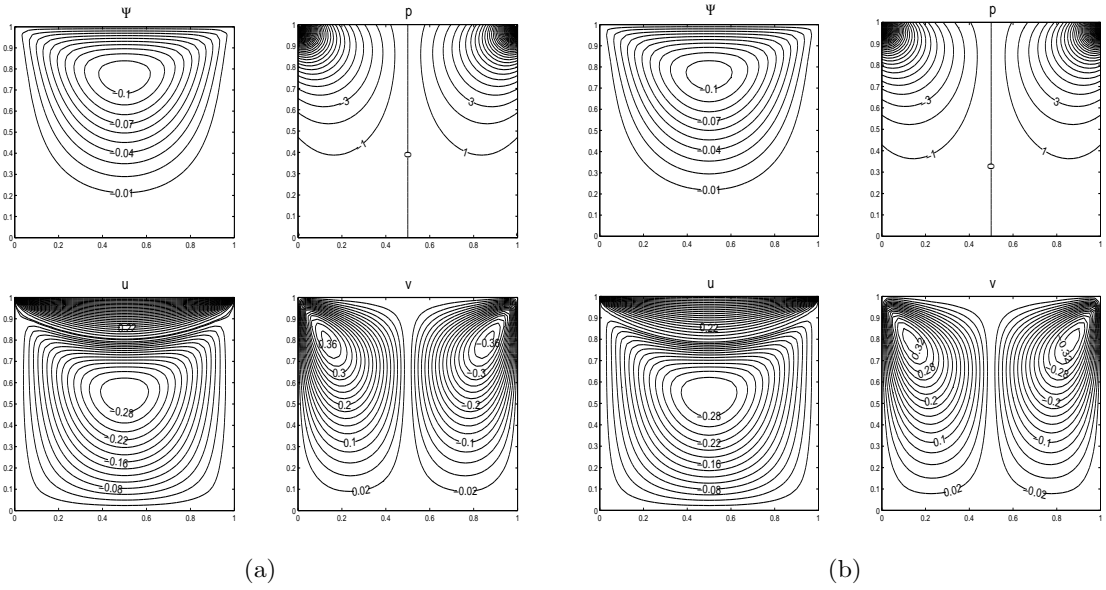


Figure 3.5: Stokes flow in a lid-driven square cavity, $M = 0$, (a) constant element approximation (b) linear element approximation.

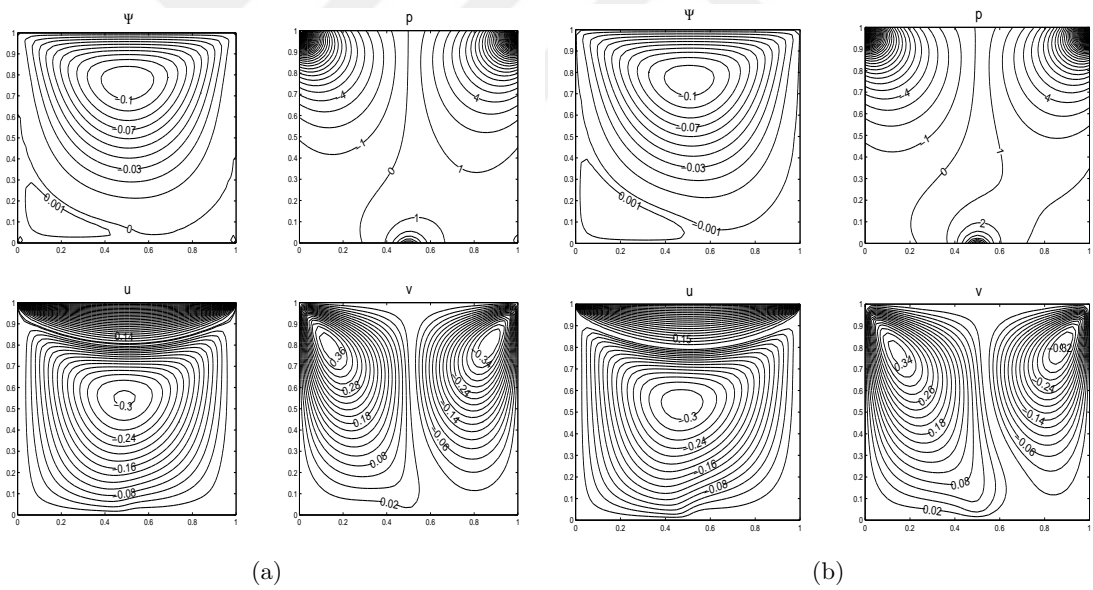


Figure 3.6: Stokes flow in a lid-driven square cavity, $M = 10$, (a) constant element approximation (b) linear element approximation.

The influence of the point magnetic source is visible when $M = 10$ (Figure 3.6) as disturbing the symmetry in the profiles, but the flow is still governed by the moving lid. Pressure around the source starts to increase and a weak secondary

flow occurs at the left bottom corner of the cavity.

When M increases to 150 (Figure 3.7), the vortex caused by the moving lid shifts to the right and the secondary flow strengthens. The right vortices in v -velocity and the pressure squeeze through the right top corner. A new vortex appears at the bottom of the cavity in u -velocity and a boundary layer is developed around the source point in v -velocity showing the pushing effect of the point magnetic source.

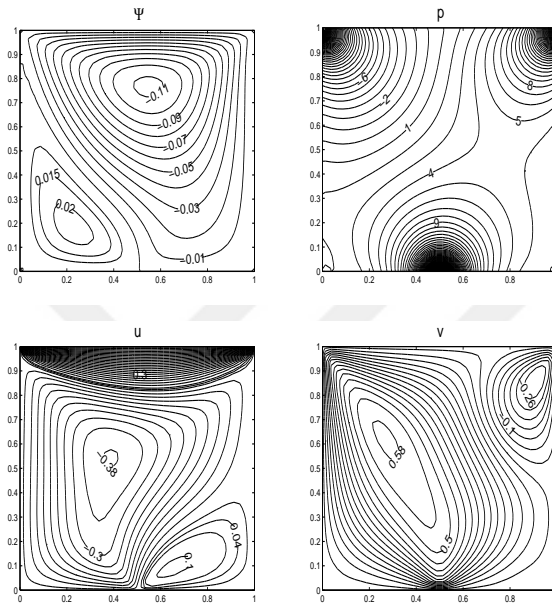


Figure 3.7: Stokes flow in a lid-driven square cavity, $M = 150$.

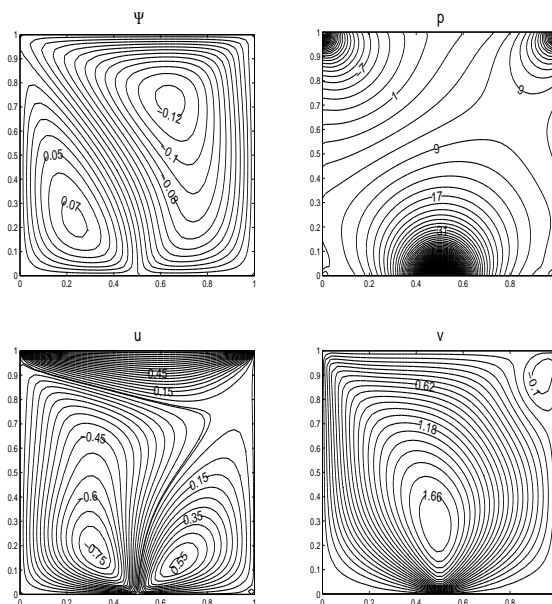


Figure 3.8: Stokes flow in a lid-driven square cavity, $M = 500$.

Figures 3.8 and 3.9 show that, as M increases further the main and the secondary flows in u -velocity and streamlines are separated almost symmetrically with respect to $x = 0.5$ line and pressure around the source spreads through the cavity. This means that the force caused by the point magnetic source starts to govern the flow behavior and the moving lid loses its effect as $M = 5000$.

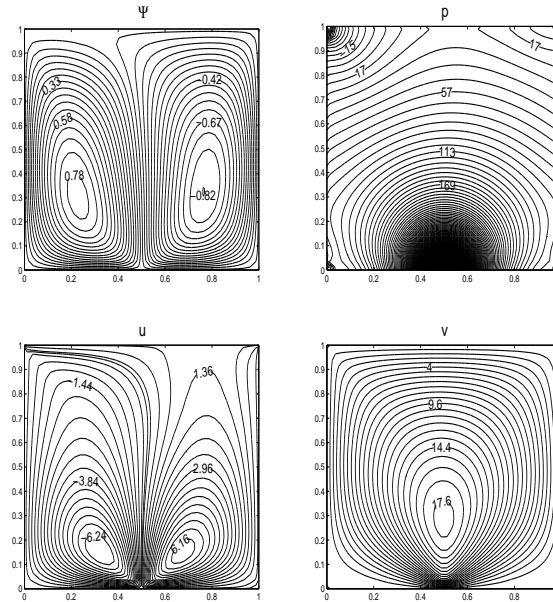


Figure 3.9: Stokes flow in a lid-driven square cavity, $M = 5000$.

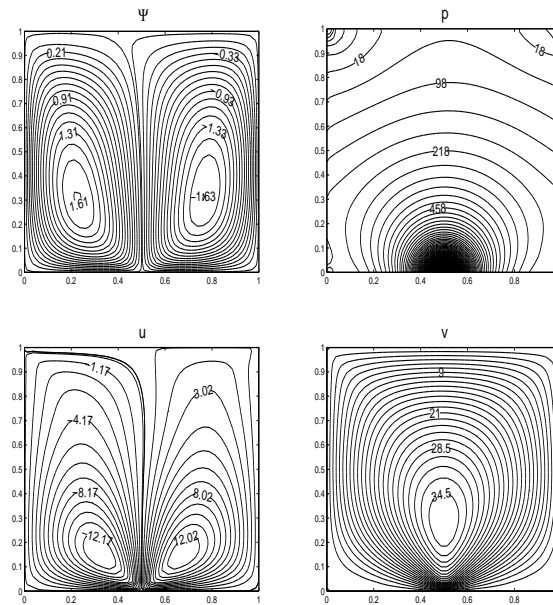


Figure 3.10: Stokes flow in a lid-driven square cavity, $M = 10000$.

As $M = 10000$ (Figure 3.10) the moving lid effect disappears completely in

u -velocity and streamlines. The flow and the pressure show symmetric behaviors due to the magnetic source and the fluid moves almost with the magnetization force.

3.1.2 Stokes flow in a square cavity with point magnetic source

The difference of this problem than the previous one is the absence of the moving lid. The boundary conditions and the problem geometry are given in Figure 3.11. The aim is to simulate the influence of only the magnetic field on the Stokes flow.

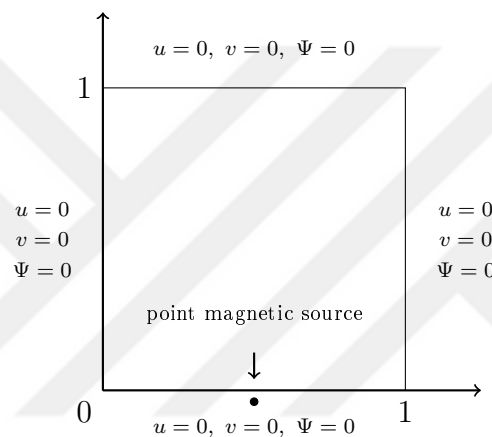


Figure 3.11: Stokes flow in a square cavity.

The pressure boundary conditions are derived by a similar technique described in Section 3.1.1. The discretized equations (3.1)-(3.4) for the Stokes flow are solved with homogeneous boundary conditions for the flow and the boundary is discretized by $N = 160$ constant elements. The point magnetic source position is $(0.5, -0.05)$. The tolerance for the iteration is 10^{-4} and $p^{(0)} = 1$ initially. $\kappa = 0.5$ is the relaxation parameter used for pressure convergence.

Figures 3.12-3.15 present the flow characteristics for different M values. When $M = 0$, since $(u, v) = (0, 0)$ on the boundary, from equation (3.21) and the strong maximum principle [83], the pressure Laplace equation has constant solution (near $p^{(0)}$) in the absence of magnetic effect. This means that, the u -velocity and the v -velocity equations reduce to Laplace equations with homogeneous

boundary conditions, hence the x - and y -components of the velocity are zero, so is the stream function. Thus, the point magnetic field is the driving mechanism of the Stokes flow in a square cavity with no-slip walls.

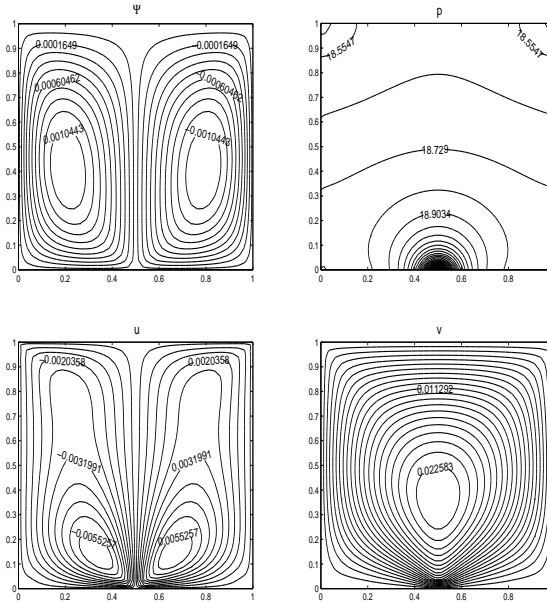


Figure 3.12: Stokes flow in a square cavity, $M = 5$.

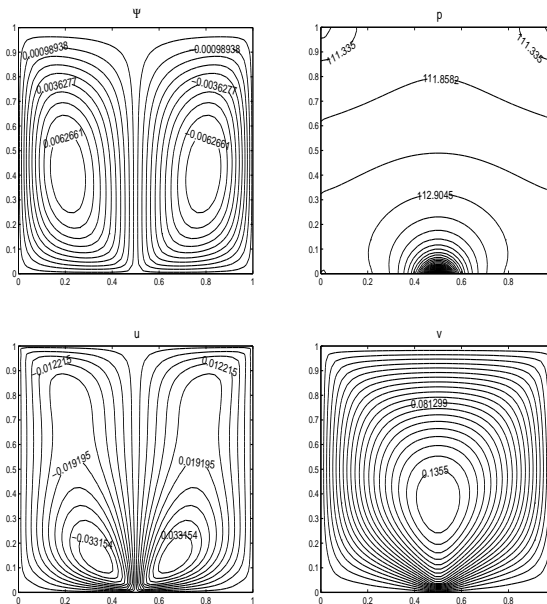


Figure 3.13: Stokes flow in a square cavity, $M = 30$.

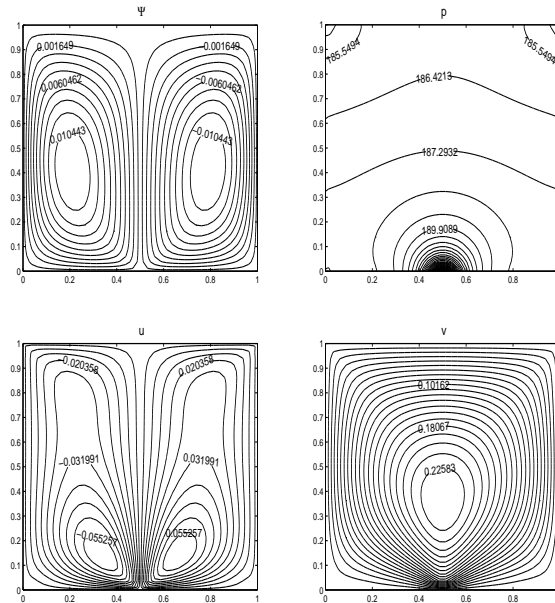


Figure 3.14: Stokes flow in a square cavity, $M = 50$.

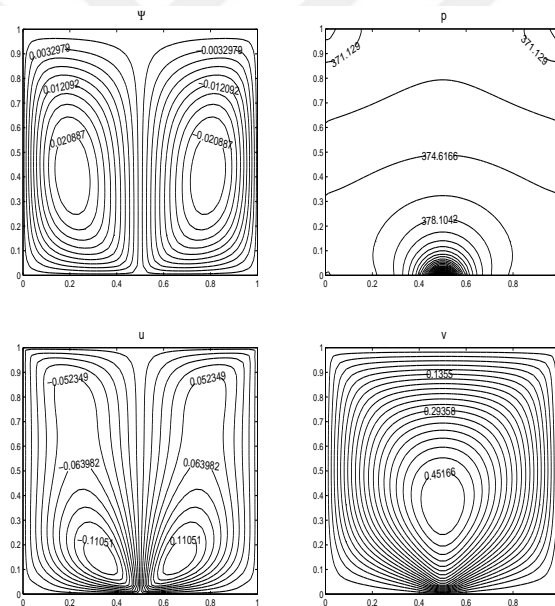


Figure 3.15: Stokes flow in a square cavity, $M = 100$.

From Figures 3.12-3.15 one can notice that, the point magnetic source divides the flow into two antisymmetric parts. High pressure occurs around the source since the magnetic source pushes the fluid upwards. Contour values of the velocities and the stream function increase at the same rate with M . As M increases, symmetry in the v -velocity and in pressure, and also the antisymmetry in u -velocity and the stream function are preserved.

3.1.3 Stokes flow in a lid-driven circular cavity with point magnetic source

In this problem, the magnetic effect on the Stokes flow in a lid-driven circular cavity is investigated. The upper lid of the cavity is moving to the right as in the case of lid driven square cavity. The problem geometry and the boundary conditions are presented in Figure 3.16.

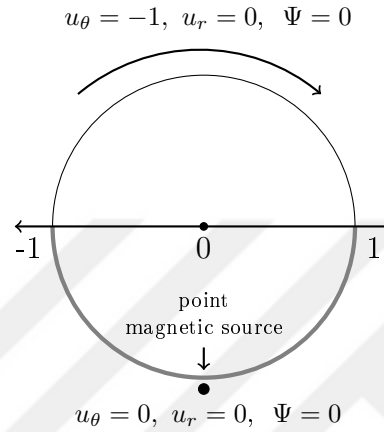


Figure 3.16: Stokes flow in a lid-driven circular cavity.

The pressure boundary conditions are generated with a similar procedure expressed in the case of lid-driven square cavity. This time a general formula which is valid for all parts of the boundary is obtained. (Figure 3.17)

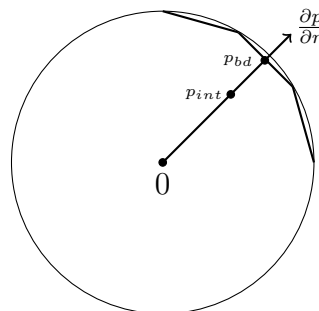


Figure 3.17: Stokes flow in a unit circular cavity: Derivation of wall pressure values.

Using the chain rule

$$\frac{\partial p}{\partial r} = \frac{\partial p}{\partial x} \frac{\partial x}{\partial r} + \frac{\partial p}{\partial y} \frac{\partial y}{\partial r} \quad (3.22)$$

and the transformation from the Cartesian coordinates to the polar coordinates

$x = r \cos(\theta)$, $y = r \sin(\theta)$ one has

$$\frac{\partial p}{\partial r} = \frac{\partial p}{\partial x} \cos(\theta) + \frac{\partial p}{\partial y} \sin(\theta) = \frac{\partial p}{\partial x} \frac{x}{r} + \frac{\partial p}{\partial y} \frac{y}{r} \quad (3.23)$$

on the boundary since $r = 1$

$$\frac{\partial p}{\partial r} = \frac{\partial p}{\partial x} x + \frac{\partial p}{\partial y} y . \quad (3.24)$$

Then, from the momentum equations (3.13) and (3.14) one gets

$$\frac{\partial p}{\partial r} = \left(\nabla^2 u + MH \frac{\partial H}{\partial x} \right) x + \left(\nabla^2 v + MH \frac{\partial H}{\partial y} \right) y . \quad (3.25)$$

Approximating the left-hand side by the forward difference and the right-hand side by the DRBEM coordinate matrix \mathbf{F} , pressure boundary condition for a circular region is obtained at $(k + 1)$ -st iteration.

$$p_{bd}^{(k+1)} = p_{int}^{(k)} + \Delta r \left((\mathbf{S}_{\nabla} u^{(k+1)} + MH \frac{\partial H}{\partial x}) x + (\mathbf{S}_{\nabla} v^{(k+1)} + MH \frac{\partial H}{\partial y}) y \right) \quad (3.26)$$

with the use of k -th iteration values and

$$\nabla^2 \approx \mathbf{S}_{\nabla} = \frac{\partial \mathbf{F}}{\partial x} \mathbf{F}^{-1} \frac{\partial \mathbf{F}}{\partial x} \mathbf{F}^{-1} + \frac{\partial \mathbf{F}}{\partial y} \mathbf{F}^{-1} \frac{\partial \mathbf{F}}{\partial y} \mathbf{F}^{-1} . \quad (3.27)$$

In the numerical solution procedure $N = 80$ constant boundary elements are used.

The magnetic field strength in non-dimensional form for the circular cavity is given by

$$H(x, y) = \frac{|c|}{\sqrt{(x - a_1)^2 + (y - a_2)^2}} \quad (3.28)$$

where $c = 0.05$ is the closest distance from the point source to the cavity and $(a_1, a_2) = (0, -1.05)$ is the place of the point magnetic source. $tol = 10^{-3}$ tolerance is used for the convergence criteria and the relaxation parameter for pressure is $\kappa = 0.1$. Figures 3.18 - 3.21 display the numerical results in terms of the fluid velocity, pressure and the stream function profiles.

When the flow is under the control of only the moving lid ($M = 0$, Figure 3.18), the flow and the pressure profiles are similar to the case of Stokes flow in a lid driven square cavity. The flow consist of one vortex with clockwise rotation, symmetric behaviors are observed in pressure and v -velocity profiles and u -velocity is divided into two vortices. Pressure around the discontinuity

points is high. The obtained numerical results are in good agreement with the ones in [22].

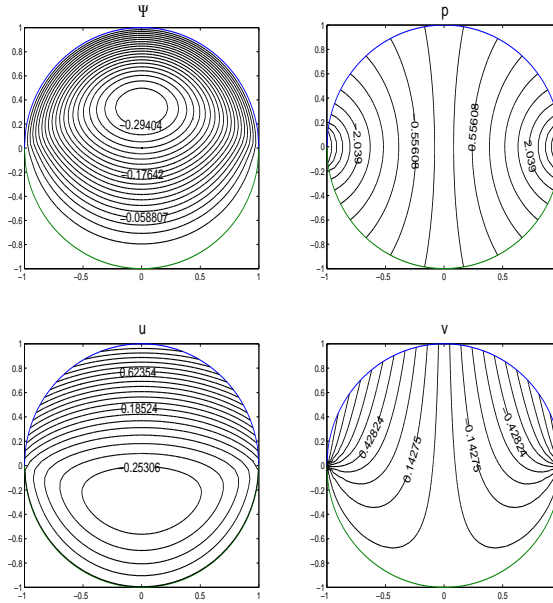


Figure 3.18: Stokes flow in a lid-driven circular cavity, $M = 0$.

The influence of the magnetization force is similar in square and circular cavities as $M = 10$ (Figure 3.19) in the sense that the symmetries in the flow and pressure profiles are disappeared, pressures around the sources increase and secondary flows develop at the left bottom parts of the cavities.

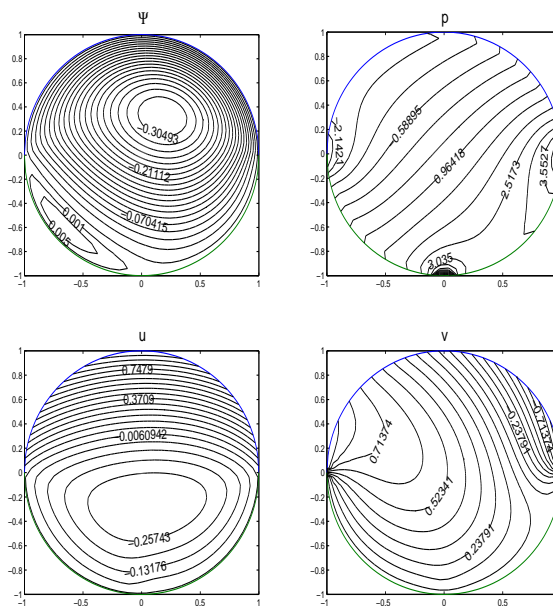


Figure 3.19: Stokes flow in a lid-driven circular cavity, $M = 10$.

When $M = 300$ (Figure 3.20), flow consists of two symmetric vortices with rotation in opposite directions. A new vortex appears at the right bottom part of the cavity and divides the vortex at the bottom into two parts in the u -velocity. The right vortex in the v -velocity vanishes and pressure contours become horizontal.

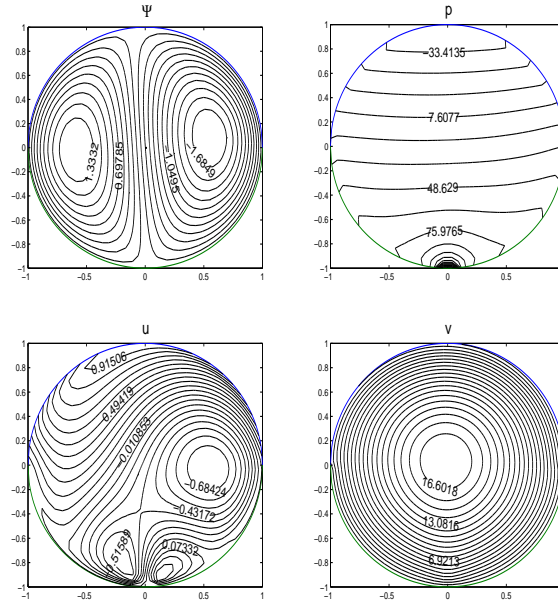


Figure 3.20: Stokes flow in a lid-driven circular cavity, $M = 300$.

Figure 3.21 shows the flow characteristics when $M = 1000$. In this case the flow is totally governed by the magnetic field. Flow accelerates and pressure in the cavity increases. The influence of the magnetization force is high in the circular cavity than in the case of square cavity since the moving lid loses its effect when $M = 1000$ in circular cavity and when $M = 5000$ in the square cavity. The difference may be caused from the disturbances coming from the corners of the square cavity since the profile of the point source magnetic field is in accordance with the circular shape of the cavity.

The flow behavior stays the same after $M = 5000$ in the circular cavity and $M = 10000$ in the square cavity for the Stokes flow.

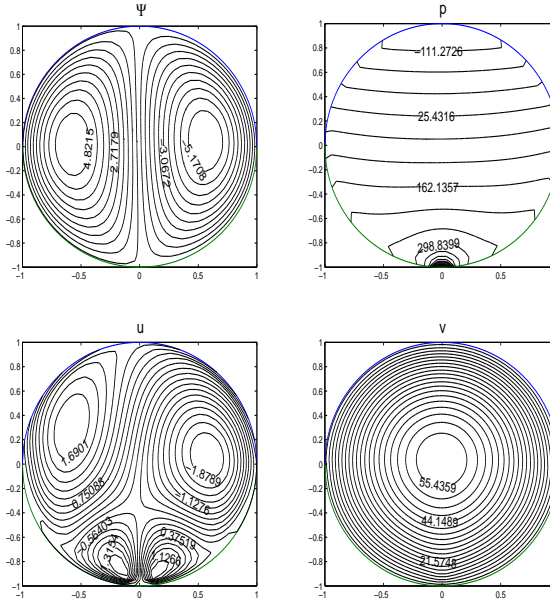


Figure 3.21: Stokes flow in a lid-driven circular cavity, $M = 1000$.

3.2 Incompressible Flow in Cavities with Point Magnetic Source

The flow of non-conducting, viscous fluid under the effect of magnetic field has many industrial applications such as in seals, power transformer cooling [84], detection of cracks in magnetic recording media, audio speakers, sensors, switches and solenoids. In this section, the influence of the point magnetic source on the incompressible flows in pipes with rectangular and circular cross-sections, and also in annular pipes is investigated. The nonlinear, coupled system of partial differential equations (2.93)-(2.97) are discretized using the DRBEM with constant elements. This time, because of the convection terms, the axial velocity profile is also effected by the applied magnetic field depending on the variations in the planar velocities (u, v) . The nonlinear terms in the equations are easily handled by the use of the DRBEM coordinate matrix \mathbf{F} . The flow behavior is investigated in terms of the velocity and pressure of the fluid. The system of DRBEM discretized matrix-vector equations, presented in Chapter 2 (equations (2.103)-(2.107)), are

$$(\mathbf{H} - \mathbf{D}(u\mathbf{S}_x + v\mathbf{S}_y))u - \mathbf{G} \frac{\partial u}{\partial n} = \mathbf{D}\{\mathbf{S}_x p - MnH \frac{\partial H}{\partial x}\} \quad (3.29)$$

$$(\mathbf{H} - \mathbf{D}(u\mathbf{S}_x + v\mathbf{S}_y))v - \mathbf{G} \frac{\partial v}{\partial n} = \mathbf{D}\{\mathbf{S}_y p - MnH \frac{\partial H}{\partial y}\} \quad (3.30)$$

$$(\mathbf{H} - \mathbf{D}(u\mathbf{S}_x + v\mathbf{S}_y))w - \mathbf{G}\frac{\partial w}{\partial n} = \mathbf{D}\{P_z\} \quad (3.31)$$

$$\begin{aligned} \mathbf{H}p - \mathbf{G}\frac{\partial p}{\partial n} &= \mathbf{D}\{Mn((\frac{\partial H}{\partial x})^2 + (\frac{\partial H}{\partial y})^2 + H\nabla^2 H) \\ &- (\mathbf{S}_x u)^2 - (\mathbf{S}_y v)^2 - 2(\mathbf{S}_x v)(\mathbf{S}_y u)\} \end{aligned} \quad (3.32)$$

$$\mathbf{H}\Psi - \mathbf{G}\frac{\partial \Psi}{\partial n} = \mathbf{D}\{\mathbf{S}_y u - \mathbf{S}_x v\} . \quad (3.33)$$

where $H(x, y)$ is the magnetic field strength of a point magnetic source placed at (a_1, a_2) (for square regions equation (3.6) and for circular regions equation (3.28)). The entries of the matrices \mathbf{D} , \mathbf{S}_x , \mathbf{S}_y are as in equation (3.5) and Mn is the magnetic number. The system of equations are solved iteratively using the following algorithm:

S.1 Define the place of the point source (a_1, a_2) , the magnetic number Mn , convergence criteria tolerance tol and a relaxation parameter κ for pressure.

S.2 Compute the spatial derivatives $\frac{\partial H}{\partial x}$, $\frac{\partial H}{\partial y}$, $\frac{\partial^2 H}{\partial x^2}$, $\frac{\partial^2 H}{\partial y^2}$ by using the definitions (3.6) or (3.28) of $H(x, y)$.

S.3 Take initial guesses for the pressure gradients $\frac{\partial p^{(0)}}{\partial x}$ and $\frac{\partial p^{(0)}}{\partial y}$ and initial values of velocity components as $u^{(0)}$, $v^{(0)}$.

S.4 Solve

$$(\mathbf{H} - \mathbf{D}(\mathbf{u}^{(k)}\mathbf{S}_x + \mathbf{v}^{(k)}\mathbf{S}_y))u^{(k+1)} - \mathbf{G}\frac{\partial u^{(k+1)}}{\partial n} = \mathbf{D}\{\frac{\partial p^{(k)}}{\partial x} - MnH\frac{\partial H}{\partial x}\} \quad (3.34)$$

for u using the boundary condition for the u -velocity. Here $\mathbf{u}^{(k)}$ and $\mathbf{v}^{(k)}$ are diagonal matrices with entries $u^{(k)}$ and $v^{(k)}$.

S.5 Solve

$$(\mathbf{H} - \mathbf{D}(\mathbf{u}^{(k+1)}\mathbf{S}_x + \mathbf{v}^{(k)}\mathbf{S}_y))v^{(k+1)} - \mathbf{G}\frac{\partial v^{(k+1)}}{\partial n} = \mathbf{D}\{\frac{\partial p^{(k)}}{\partial y} - MnH\frac{\partial H}{\partial y}\} \quad (3.35)$$

for v using the boundary condition for the v -velocity.

S.6 Generate boundary conditions for pressure by the use of x - and y - components of the momentum equations and newly obtained solutions for the

u - and the v -velocities. Approximate pressure gradients using forward difference and the DRBEM coordinate matrix \mathbf{F} for all the partial derivatives. The details are given in the corresponding sections.

S.7 Solve

$$\begin{aligned} \mathbf{H}p^{(k+1)} - \mathbf{G}\frac{\partial p^{(k+1)}}{\partial n} &= \mathbf{D}\{Mn\left(\left(\frac{\partial H}{\partial x}\right)^2 + \left(\frac{\partial H}{\partial y}\right)^2 + H\nabla^2 H\right) \\ &- (\mathbf{S}_x u^{(k+1)})^2 - (\mathbf{S}_y v^{(k+1)})^2 - 2(\mathbf{S}_x v^{(k+1)})(\mathbf{S}_y u^{(k+1)})\} \end{aligned} \quad (3.36)$$

using the obtained pressure boundary conditions in step **S.6**.

S.8 Solve the flow

$$\mathbf{H}\Psi^{(k+1)} - \mathbf{G}\frac{\partial \Psi^{(k+1)}}{\partial n} = \mathbf{D}\{\mathbf{S}_y u^{(k+1)} - \mathbf{S}_x v^{(k+1)}\} \quad (3.37)$$

using the natural boundary condition for the stream function.

S.9 Solve the axis-velocity w from

$$(\mathbf{H} - \mathbf{D}(\mathbf{u}^{(k+1)}\mathbf{S}_x + \mathbf{v}^{(k+1)}\mathbf{S}_y))w^{(k+1)} - \mathbf{G}\frac{\partial w^{(k+1)}}{\partial n} = \mathbf{D}\{P_z\} \quad (3.38)$$

with homogeneous boundary condition for w .

S.10 Relax pressure to accelerate convergence as

$$p^{(k+1)} = \kappa p^{(k+1)} + (1 - \kappa)p^{(k)}, \quad 0 < \kappa \leq 1 \quad (3.39)$$

S.11 Compute

$$\frac{\partial p^{(k+1)}}{\partial x} = \mathbf{S}_x p^{(k+1)}, \quad \frac{\partial p^{(k+1)}}{\partial y} = \mathbf{S}_y p^{(k+1)} \quad (3.40)$$

with $\mathbf{S}_x, \mathbf{S}_y$ given in (3.5).

S.12 Check the convergence criteria

$$\frac{\|z^{(k+1)} - z^{(k)}\|_\infty}{\|z^{(k)}\|_\infty} < tol \quad (3.41)$$

where $\|z\|_\infty = \max\{|z_1|, |z_2|, \dots, |z_{N+L}|\}$ denotes u, v, p, Ψ and w , and k is the iteration level.

S.13 If the criteria is satisfied for all of the problem unknowns stop, otherwise go to step **S.4** with the newly obtained solutions.

For all of the test problems presented in this section the axial pressure gradient $P_z = -8000$ as in [42]. Planar velocities are assumed to be zero initially (i.e. $u^{(0)} = v^{(0)} = 0$). In the stagnant situation of the fluid the magnetization forces are balanced by the pressure gradients [3], hence to be able to start the iteration

$$\frac{\partial p^{(0)}}{\partial x} = MnH\left(\frac{\partial H}{\partial x}\right) + 10^{-12}, \quad \frac{\partial p^{(0)}}{\partial y} = MnH\left(\frac{\partial H}{\partial y}\right) + 10^{-12} \quad (3.42)$$

are taken. The tolerance of the iteration is 10^{-3} .

The numerical results are presented in terms of the velocity (u, v, w) , pressure p of the fluid and the stream function Ψ to depict the flow with all problem variables. In this problem, the number of constant boundary elements are needed to be increased according to the magnetic field intensity in order to achieve the results for high magnetic numbers. The point magnetic source is placed at $(0.5, -0.05)$ for the square cavity and $(0, -1.05)$ for the circular cavity.

3.2.1 Incompressible flow in a square cavity with point magnetic source

The flow and pressure behaviors of an incompressible fluid under the influence of the unique point magnetic source is investigated in a square cross-section of a long pipe. The DRBEM discretized matrix-vector equations (3.29)-(3.33) are solved with the boundary conditions presented in Figure 3.22 where the walls are motionless.

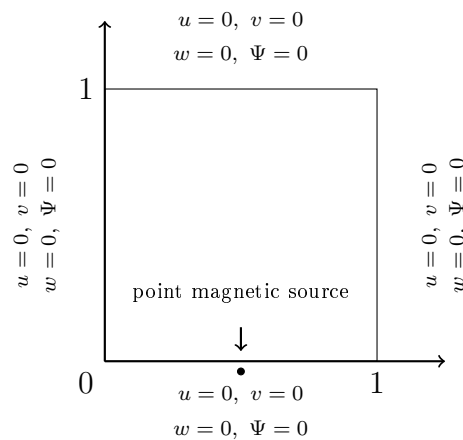


Figure 3.22: Flow in a square cavity.

Pressure boundary conditions are generated using a similar procedure as explained in Section 3.1.1. Then, the approximate values of pressure on the boundaries are

$$\begin{aligned}
\text{SIDE 1: } \quad p_{bd}^{(k+1)} &= p_{int}^{(k)} - \Delta y \mathbf{S}_I v^{(k+1)} - \Delta y Mn H \frac{\partial H}{\partial y} \\
\text{SIDE 2: } \quad p_{bd}^{(k+1)} &= p_{int}^{(k)} + \Delta x \mathbf{S}_I u^{(k+1)} + \Delta x Mn H \frac{\partial H}{\partial x} \\
\text{SIDE 3: } \quad p_{bd}^{(k+1)} &= p_{int}^{(k)} + \Delta y \mathbf{S}_I v^{(k+1)} + \Delta y Mn H \frac{\partial H}{\partial y} \\
\text{SIDE 4: } \quad p_{bd}^{(k+1)} &= p_{int}^{(k)} - \Delta x \mathbf{S}_I u^{(k+1)} - \Delta x Mn H \frac{\partial H}{\partial x}
\end{aligned} \tag{3.43}$$

where $\mathbf{S}_I = \frac{\partial \mathbf{F}}{\partial x} \mathbf{F}^{-1} \frac{\partial \mathbf{F}}{\partial x} \mathbf{F}^{-1} + \frac{\partial \mathbf{F}}{\partial y} \mathbf{F}^{-1} \frac{\partial \mathbf{F}}{\partial y} \mathbf{F}^{-1} - \mathbf{u}^{(k+1)} \frac{\partial \mathbf{F}}{\partial x} \mathbf{F}^{-1} - \mathbf{v}^{(k+1)} \frac{\partial \mathbf{F}}{\partial y} \mathbf{F}^{-1}$ and $\mathbf{u}^{(k+1)}$, $\mathbf{v}^{(k+1)}$ are the diagonal matrices having velocity nodal values as the diagonal elements.

The numerical results are obtained with $N = 120$ constant boundary elements except the case $Mn = 30000$ where $N = 160$. Convergence for the pressure equation is achieved by taking the relaxation parameter $\kappa = 0.05$ when $Mn > 0$ and $\kappa = 0.005$ for $Mn = 0$.

Figures 3.23-3.28 display the influence of the magnetic field, generated by a point magnetic source, for increasing magnetic field intensities on the incompressible flow behavior in the square cavity. The obtained streamline and axial velocity behaviors are in agreement with the ones in [42].

When the fluid is free of magnetization force ($Mn = 0$, Figure 3.23) all problem variables except the axial velocity are nearly zero. That is, the movement in the axial direction uses all the kinetic energy of the fluid. The flow in the axial direction shows a parabolic profile.

Figure 3.24 displays the flow behavior for $Mn = 500$. The magnetization force divides the flow on the transverse plane into two symmetric vortices rotating in opposite directions. The pushing effect of the magnetization force is observed in the velocity components. The v -velocity is expanded through the channel section starting from the magnetic source and the maximum velocity occurs at the axis of symmetry $x = 0.5$ close to the magnetic source. u -velocity has two antisymmetric loops reaching maximum values close to the axis of symmetry $x = 0.5$. The pressure is highly concentrated near the magnetic source. Since the kinetic energy on the axial direction is converted to the kinetic energy on

the transverse plane, the flow in the axial direction starts to retard around the magnetic source.

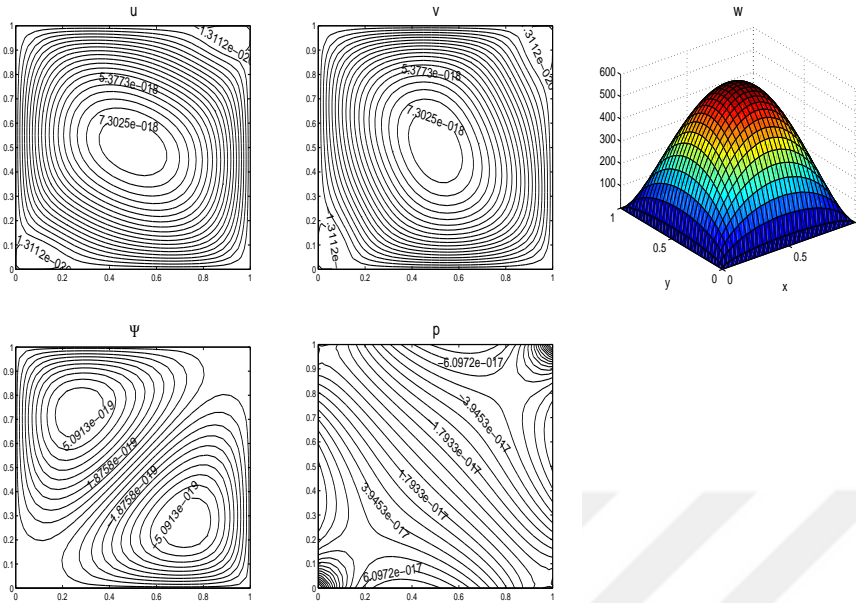


Figure 3.23: Flow in a square cavity, $Mn = 0$.

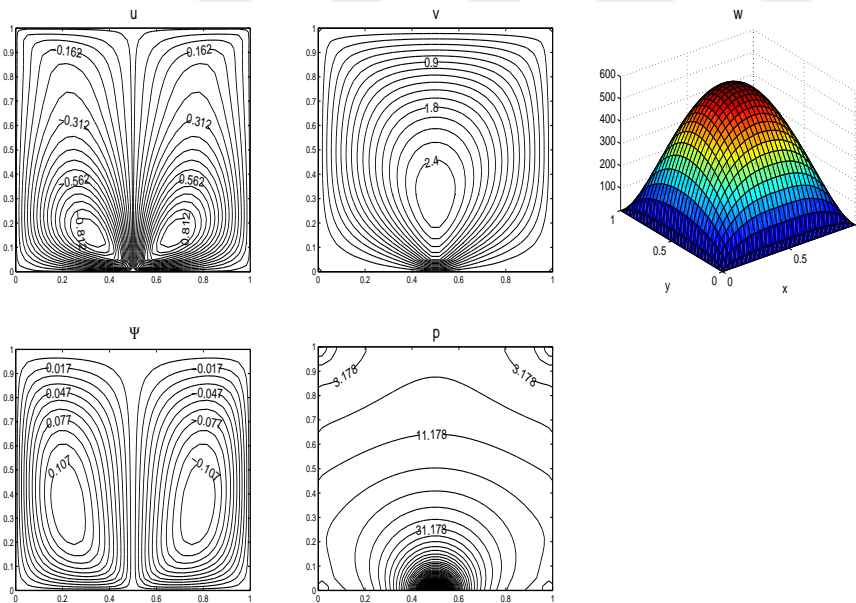


Figure 3.24: Flow in a square cavity, $Mn = 500$.

An increase in the magnetic number Mn causes the increase in the magnitudes of streamlines, flow velocities and pressure as can be seen from Figure 3.25 which is for $Mn = 3000$. The centers of vortices in secondary flows move upwards and the highest velocity in the z - direction appears close to the top-lid. Pressure

starts to concentrate also at the top of the cavity and two new vortices appear in the u -velocity.

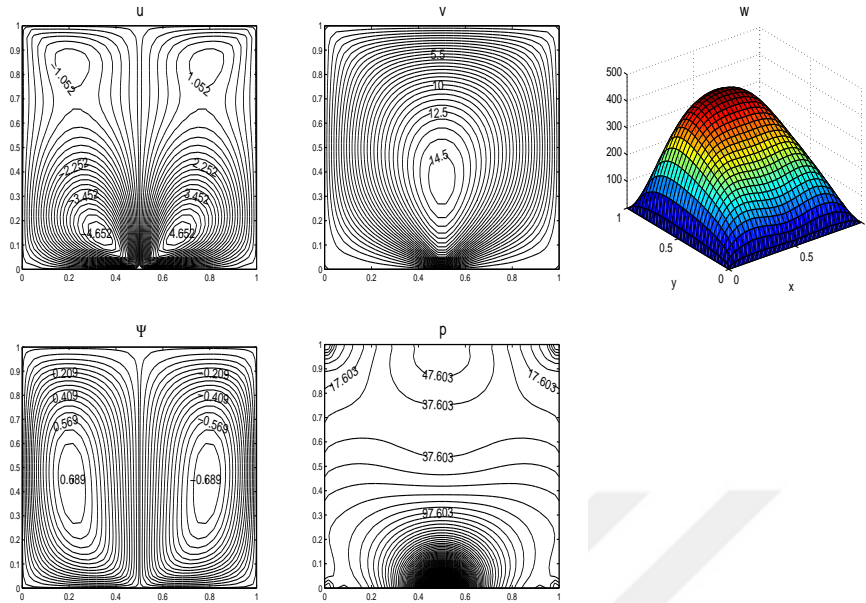


Figure 3.25: Flow in a square cavity, $Mn = 3000$.

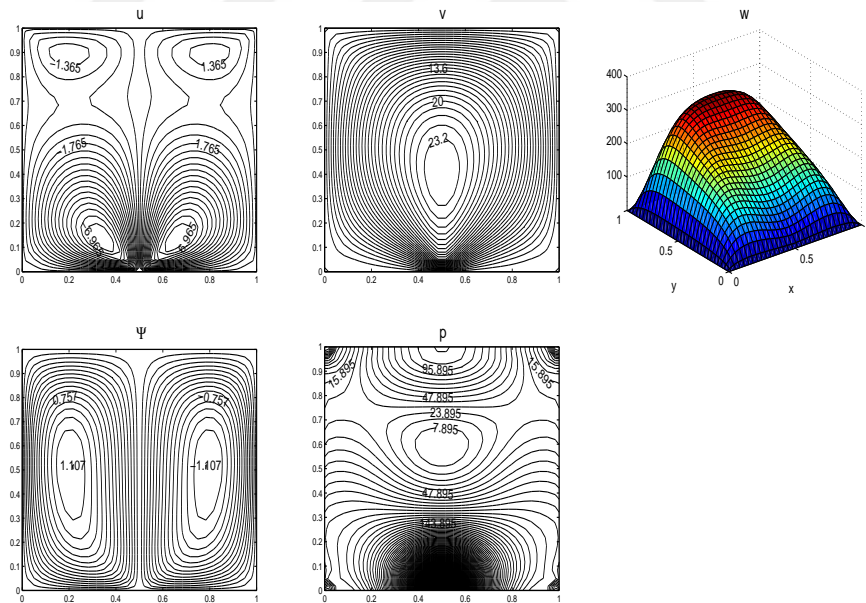


Figure 3.26: Flow in a square cavity, $Mn = 5000$.

Figures 3.26-3.28 show that as the magnetic number increases further, new loops at the top of the cavity in the u -velocity are strengthened and the vortex centers in streamlines enlarge. The flow deceleration in the axial direction is more prominent and negative pressure occurs at the center of the cavity. The maximum

v -velocity region moves through the center of the cavity.

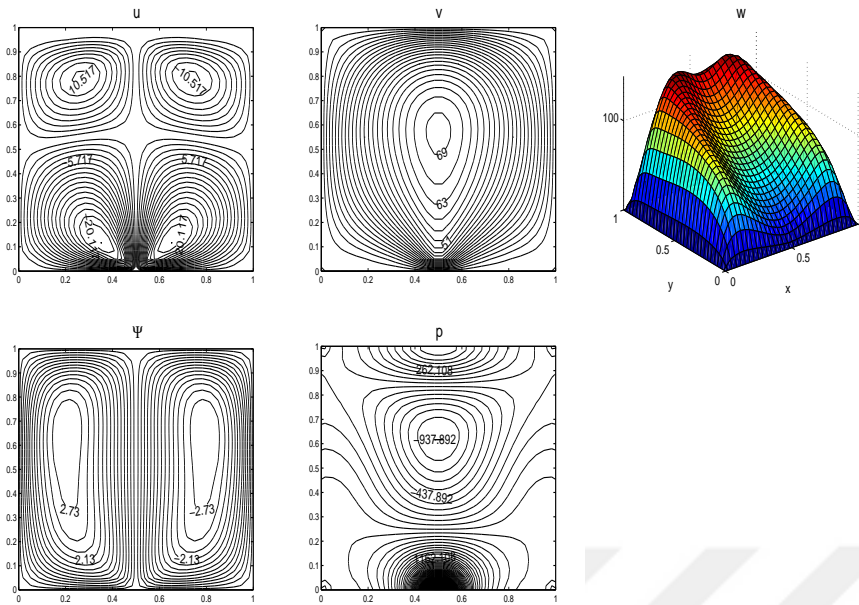


Figure 3.27: Flow in a square cavity, $Mn = 17000$.

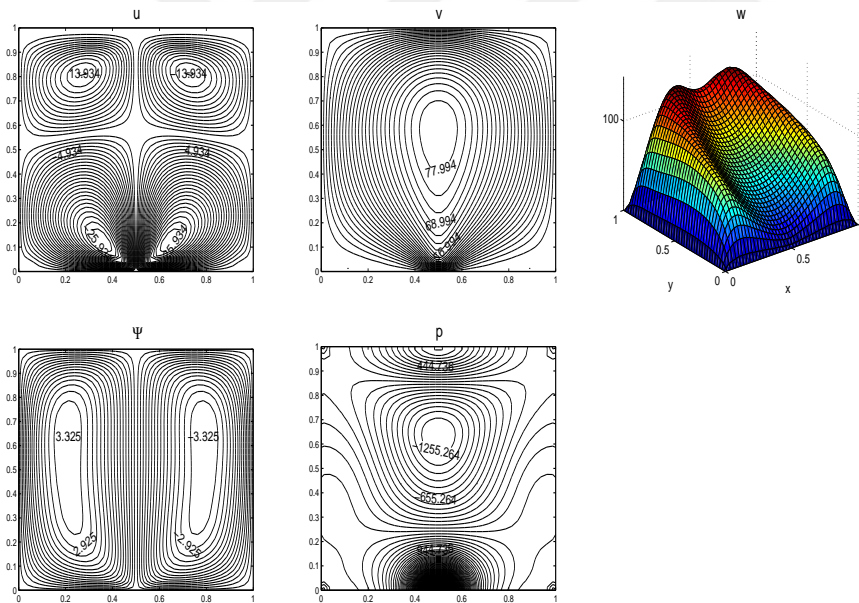


Figure 3.28: Flow in a square cavity, $Mn = 30000$.

When the numerical results for the Stokes flow (Section 3.1.2) and the incompressible flow (Section 3.2.1) in a square cavity under the influence of a point source magnetic field are compared, the influence of the convection terms in the momentum equations are observed. In the case of Stokes flow the axial velocity profile stays the same due to the absence of the convection terms, however in the

case of incompressible flow the axial velocity profile shows a retardation around the point source depending on the variations in the u - and v -velocities.

The Reynolds number of the flow depending on the mean velocity in the axial direction is given by [42]:

$$Re = \bar{w}_m h / \nu = \int_0^1 \int_0^1 w dx dy \quad (3.44)$$

where

$$w_m = \frac{\bar{w}_m h}{\nu} = \int_0^1 \int_0^1 w dx dy \quad (3.45)$$

is the dimensionless mean velocity.

The Reynolds number variation with increasing Mn is displayed in Table 3.2. Depending on the axial velocity, as magnetic field intensity increases Reynolds number decreases. This shows the well-known flattening tendency of the flow under the influence of a magnetic field which is observed from Figures 3.23-3.28.

Table 3.2: Variation of the Reynolds number with magnetic field intensity.

Mn	0	30	500	1000	3000
<i>Re</i>	280.8054	280.6611	277.7210	265.8172	197.2229
Mn	5000	10000	17000	20000	30000
<i>Re</i>	152.8589	103.4248	76.2046	69.2253	68.1212

3.2.2 Incompressible flow in a lid-driven square cavity with point magnetic source

In this section, the DRBEM equations (3.29)-(3.33) are solved when the top-lid of the cavity moves to the right with a constant velocity. Numerical solution procedure is carried with $N = 120$ constant elements and the relaxation parameter for the pressure $\kappa = 0.1$. The behavior of the flow is investigated according to the increasing magnetic number Mn values. The problem geometry and the boundary conditions are given in Figure 3.29.

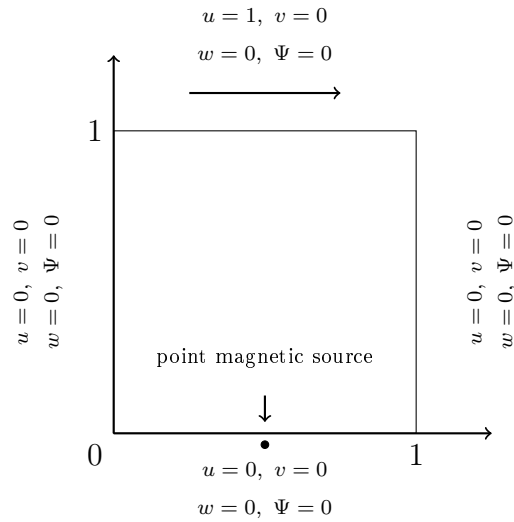


Figure 3.29: Flow in a lid-driven square cavity.

The pressure boundary conditions are approximated using the similar scheme presented in Section 3.2.1.

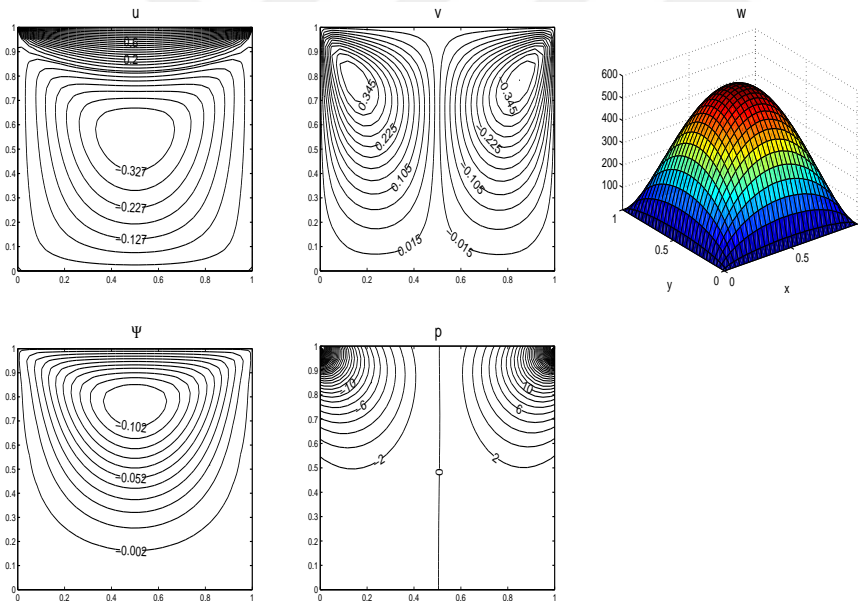


Figure 3.30: Flow in a lid-driven square cavity, $Mn = 0$.

From Figures 3.30-3.32 one can observe that, when $Mn \leq 500$ the flow behaviors are similar to the case of Stokes flow with $M \leq 500$ (Section 3.1.1). As Mn reaches to 500 the moving lid loses its influence on the flow and the retardation around the point magnetic source in the axial velocity is observed. The flow behavior of the Stokes flow for $M = 150$ and incompressible flow for $Mn =$

100 with a moving lid are alike comparing Figure 3.7 and Figure 3.31. In the incompressible flow the Reynolds number corresponding to $Mn = 100$ is $Re = 280.6626$. That is $M = Mn/Re \approx 0.3562$. Hence, M has to be higher in the Stokes flow than that of in the incompressible flow in order to obtain similar behaviors. This may be due to the very high viscosity in the Stokes flow case.

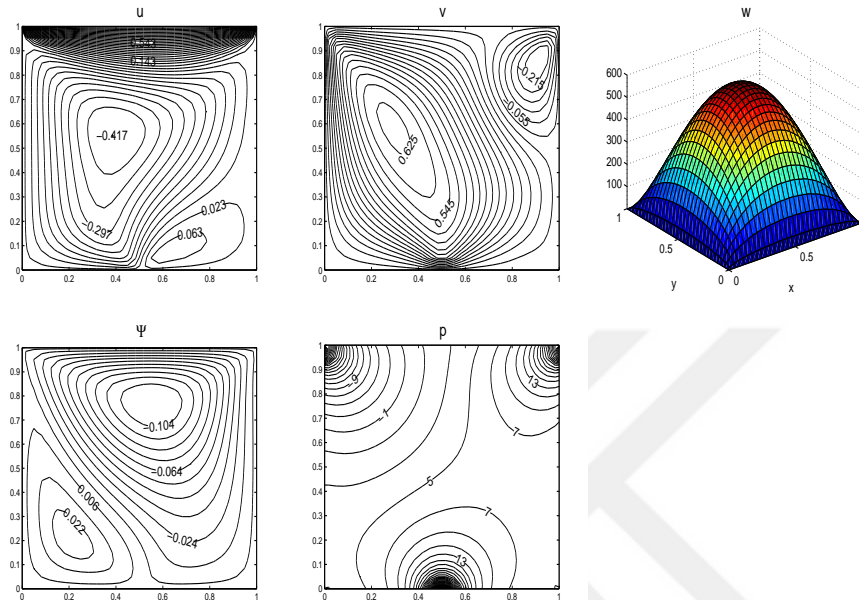


Figure 3.31: Flow in a lid-driven square cavity, $Mn = 100$.

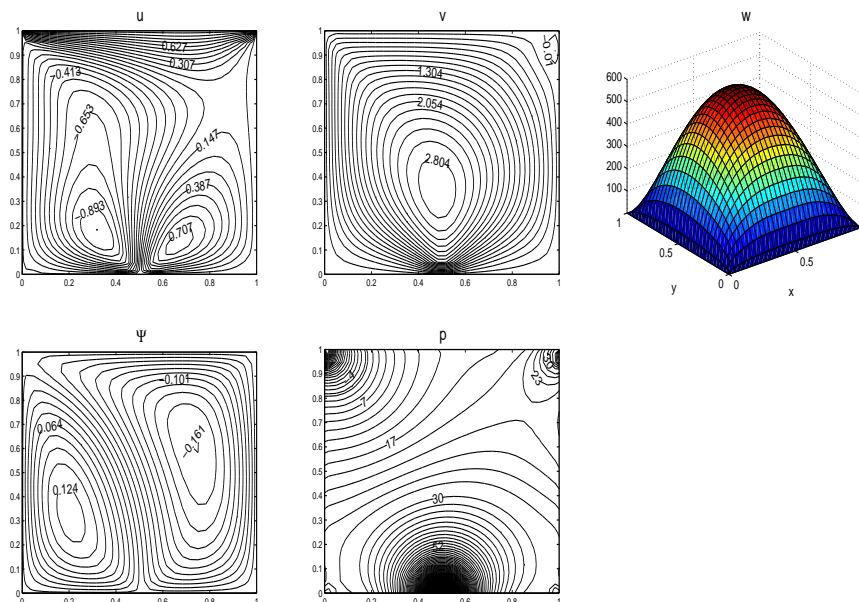


Figure 3.32: Flow in a lid-driven square cavity, $Mn = 500$.

Figure 3.33 shows that, when $Mn = 1000$ the influence of the moving top lid

weakens and the pressure concentration at the top right corner vanishes.

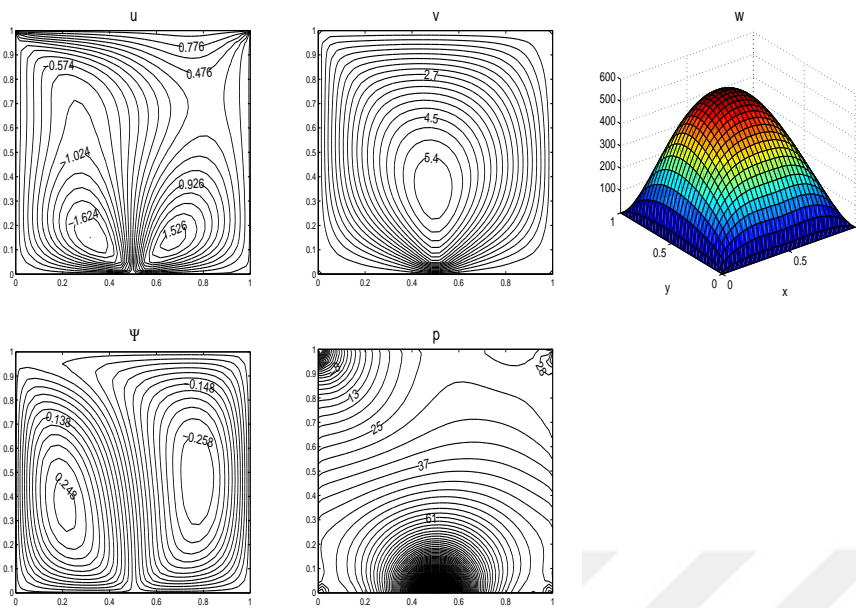


Figure 3.33: Flow in a lid-driven square cavity, $Mn = 1000$.

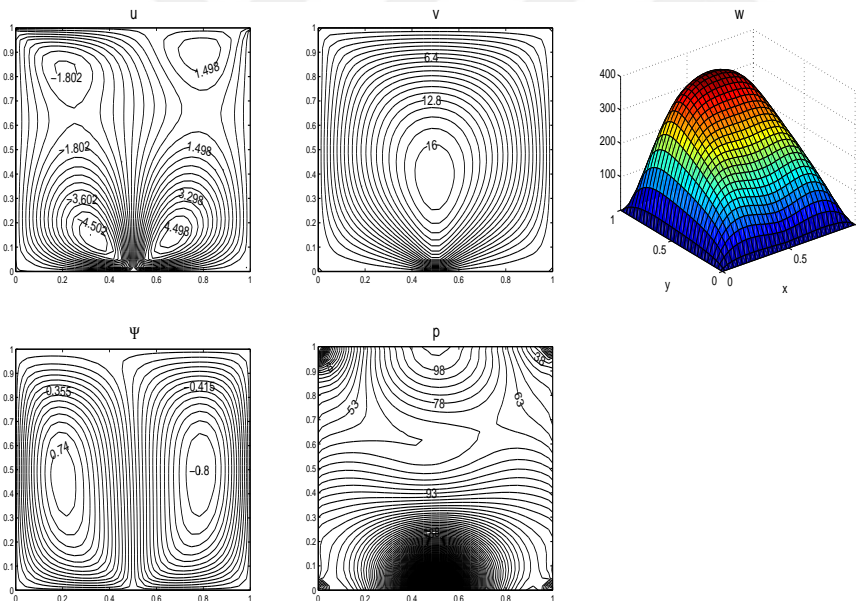


Figure 3.34: Flow in a lid-driven square cavity, $Mn = 3000$.

As the magnetic field intensity increases further (Figures 3.34 and 3.35) the flow behavior starts to resemble to the incompressible flow in a square cavity. Similar flow behaviors are observed in square and lid driven cavities for $Mn \geq 3000$. Two additional vortices are developed near the top lid in the u -velocity. However this is not the case for the Stokes flow since the flow is slow although the top

lid of the cavity is moving.

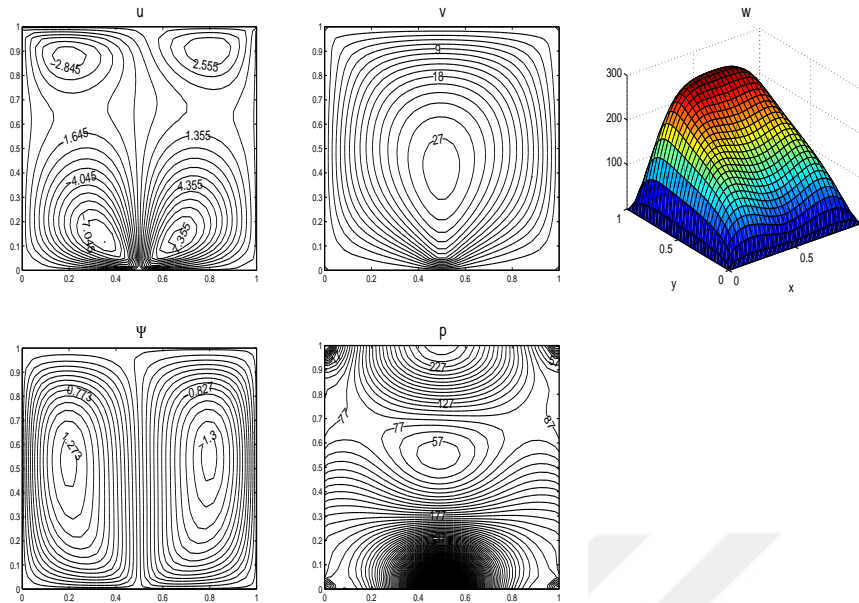


Figure 3.35: Flow in a lid-driven square cavity, $Mn = 5000$.

3.2.3 Incompressible flow in a circular cavity with point magnetic source

In this problem, the system of equations (3.29)-(3.33) are solved for the circular cavity (Figure 3.36). The magnetic field strength $H(x, y)$ for the circular cavity is defined by the equation (3.28). The aim is to investigate the influence of only the point magnetic source on the incompressible flow behavior in a circular cavity and compare it with the square cavity case.

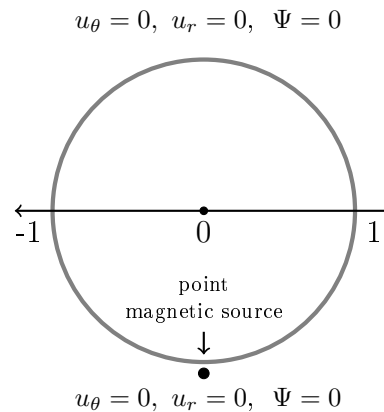


Figure 3.36: Flow in a circular cavity.

Pressure boundary conditions are found similarly as in the case of Stokes flow in a lid-driven circular cavity (Section 3.1.3) by taking into consideration of the convection terms also. That is,

$$p_{bd}^{(k+1)} = p_{int}^{(k)} + \Delta r \left((\mathbf{S}_I \mathbf{u}^{(k+1)} + MnH \frac{\partial H}{\partial x})x + (\mathbf{S}_I \mathbf{v}^{(k+1)} + MnH \frac{\partial H}{\partial y})y \right) \quad (3.46)$$

where $\mathbf{S}_I = \frac{\partial \mathbf{F}}{\partial x} \mathbf{F}^{-1} \frac{\partial \mathbf{F}}{\partial x} \mathbf{F}^{-1} + \frac{\partial \mathbf{F}}{\partial y} \mathbf{F}^{-1} \frac{\partial \mathbf{F}}{\partial y} \mathbf{F}^{-1} - \mathbf{u}^{(k+1)} \frac{\partial \mathbf{F}}{\partial x} \mathbf{F}^{-1} - \mathbf{v}^{(k+1)} \frac{\partial \mathbf{F}}{\partial y} \mathbf{F}^{-1}$ with $\mathbf{u}^{(k+1)}$ and $\mathbf{v}^{(k+1)}$ being diagonal matrices with nodal velocity values on the diagonals.

Figures 3.37-3.40 display the numerical results achieved for $Mn = 0, 100, 500$ and 1000 by discretizing the boundary with $N = 60, 80, 80$ and 140 elements, respectively, and the pressure relaxation parameter is $\kappa = 0.05$. When there is no magnetic field ($Mn = 0$) pressure and velocity values on the cross-section of the pipe are nearly zero. The kinetic energy of the fluid is used to continue the movement in the axial direction. The axial velocity presents a parabolic profile due to the no-slip boundary conditions as expected. When the magnetic effect is introduced ($Mn = 100$) flow starts to develop on the transverse plane. Two symmetric vortices appear rotating in different directions. The u -velocity profile is divided into 4 vortices and the ones close to the top lid are stronger in magnitude than the others. The v -velocity spreads to all parts of the cavity. Pressure contours are horizontal and they are highly concentrated at the bottom of the cavity close to the point source. Since the kinetic energy used for the movement in the axial direction is converted to the kinetic energy on the transverse plane, a retarded flow is observed in the axial direction as in the square cavity case. When the magnetic field intensity increases ($Mn = 500, 1000$) the centers of vortices in streamlines and v -velocity move upwards. The bottom vortices in u -velocity strengthen and squeeze the upper ones through the top of the cavity. The pushing effect of the magnetic source is clearly seen from the denser contours of the v -velocity close to the point source. As magnetic number increases pressure decreases at the center of the cavity and this behavior results in a collapse in the axial velocity on the $x = 0$ line. As in the case of Stokes flow, the influence of the magnetic field on the flow is higher in the circular cavity than the one in the square cavity. For the same magnetic number, the flow on the transverse plane is faster in the circular cavity than in the square cavity, as

a result, the flow retardation around the source is observed for smaller values of Mn in the circular cavities.

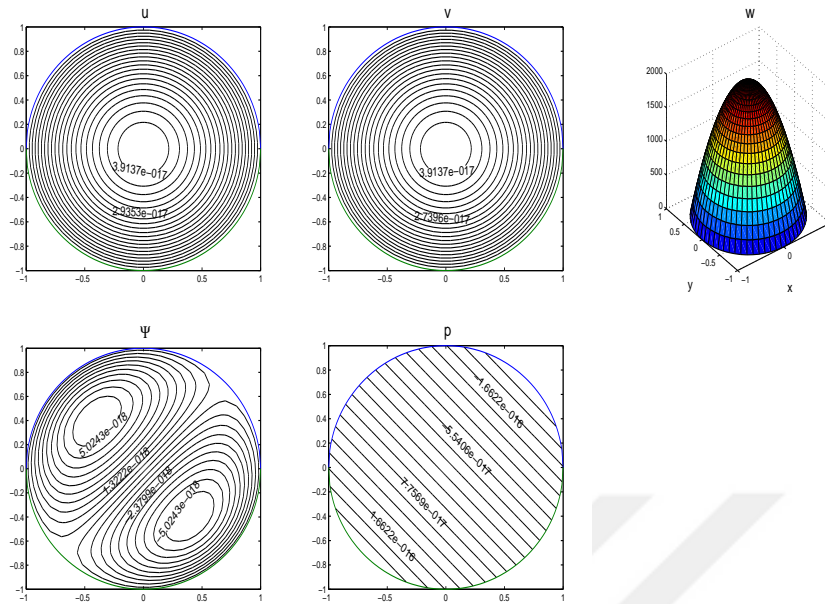


Figure 3.37: Flow in a circular cavity, $Mn = 0$.

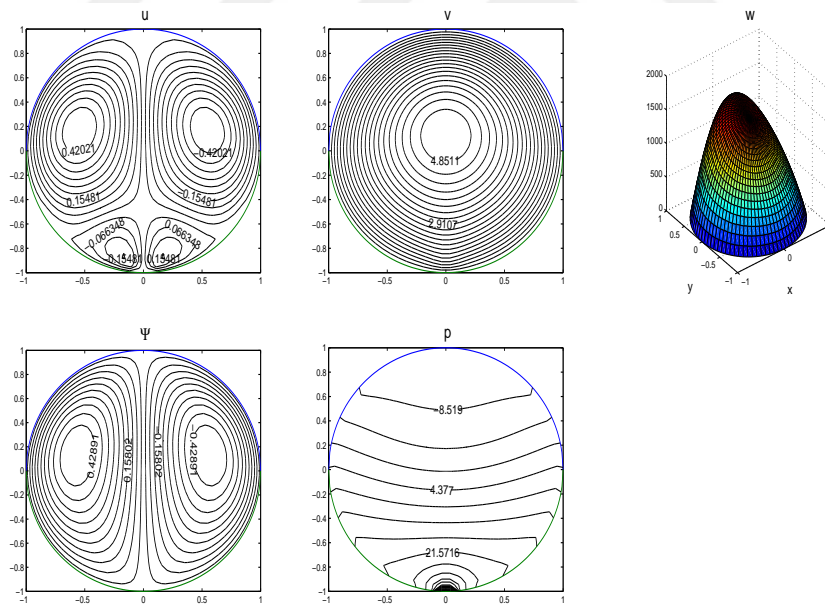


Figure 3.38: Flow in a circular cavity, $Mn = 100$.

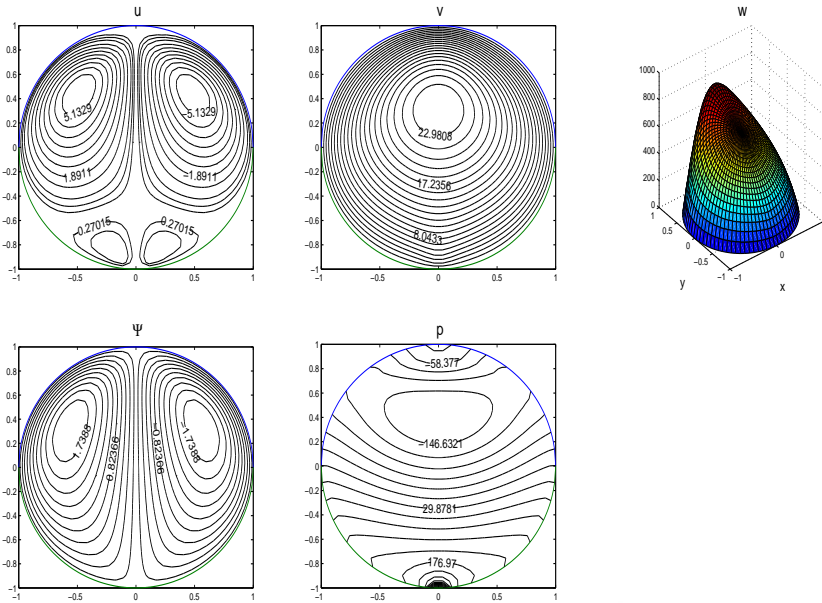


Figure 3.39: Flow in a circular cavity, $Mn = 500$.

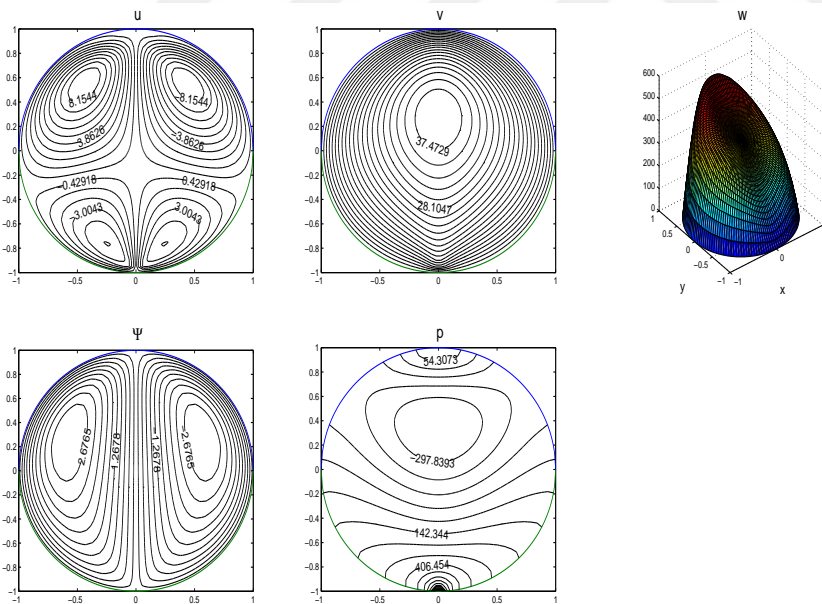


Figure 3.40: Flow in a circular cavity, $Mn = 1000$.

3.2.4 Incompressible flow in a square cavity with an obstacle (annular pipes) under point magnetic source

In this problem, the fully developed flow of an electrically non-conducting fluid is studied in a pipe containing a solid obstacle. The obstacle can be considered again a pipe inside the outer pipe. The fluid is in the annular region between the solid and the pipe. The flow is subjected to an applied magnetic field generated by a thin wire, carrying electric current, below the outer pipe. On the cross-section of the pipes the magnetic wire serves as a point magnetic source with magnetic field strength $H(x, y)$ (equation (3.6)) and the inner pipe acts as an obstacle. The point magnetic source is placed at $(0.5, -0.05)$. 10^{-3} tolerance is taken for the convergence criteria. The problem geometry for the cross-section of the pipes is presented in Figure 3.41.

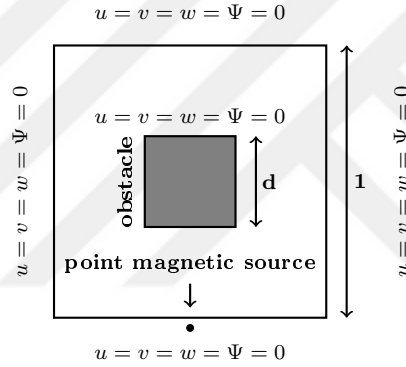


Figure 3.41: Flow in a cavity with an obstacle.

The pressure boundary conditions are generated through the momentum equations, now having 8 boundaries (Figure 3.42).

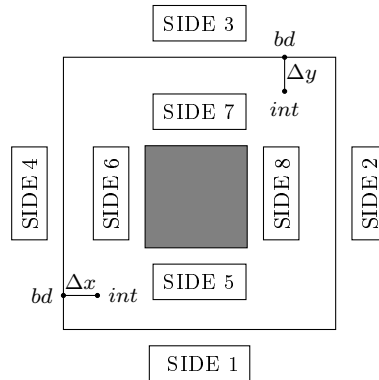


Figure 3.42: Flow in a cavity with an obstacle: Derivation of pressure wall conditions.

Then, for each side, the pressure boundary conditions are approximated using the following formulas

$$\begin{aligned}
\text{Side 1: } p_{bd}^{(k+1)} &= p_{int}^{(k)} - \Delta y(\mathbf{S_I}v^{(k+1)} + MnH \frac{\partial H}{\partial y}) \\
\text{Side 2: } p_{bd}^{(k+1)} &= p_{int}^{(k)} + \Delta x(\mathbf{S_I}u^{(k+1)} + MnH \frac{\partial H}{\partial x}) \\
\text{Side 3: } p_{bd}^{(k+1)} &= p_{int}^{(k)} + \Delta y(\mathbf{S_I}v^{(k+1)} + MnH \frac{\partial H}{\partial y}) \\
\text{Side 4: } p_{bd}^{(k+1)} &= p_{int}^{(k)} - \Delta x(\mathbf{S_I}u^{(k+1)} + MnH \frac{\partial H}{\partial x}) \\
\text{Side 5: } p_{bd}^{(k+1)} &= p_{int}^{(k)} + \Delta y(\mathbf{S_I}v^{(k+1)} + MnH \frac{\partial H}{\partial y}) \\
\text{Side 6: } p_{bd}^{(k+1)} &= p_{int}^{(k)} + \Delta x(\mathbf{S_I}u^{(k+1)} + MnH \frac{\partial H}{\partial x}) \\
\text{Side 7: } p_{bd}^{(k+1)} &= p_{int}^{(k)} - \Delta y(\mathbf{S_I}v^{(k+1)} + MnH \frac{\partial H}{\partial y}) \\
\text{Side 8: } p_{bd}^{(k+1)} &= p_{int}^{(k)} - \Delta x(\mathbf{S_I}u^{(k+1)} + MnH \frac{\partial H}{\partial x}).
\end{aligned} \tag{3.47}$$

where $\mathbf{S_I} = \frac{\partial \mathbf{F}}{\partial x} \mathbf{F}^{-1} \frac{\partial \mathbf{F}}{\partial x} \mathbf{F}^{-1} + \frac{\partial \mathbf{F}}{\partial y} \mathbf{F}^{-1} \frac{\partial \mathbf{F}}{\partial y} \mathbf{F}^{-1} - \mathbf{u}^{(k+1)} \frac{\partial \mathbf{F}}{\partial x} \mathbf{F}^{-1} - \mathbf{v}^{(k+1)} \frac{\partial \mathbf{F}}{\partial y} \mathbf{F}^{-1}$ with $\mathbf{u}^{(k+1)}$ and $\mathbf{v}^{(k+1)}$ being diagonal matrices made of $u^{(k+1)}$ and $v^{(k+1)}$ values, respectively.

The convergence of the pressure equation is provided when $\kappa = 0.05$. The influence of the magnetic field on the flow between pipes is first studied by taking a medium sized obstacle at the center of the cavity where $d = 1/3$. The flow profiles are presented for $Mn = 0, 30, 500, 14000$ values in Figures 3.43-3.46, where the boundary of the flow region is discretized by taking $N = 160, 160, 160, 320$ constant boundary elements, respectively. The numerical results show that when there is no magnetic source ($Mn = 0$), the flow is in action only in the axial direction. Due to the obstacle, the axial flow collapses at the center of the cavity and a parabola like profile is observed between the corners of the cavity and the obstacle.

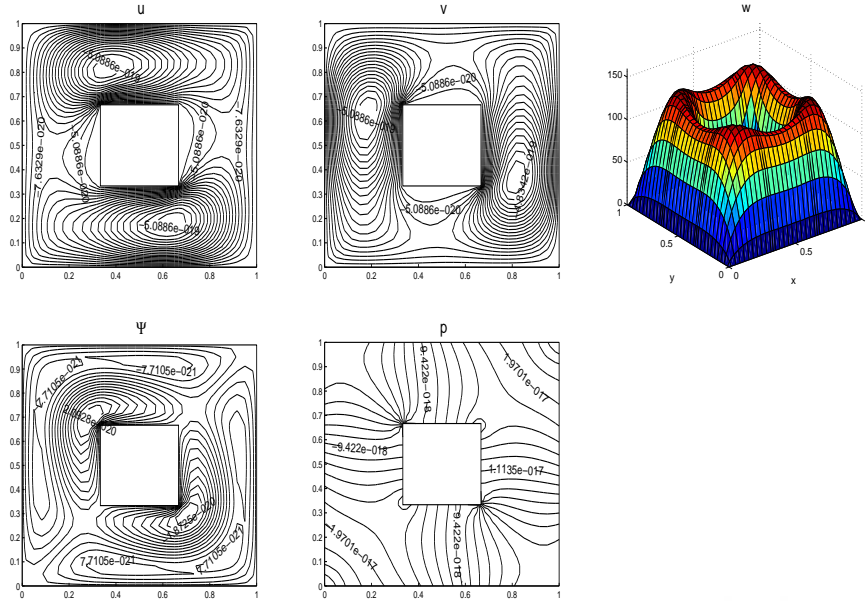


Figure 3.43: Flow in a square cavity with a medium obstacle at the center, $d = 1/3$, $Mn = 0$.

When the magnetic field is included (Figure 3.44) a flow is created on the transverse plane consisting of two symmetrical domains. Two eddies are attached to the vertical walls of the obstacle squeezing the main flow through the walls of the cavity and enlarging with an increase in the magnetic field intensity. Boundary layers are observed at the bottom of the cavity and the vertical walls of the obstacle. The u -velocity is decomposed into 4 vortices mainly emanating from the corners of the obstacle. The vortices attached to the top corners are weaker in magnitude than the ones attached to the bottom corners since the magnetic source is close to the bottom wall. The v -velocity is divided into 5 vortices with two small eddies appearing at the bottom corners and enlarging with increasing values of magnetic number Mn . Pressure is concentrated with large magnitude around the magnetic source. The flow and pressure profiles are alike to the ones obtained in the square cavity without an obstacle Section 3.2.1 as entering and then leaving the hole.

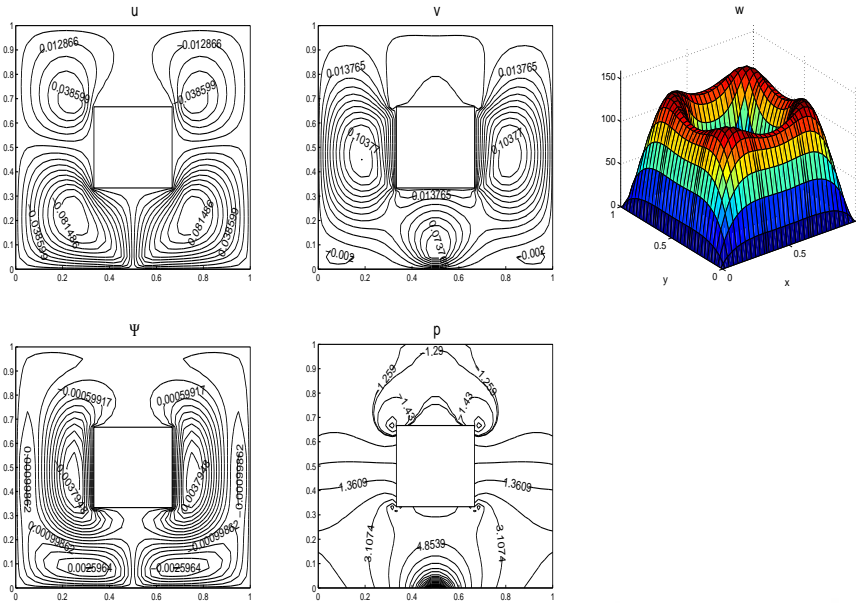


Figure 3.44: Flow in a square cavity with a medium obstacle at the center, $d = 1/3$, $Mn = 30$.

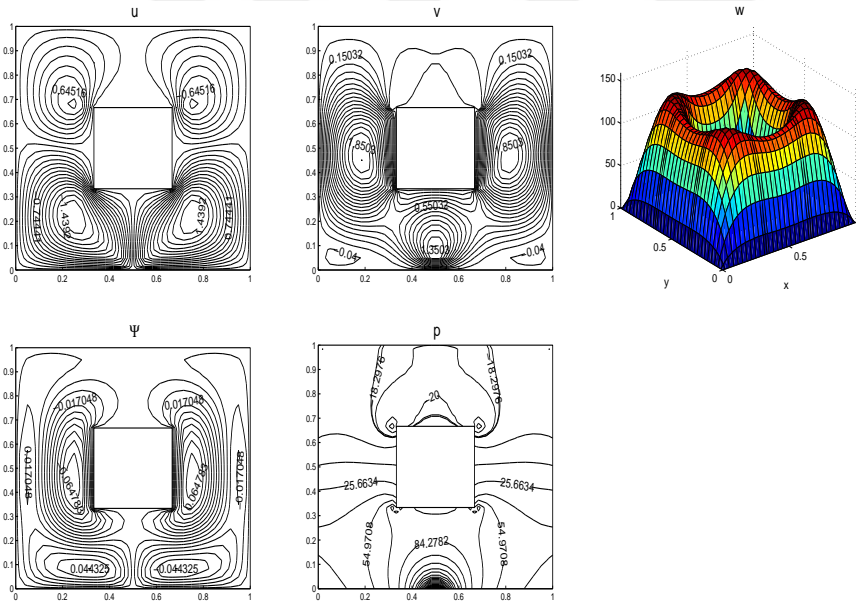


Figure 3.45: Flow in a square cavity with a medium obstacle at the center, $d = 1/3$, $Mn = 500$.

Increasing magnetic field intensity (Figures 3.45 and 3.46) accelerates the flow on the transverse plane and decelerates it in the axial direction around the point magnetic source. When $Mn \geq 14000$ no significant change is observed in the flow behavior, only planar velocities and the pressure increase, and the axial

velocity retardation around $x = 0.5$ is more pronounced.

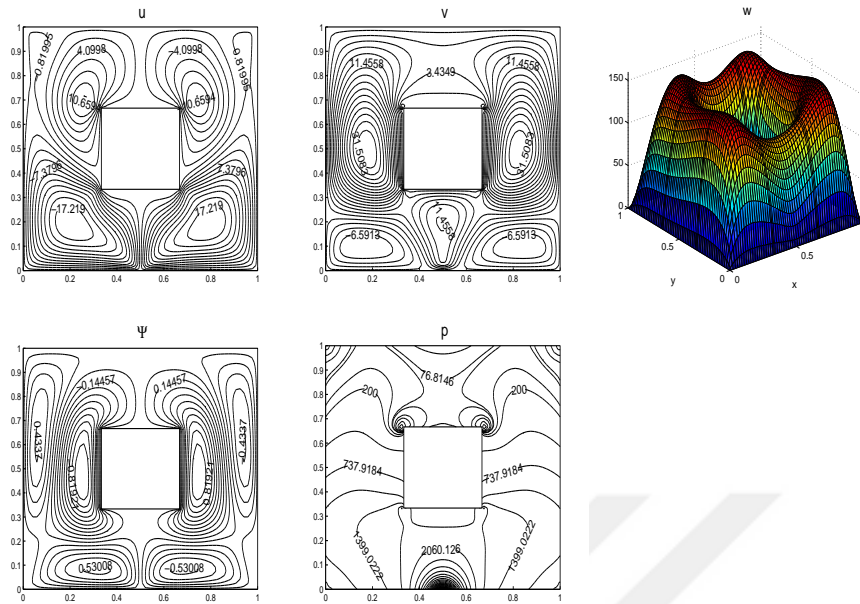


Figure 3.46: Flow in a square cavity with a medium obstacle at the center, $d = 1/3$, $Mn = 14000$.

The effect of the obstacle size is investigated in Figures 3.47-3.49 for $Mn = 5000$. $N = 168$ boundary elements are used when $d = 1/5$, $d = 1/2$ and $N = 160$ boundary elements are used for $d = 1/3$. As the obstacle dimension increases both the eddies attached to the obstacle and the ones close to the bottom wall are squeezed. Meantime new vortices appear above the obstacle. Pressure shows a profile as if emanating from the obstacle corners and increases with an increase in the size of the obstacle. The u -velocity is divided into new symmetric vortices between the upper wall of the cavity and the obstacle. The vortex below the obstacle in v -velocity enlarges. The axial velocity decreases with the enlargement of the obstacle due to the increase in the shear stress.

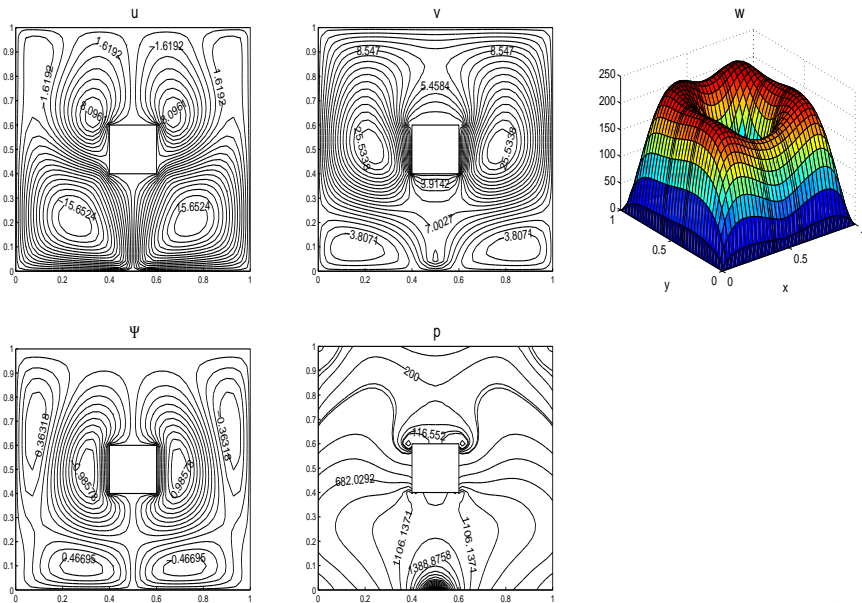


Figure 3.47: Flow in a square cavity with a small obstacle at the center, $d = 1/5$, $Mn = 5000$.

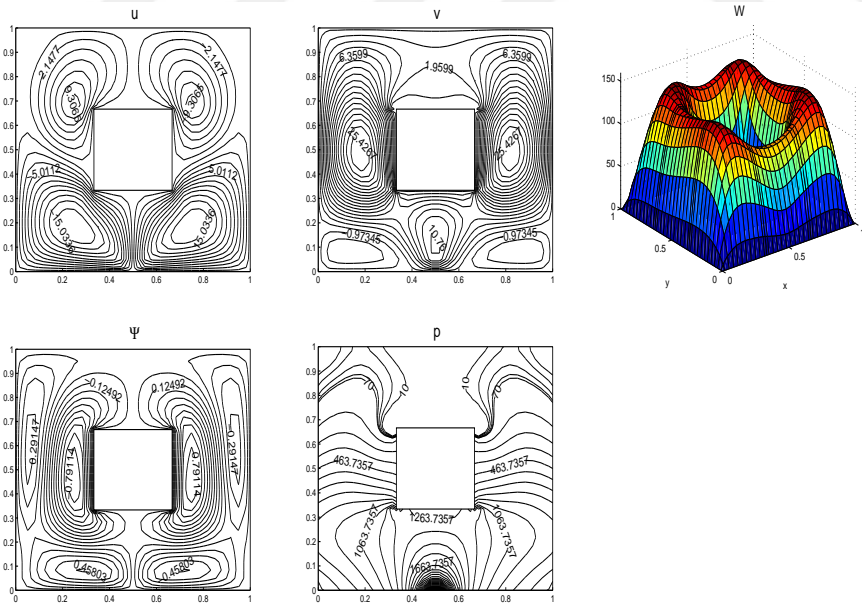


Figure 3.48: Flow in a square cavity with a medium obstacle at the center, $d = 1/3$, $Mn = 5000$.

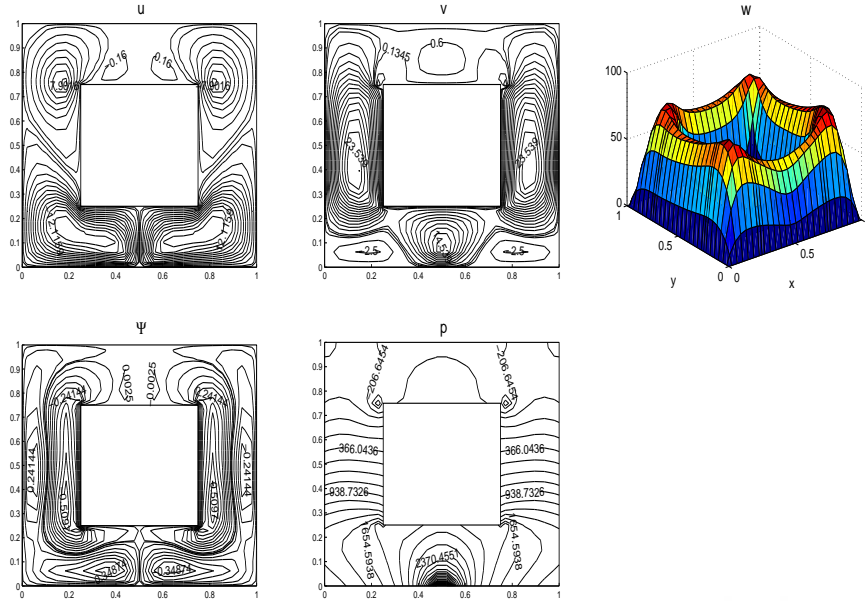


Figure 3.49: Flow in a square cavity with a large obstacle at the center, $d = 1/2$, $Mn = 5000$.

As the last case, the influence of the obstacle imposition is studied by taking a small sized obstacle ($d = 1/5$) for $Mn = 5000$. The computations are carried by using $N = 288$ boundary elements. Figures 3.50 and 3.51 present the flow profiles when the obstacle at the center is shifted $1/5$ units above and to the right, respectively. When the obstacle is shifted above, the planar velocity and stream function profiles stay the same with enlarged vortices below the obstacle. Pressure is moved to the obstacle area. When the obstacle is shifted $1/5$ units to the right (Figure 3.51), as expected, the symmetry in the profiles is destroyed. The left eddy attached to the vertical wall of the obstacle strengthens and meets with the right bottom vortex while the eddy close to the right vertical wall is weakening. Similarly, the vortices on the right of the obstacle shrink through the right vertical wall of the cavity in the u - and v -velocity. The left main vortex in the v -velocity covers almost all parts of the cavity. Pressure around the point magnetic source extends through the top of the cavity.

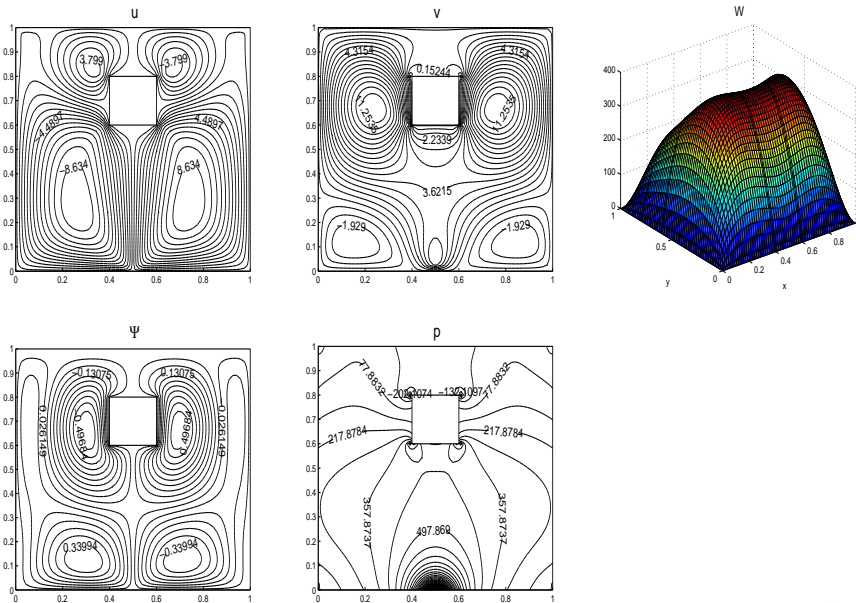


Figure 3.50: Flow in a square cavity with a small obstacle, left bottom corner placed at $(2/5, 3/5)$, $d = 1/5$, $Mn = 5000$.

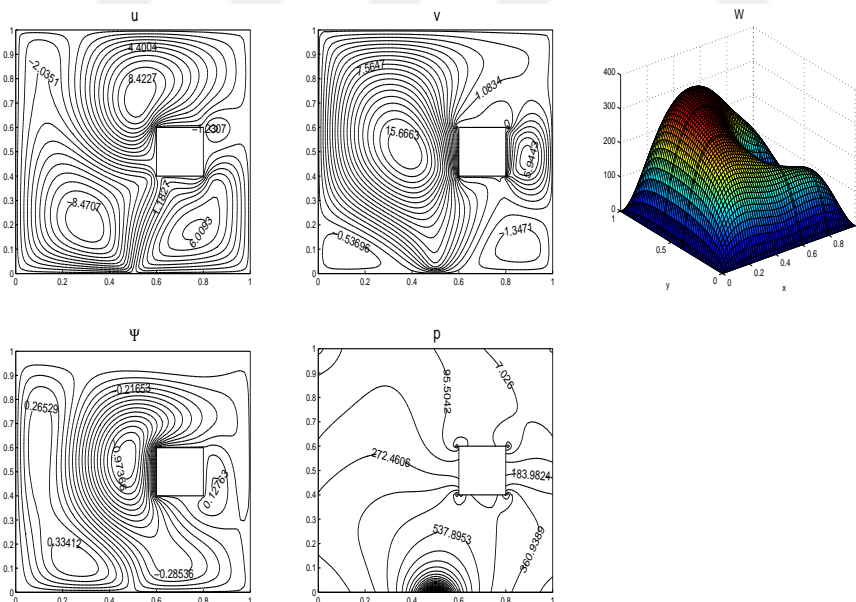


Figure 3.51: Flow in a square cavity with a small obstacle, left bottom corner placed at $(3/5, 2/5)$, $d = 1/5$, $Mn = 5000$.

3.3 Incompressible Flow in Rectangular Cavities with Multiple Point Magnetic Sources

The steady, laminar, fully developed flow of an incompressible, electrically non-conducting, magnetizable fluid is considered in a long impermeable pipe with rectangular cross-section. The flow through the pipe is due to a given constant pressure in the z -direction and it is affected by a non-uniform magnetic field generated by multiple wires carrying electric current. The aim is to obtain a flow behavior similar to the single wire case with even a considerably small magnetic number. Figure 3.52 displays the flow configuration for the two wires located below the bottom wall.

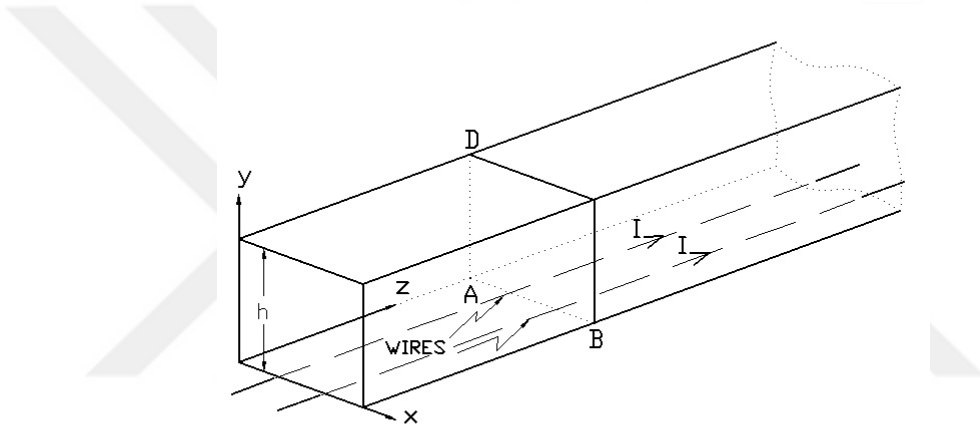


Figure 3.52: The flow configuration- two wires below the bottom wall.

The magnetic field generated by a series of infinitely long straight wires with the same current intensity I flowing in the same direction is defined by [39]

$$\bar{H}_x = -\frac{I}{2\pi} \sum_{i=1}^s \frac{(\bar{y} - \bar{b}_i)}{(\bar{x} - \bar{a}_i)^2 + (\bar{y} - \bar{b}_i)^2} \quad \bar{H}_y = \frac{I}{2\pi} \sum_{i=1}^s \frac{(\bar{x} - \bar{a}_i)}{(\bar{x} - \bar{a}_i)^2 + (\bar{y} - \bar{b}_i)^2} \quad (3.48)$$

where s is the number wires and (\bar{a}_i, \bar{b}_i) is the location of the i -th wire on the cross-section. Since all the numerical simulations are done on the cross-section of the pipe, wires around the pipe act as point magnetic sources.

Then, the magnetic field intensity in dimensional form is given by

$$\bar{H} = \sqrt{\bar{H}_x^2 + \bar{H}_y^2} . \quad (3.49)$$

In the DRBEM discretized matrix-vector equations (3.29)-(3.33), $H = \bar{H}/H_0$

where H_0 is the magnetic field strength at $(h/2, 0)$ with h being the height of the cavity.

The effect of multiple point magnetic sources on the flow is investigated in three different cases. In Section 3.3.1 and Section 3.3.2 the influence of multiple sources located below the bottom wall is studied in square and rectangular cavities, respectively. Then, sources are located oppositely below the bottom and above the top walls (Section 3.3.3).

The numerical simulations are done by taking constant boundary elements and sufficient number of interior nodes to depict the flow behavior in the cavities. The pressure boundary condition is obtained using the same procedure as explained in Section 3.2.1 for all of the test problems presented, and pressure relaxation parameter is taken as $\kappa = 0.05$. The numerical solution algorithm is the same as explained in Section 3.2, only the equation for the axial velocity is taken out from the iteration and solved once after all the other problem unknowns are computed. This difference does not contradict with the previous algorithm since the axial velocity reaches the convergence criteria very early. That is, the convergence criteria of the axial velocity does not have any influence on the number of iterations needed to obtain the numerical solution with the assigned tolerance. Although it is possible to put out the stream function equation from the iterative procedure it is kept since the stream function satisfies the continuity equation implicitly.

3.3.1 Square cavity with two or three sources below the bottom wall

Figure 3.53 displays the problem geometries and the boundary conditions for two and three sources cases. The point magnetic sources are placed at $(0.25, -0.05)$ and $(0.75, -0.05)$ for the two sources, and $(0.25, -0.05)$, $(0.5, -0.05)$ and $(0.75, -0.05)$ for the three sources cases, respectively. All the numerical results of this section are achieved by taking $N = 120$ boundary nodes.

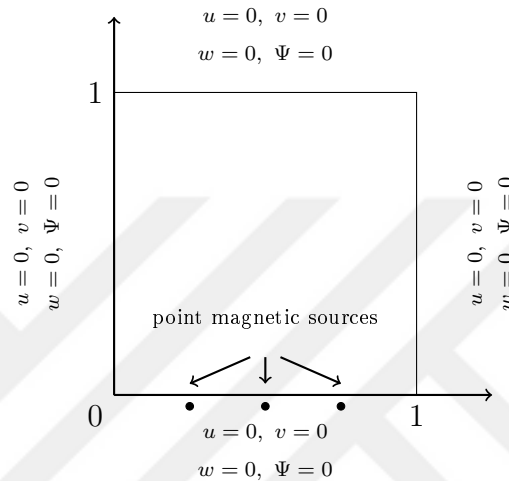


Figure 3.53: Problem geometry and the boundary conditions for square cavity with one, two and three sources.

The influence of the unique point magnetic source placed below the pipe was presented in Section 3.2.1. The main effect of a unique point magnetic source is to divide the flow and the u -velocity profiles into two symmetric vortices rotating in different directions and pressure is highly concentrated around the source. A boundary layer develops opposite to the magnetic source in the v -velocity showing the pushing effect of the source. As magnetic field intensity increases the flow on the transverse plane accelerates and pressure in the cavity increases. Since the kinetic energy of the flow in the axial direction is converted to the kinetic energy on the transverse plane, axial velocity retards around the magnetic source. This is the well-known flattening tendency of the fluid flow subjected to a magnetic field.

When the number of magnetic sources is increased it is expected that more fluctuations of the flow will be observed. Thus, first the grid dependence test is

carried by increasing the number of boundary points.

The variations of planar velocities with respect to the number of boundary points at $y = 0.1$ line for $Mn = 10$ in the case of two sources are displayed in Figure 3.54. It is observed that as N increases the solution gets smoother and $N \geq 100$ is required for solving pipe flow under magnetic source. Thus, the rest of the computations are carried with $N = 120 - 240$ elements for increasing Mn values.

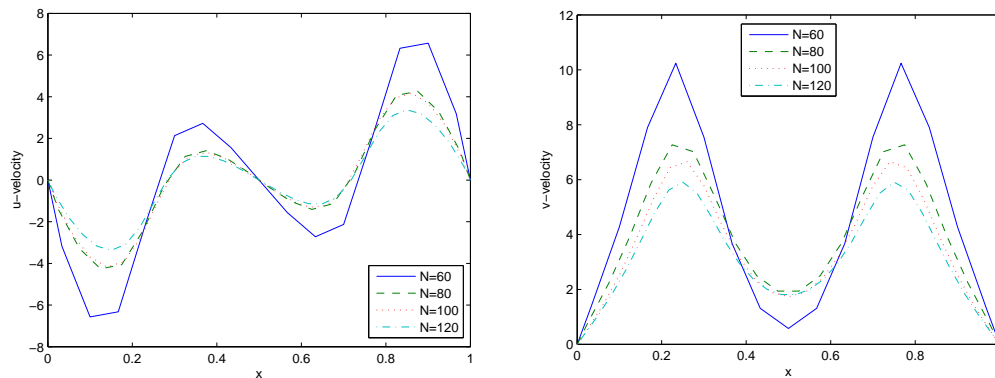


Figure 3.54: Planar velocity profiles on $y = 0.1$ line for two sources case $Mn = 10$ with $N = 60, 80, 100, 120$.

Figure 3.55 presents the flow and the pressure behaviors for two and three sources with $Mn = 10$. In the two sources case, fluid develops new secondary flows between the magnetic sources pushing the main vortices upwards. In addition, two vortices are developed close to the top wall in streamlines. Pressure highly concentrates around the sources with the same magnitudes and its distribution at the center of the cavity is similar to the case of unique source. The v -velocity profile consists of one main vortex forming boundary layers around the magnetic sources. The flow retardation in the axial direction occurs much earlier than the unique source case due to the combined effects of two sources. The flow behavior in three sources case is very similar to the one source case except the additional vortices in the u -velocity and again boundary layer formation in the v -velocity near the bottom wall. Also, axial velocity is not affected yet as if one source is present. Pressure is concentrated in front of the sources. Thus, for seeing the effect of more sources below the bottom wall, the width of the channel should

be increased.

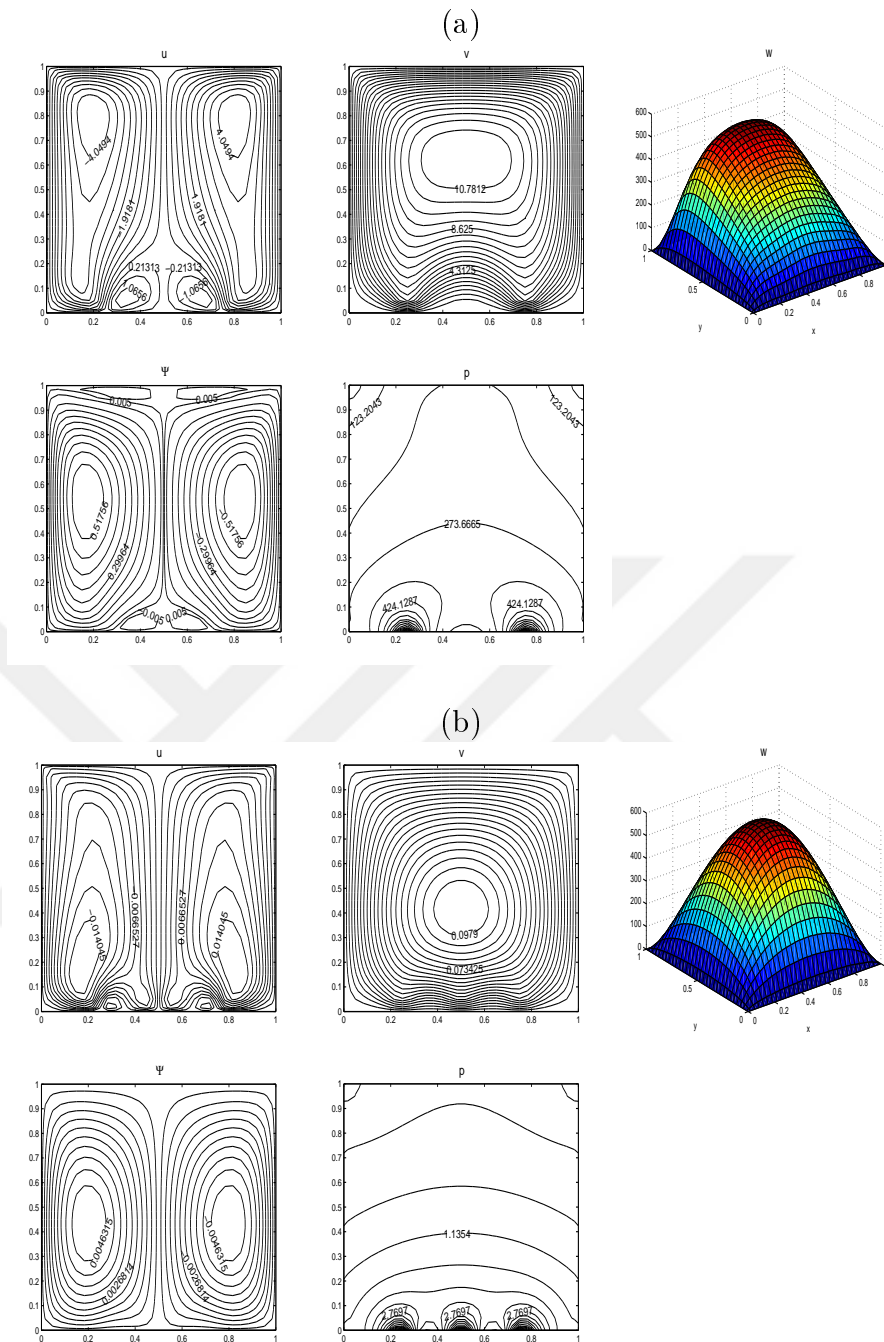


Figure 3.55: Square cavity, (a) two sources (b) three sources, $Mn = 10$.

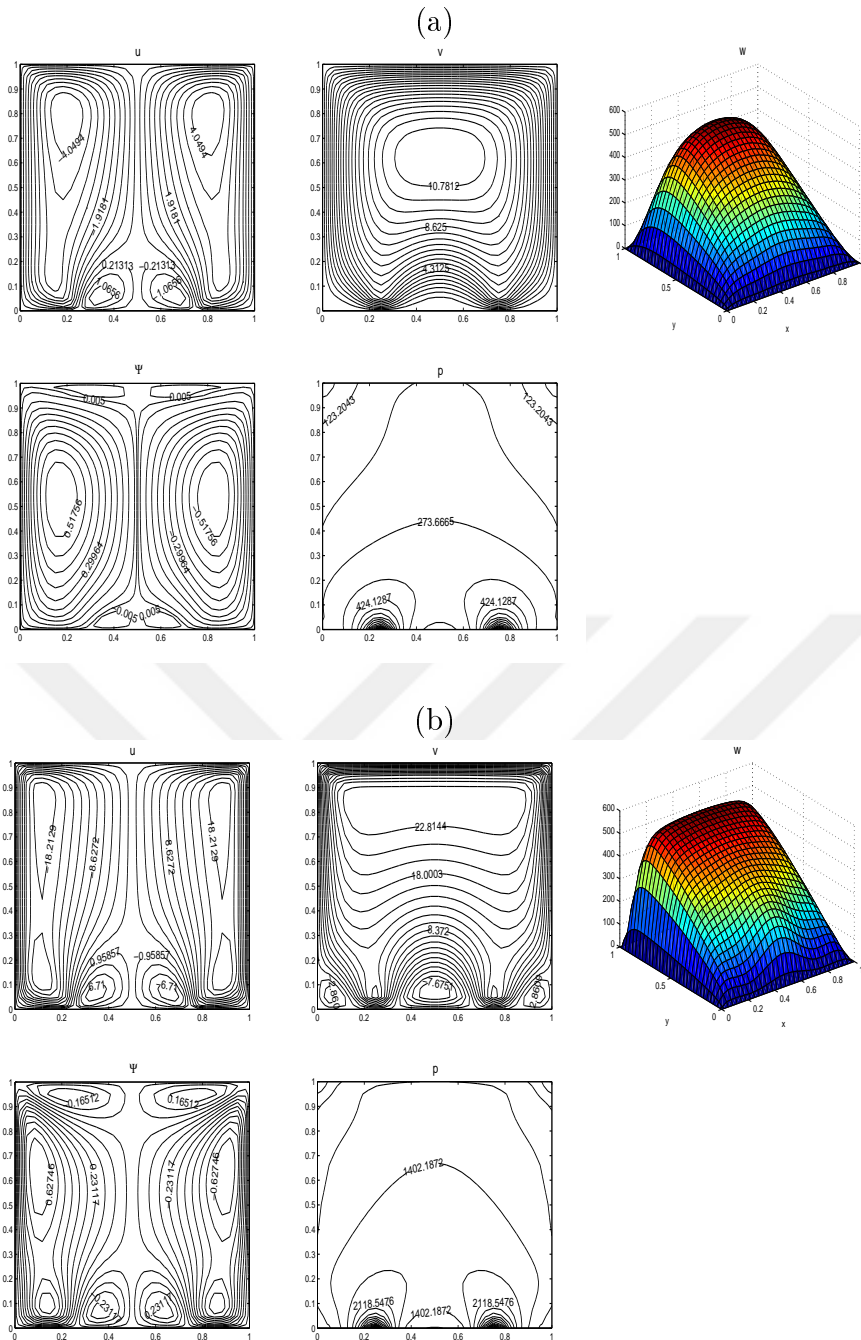


Figure 3.56: Square cavity, two sources, (a) $Mn = 10$, (b) $Mn = 50$.

When the magnetic field intensity is increased for two sources below the bottom wall (Figure 3.56), the flow accelerates forming new vortices on the transverse plane and pressure increases, at the same time the flow retardation around the magnetic sources in axial direction is more pronounced.

3.3.2 Rectangular cavity with two or three sources below the bottom wall

The influence of two and three sources on the FHD flow is also investigated in a rectangular cavity when its width is two times of its height. The point magnetic sources are placed at $(0.5, -0.05)$ and $(1.5, -0.05)$ for two sources, $(0.5, -0.05)$, $(1, -0.05)$ and $(1.5, -0.05)$ for three sources. The aim is to capture the effect of more sources on the bottom wall. The numerical results are presented for $Mn = 10$ and $Mn = 1000$ with $N = 180$ boundary nodes. The geometry and the boundary conditions are displayed in Figure 3.57.

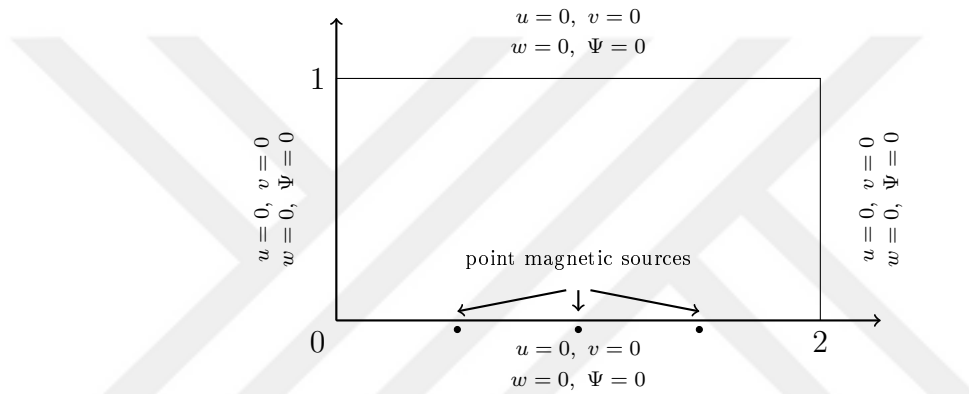


Figure 3.57: Problem geometry and the boundary conditions for the rectangular cavity with two and three sources.

Figure 3.58 displays the flow characteristics in the rectangular cavity with two and three sources placed below the bottom wall. The two sources case (Figure 3.58-(a)) shows in the half of the channel, the same behavior of the flow and pressure obtained in the square cavity with one source. It looks like the flow and the pressure in the first half of the channel repeats itself in the other half but the vortices in streamlines and the u -velocity at the middle of the channel tend to be decreased. When the number of sources are increased from two to three (Figure 3.58-(a),(b)) due to the distance between successive sources, the middle vortices in streamlines and the u -velocity squeeze. Also, the center of the vortices in the v -velocity meets at the center of the cavity. When compared to square cavity with three sources, planar velocity behaviors are similar. The effects of three sources combine and result in two antisymmetric vortices as if emanating from

the source in the middle, meantime small vortices appear between the sources. The flow retardation is not yet observed in the axial velocity for $Mn = 10$. As magnetic field intensity increases (Figure 3.58-(c)) new vortices in streamlines are developed close to the top wall. The planar velocity components increase and the axial velocity decreases. Pressure in the cavity also increases with an increase in Mn .

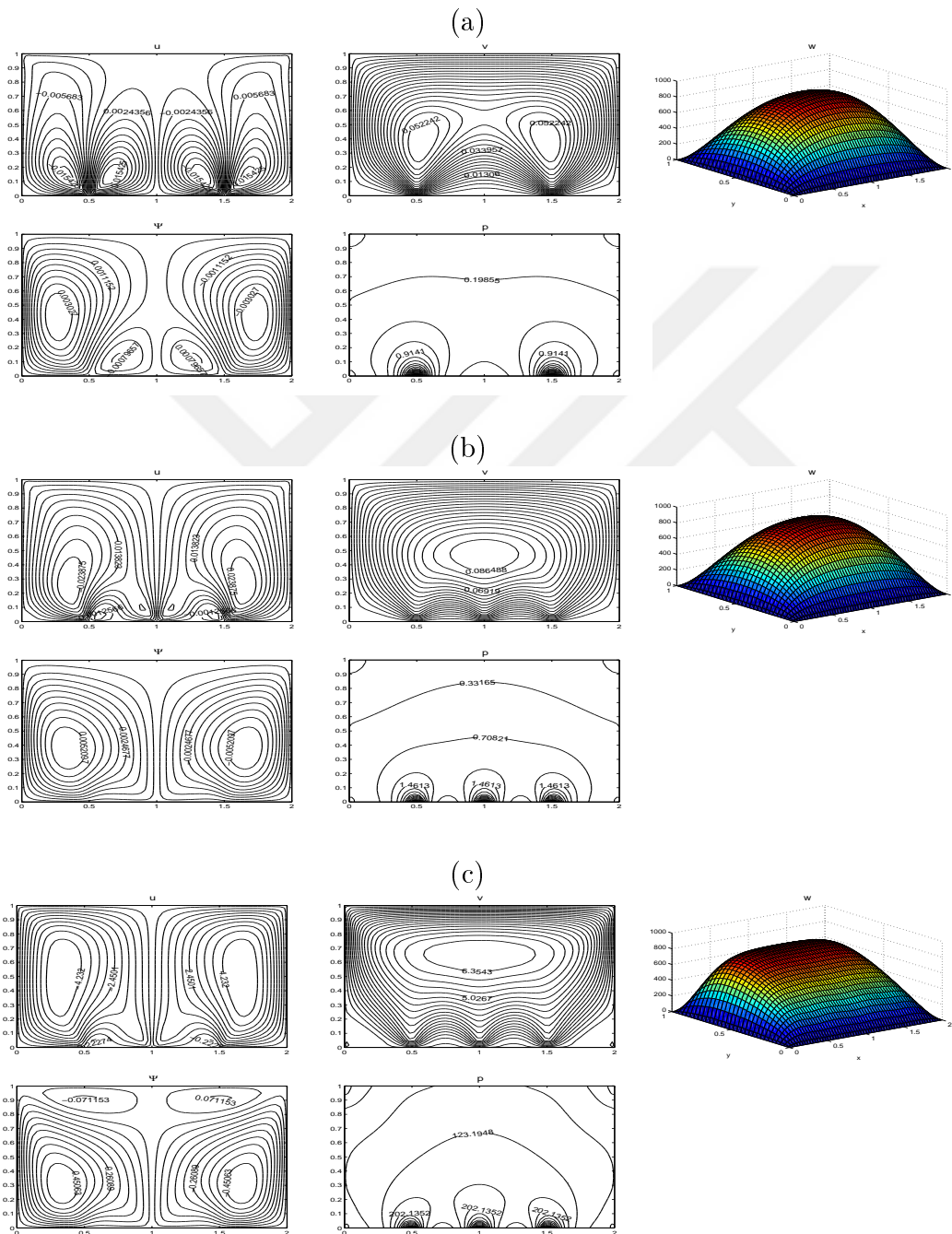


Figure 3.58: Rectangular cavity, (a) two sources $Mn = 10$, (b) three sources $Mn = 10$, (c) three sources $Mn = 1000$.

3.3.3 Square and rectangular cavities with sources on opposite walls

The influence of oppositely located multiple sources on the FHD flow is studied in square and rectangular cavities by taking two and four sources. In the square cavity, the magnetic point sources are placed oppositely at $(0.5, -0.05)$, $(0.5, 1.05)$ and in the rectangular cavity at $(0.66, -0.05)$, $(1.33, -0.05)$, $(0.66, 1.05)$ and $(1.33, 1.05)$ as shown in Figure 3.59.

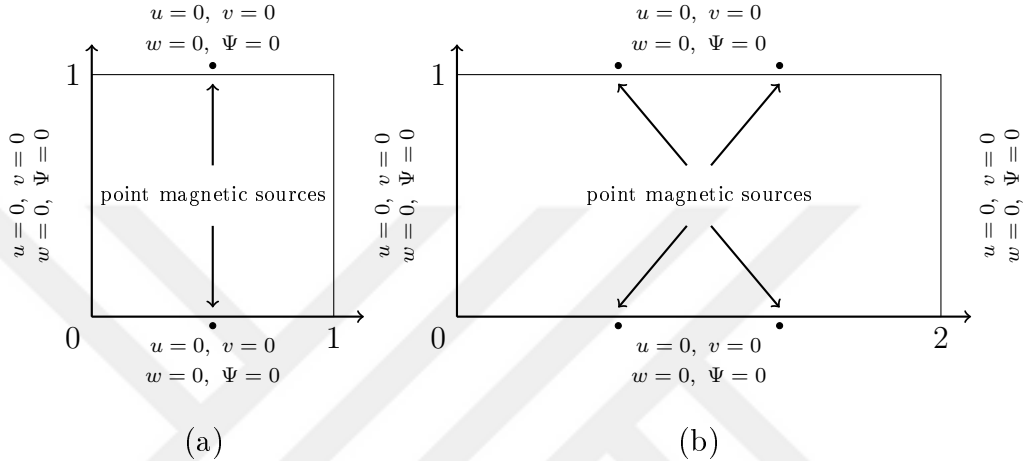


Figure 3.59: Problem geometry and boundary conditions for oppositely located sources (a) square cavity-two sources, (b) rectangular cavity-four sources.

Figure 3.60 represents the flow behaviors in a square cavity with two oppositely located magnetic sources for $Mn = 10$ and $Mn = 2000$ using $N = 120$, $N = 160$ boundary elements.

When the sources are oppositely located on the vertical symmetry axis (Figures 3.59-(a), 3.60-(a)) the flow and the pressure are symmetrically divided with respect to center lines with the same magnitudes. The u -velocity behavior is a continuation of the behavior shown in the one source case below the bottom wall. The v -velocity develops new vortices near the corners of the cavity.

Increasing magnetic field intensity accelerates the flow and increases the pressure in the cavity as in the previous cases. The vortices at the corners enlarge through the center of the cavity in the v -velocity. The retardation of the flow in the axial direction is now seen around both the sources and this preserves the symmetry in the axial velocity profile (Figure 3.60-(b), back and front views of the profile). When compared to the single source case, the retardation of the flow in the axial

direction is observed for a higher magnetic number since both of the sources push the fluid to the opposite wall.

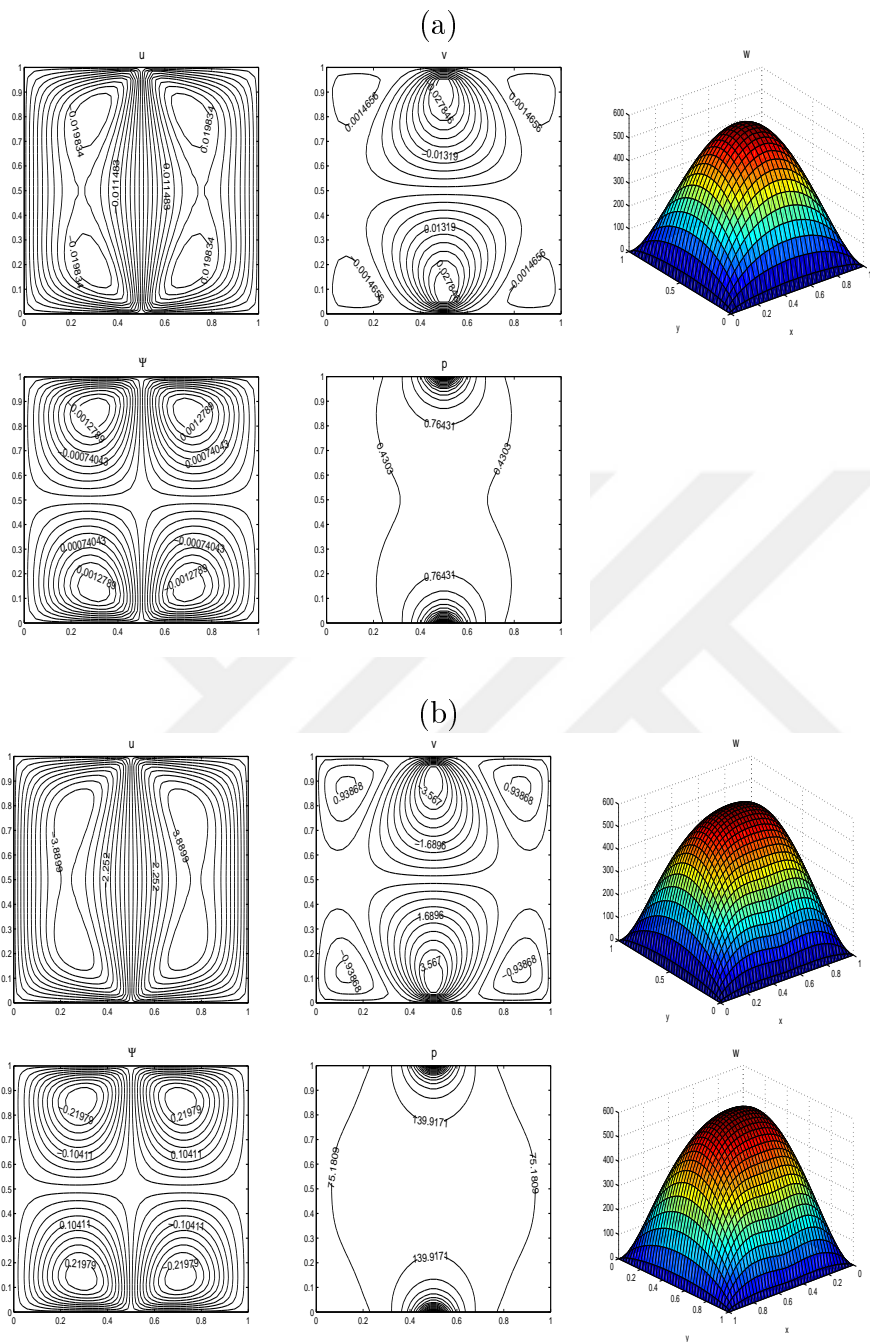


Figure 3.60: Square cavity, two opposite sources, (a) $Mn=10$, (b) $Mn = 2000$.

The flow and pressure behaviors in a rectangular cavity with four oppositely located sources are obtained by using $N = 180$, $N = 240$ boundary nodes for $Mn = 10$ and $Mn = 300$, respectively and displayed in Figure 3.61.

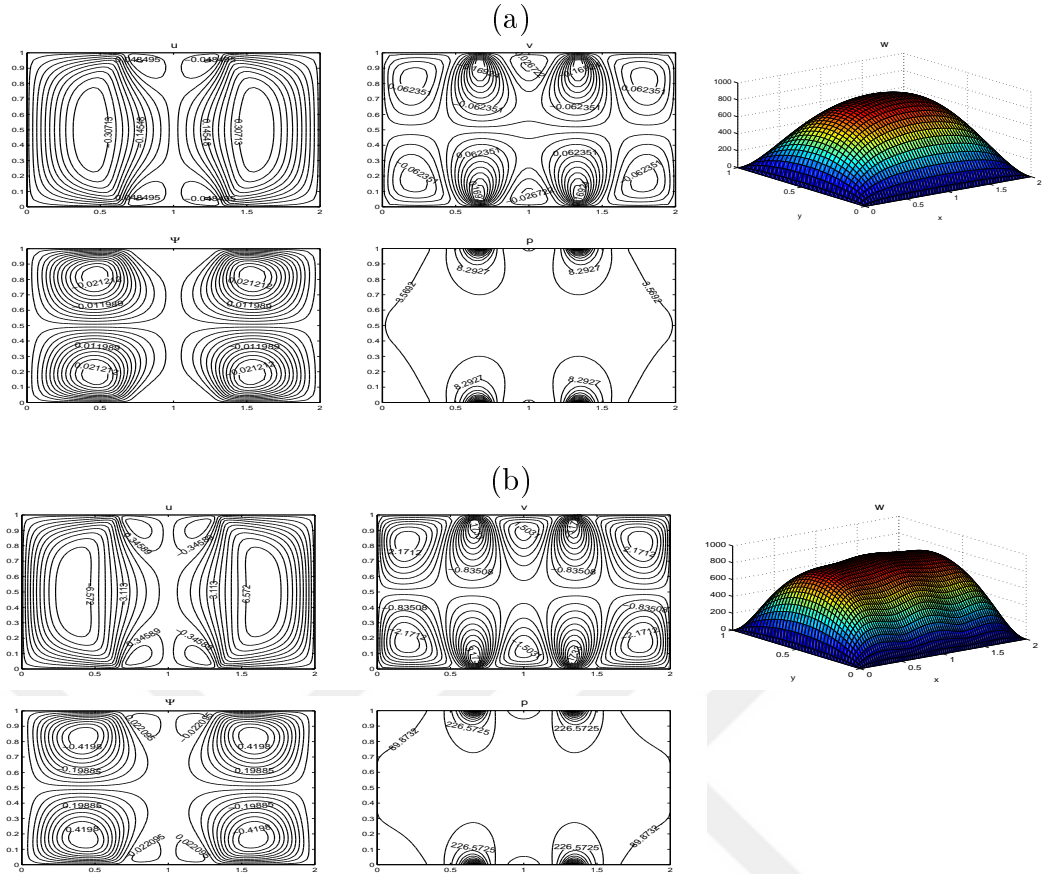


Figure 3.61: Rectangular cavity, four opposite sources, (a) $Mn = 10$, (b) $Mn = 300$.

When $Mn = 10$ (Figure 3.61-(a)) the flow in the cavity consist of four vortices as in the case of square cavity with two oppositely located sources. The u -velocity and pressure profiles again symmetrically divided with respect to $x = 1$ and $y = 0.5$ lines. In the v -velocity, secondary flows develop on the corners of the cavity and between the sources. Retardation of the axial velocity can be seen only when Mn increases ($Mn=300$).

As magnetic field intensity increases to 300 (Figure 3.61-(b)), pressure and planar velocities increase in magnitude as expected and the axial flow decelerates around the magnetic sources. New vortices develop in streamlines close to the source points.

3.4 Forced Convection Flow of Biomagnetic Fluid in Square, Lid-driven and Circular Cavities with Point Magnetic Source

In this section, the fully developed, steady flow of blood which exhibits magnetization and viscous dissipation is investigated in the cross-section of a long pipe (cavity) under the influence of magnetization and buoyancy forces. The flow configuration, pressure and the temperature disturbance are visualized for various values of magnetic and Rayleigh numbers in the square, lid-driven and circular cavities with the temperature differences between opposite vertical or horizontal walls keeping the other walls adiabatic. The axial velocity profile is presented. Viscous dissipation effect on the flow and the heat transfer is also studied. The system of equations discretized by the DRBEM is given in Chapter 2, equations (2.120)-(2.125) as

$$(\mathbf{H} - \mathbf{D}(u\mathbf{S}_x + v\mathbf{S}_y))u - \mathbf{G}\frac{\partial u}{\partial n} = \mathbf{D}\{\mathbf{S}_x p - Mn(T_c - T)H\frac{\partial H}{\partial x}\} \quad (3.50)$$

$$(\mathbf{H} - \mathbf{D}(u\mathbf{S}_x + v\mathbf{S}_y))v - \mathbf{G}\frac{\partial v}{\partial n} = \mathbf{D}\{\mathbf{S}_y p - Mn(T_c - T)H\frac{\partial H}{\partial y} - \frac{Ra}{Pr}T\} \quad (3.51)$$

$$(\mathbf{H} - \mathbf{D}(u\mathbf{S}_x + v\mathbf{S}_y))w - \mathbf{G}\frac{\partial w}{\partial n} = \mathbf{D}\{P_z\} \quad (3.52)$$

$$\begin{aligned} & (\mathbf{H} - Pr\mathbf{D}(u\mathbf{S}_x + v\mathbf{S}_y - MnEcH(u\frac{\partial H}{\partial x} + v\frac{\partial H}{\partial y})))T - \mathbf{G}\frac{\partial T}{\partial n} = \\ & = \mathbf{D}\{-MnEcPr\epsilon H(u\frac{\partial H}{\partial x} + v\frac{\partial H}{\partial y}) - EcPr(2(\mathbf{S}_x u)^2 + 2(\mathbf{S}_y v)^2 \\ & + (\mathbf{S}_x v + \mathbf{S}_y u)^2)\} \end{aligned} \quad (3.53)$$

$$\begin{aligned} \mathbf{H}p - \mathbf{G}\frac{\partial p}{\partial n} = & \mathbf{D}\{\frac{Ra}{Pr}\mathbf{S}_y T - (\mathbf{S}_x u)^2 - (\mathbf{S}_y v)^2 - 2(\mathbf{S}_x v)(\mathbf{S}_y u) \\ & - Mn(\mathbf{S}_x T H\frac{\partial H}{\partial x} + \mathbf{S}_y T H\frac{\partial H}{\partial y}) \\ & + Mn(T_c - T)((\frac{\partial H}{\partial x})^2 + (\frac{\partial H}{\partial y})^2 + H\nabla^2 H)\} \end{aligned} \quad (3.54)$$

$$\mathbf{H}\Psi - \mathbf{G}\frac{\partial \Psi}{\partial n} = \mathbf{D}\{\mathbf{S}_y u - \mathbf{S}_x v\} . \quad (3.55)$$

where Mn , Ec , Pr , Ra , ϵ are the magnetic, Eckert, Prandtl, Rayleigh and temperature numbers, and

$$\mathbf{D} = (\mathbf{H}\hat{\mathbf{U}} - \mathbf{G}\hat{\mathbf{Q}})\mathbf{F}^{-1} \quad \mathbf{S}_x = \frac{\partial \mathbf{F}}{\partial x}\mathbf{F}^{-1} \quad \mathbf{S}_y = \frac{\partial \mathbf{F}}{\partial y}\mathbf{F}^{-1} . \quad (3.56)$$

The system of matrix-vector equations are iteratively solved as in the following algorithm.

S.1 Define the place of the point source (a_1, a_2) , the problem parameters as $Mn, Ec, Ra, Pr, \epsilon, T_c$, the convergence criteria tolerance tol , pressure relaxation parameter κ and temperature relaxation parameter τ .

S.2 Compute the magnetic field intensity function $H(x, y)$ and its spatial derivatives $\frac{\partial H}{\partial x}, \frac{\partial H}{\partial y}, \frac{\partial^2 H}{\partial x^2}, \frac{\partial^2 H}{\partial y^2}$.

S.3 Set initial guesses for pressure gradients, $\frac{\partial p^{(0)}}{\partial x}$ and $\frac{\partial p^{(0)}}{\partial y}$, u -velocity, $u^{(0)}$, v -velocity, $v^{(0)}$ and the temperature $T^{(0)}$.

S.4 Solve the velocity components from

$$(\mathbf{H} - \mathbf{D}(\mathbf{u}^{(k)}\mathbf{S}_x + \mathbf{v}^{(k)}\mathbf{S}_y))u^{(k+1)} - \mathbf{G}\frac{\partial u^{(k+1)}}{\partial n} = \mathbf{D}\left\{\frac{\partial p^{(k)}}{\partial x} - Mn(T_c - T^{(k)})H\frac{\partial H}{\partial x}\right\} \quad (3.57)$$

$$(\mathbf{H} - \mathbf{D}(\mathbf{u}^{(k+1)}\mathbf{S}_x + \mathbf{v}^{(k)}\mathbf{S}_y))v^{(k+1)} - \mathbf{G}\frac{\partial v^{(k+1)}}{\partial n} = \mathbf{D}\left\{\frac{\partial p^{(k)}}{\partial y} - Mn(T_c - T^{(k)})H\frac{\partial H}{\partial y} - \frac{Ra}{Pr}T^{(k)}\right\} \quad (3.58)$$

using no-slip boundary conditions, where $\mathbf{u}^{(k)}$ and $\mathbf{v}^{(k)}$ are the diagonal matrices with diagonal entries $u^{(k)}$ and $v^{(k)}$, respectively.

S.5 Solve the temperature

$$\begin{aligned} & (\mathbf{H} - Pr\mathbf{D}(\mathbf{u}^{(k+1)}\mathbf{S}_x + \mathbf{v}^{(k+1)}\mathbf{S}_y - MnEcH(\mathbf{u}^{(k+1)}\frac{\partial H}{\partial x} + \mathbf{v}^{(k+1)}\frac{\partial H}{\partial y})))T^{(k+1)} \\ & - \mathbf{G}\frac{\partial T^{(k+1)}}{\partial n} = \mathbf{D}\left\{-MnEcPr\epsilon H(\mathbf{u}^{(k+1)}\frac{\partial H}{\partial x} + \mathbf{v}^{(k+1)}\frac{\partial H}{\partial y}) \right. \\ & \left. - EcPr(2(\mathbf{S}_x u^{(k+1)})^2 + 2(\mathbf{S}_y v^{(k+1)})^2 + (\mathbf{S}_x v^{(k+1)} + \mathbf{S}_y u^{(k+1)})^2)\right\} \end{aligned} \quad (3.59)$$

with imposed wall condition.

S.6 Generate boundary conditions for pressure using the momentum equations with newly obtained velocity components. Approximate pressure gradients with forward differences and the space derivatives by the DRBEM coordinate matrix \mathbf{F} .

S.7 Solve the pressure equation

$$\begin{aligned} \mathbf{H}p^{(k+1)} - \mathbf{G} \frac{\partial p^{(k+1)}}{\partial n} &= \mathbf{D} \left\{ \frac{Ra}{Pr} \mathbf{S}_y T^{(k+1)} - (\mathbf{S}_x u^{(k+1)})^2 - (\mathbf{S}_y v^{(k+1)})^2 \right. \\ &- 2(\mathbf{S}_x v^{(k+1)})(\mathbf{S}_y u^{(k+1)}) - Mn(\mathbf{S}_x T^{(k+1)} H \frac{\partial H}{\partial x} + \mathbf{S}_y T^{(k+1)} H \frac{\partial H}{\partial y}) \\ &\left. + Mn(T_c - T^{(k+1)}) \left(\left(\frac{\partial H}{\partial x} \right)^2 + \left(\frac{\partial H}{\partial y} \right)^2 + H \nabla^2 H \right) \right\} \end{aligned} \quad (3.60)$$

using the obtained pressure boundary condition in step **S.6**.

S.8 Solve

$$\mathbf{H}\Psi^{(k+1)} - \mathbf{G} \frac{\partial \Psi^{(k+1)}}{\partial n} = \mathbf{D} \{ \mathbf{S}_y u^{(k+1)} - \mathbf{S}_x v^{(k+1)} \} \quad (3.61)$$

using the natural boundary condition for the stream function.

S.9 Solve the axial velocity

$$(\mathbf{H} - \mathbf{D}(\mathbf{u}^{(k+1)} \mathbf{S}_x + \mathbf{v}^{(k+1)} \mathbf{S}_y)) w^{(k+1)} - \mathbf{G} \frac{\partial w^{(k+1)}}{\partial n} = \mathbf{D} \{ P_z \} \quad (3.62)$$

with no-slip wall condition.

S.10 Relax the temperature and pressure

$$\begin{aligned} p^{(k+1)} &= \kappa p^{(k+1)} + (1 - \kappa) p^{(k)} & 0 < \kappa \leq 1 \\ T^{(k+1)} &= \tau T^{(k+1)} + (1 - \tau) T^{(k)} & 0 < \tau \leq 1 \end{aligned} \quad (3.63)$$

for accelerating the convergence.

S.11 Compute pressure space derivatives

$$\frac{\partial p^{(k+1)}}{\partial x} = \mathbf{S}_x p^{(k+1)}, \quad \frac{\partial p^{(k+1)}}{\partial y} = \mathbf{S}_y p^{(k+1)} \quad (3.64)$$

S.12 Check the convergence criteria

$$\frac{\|z^{(k+1)} - z^{(k)}\|_\infty}{\|z^{(k)}\|_\infty} < tol \quad (3.65)$$

where $\|z\|_\infty = \max\{|z_1|, |z_2|, \dots, |z_{N+L}|\}$ denotes u, v, w, T, p, Ψ and k is the iteration level.

S.13 If the criteria is satisfied for all of the problem unknowns stop.

S.14 If the criteria is not satisfied for one of the unknowns go to step **S.4**.

The iteration procedure is started by taking

$$u^{(0)} = v^{(0)} = 0 \quad \text{in } \Omega \cup \Gamma \quad (3.66)$$

and

$$T^{(0)} = \begin{cases} 1 & \text{on the hot boundary} \\ 0 & \text{otherwise} \end{cases} \quad (3.67)$$

initially. In the stagnant situation of the fluid the transverse pressure gradient forces are balanced by the effect of the magnetic and buoyancy forces hence, the initial pressure gradients are

$$\begin{aligned} \frac{\partial p^{(0)}}{\partial x} &= Mn(T - T_c)H\left(\frac{\partial H}{\partial x}\right) + 10^{-12} \\ \frac{\partial p^{(0)}}{\partial y} &= Mn(T - T_c)H\left(\frac{\partial H}{\partial y}\right) + \frac{Ra}{Pr}T + 10^{-12} . \end{aligned} \quad (3.68)$$

The physical properties of blood presented in [17] (density $\rho = 1050 \text{ kg/m}^3$, dynamic viscosity $\mu = 3.2 \times 10^{-3} \text{ kg/ms}$, specific heat $c_p = 14.65 \text{ J/kgK}$, thermal conductivity $k = 2.2 \times 10^{-3} \text{ J/msK}$) are considered to set the dimensionless parameters. The temperatures of the hot and the cold walls are $T_{hot} = 43^\circ\text{C}$ and $T_{cold} = 3.5^\circ\text{C}$. The width of the square cavity or the radius of the circular cavity is $h = 1.1 \times 10^{-3} \text{ m}$. $Pr = 20$, $Ec = 1.25 \times 10^{-8}$, $\epsilon = 7$ are taken. The pressure gradient given to the fluid in the axial direction is $P_z = -8000$ [42]. The point magnetic source is placed at $(a_1, a_2) = (0.5, -0.05)$ for the square and $(a_1, a_2) = (0, -1.05)$ for the circular cavities.

3.4.1 Forced convection flow in a square cavity with horizontal adiabatic walls and point magnetic source

In this problem, the influence of the buoyancy and the magnetization forces on the FHD fluid are studied in the square cavity where the horizontal walls are adiabatic, left vertical wall is hot and the right vertical wall is cold. The viscous dissipation effect is also studied. $N = 160$ constant boundary elements are used for the discretization of the boundary, except $Mn = 200$ case where the

number of elements is needed to be increased ($N = 200$) due to the significant change in the flow along the boundaries. The relaxation parameters for pressure and the temperature are $\kappa = \tau = 0.05$ in general but in order to achieve the numerical solutions for high Rayleigh numbers τ is decreased. The comparison of the results obtained for $Mn = 10$, $Ra = 10^2$ with constant and linear elements is also done. The problem geometry and the boundary conditions are presented in Figure 3.62

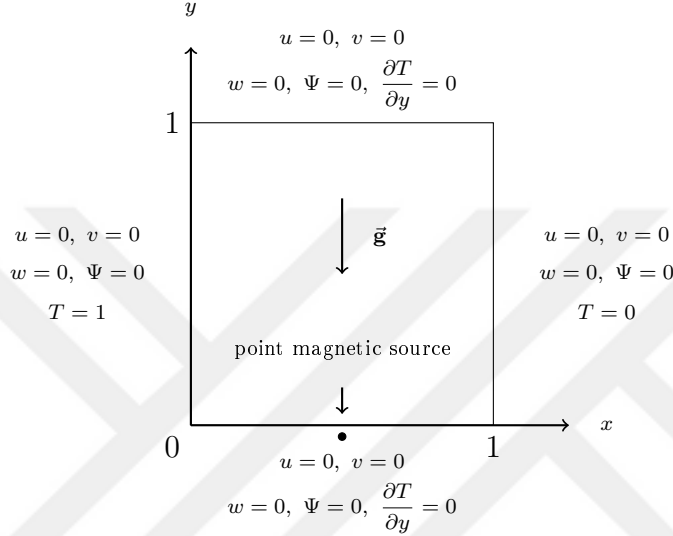


Figure 3.62: Forced convection flow in a square cavity with horizontal adiabatic walls.

Pressure boundary conditions are approximated using the same technique as explained in the previous problems. Thus,

$$\begin{aligned}
 \text{Side 1: } \quad p_{bd}^{(k+1)} &= p_{int}^{(k)} - \Delta y (\mathbf{S}_I v^{(k+1)}) + \frac{Ra}{Pr} T^{(k+1)} + Mn(T_c - T^{(k+1)}) H \frac{\partial H}{\partial y} \\
 \text{Side 2: } \quad p_{bd}^{(k+1)} &= p_{int}^{(k)} + \Delta x (\mathbf{S}_I u^{(k+1)}) + Mn(T_c - T^{(k+1)}) H \frac{\partial H}{\partial x} \\
 \text{Side 3: } \quad p_{bd}^{(k+1)} &= p_{int}^{(k)} + \Delta y (\mathbf{S}_I v^{(k+1)}) + \frac{Ra}{Pr} T^{(k+1)} + Mn(T_c - T^{(k+1)}) H \frac{\partial H}{\partial y} \\
 \text{Side 4: } \quad p_{bd}^{(k+1)} &= p_{int}^{(k)} - \Delta x (\mathbf{S}_I u^{(k+1)}) + Mn(T_c - T^{(k+1)}) H \frac{\partial H}{\partial x} .
 \end{aligned} \tag{3.69}$$

with $\mathbf{S}_I = \frac{\partial \mathbf{F}}{\partial x} \mathbf{F}^{-1} \frac{\partial \mathbf{F}}{\partial x} \mathbf{F}^{-1} + \frac{\partial \mathbf{F}}{\partial y} \mathbf{F}^{-1} \frac{\partial \mathbf{F}}{\partial y} \mathbf{F}^{-1} - \mathbf{u}^{(k+1)} \frac{\partial \mathbf{F}}{\partial x} \mathbf{F}^{-1} - \mathbf{v}^{(k+1)} \frac{\partial \mathbf{F}}{\partial y} \mathbf{F}^{-1}$. $\mathbf{u}^{(k+1)}$ and $\mathbf{v}^{(k+1)}$ being the diagonal matrices with diagonal entries $u^{(k+1)}$ and $v^{(k+1)}$, respectively.

The proposed numerical scheme and results are validated with the natural con-

vection flow of air in a square cavity without magnetization force by taking $Pr = 0.7$ and $Ra = 10^3$. Figure 3.63 displays the numerical results obtained with $N = 120$ constant elements and $tol = 10^{-4}$ tolerance. The relaxation parameters for pressure and the temperature are $\kappa = 0.1$ and $\tau = 0.1$, respectively.

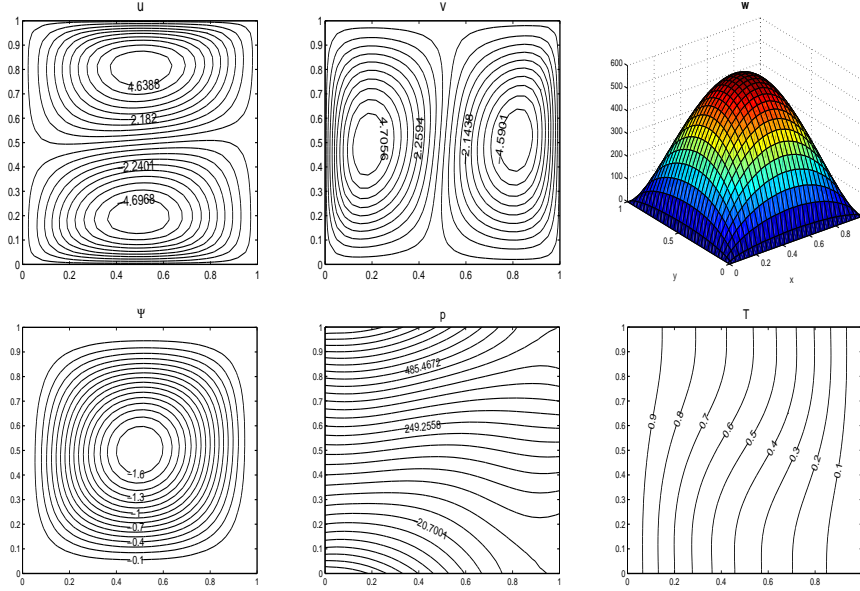


Figure 3.63: Natural convection flow of air, $Mn = 0$, $Ra = 10^3$.

The numerical results show the influence of only the buoyancy force. The fluid rises up around the hot, left vertical wall and falls down around the cold, right vertical wall which yields a clockwise rotation. Pressure highly concentrates at the left top corner of the cavity and the heat transfers from the hot wall to the cold wall uniformly. The u - and v -velocity profiles consist of two vortices.

The average Nusselt number at the heated wall of the cavity is calculated by

$$Nu_{avg} = \int_0^1 \left(-\frac{\partial T}{\partial x} \right) \Big|_{x=0} dy . \quad (3.70)$$

Table 3.3 is the comparison of the average Nusselt numbers obtained in the present study and by Lo et al. [85] using the DRBEM and the differential quadrature method, respectively.

Table 3.3: Average Nusselt numbers, $Mn = 0$, $Ra = 10^{-3}$.

<i>present study</i>	<i>(Lo et al., 2007) [85]</i>
1.1189	1.118

The obtained results and the average Nusselt numbers are in good agreement with the ones in [85].

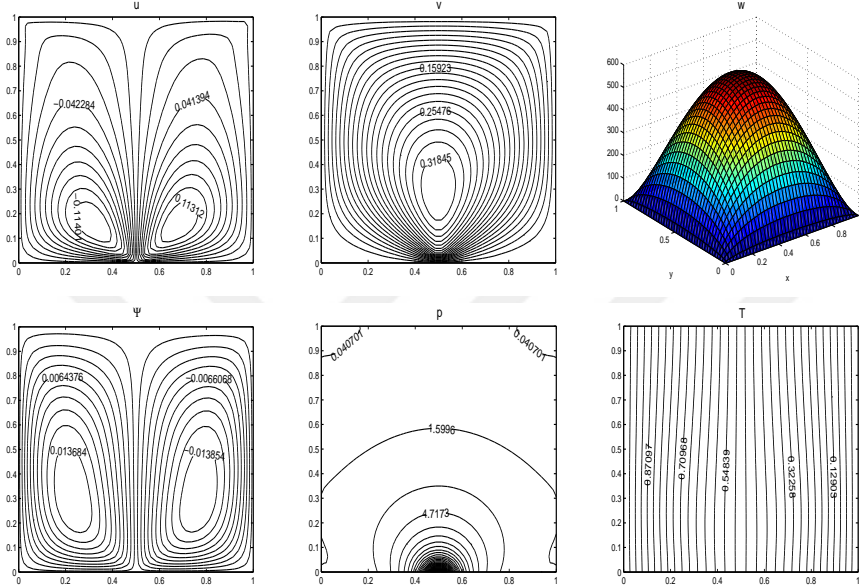


Figure 3.64: Forced convection flow in a square cavity with horizontal adiabatic walls, viscous dissipation is neglected. $Ra = 0$, $Mn = 5$.

Figures 3.64-3.65 show the flow, pressure and the temperature behaviors for increasing Magnetic number ($Mn = 5, 200$) in the absence of the buoyancy force ($Ra = 0$). As Mn increases the planar velocities and pressure advance at the same time the axial velocity collapses around the point magnetic source. Two symmetric vortices are observed in the u -velocity and stream function profiles. The v -velocity spreads through the cavity and develops new vortices close to the bottom corners of the cavity as Mn increases. Pressure around the point magnetic source is very high. The isotherms are shifted through the hot and cold walls when the magnetic number increases. For $Mn = 200$ they are divided almost symmetrically, that is, the temperature at the center of the cavity is the average of the hot and cold wall temperatures.

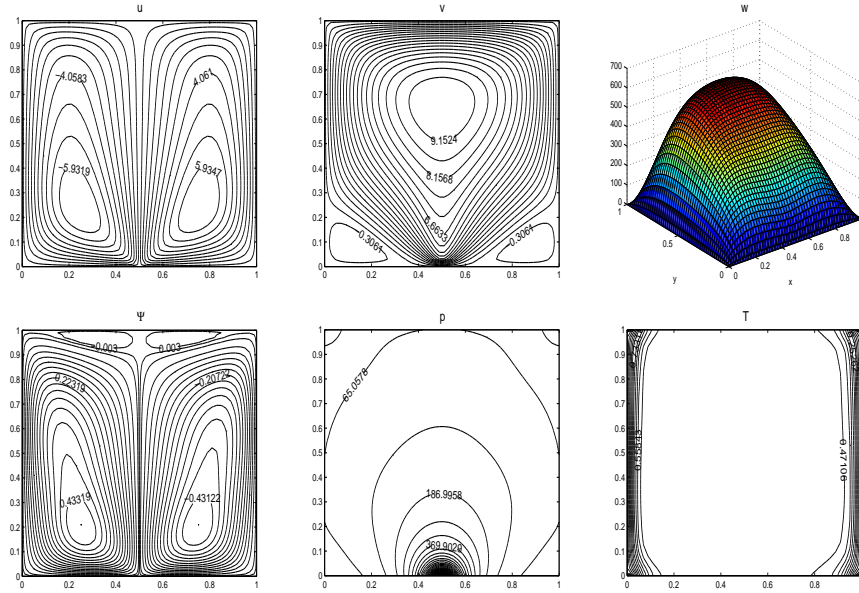


Figure 3.65: Forced convection flow in a square cavity with horizontal adiabatic walls, viscous dissipation is neglected. $Ra = 0$, $Mn = 200$.

When magnetization force is included ($Mn = 10$) and Rayleigh number increases $Ra = 10^2, 10^5$ (Figures 3.66-3.68) the flow, pressure and temperature behaviors change completely, especially when $Ra = 10^5$ only buoyancy force controls the flow. Since the thermal convection dominates the magnetization, the symmetry in streamlines and the u -velocity vanish and one of the vortices enlarges. The right vortex center in the u -velocity squeezes at the left upper corner of the cavity and the v -velocity develops a boundary layer close to the left vertical wall. Isotherms shift to the hot wall leaving the center of the cavity cold. This means that, high thermal convection blocks the heat transfer from the hot wall. As Ra increases, high pressure around the magnetic source moves to the top wall. The behavior of the axial velocity does not alter much.

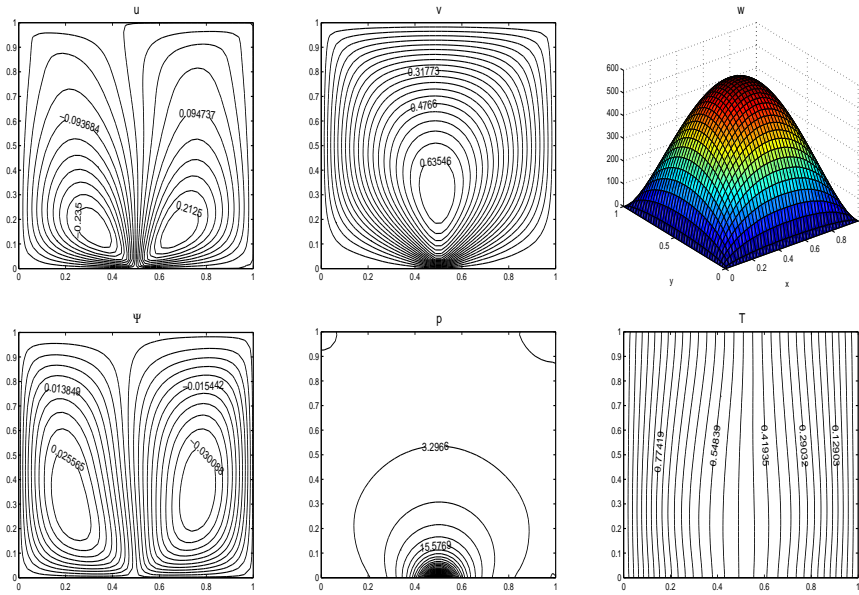


Figure 3.66: Forced convection flow in a square cavity with horizontal adiabatic walls, viscous dissipation is neglected. $Mn = 10$, $Ra = 10^2$.

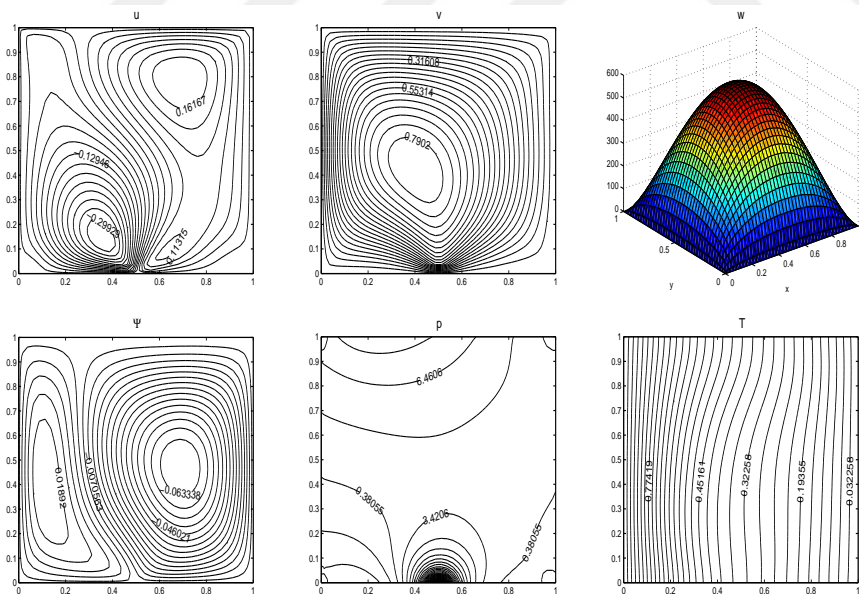


Figure 3.67: Forced convection flow in a square cavity with horizontal adiabatic walls, viscous dissipation is neglected. $Mn = 10$, $Ra = 10^3$.

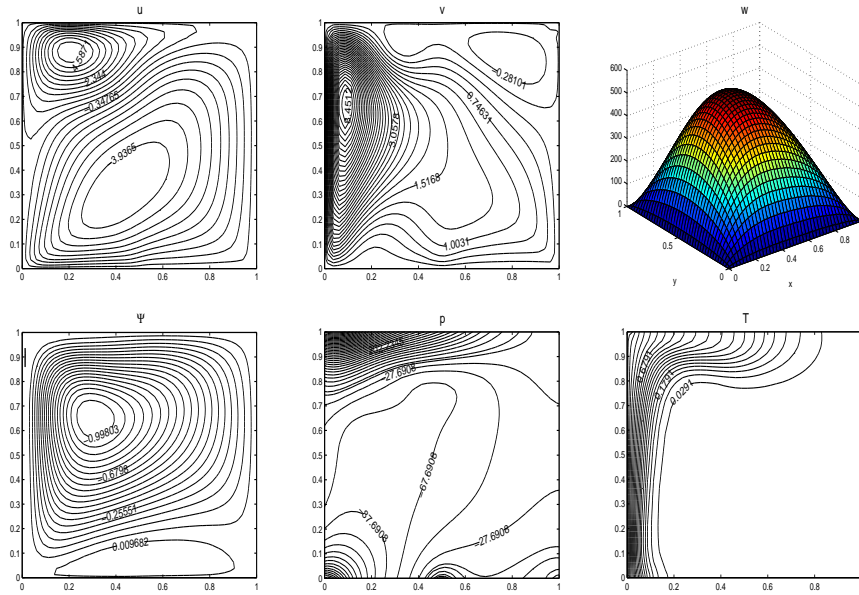


Figure 3.68: Forced convection flow in a square cavity with horizontal adiabatic walls, viscous dissipation is neglected. $Mn = 10$, $Ra = 10^5$.

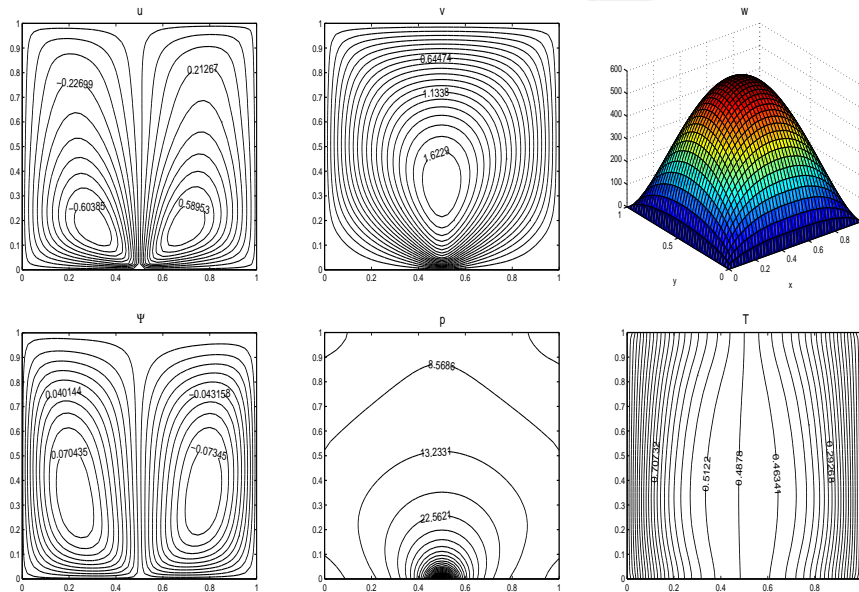


Figure 3.69: Linear elements-forced convection flow in a square cavity with horizontal adiabatic walls, viscous dissipation is neglected. $Mn = 10$, $Ra = 10^2$.

The numerical results for $Mn = 10$, $Ra = 10^2$ in the absence of viscous dissipation are also obtained by discretizing the boundary with 160 linear elements. As can be seen from Figure 3.69 that the behaviors of the flow and the heat transfer do not alter compared to the same number of constant elements case in Figure

3.66. Thus, concerning the computational cost, the rest of the computations are carried with constant element discretization.

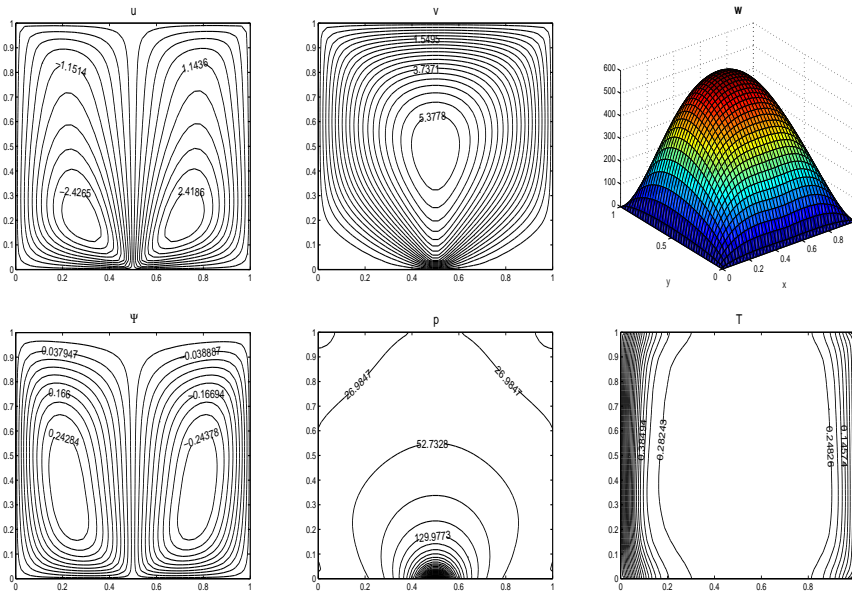


Figure 3.70: Forced convection flow in a square cavity with horizontal adiabatic walls, viscous dissipation is neglected. $Mn = 80$, $Ra = 10^2$.

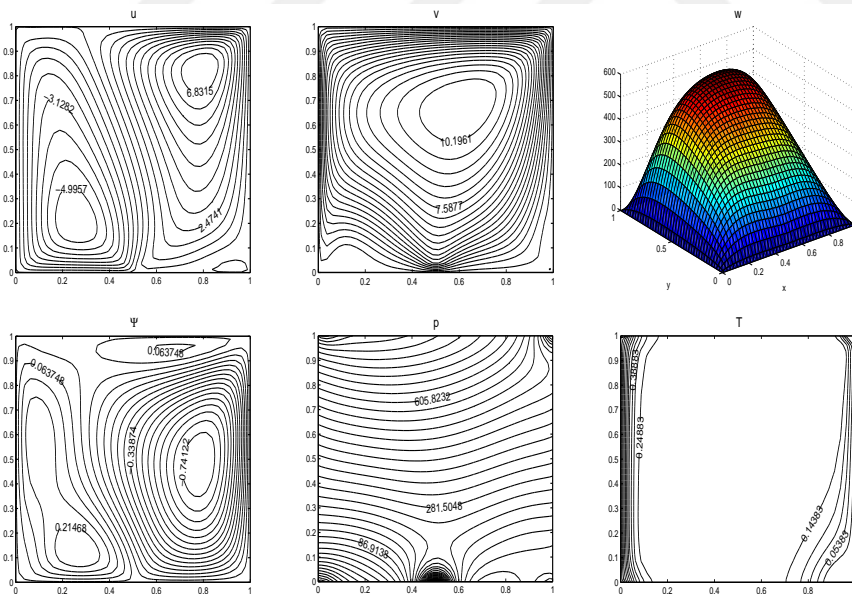


Figure 3.71: Forced convection flow in a square cavity with horizontal adiabatic walls, viscous dissipation is neglected. $Mn = 80$, $Ra = 10^5$.

When magnetic number is increased to $Mn = 80$ and Rayleigh number varies in the range $Ra = 10^2 - 10^5$ magnetic source dominates the thermal convection

this time up to $Ra = 10^5$ (Figures 3.70-3.71). The buoyancy force effect on the temperature of the fluid is the formation of a thin layer close to the hot wall of the cavity. The symmetry in streamlines and the planar velocities disappears when $Ra = 10^5$. The left vortex in streamlines shifts to the hot wall leaving its place to the right vortex. Pressure around the source loses its effect and thermal convection is still observed near the cold wall.

Viscous dissipation effect on the flow, pressure and the temperature is visualized in Figures 3.72-3.73, respectively for $Mn = 10$ and 80 when $Ra = 10^5$. When magnetic number is small ($Mn = 10$), flow and temperature behaviors stay the same with viscous dissipation when it is compared with Figure 3.68. The viscous dissipation effect is observed on isotherms only when both magnetic and buoyancy forces are high ($Mn = 80$ and $Ra = 10^5$) comparing with Figure 3.71. The convection from the right cold wall still extends through the center of the cavity. Magnitude of velocities and stream function values are reduced. That is, the viscous dissipation retards the flow and the heat transfer in the cavity. Also, the v -velocity profile becomes nearly symmetric.

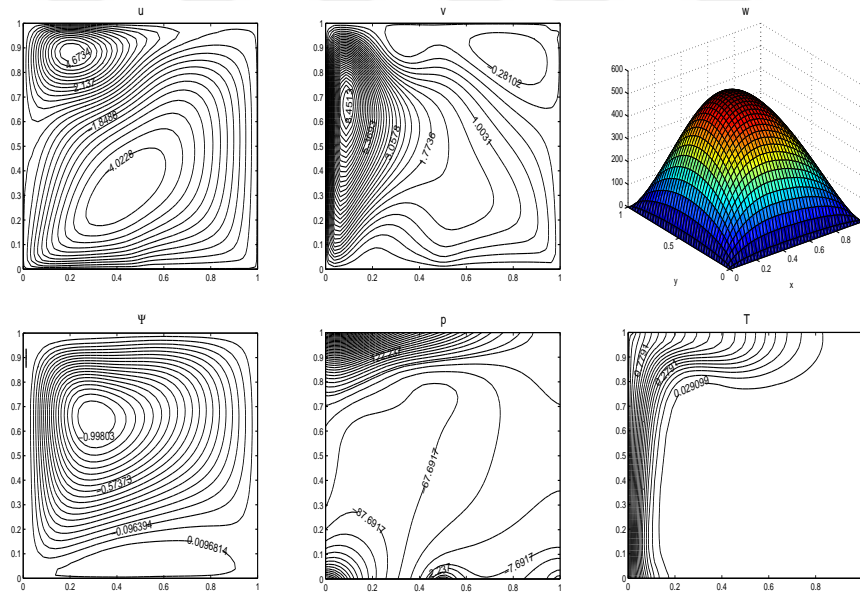


Figure 3.72: Forced convection flow in a square cavity with horizontal adiabatic walls, viscous dissipation is included. $Mn = 10$, $Ra = 10^5$.

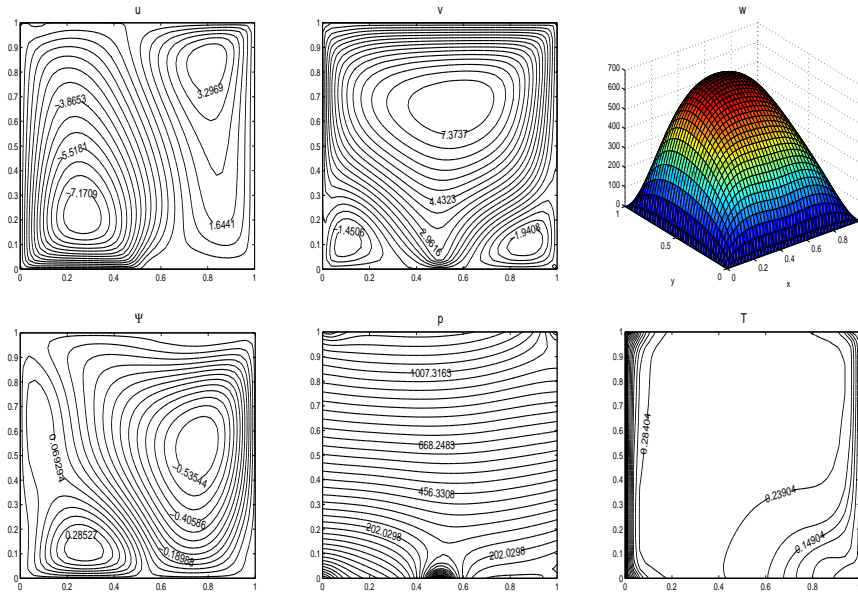


Figure 3.73: Forced convection flow in a square cavity with horizontal adiabatic walls, viscous dissipation is included. $Mn = 80$, $Ra = 10^5$.

3.4.2 Forced convection flow in a lid-driven square cavity with horizontal adiabatic walls and point magnetic source

The aim of this study is to analyze the influence of the moving lid together with the effects of buoyancy and magnetic forces. The flow configuration and the boundary conditions are presented in Figure 3.74.

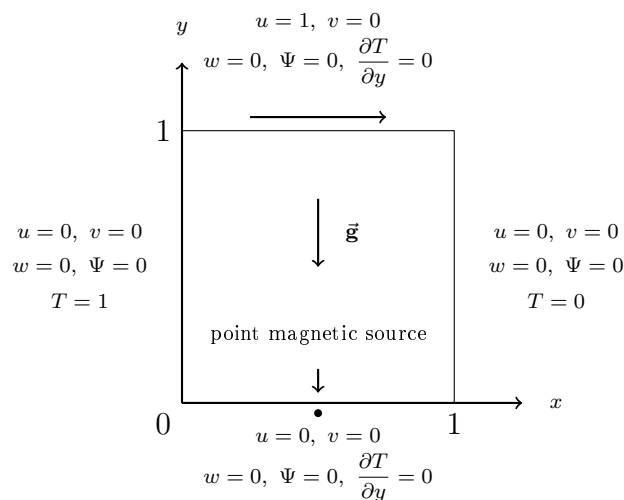


Figure 3.74: Forced convection flow in a lid-driven square cavity with horizontal adiabatic walls.

Pressure boundary conditions are similarly obtained as explained in Section 3.4.1. $N = 160$ constant elements are used for the discretization of the boundary. Relaxation parameters $\kappa = 0.05$ and $\tau = 0.05, 0.001$ are taken for $Mn = 10, 80$, respectively.

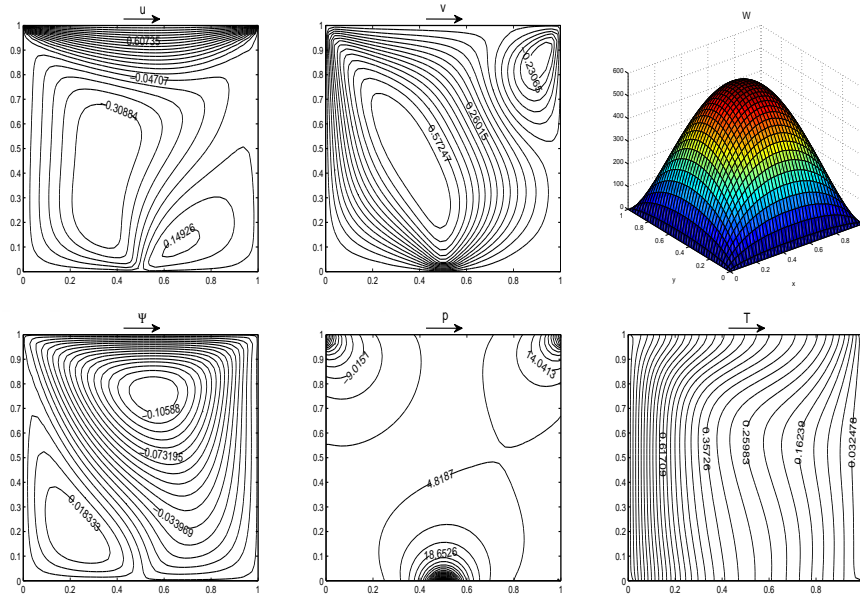


Figure 3.75: Forced convection flow in a lid-driven square cavity with horizontal adiabatic walls, viscous dissipation is neglected. $Mn = 10$, $Ra = 10^2$.

In Figure 3.75, the flow behavior, pressure and the temperature disturbances are visualized for small magnetic and Rayleigh numbers ($Mn = 10$, $Ra = 10^2$) in the absence of viscous dissipation. When it is compared with the behaviors obtained in square cavity for the same parameter values (Figure 3.66) a significant effect is observed in both the flow and temperature behaviors as the deterioration from the symmetric behavior. The moving upper lid causes the shrink of the left vortex to the left lower corner for streamlines, and the development of the new vortices in the right lower and right upper corners for the u - and v -velocities, respectively. The u -velocity is mostly concentrated on the moving lid. Pressure is also increased through the right half of the cavity. Axial velocity is not affected much and the heat transfer is increased through the cold wall around the moving lid. However when both Mn and Ra are increased and viscous dissipation is added (Figure 3.76), the flow, pressure and the temperature of the fluid get

beyond the moving lid's control and show almost the same behavior observed in the square cavity as compared with Figure 3.73. Thus, the main control mechanism of the flow and temperature of the fluid lies in the variations of magnetic and buoyancy forces. Viscous dissipation effect can only be observed when both Mn and Ra are high.

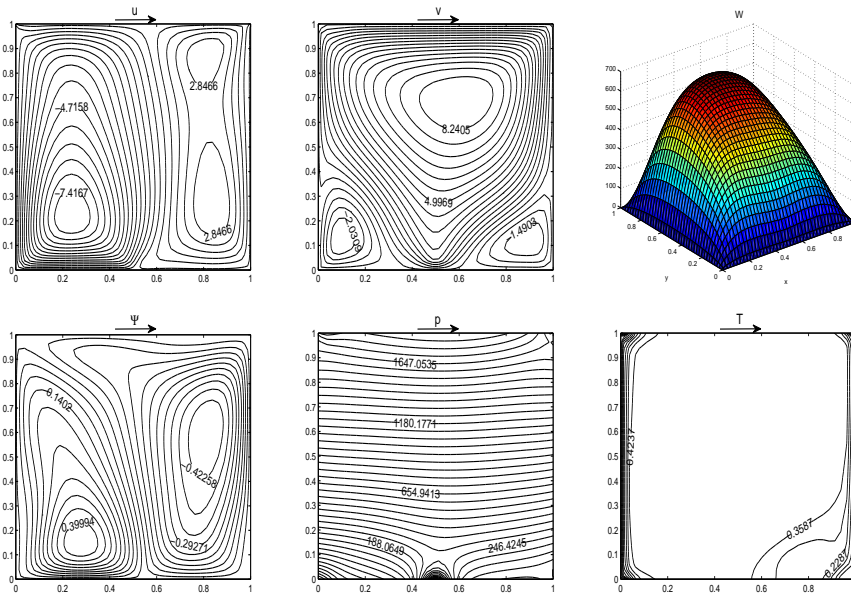


Figure 3.76: Forced convection flow in a lid-driven square cavity with horizontal adiabatic walls, viscous dissipation is included. $Mn = 80$, $Ra = 10^5$.

3.4.3 Forced convection flow in a square cavity with vertical adiabatic walls and point magnetic source

As a last case in the square cavity, the heat transfer is considered between the top and bottom walls. Thus, the square cavity is heated from the top and cooled from the bottom walls keeping the vertical walls adiabatic. The problem geometry and the boundary conditions are presented in Figure 3.77.

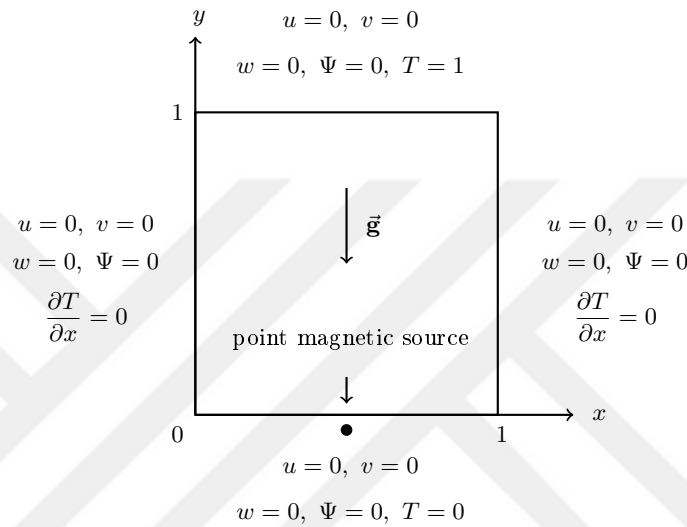


Figure 3.77: Forced convection flow in a square cavity with vertical adiabatic walls.

Pressure boundary conditions are obtained as explained in Section 3.4.1. The boundary is discretized with 160 constant elements, $\kappa = 0.05$ and $\tau = 0.05$ are taken. The number of constant elements is increased to 200 for the case of $Mn = 200$.

The effect of only buoyancy force is seen when $Mn = 0$ as observed from Figures 3.78-3.80. The buoyancy force divides the flow into two vortices with centers on $y = 0.5$ line. Pressure is highly concentrated at the top of the cavity showing a drop at the center. The u -velocity consists of four loops emanating from the corners and vertical velocity spreads through the cavity. The buoyancy force shifts the isotherms through the hot wall. Thus, an increase in the Rayleigh number, increases magnitudes of the planar velocities and pressure, and squeezes the isotherms through the hot wall.

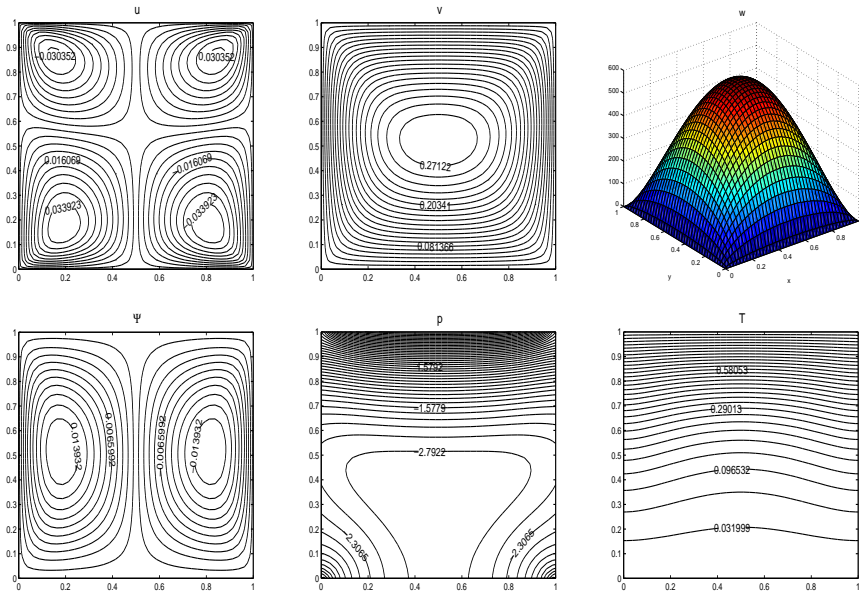


Figure 3.78: Forced convection flow in a square cavity with vertical adiabatic walls, viscous dissipation is neglected. $Ra = 10^3$, $Mn = 0$.

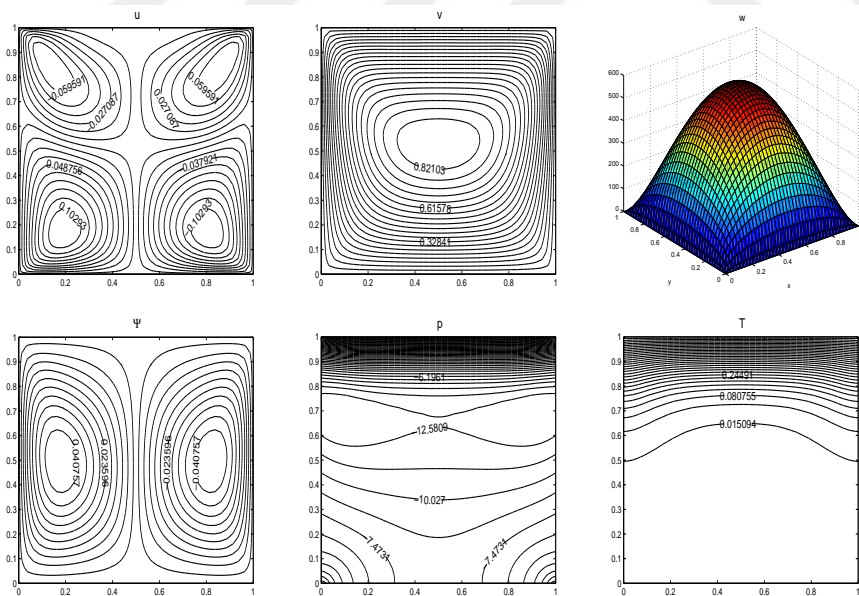


Figure 3.79: Forced convection flow in a square cavity with vertical adiabatic walls, viscous dissipation is neglected. $Ra = 10^4$, $Mn = 0$.

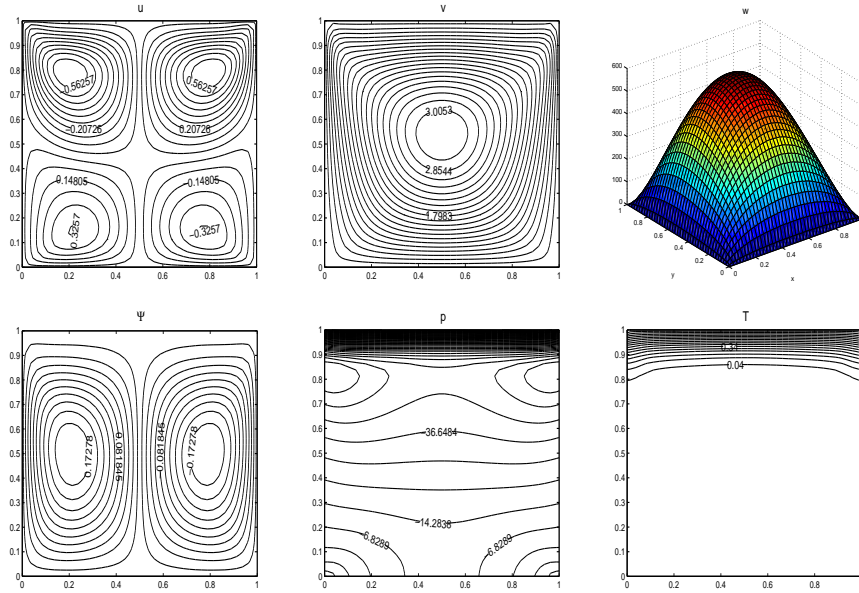


Figure 3.80: Forced convection flow in a square cavity with vertical adiabatic walls, viscous dissipation is neglected. $Ra = 10^5$, $Mn = 0$.

Figures 3.81-3.83 show the effect of the magnetic source on the flow profiles, pressure and the temperature of the fluid for $Mn = 5, 80, 200$ with $Ra = 0$. An increase in magnetic number causes an increase in the magnitude of the planar velocities and the pressure. The axial velocity shows, as expected, a flattening tendency around the point magnetic source and the pressure around the magnetic source extends through the cavity. Flow on the transverse plane is divided into two vortices rotating in opposite directions. A further increase in Mn moves the center of vortices through the magnetic source. The main effect of the point magnetic source below the cold wall is the cooling of the channel starting from the bottom wall. For values of $Mn \geq 80$ the fluid in the channel is completely cooled except a thin layer near the upper wall and secondary flows show up through bottom and top corners. The v -velocity shows the pushing effect of the magnetic point source and a thin boundary layer occurs just above and around the source.

The main effect of the magnetic source (and its increasing intensity) is to accelerate the fluid flow and increase the pressure on the fluid, and thus to cool down the channel through the upper wall. This is also the idea of cooling the head capsules of nuclear reactors.

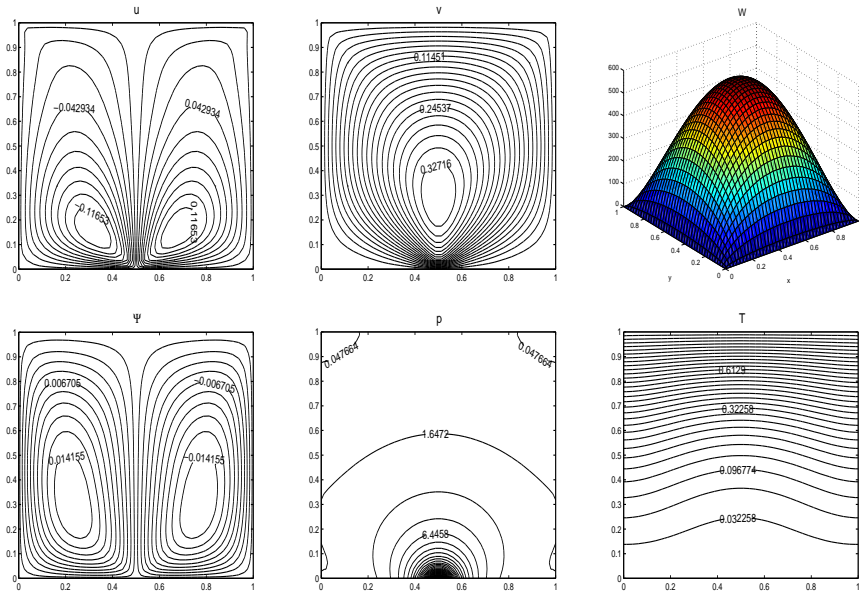


Figure 3.81: Forced convection flow in a square cavity with vertical adiabatic walls, viscous dissipation is neglected. $Ra = 0$, $Mn = 5$.

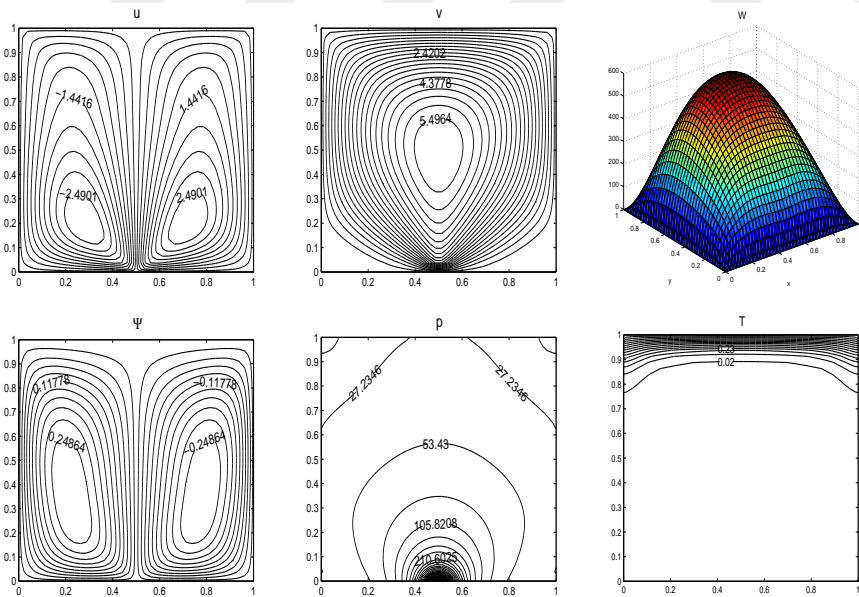


Figure 3.82: Forced convection flow in a square cavity with vertical adiabatic walls, viscous dissipation is neglected. $Ra = 0$, $Mn = 80$.

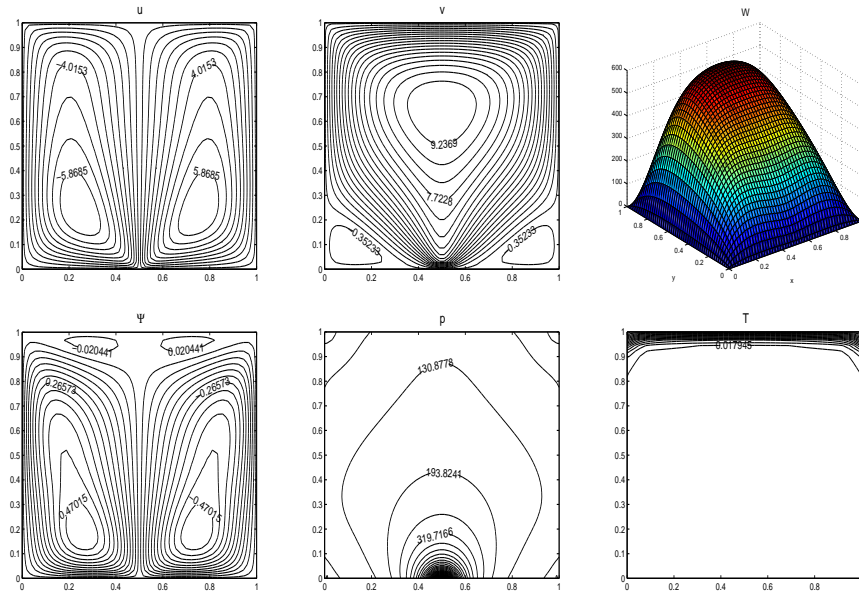


Figure 3.83: Forced convection flow in a square cavity with vertical adiabatic walls, viscous dissipation is neglected. $Ra = 0$, $Mn = 200$.

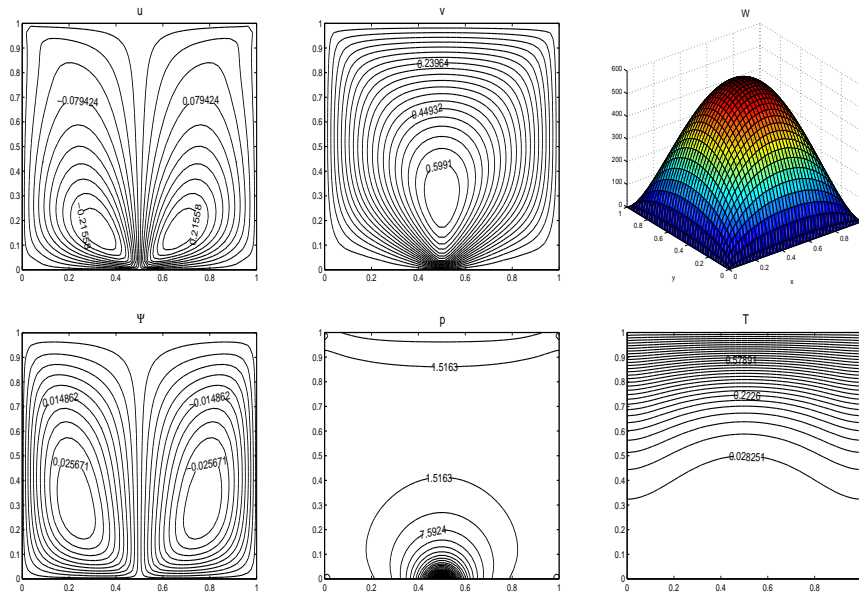


Figure 3.84: Forced convection flow in a square cavity with vertical adiabatic walls, viscous dissipation is neglected. $Mn = 10$, $Ra = 10^3$.

Both the buoyancy force and magnetic source effects are seen when $Mn = 10$ and $Ra = 10^3, 10^5$ in Figures 3.84, 3.85. For small Mn the buoyancy effect starts to dominate the flow as Ra increases. When $Ra \geq 10^4$ the thermal convection in the flow reduces the pushing effect of the magnetic source and viscous effect

is reduced.

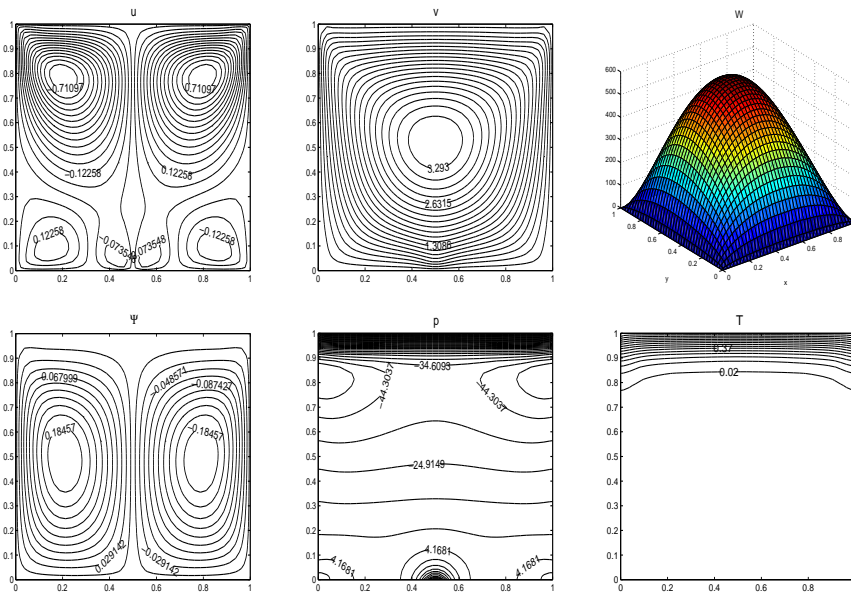


Figure 3.85: Forced convection flow in a square cavity with vertical adiabatic walls, viscous dissipation is neglected. $Mn = 10$, $Ra = 10^5$.

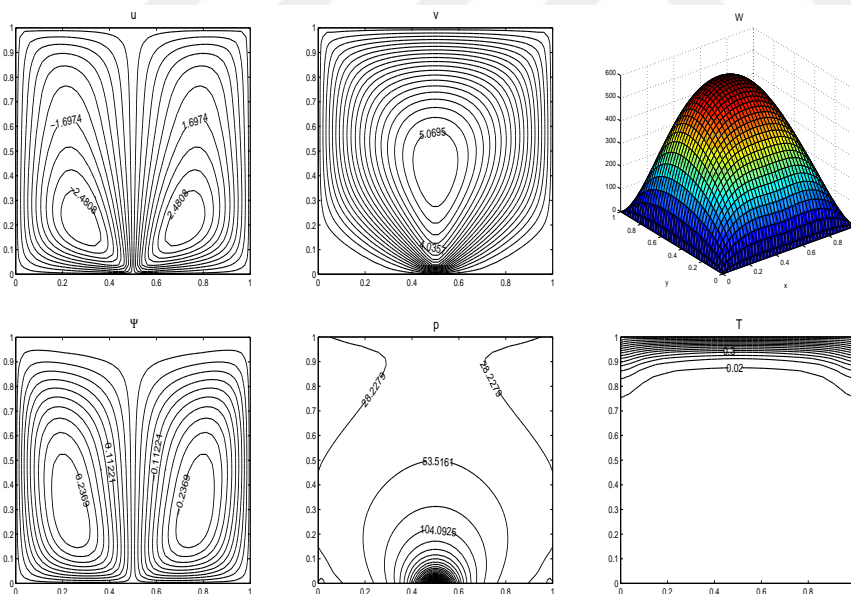


Figure 3.86: Forced convection flow in a square cavity with vertical adiabatic walls, viscous dissipation is neglected. $Mn = 80$, $Ra = 10^4$.

When the value $Mn = 80$ is reached (Figures 3.86-3.87) the magnetization force dominates the buoyancy force up to $Ra = 10^4$. The influence of buoyancy force is observed in streamlines and pressure as the center of vortices move upwards and pressure starts to concentrate close to the top heated wall. But with an increase in the magnetic number the cooling of the channel is much faster compared to an increase in Rayleigh number.

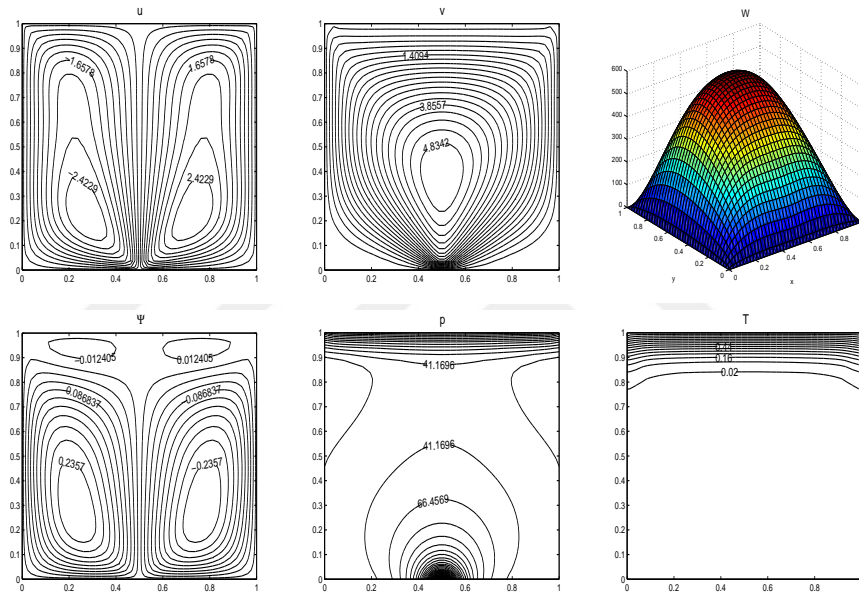


Figure 3.87: Forced convection flow in a square cavity with vertical adiabatic walls, viscous dissipation is neglected. $Mn = 80$, $Ra = 10^5$.

Figures 3.88 and 3.89 show the flow behavior and heat exchange of a biomagnetic dissipative viscous fluid. It is observed that, the viscous dissipation does not influence the flow and the heat transfer characteristics for small Rayleigh numbers. A slight difference is observed only when $Mn = 80$, $Ra = 10^5$ (See Figures 3.85, 3.88 and 3.87, 3.89).

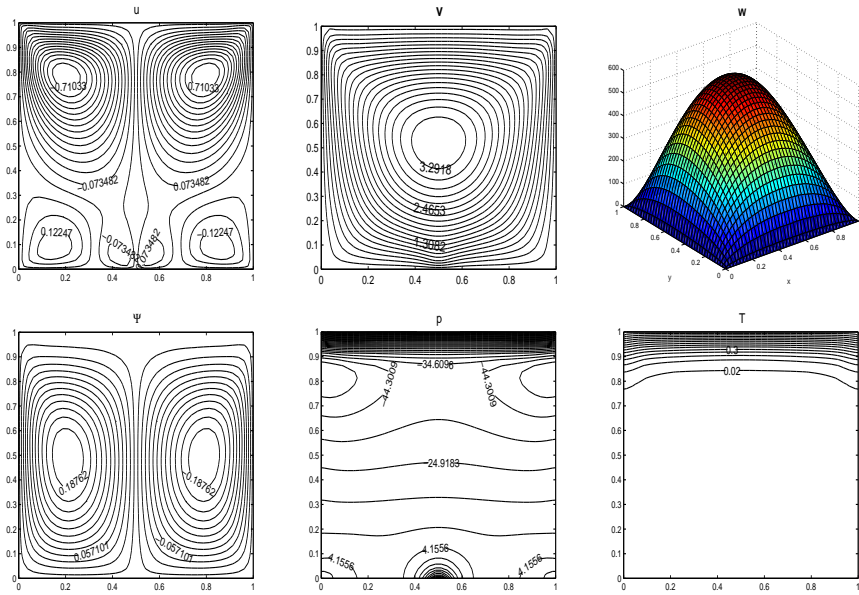


Figure 3.88: Forced convection flow in a square cavity with vertical adiabatic walls, viscous dissipation is added. $Mn = 10$, $Ra = 10^5$.

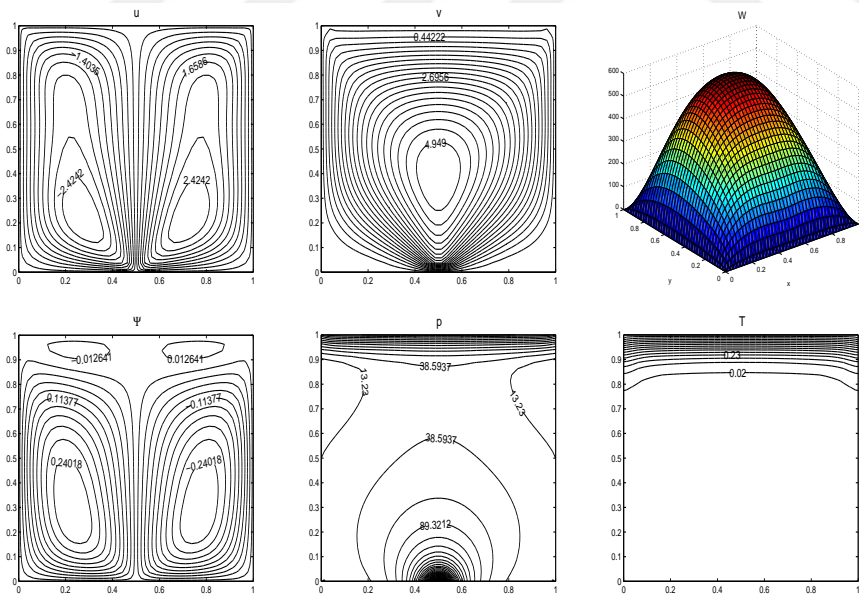


Figure 3.89: Forced convection flow in a square cavity with vertical adiabatic walls, viscous dissipation is added. $Mn = 80$, $Ra = 10^5$.

3.4.4 Forced convection flow in a circular cavity with point magnetic source

Finally, the problem of the blood flow and its temperature disturbance is studied in a circular cavity heated on the upper half wall which is a more realistic case. The flow configuration is presented in Figure 3.90.

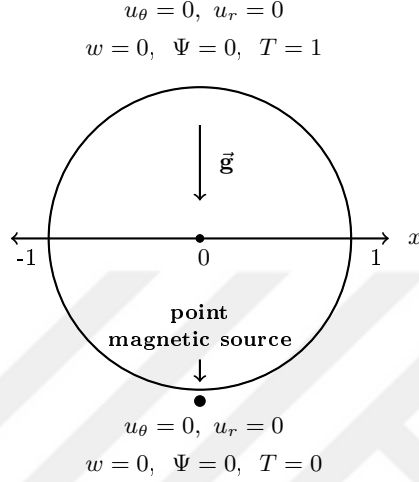


Figure 3.90: Forced convection flow in a circular cavity.

The pressure boundary conditions are approximated through the x - and y -components of the momentum equations using a forward difference for the pressure gradients and the DRBEM coordinate matrix \mathbf{F} for all the other derivative terms. Then, from the Figure 3.17,

$$\begin{aligned}
 p_{bd}^{(k+1)} = p_{int}^{(k)} + \Delta r \left((\mathbf{S}_I \mathbf{u}^{(k+1)} + Mn(T_c - T^{(k+1)})H \frac{\partial H}{\partial x})x \right. \\
 \left. + (\mathbf{S}_I \mathbf{v}^{(k+1)} + \frac{Ra}{Pr} T^{(k+1)} + Mn(T_c - T^{(k+1)})H \frac{\partial H}{\partial y})y \right)
 \end{aligned} \quad (3.71)$$

where

$$\mathbf{S}_I = \frac{\partial \mathbf{F}}{\partial x} \mathbf{F}^{-1} \frac{\partial \mathbf{F}}{\partial x} \mathbf{F}^{-1} + \frac{\partial \mathbf{F}}{\partial y} \mathbf{F}^{-1} \frac{\partial \mathbf{F}}{\partial y} \mathbf{F}^{-1} - \mathbf{u}^{(k+1)} \frac{\partial \mathbf{F}}{\partial x} \mathbf{F}^{-1} - \mathbf{v}^{(k+1)} \frac{\partial \mathbf{F}}{\partial y} \mathbf{F}^{-1}$$

with $u^{(k+1)}$, $v^{(k+1)}$ values on the diagonal matrices $\mathbf{u}^{(k+1)}$, $\mathbf{v}^{(k+1)}$.

The influence of buoyancy force is the acceleration of planar velocities as in the case of square cavity. The pressure is concentrated around the hot wall and the discontinuity points since there is no adiabatic wall. The cavity is nearly cooled down for $Ra \approx 10^4$ (Figures 3.91-3.92).

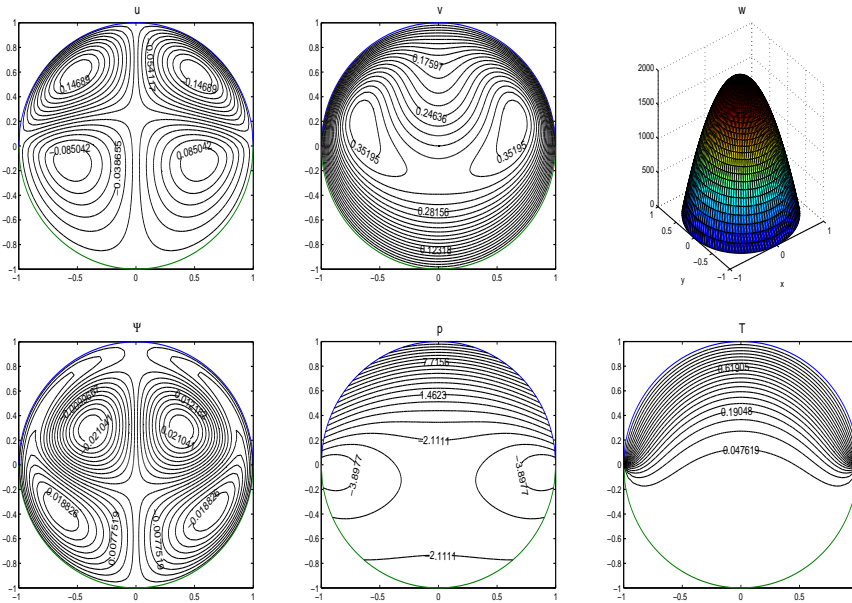


Figure 3.91: Forced convection flow in a circular cavity, viscous dissipation is neglected. $Mn = 0$, $Ra = 10^3$.

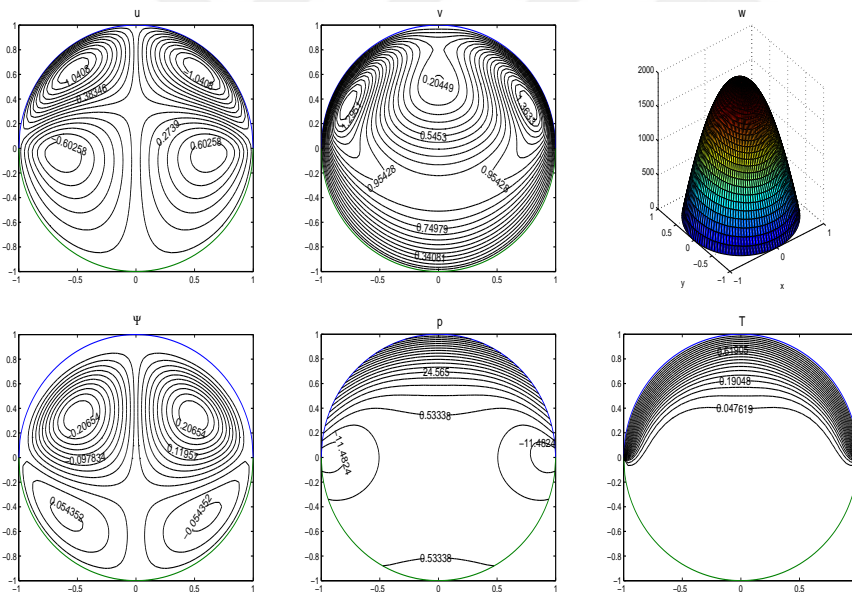


Figure 3.92: Forced convection flow in a circular cavity, viscous dissipation is neglected. $Mn = 0$, $Ra = 10^4$.

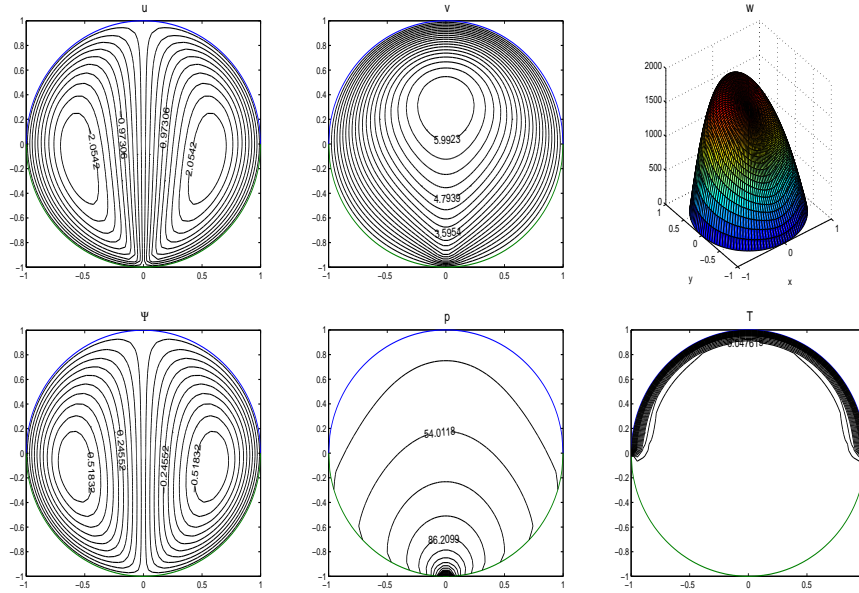


Figure 3.93: Forced convection flow in a circular cavity, viscous dissipation is neglected. $Mn = 10$, $Ra = 0$.

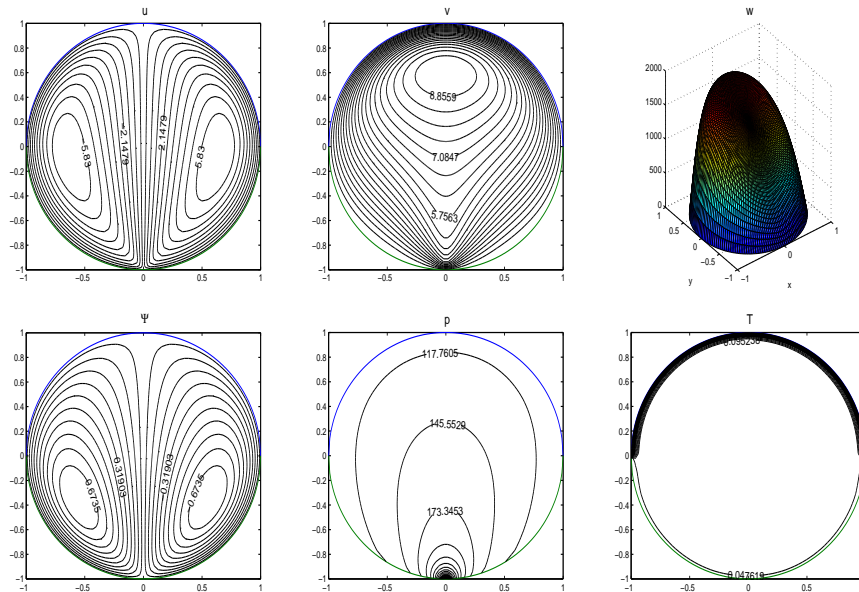


Figure 3.94: Forced convection flow in a circular cavity, viscous dissipation is neglected. $Mn = 30$, $Ra = 0$.

Figures 3.93-3.94 display the velocity, pressure and the temperature variations for increasing magnetic effect $Mn = 10, 30$ when $Ra = 0$. The flow behavior is similar to the square cavity case. Increasing magnetic field intensity accelerates the flow in the cavity and decelerates it in the axial direction. The heat transfers

directly between the hot and cold walls. Pressure increases and center of vortices move through the source point.

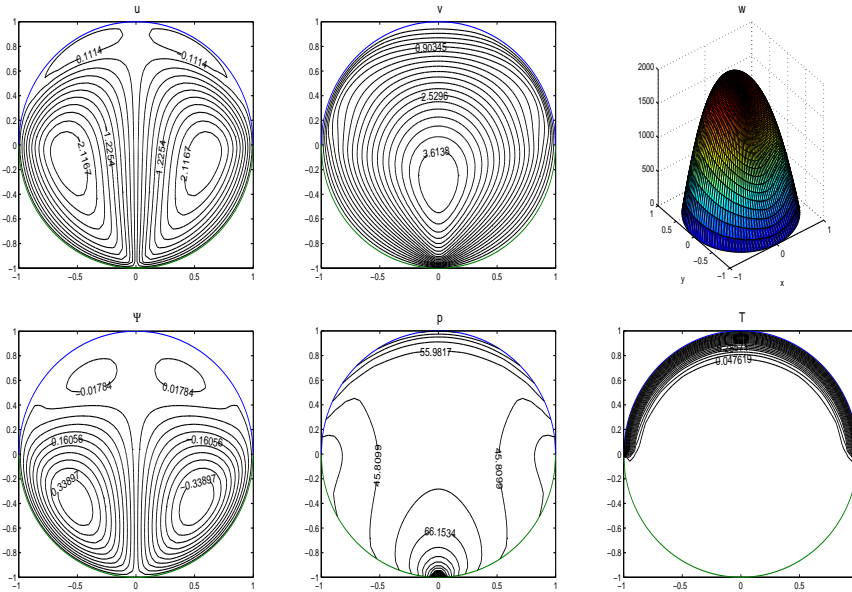


Figure 3.95: Forced convection flow in a circular cavity, viscous dissipation is neglected. $Mn = 10$, $Ra = 10^4$.

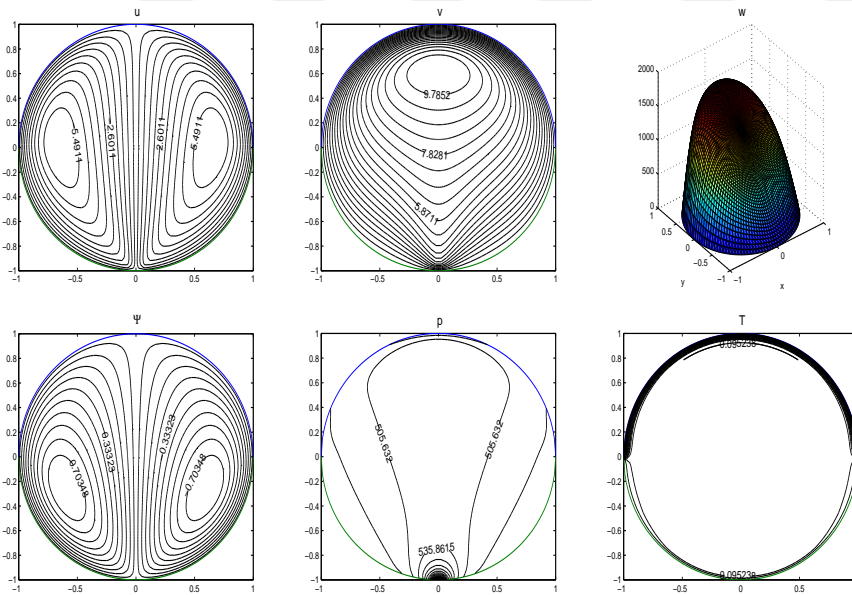


Figure 3.96: Forced convection flow in a circular cavity, viscous dissipation is neglected. $Mn = 50$, $Ra = 10^4$.

When both magnetic source and buoyancy force are present, the buoyancy force dominates the magnetization force when $Ra = 10^4$ is reached for small $Mn = 10$

(Figure 3.95). But, for larger Mn 's the blood flow and its heat exchange are under the control of magnetic source up to $Ra = 10^4$. (Figure 3.96)

The viscous dissipation effect on the flow in a circular cavity is not observed due to the sudden passage from the hot wall to the cold wall for the studied magnetic and Rayleigh number ranges. This is also the main difference in the flow and temperature between circular and square cavities.

In Chapter 3, the DRBEM solutions of the Stokes, incompressible and forced convection flows under the influence of magnetic source(s) are presented. Pressure driven, fully developed, laminar, steady flows of electrically non-conducting fluids are considered in long pipes with rectangular or circular cross-sections. The two-dimensional flows are studied in the cross-sections of the pipes. Numerical solutions are presented in terms of all problem variables (velocity, pressure and the temperature). The missing pressure boundary conditions are approximated by the use of FDM (finite difference method) and the DRBEM coordinate matrix. First, neglecting the convection terms in the momentum equations, Stokes equation is solved in cavities. The numerical solution procedure and the computer code are validated with the numerical solutions of Stokes flow in lid-driven square and circular cavities that are available in the literature. Then, the magnetization force generated by a point magnetic source is included forming one of the original part of this thesis. The interaction between the magnetization force and the moving boundary is investigated. Also, a comparison for the magnetization force effect in square and circular cavities is given. The obtained numerical results reveal that:

- Discretization of the boundary with constant or linear elements does not bring a significant change in the flow profiles.
- When the point magnetic source is placed below the cavity on the symmetry axis, the arose magnetization force pushes the fluid upwards dividing the flow into two vortices which are rotating in opposite directions. Pres-

sure is highly concentrated around the point source.

- An increase in the magnetic number accelerates the flow and increases the pressure in the cavity.
- The influence of the magnetization force is high in circular cavities than in square cavities due to the disturbances coming from the corners of the square cavity.

Second, the convection terms are added to the momentum equations and the full Navier-Stokes equations with the magnetization force terms are studied. As a difference, the pressure equation is also derived and added to the system of equations to see its effect also on the flow which was not considered in the previous studies in the literature. The DRBEM enables one to easily handle the nonlinearities in the convection terms. The influence of the magnetization force in the axial velocity profile is also studied. The numerical results presented for square, circular cavities and annular pipes show that:

- In the presence of the magnetic field, flow starts to develop on the transverse plane and the axial velocity magnitude decreases around the point magnetic source due to the conversion of the kinetic energy in the axial direction to the kinetic energy on the transverse plane.
- As the magnetic number increases the flow Reynolds number decreases depending on the axial velocity.
- In order to obtain similar behaviors in Stokes and incompressible flows $M = Mn/Re$ has to be higher for Stokes flow than for the incompressible flow. This may be caused by the high viscosity of the Stokes fluid.
- The existence of an obstacle in the cavity disturbs the flow due to the magnetization force and two additional eddies are attached to the obstacle horizontally.

Third, the effect of multiple magnetic sources placed oppositely or below the rectangular cavities is taken into consideration. The numerical simulations display that:

- Increasing the number of wires forms secondary flows in front of the sources.
- The axial flow retardation in the square cavity occurs for smaller magnetic numbers in two sources case than in the single source case due to the combined effects of multiple sources.
- Location of sources oppositely, preserves the symmetry with respect to the horizontal and vertical center lines.

Lastly, the energy equation is added to the system of Navier-Stokes equations. The numerical solution procedure is validated with the natural convection flow of air. The connection between the magnetization and buoyancy forces is analyzed on the blood flow with different combinations of wall temperature conditions. The action of the viscous dissipation in the energy equation is also investigated for increasing values of Mn and Ra . The obtained results show that:

- When the point source is below the adiabatic wall the main effect of the point magnetic force is to keep the center of the cavity at nearly a constant temperature.
- When the point magnetic source is placed below the cold wall the main influence of the magnetization and buoyancy forces is the cooling of the channel.
- Increasing magnetization force is more effective than increasing the buoyancy force for cooling of the cavity.
- The viscous dissipation effect can only be observed when both Mn and Ra are high.
- The cavity cools down quicker in the circular cavity than in the square cavity.

The condition numbers of the coefficient matrices of the system of equations in the FHD Stokes and incompressible flow problems are in the moderate range that they do not cause difficulties in obtaining the solutions when the number of

boundary elements is at most 160. The condition number becomes large when the energy equation is combined as FHD forced convection incompressible flow. However, the solution can be obtained in the expense of long computational time.

In the next chapter the slip velocity condition on the MHD flows will be studied.



CHAPTER 4

MHD FLOW IN DUCTS AND BETWEEN PARALLEL PLATES WITH SLIP CONDITIONS

In this chapter, the DRBEM solutions of MHD flows in ducts and between parallel plates with slip boundary condition for the velocity are presented. MHD covers the fluid mechanics and the electrodynamics areas, investigating the flow of electrically conducting fluids under the influence of magnetic field. An electric current is induced in the fluid by the magnetic field and generates an electromagnetic force so called Lorentz force. In MHD flows the walls perpendicular to the applied magnetic field are called Hartmann walls and the walls parallel to the magnetic field are the side walls. MHD duct flows with no-slip velocity conditions are known to exhibit boundary layers. Hartmann layers, at the Hartmann walls, whose thickness δ_{Ha} scales with $1/Ha$ and side layers, at the side walls, whose thickness δ_s scales with $1/\sqrt{Ha}$ are formed where Ha is the Hartmann number. Due to the coupling of the governing equations in MHD flow in ducts, analytical solutions can be obtained only for special boundary conditions such as insulated walls or perfectly conducting walls or two opposite insulated walls with the other two conducting. The velocity has no-slip boundary condition in these analytical studies [18] under the assumption of good wettability at the fluid-solid interface. On the contrary, in the case of surface roughness as the flow over hydrophobic surfaces, in microfluidic devices and thin film dynamics fluid has slipping velocity relative to the fluid-solid interface and the hydrodynamic slip condition has to be imposed. The slip in MHD flow may occur in fusion applications containing liquid metal flows in contact with ceramics, as current experimental data suggests [86]. The slip length can be comparable or even larger than the Hartmann layer in strong magnetic field applications. This

may result in a dramatic impact on the MHD pressure drop and heat transfer enhancement. The degree of the slip is quantified through the slip length L_s which is the distance from the fluid to the surface within the solid phase where the extrapolated flow velocity vanishes [62]. In the presence of the slip, the boundary condition at the liquid-solid interface is given in terms of the slip length and the tangential stress as

$$U_s = L_s \frac{dU}{dn}. \quad (4.1)$$

where U_s is the slip velocity.

The influence of slip on the velocity of the fluid is measured by

$$\bar{s}_1 = \frac{L_s}{\delta_s} \text{ (on the side walls)} \quad \text{and} \quad \bar{s}_2 = \frac{L_s}{\delta_{Ha}} \text{ (on the Hartmann walls)}. \quad (4.2)$$

For each problem presented in this chapter the discretized system of equations in terms of velocity and the induced magnetic field are combined into a large system and solved in one stroke. In the numerical solution process, linear radial basis functions are employed for the approximation of inhomogeneities in the Poisson's type of equations.

The problems considered in this chapter are listed in Table 4.1.

Table 4.1: Problems considered in Chapter 4.

4.1.1	MHD duct flow-Problem 1 (slip at the side walls)
4.1.2	MHD duct flow-Problem 2 (slip at the insulated Hartmann walls)
4.1.3	MHD duct flow-Problem 3 (slip at the perfectly conducting Hartmann walls)
4.1.4	MHD duct flow-Problem 4 (slip at all of the duct walls)
4.2.1	Problem 1, $d = 0$ case (perfectly conducting walls)
4.2.2	Problem 1, $d = 1$ case (insulated portion at the perfectly conducting walls)
4.2.3	Problem 2, $d = 0$ case (insulated Hartmann walls)
4.2.4	Problem 2, $d = 1$ case (perfectly conducting portion at the insulated walls)
4.3.1	Case 1: $s_2 = 0$, electrode length $l = 0$, Ha increases
4.3.2	Case 2: $l = 0$, $Ha = 10$, s_2 varies as $s_2 < 1$, $s_2 = 1$, $s_2 > 1$
4.3.3	Case 3: $s_2 = 0$, $Ha = 50$, l varies as $l = 0.1, 0.3, 0.5$
4.3.4	Case 4: $Ha = 10$, s_2 varies as $s_2 < 1$, $s_2 = 1$, $s_2 > 1$ and l varies as $l = 0.3, l = 0.5$
4.3.5	Electric potential computations

4.1 MHD Duct Flow with Slipping Walls

In this section, pressure driven, fully developed flow of an electrically conducting fluid is considered in a long rectangular pipe with square cross-section. The flow in the axial direction is influenced by a horizontally applied uniform magnetic field $\mathbf{B} = B_0 \mathbf{e}_x$ and either Hartmann walls or side walls of the duct admit slip. The flow configuration is presented in Figure 4.1.

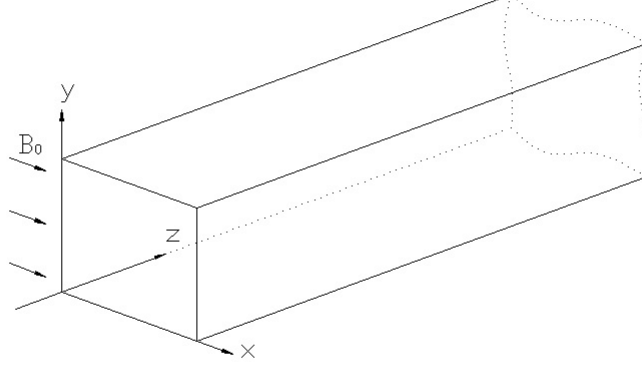


Figure 4.1: Flow configuration of MHD duct flow subjected to a horizontally applied uniform magnetic field.

The DRBEM discretized equations (2.127) and the numerical solution procedure are given in Section 2.6 as

$$\begin{aligned} \mathbf{H}V - \mathbf{G} \frac{\partial V}{\partial n} &= -(\mathbf{H}\hat{\mathbf{U}} - \mathbf{G}\hat{\mathbf{Q}})\mathbf{F}^{-1}\left\{Ha \frac{\partial B}{\partial x} + 1\right\} \\ \mathbf{H}B - \mathbf{G} \frac{\partial B}{\partial n} &= -(\mathbf{H}\hat{\mathbf{U}} - \mathbf{G}\hat{\mathbf{Q}})\mathbf{F}^{-1}\left\{Ha \frac{\partial V}{\partial x}\right\}. \end{aligned} \quad (4.3)$$

where $V(x, y)$ and $B(x, y)$ are the velocity and the induced magnetic field in the pipe-axis direction, respectively, and they have variations in the cross-section of the pipe $\Omega = \{(x, y) : -1 \leq x \leq 1, -1 \leq y \leq 1\}$.

The slip wall effects on the flow velocity and induced magnetic field profiles are investigated for various values of Hartmann number ($1 \leq Ha \leq 100$) and non-dimensional slip ratios

$$s_1 = \alpha\sqrt{Ha} \text{ (on the side walls)}, \quad s_2 = \alpha Ha \text{ (on the Hartmann walls)} \quad (4.4)$$

covering the cases $s_i = 0$, $s_i < 1$ and $s_i > 1$ for $i = 1, 2$. Here, $\alpha = \frac{L_s}{L}$ is the dimensionless slip ratio where L is the half-height of the duct. Various combinations of wall conductivities and slip conditions are considered and the

boundaries of the cavities are discretized with $N = 320 - 400$ constant elements. For small and moderate Hartmann numbers a uniform distribution of boundary elements are used. In the case of high Hartmann numbers especially for $Ha = 100$ and even for $Ha = 50$, in some test problems, a finer discretization near the corners of the cavity is needed in order to obtain smooth solutions. The numerical procedure is validated with the analytical solutions of Problem 1 and Problem 2 given by Ligere et al. [63] and Smolentsev [62], respectively, in terms of infinite series. The general case of all the walls admitting slip, requires a numerical or asymptotic approach [62].

4.1.1 MHD duct flow - Problem 1

In Problem 1, the side walls are insulated and exhibit slip. Hartmann walls are the no-slip and perfectly conducting walls (Figure 4.2).

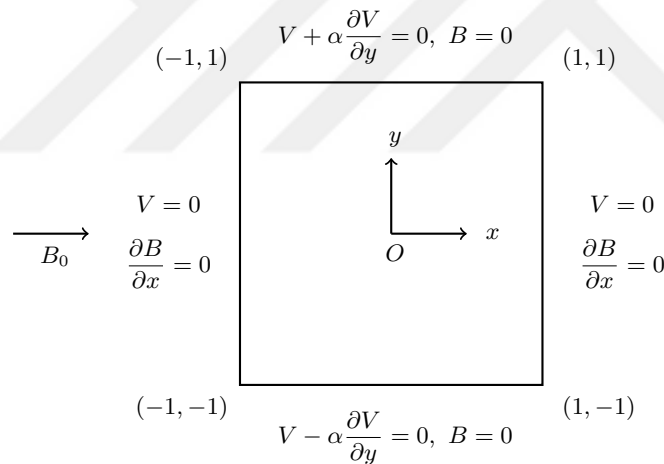


Figure 4.2: MHD duct flow - Problem 1

The obtained results are validated first with the ones presented in [63], and they are in very well agreement. In Figure 4.3 the velocity profiles V/V_m on various lines perpendicular to the magnetic field are presented for Hartmann numbers $Ha = 10, 100$, and slip lengths $\alpha = 0.04$ ($s_1 < 1$), $\alpha = 0.4$ ($s_1 > 1$) where V_m is the mean bulk velocity of the flow. It is found that, the velocity of the fluid increases with an increase in the slip length and the slip is more significant when $s_1 > 1$ and as Ha increases.

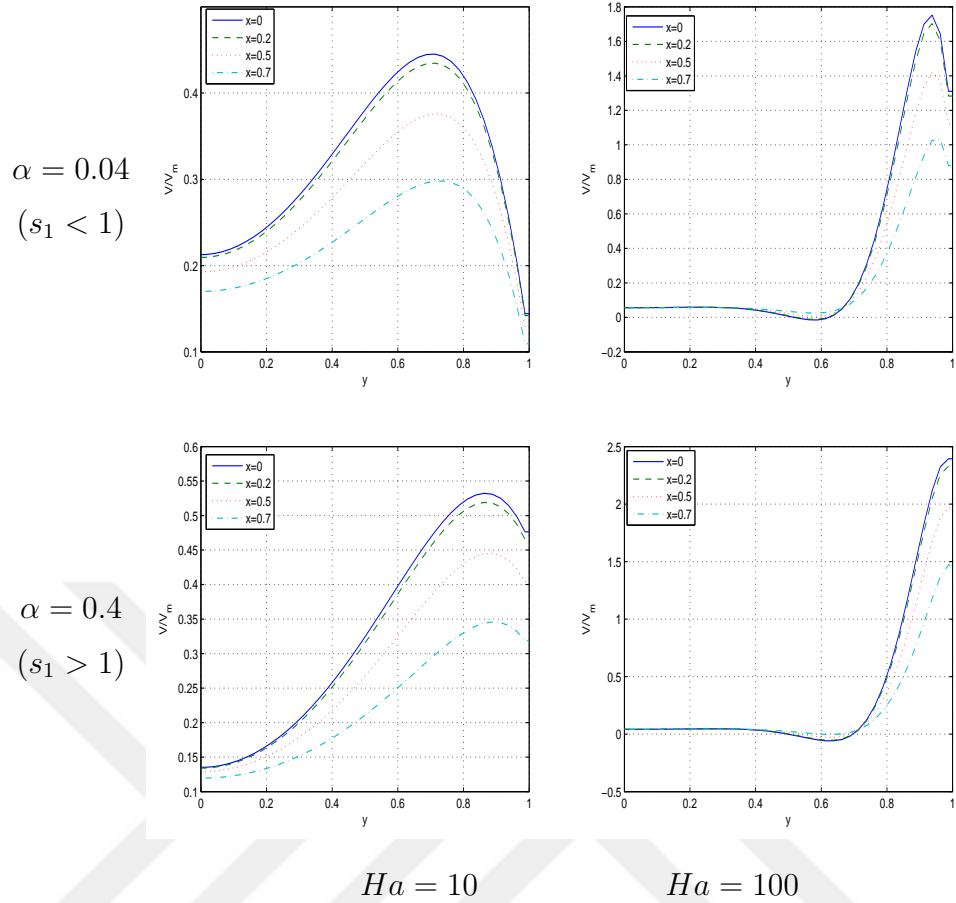


Figure 4.3: MHD duct flow -Problem 1; Velocity profiles on $x = 0$, $x = 0.2$, $x = 0.5$, $x = 0.7$.

Figure 4.4 shows equivelocity and the induced current lines for the slip ratios $s_1 = 0$, $s_1 < 1$ and $s_1 > 1$ for increasing values of Ha . From the profiles one can notice that, the slip at the side walls is negligible when $s_1 < 1$ and significant when $s_1 > 1$. The velocity boundary layers (Hartmann layers) on the vertical walls nearly diminish and the fluid flows in terms of two separated vortices in front of the side walls leaving the center of the cavity almost stagnant for increasing values of Ha . Boundary layers of order $1/\sqrt{Ha}$ on the side walls are developed for $s_1 < 1$. With the same slip length, as Ha increases the flow decelerates, the induced magnetic field decreases and develops boundary layers near the side walls. This is the well-known flattening tendency of the flow due to the external magnetic effect. As the slip length advances the thickness of the vortices stays the same, but the side layers become thinner and are diminished for $s_1 > 1$.

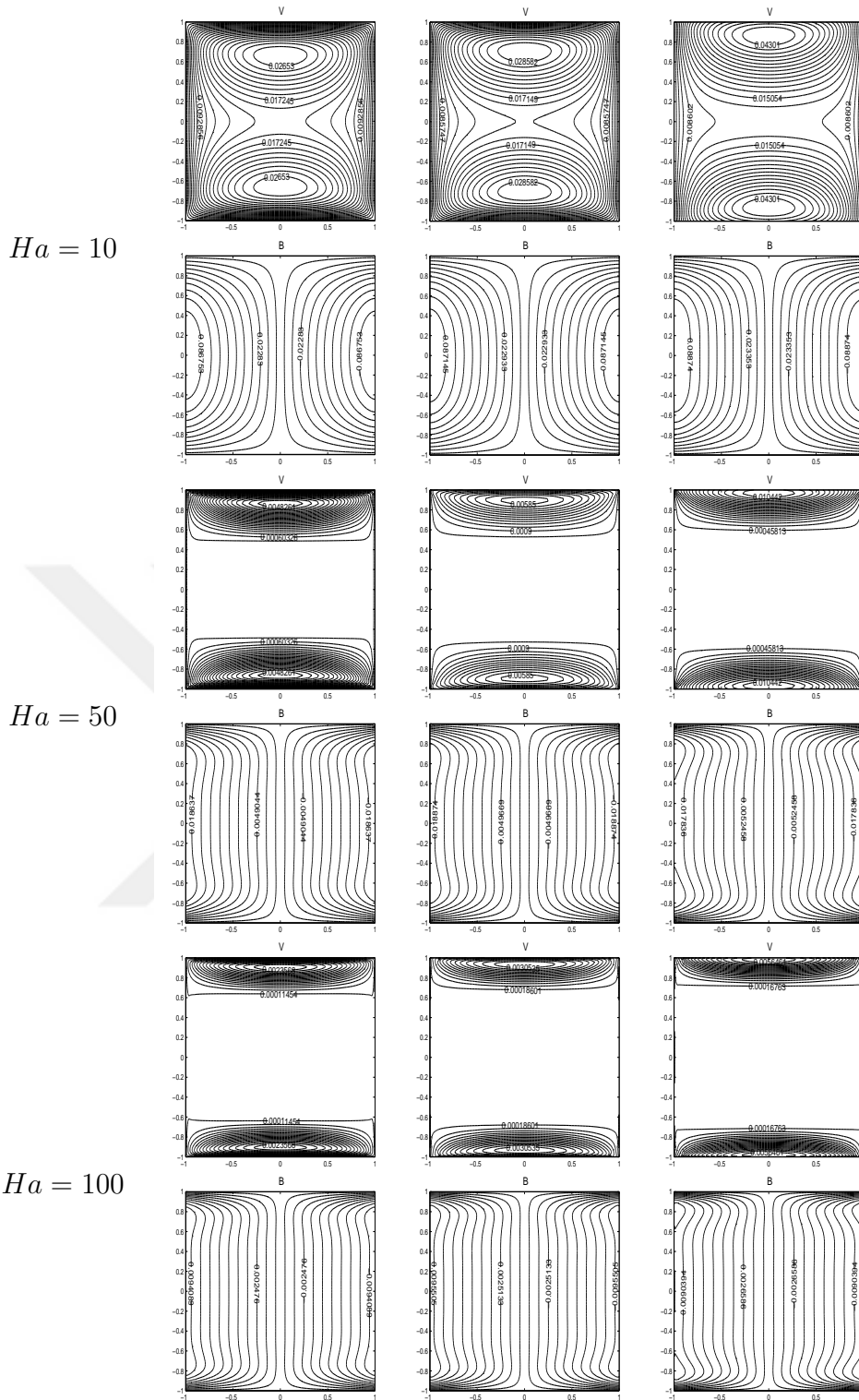


Figure 4.4: MHD duct flow-Problem 1; Velocity and induced magnetic field profiles for varying Hartmann numbers. $\alpha = 0$ ($s_1 = 0$) left, $\alpha = 0.04$ ($s_1 < 1$) center, $\alpha = 0.4$ ($s_1 > 1$) right.

In Figure 4.5 velocity level curves are presented for $Ha = 10, 50, 100$ and $\alpha = 0.04$ ($s_1 < 1$), $\alpha = 0.4$ ($s_1 > 1$). As is shown in [63] an increase in the slip length increases the magnitude of the velocity around the side layers.

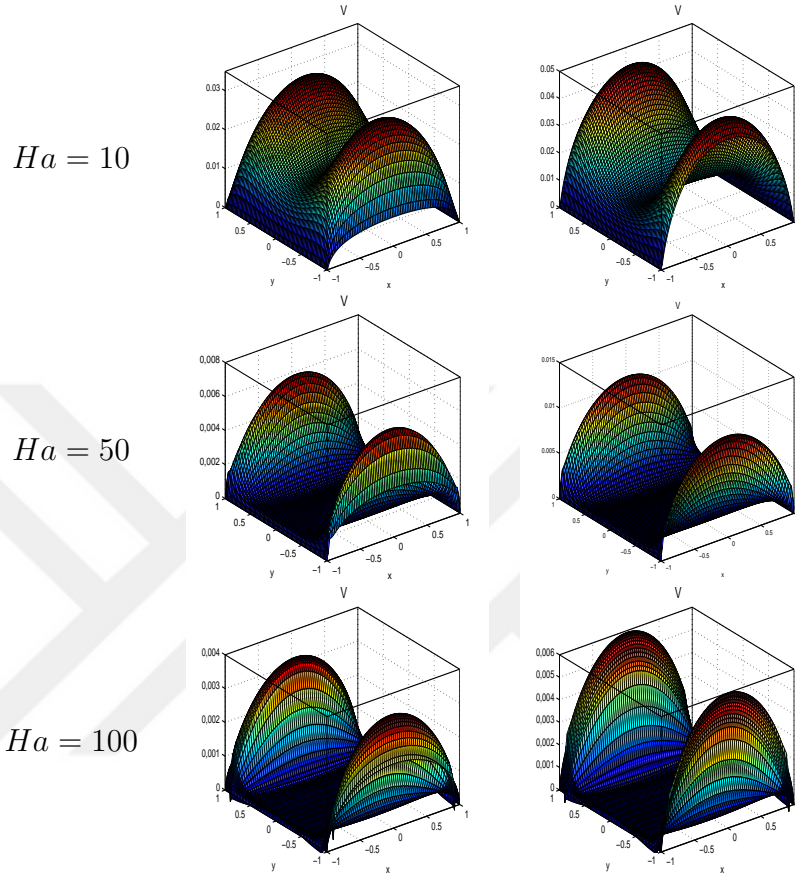


Figure 4.5: MHD duct flow -Problem 1; Velocity level curves for varying Hartmann numbers. $\alpha = 0.04$ ($s_1 < 1$) left, $\alpha = 0.4$ ($s_1 > 1$) right.

4.1.2 MHD duct flow - Problem 2

In Problem 2, Hartmann walls have the slip velocity condition and all the walls are electrically insulated. The problem domain and the boundary conditions are displayed in Figure 4.6

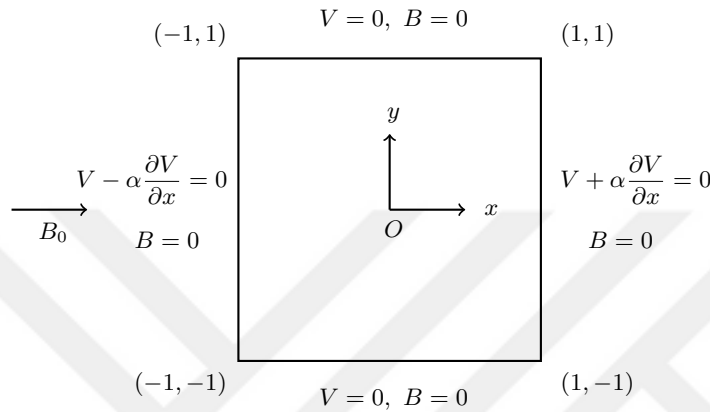


Figure 4.6: MHD duct flow - Problem 2

In Figure 4.7 and Figure 4.8 the velocity and the induced magnetic field contours and the velocity level curves are displayed, respectively, for $Ha = 10, 50, 100$ and $\alpha = 0$ ($s_2 = 0$), $\alpha = 0.001$ ($s_2 < 1$), $\alpha = 0.2$ ($s_2 > 1$). The velocity level curves and the induced magnetic field contours are in good agreement with the ones obtained in [62]. The numerical results show that, as the slip ratio advances, side layers get thicker, the flow at the core region where the fluid is stagnant shrinks and the velocity increases in magnitude. The core region enlarges and the flow decelerates as Ha increases. When $s_2 \gg 1$, the flow is fully controlled with the slip phenomenon and the induced magnetic field magnitude slightly decreases. If $s_2 \ll 1$, then the flow is similar to the corresponding MHD flow without slip. When $s_2 \approx 1$, then both MHD and slip effects are important as was observed in [62]. When both Ha and s_2 increase, Hartmann layers are almost diminished. Boundary layer development in front of the side walls for the induced magnetic field and $Ha > 10$ are weakened when $s_2 > 1$.

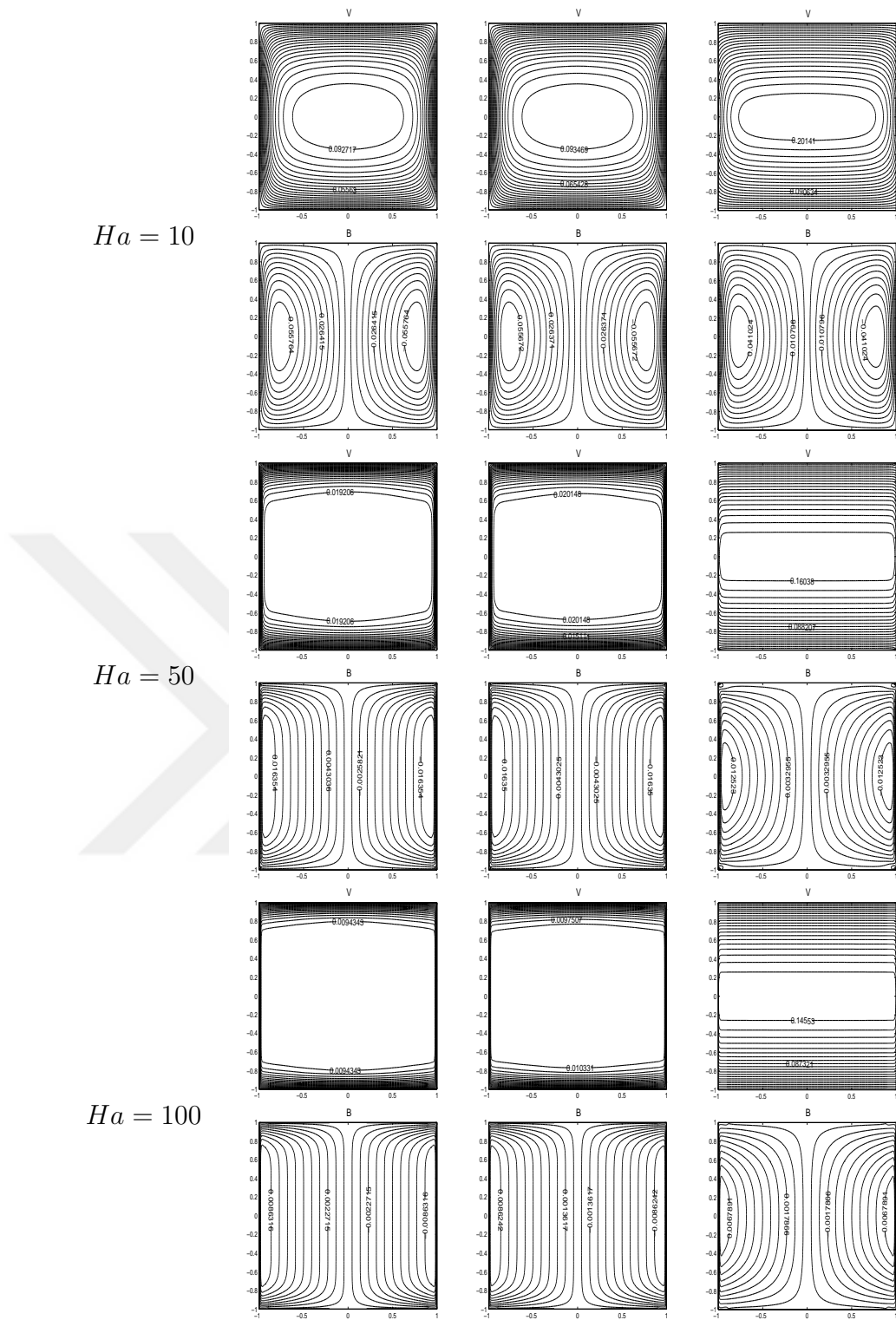


Figure 4.7: MHD duct flow -Problem 2; Velocity and induced magnetic field profiles for varying Hartmann numbers. $\alpha = 0$ ($s_2 = 0$) left, $\alpha = 0.001$ ($s_2 < 1$) center, $\alpha = 0.2$ ($s_2 > 1$) right.

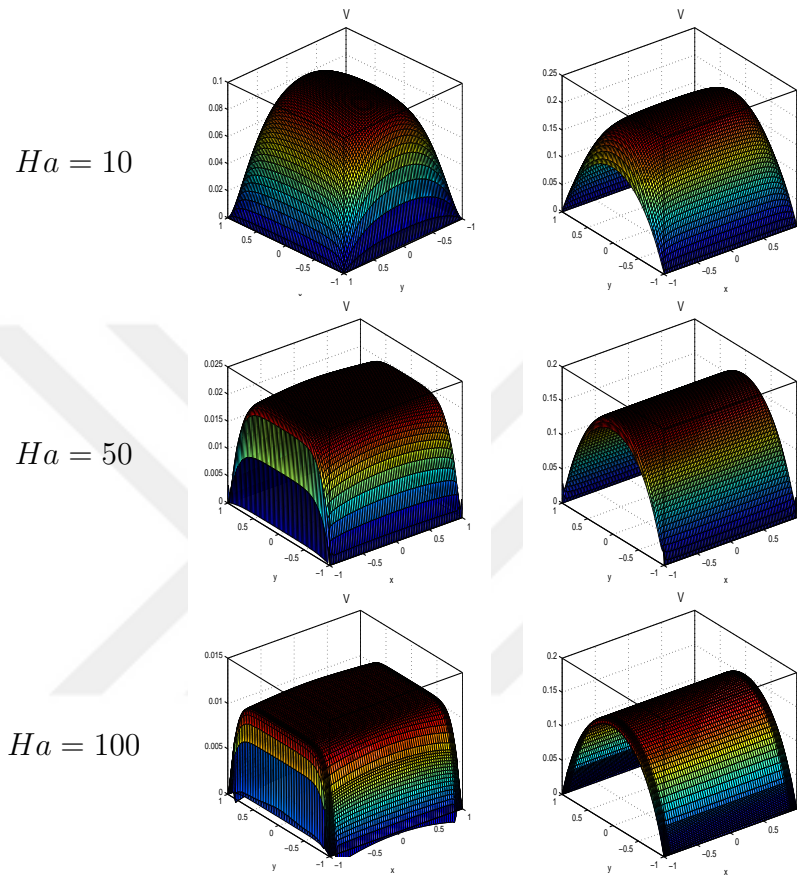


Figure 4.8: MHD duct flow - Problem 2; Velocity level curves for varying Hartmann numbers. $\alpha = 0.001$ ($s_2 < 1$) left, $\alpha = 0.2$ ($s_2 > 1$) right.

4.1.3 MHD duct flow - Problem 3

In this problem, the aim is to see the effects of both the slip and the perfectly conducting Hartmann walls on the flow behavior (Figure 4.9).

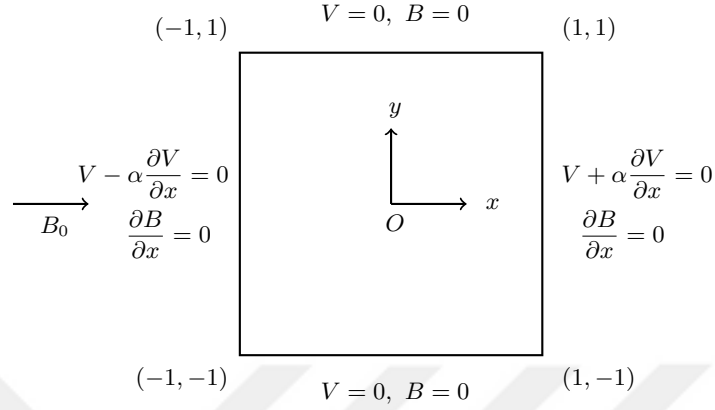


Figure 4.9: MHD duct flow - Problem 3

Figure 4.10 and Figure 4.11 present the velocity, the induced magnetic field profiles and the velocity level curves for $Ha = 10, 50, 100$ and $\alpha = 0$ ($s_2 = 0$), $\alpha = 0.001$ ($s_2 < 1$), $\alpha = 0.4$ ($s_2 > 1$). As was observed in Problem 2, as the slip ratio increases the side layers thicken, the velocity at the core region increases and the induced magnetic field decreases especially for $s_2 > 1$. The influence of the slip is observed significantly when $s_2 > 1$. For small values of Ha ($Ha = 10$) and $s_2 > 1$, fluid flows in terms of one main flow showing the strong effect of the slip on the Hartmann walls. As Ha increases the flow is again concentrated symmetrically in front of the side walls and the slip can be observed for much greater values of s_2 . Hartmann layers are almost diminished when both the Hartmann number and the slip ratio are large.

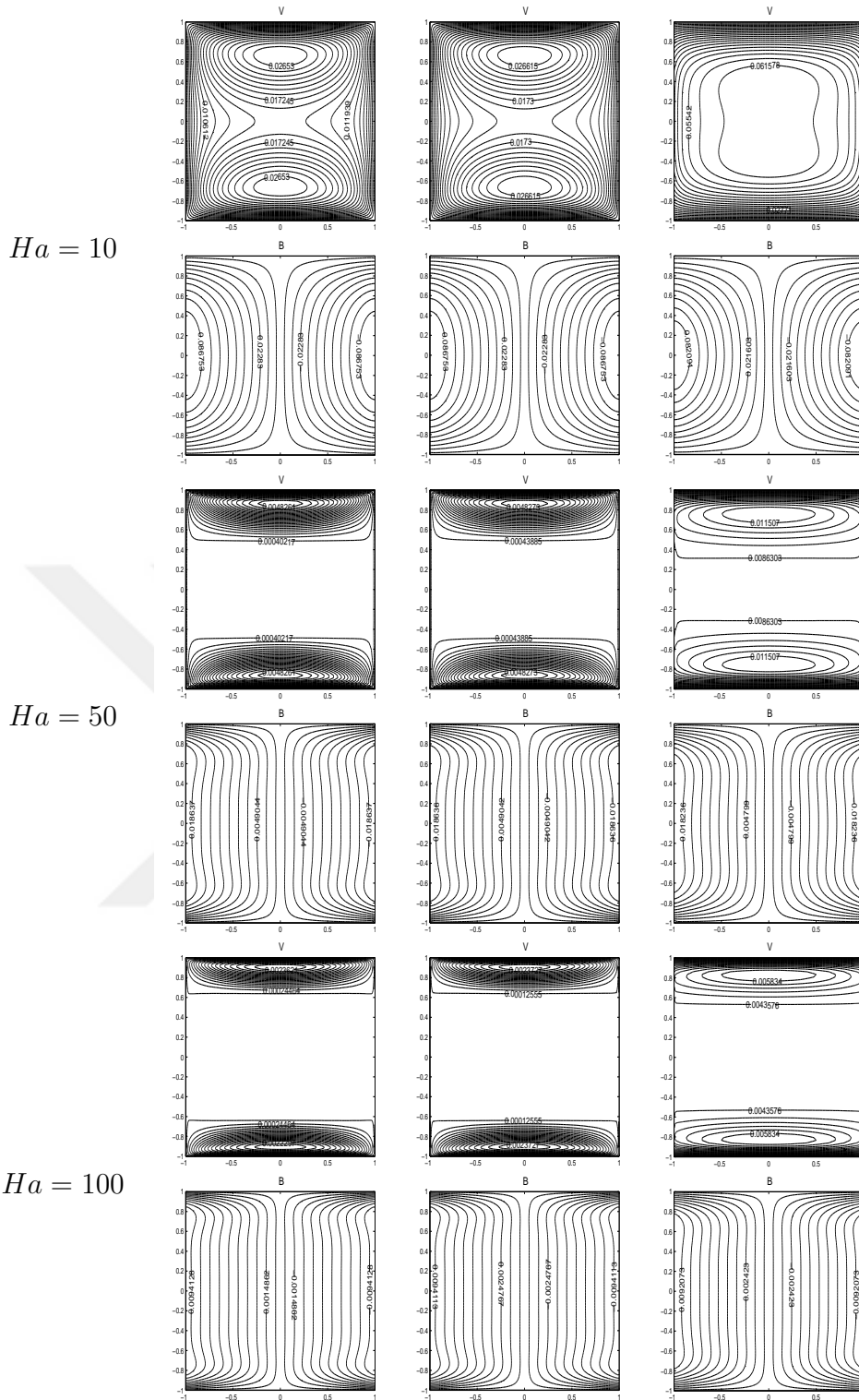


Figure 4.10: MHD duct flow -Problem 3; Velocity and induced magnetic field profiles for varying Hartmann numbers. $\alpha = 0$ ($s_2 = 0$) left, $\alpha = 0.001$ $s_2 < 1$ center, $\alpha = 0.4$ $s_2 > 1$ right.

From Figure 4.11 one can notice that when $s_2 < 1$ the flow reaches its maximum magnitude very close to the side walls developing sharp peaks and leaving the core region stagnant. However, when $s_2 > 1$ the fluid is still in action in the central part of the cavity dropping to no-slip side walls suddenly with the effect of the slipping Hartmann walls.

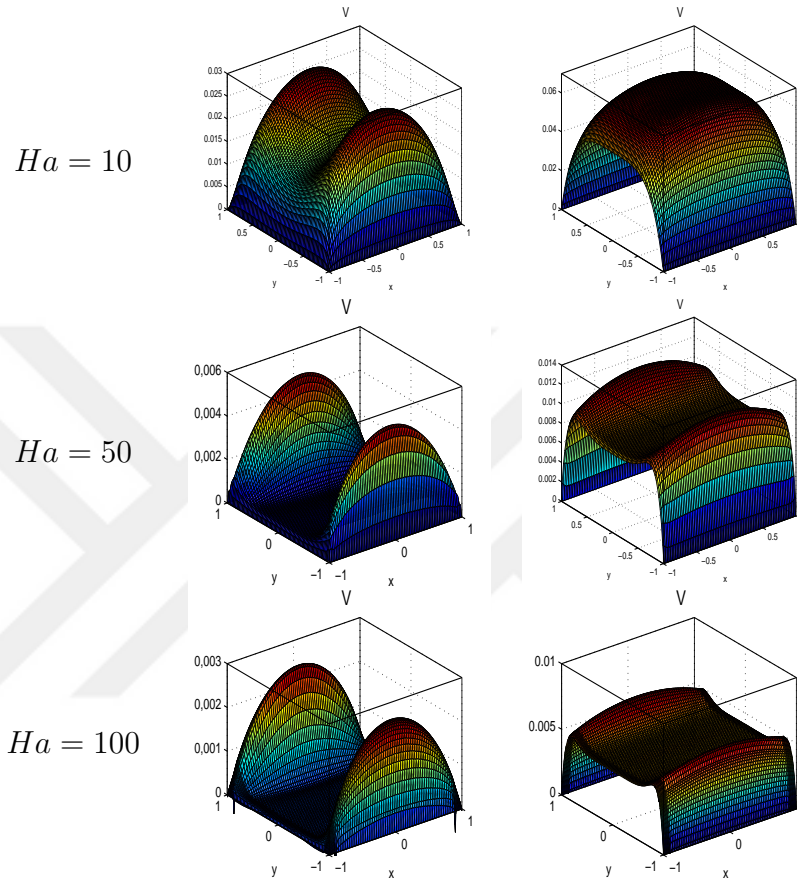


Figure 4.11: MHD duct flow-Problem 3; Velocity level curves for varying Hartmann numbers. $\alpha = 0.001$ ($s_2 < 1$) left, $\alpha = 0.4$ ($s_2 > 1$) right.

4.1.4 MHD duct flow - Problem 4

Finally, the influence of the slip on the flow and the induced magnetic field is analyzed by taking the slip velocity on all of the duct walls with the same slip length α . The side walls are perfectly conducting and the Hartmann walls are insulated (Figure 4.12).

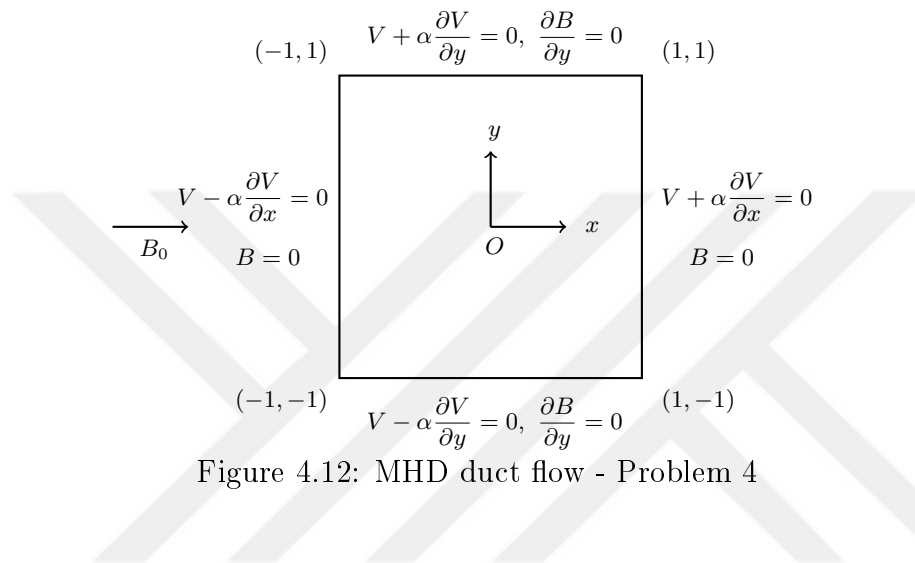


Figure 4.12: MHD duct flow - Problem 4

The velocity and the induced magnetic field profiles are presented in Figure 4.13 and Figure 4.14. The numerical results reveal that, in the case of small and moderate Hartmann numbers, the slip is visible at all of the walls although it is weak on the side walls. However, when Hartmann number is increased, slip can not be observed on the side walls even for $s_1 > 1$ and still observed on the Hartmann walls as $s_2 > 1$. When both the Ha and the slip lengths are increased, Hartmann layers are lost and the slip is nearly diminished on the side walls due to the increase in the side wall boundary layer thickness. Since the slip ratios are different on the side and the Hartmann walls ($s_1 = \alpha\sqrt{Ha}$ and $s_2 = \alpha Ha$, respectively) for the same Hartmann number and the slip length, the slip is more observed on the Hartmann walls. Similar to the Problem 2 and Problem 3, as the slip ratio increases, side layers are thickened and the core region gets smaller since the slip on the Hartmann walls is strong. Also, core region velocity magnitude increases and induced magnetic field magnitude slightly decreases.

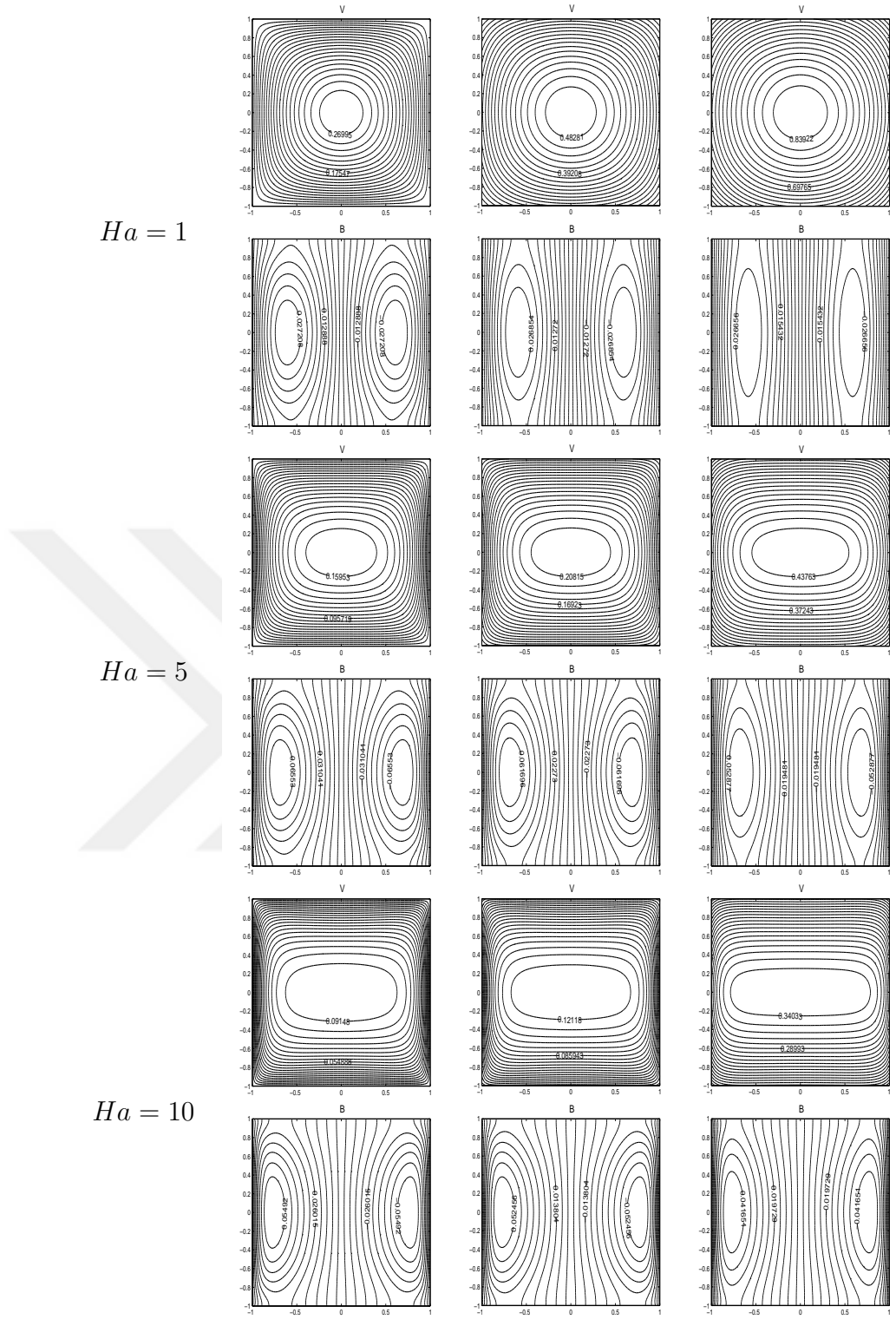


Figure 4.13: MHD duct flow -Problem 4; Velocity and induced magnetic field profiles for $Ha = 1, 5, 10$. Left: $\alpha = 0$ ($s_1 = s_2 = 0$). Center: from top to bottom $\alpha = 0.4, \alpha = 0.08, \alpha = 0.04$ ($s_1 < 1, s_2 < 1$), Right: from top to bottom $\alpha = 1.1, \alpha = 0.5, \alpha = 0.4$ ($s_1 > 1, s_2 > 1$).

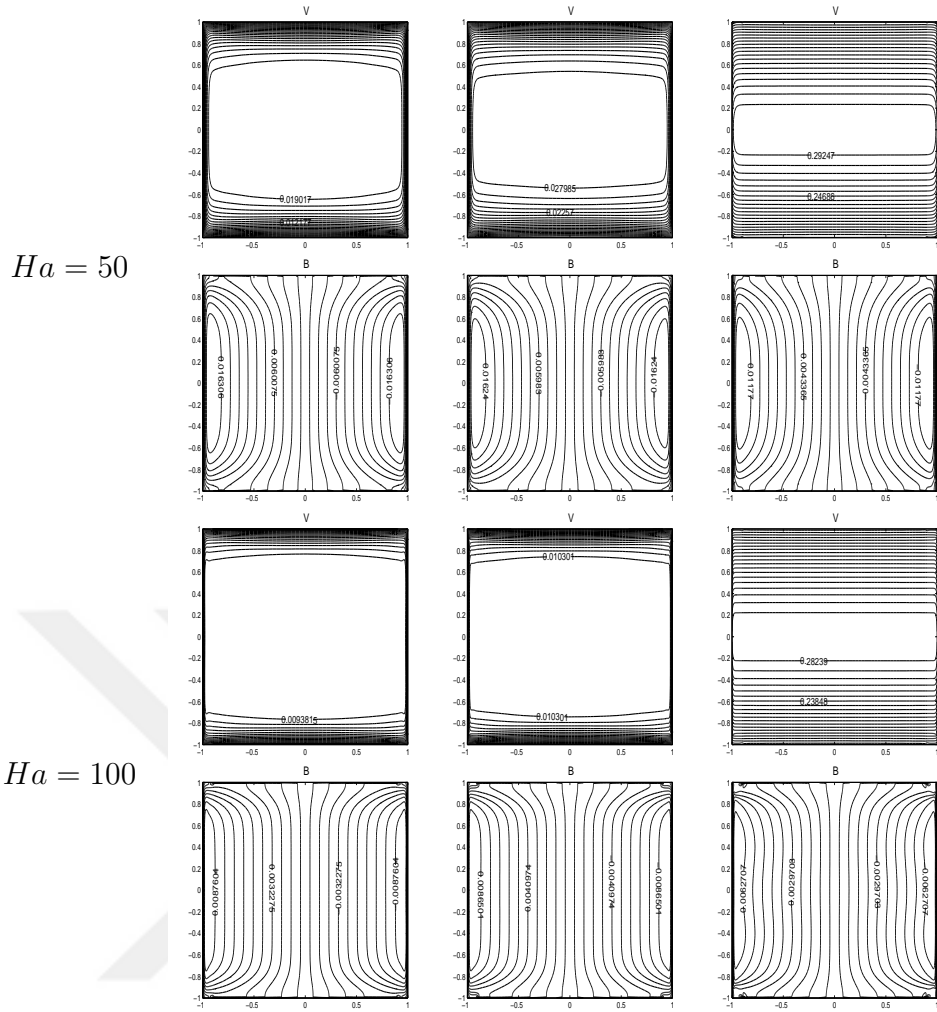


Figure 4.14: MHD duct flow -Problem 4; Velocity and induced magnetic field profiles for $Ha = 50, 100$. Left: $\alpha = 0$ ($s_1 = s_2 = 0$). Center: from top to bottom $\alpha = 0.01$, $\alpha = 0.001$ ($s_1 < 1$, $s_2 < 1$), Right: from top to bottom $\alpha = 0.4$ ($s_1 > 1$, $s_2 > 1$).

Figure 4.15 shows the velocity level curves for increasing values of Hartmann number when both the slip ratios are less than unity and greater than unity on the Hartmann and side walls. It is seen that when the Hartmann number $Ha > 10$ the slip on the side walls is nearly lost even for $s_1 > 1$, but the slip on the Hartmann walls is very strong for $s_2 > 1$.

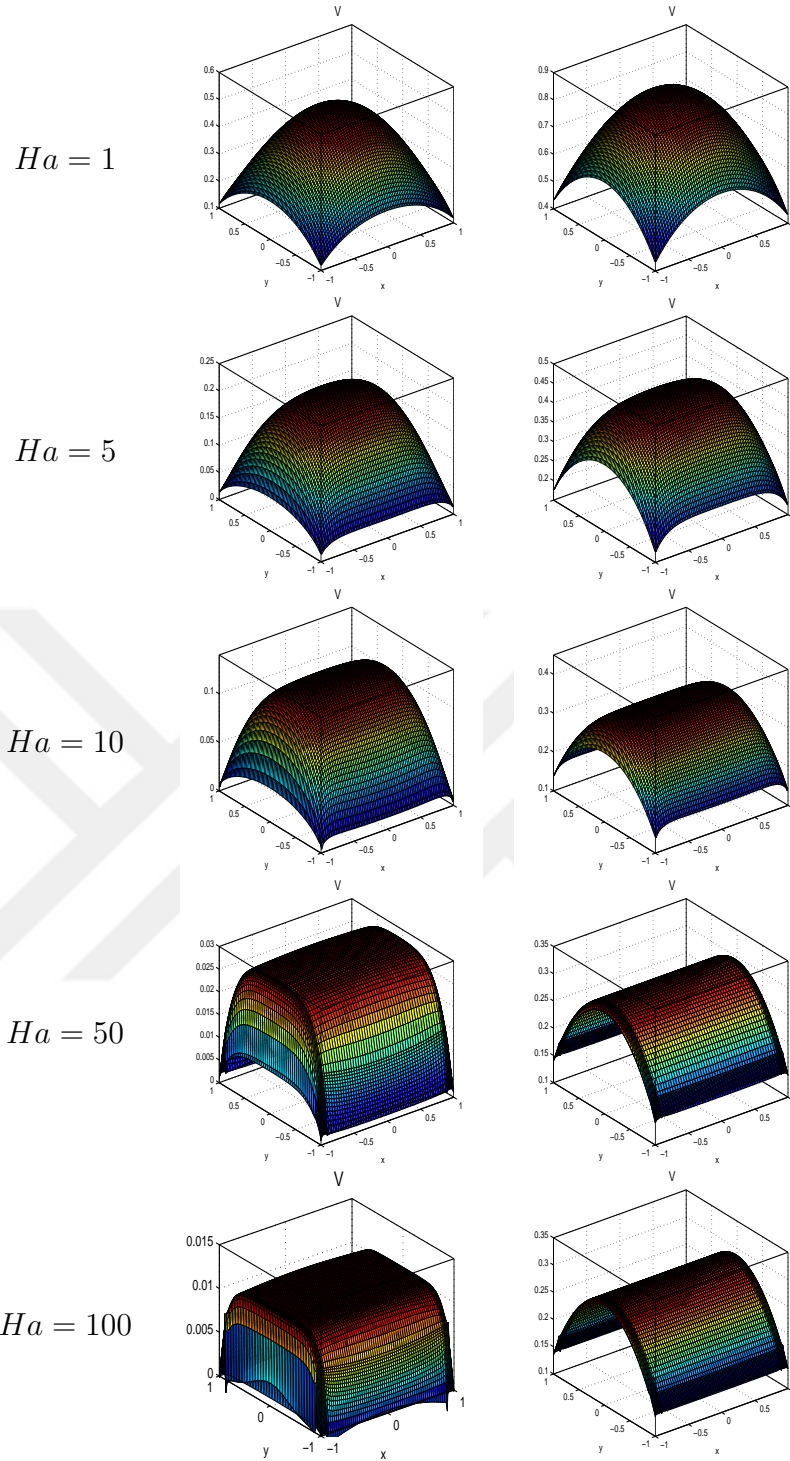


Figure 4.15: MHD duct flow -Problem 4; Velocity level curves for varying Ha numbers. Left: from top to bottom $\alpha = 0.4$, $\alpha = 0.08$, $\alpha = 0.04$, $\alpha = 0.01$, $\alpha = 0.001$ ($s_1 < 1$, $s_2 < 1$), Right: from top to bottom $\alpha = 1.1$, $\alpha = 0.5$, $\alpha = 0.4$, $\alpha = 0.4$, $\alpha = 0.4$ ($s_1 > 1$, $s_2 > 1$).

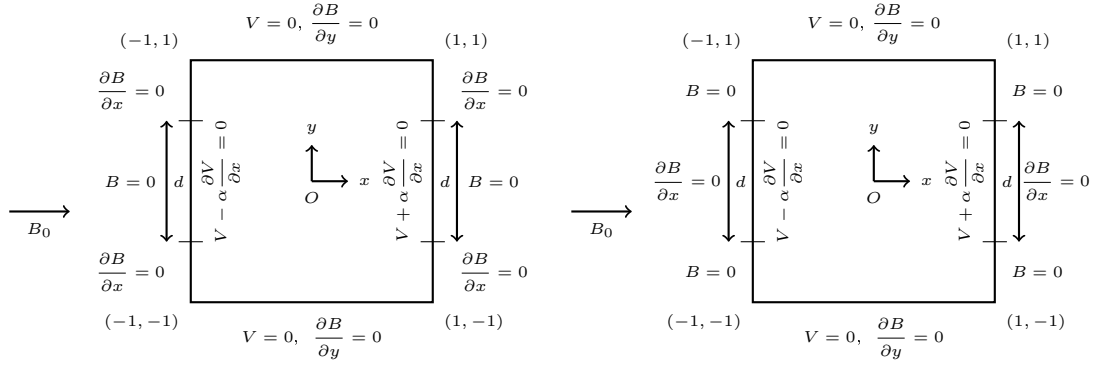
4.2 MHD Flow in Ducts with Partly Insulated Partly Perfectly Conducting Slipping Walls

In this section, the effect of partly insulated partly perfectly conducting, slipping Hartmann walls on the MHD duct flow is analyzed. A fully developed, pressure driven, flow of an electrically conducting fluid is considered in the square cross-section (duct) of a long pipe. Side walls are perfectly conducting no-slip walls and the Hartmann walls are partly insulated, partly perfectly conducting which admit slip. The flow is subjected to a horizontally applied uniform magnetic field $\mathbf{B}_0 = B_0 \mathbf{e}_x$. The DRBEM discretized matrix-vector equations are (Section 2.6)

$$\begin{aligned} \mathbf{H}V - \mathbf{G} \frac{\partial V}{\partial n} &= -(\mathbf{H}\hat{\mathbf{U}} - \mathbf{G}\hat{\mathbf{Q}})\mathbf{F}^{-1}\left\{Ha \frac{\partial B}{\partial x} + 1\right\} \\ \mathbf{H}B - \mathbf{G} \frac{\partial B}{\partial n} &= -(\mathbf{H}\hat{\mathbf{U}} - \mathbf{G}\hat{\mathbf{Q}})\mathbf{F}^{-1}\left\{Ha \frac{\partial V}{\partial x}\right\} \end{aligned} \quad (4.5)$$

where $V(x, y)$ and $B(x, y)$ denote the velocity and the induced magnetic field in the axial direction, respectively, and they have variations in the cross-section of the pipe $\Omega = \{(x, y) : -1 \leq x \leq 1, -1 \leq y \leq 1\}$. The system of equations are combined and solved in one stroke to obtain the velocity and the induced magnetic field nodal solutions both on the boundary and the interior points. The details of the numerical solution process are presented in Section 2.6. The effect of the slip at the Hartmann walls is investigated in four case problems for different combinations of wall conductivities.

The problem geometries and the boundary conditions are presented in Figure 4.16. The aim in Problem 1 is to investigate the difference in flow patterns when an insulated portion is placed at the center of the perfectly conducting, slipping Hartmann wall. In Problem 2, the influence of perfectly conducting piece at the center of an insulated, slipping Hartmann wall on the MHD flow is studied.



Problem 1

Problem 2

Figure 4.16: MHD flow with partly insulated partly perfectly conducting walls

The numerical results are presented in terms of the velocity and the induced current lines for $10 \leq Ha \leq 50$. The slip at the Hartmann walls are measured by the slip ratio $s_2 = \alpha Ha$. $N = 128 - 440$ constant elements are used for the discretization of the boundary.

4.2.1 Problem 1, $d = 0$ Case

In this problem, Hartmann walls are slipping and all the duct walls are perfectly conducting. Figures 4.17 and 4.18 present the flow characteristics for $Ha = 10, 30, 50$ and for different slip ratios. The obtained results for $s_2 = 0$ and $Ha = 10, 50$ coincide with the ones in [6]. One can realize that, as the slip length increases the thickness of the Hartmann layers is decreasing and slip is significantly observed when $s_2 \geq 1$. As Ha increases, flow is flattened, separated and concentrated near the side walls, current is completely directed between the top and bottom walls (induced magnetic field equilines are parallel to the streamlines for current within the fluid [6]), and the weakening of the Hartmann layers is achieved for much greater values of s_2 (for $Ha = 30$ when $s_2 = 6$ and for $Ha = 50$ when $s_2 = 10$). The induced magnetic field magnitude decreases with an increase in Ha and the current lines bend again through the vertical perfectly conducting walls for $s_2 > 1$.

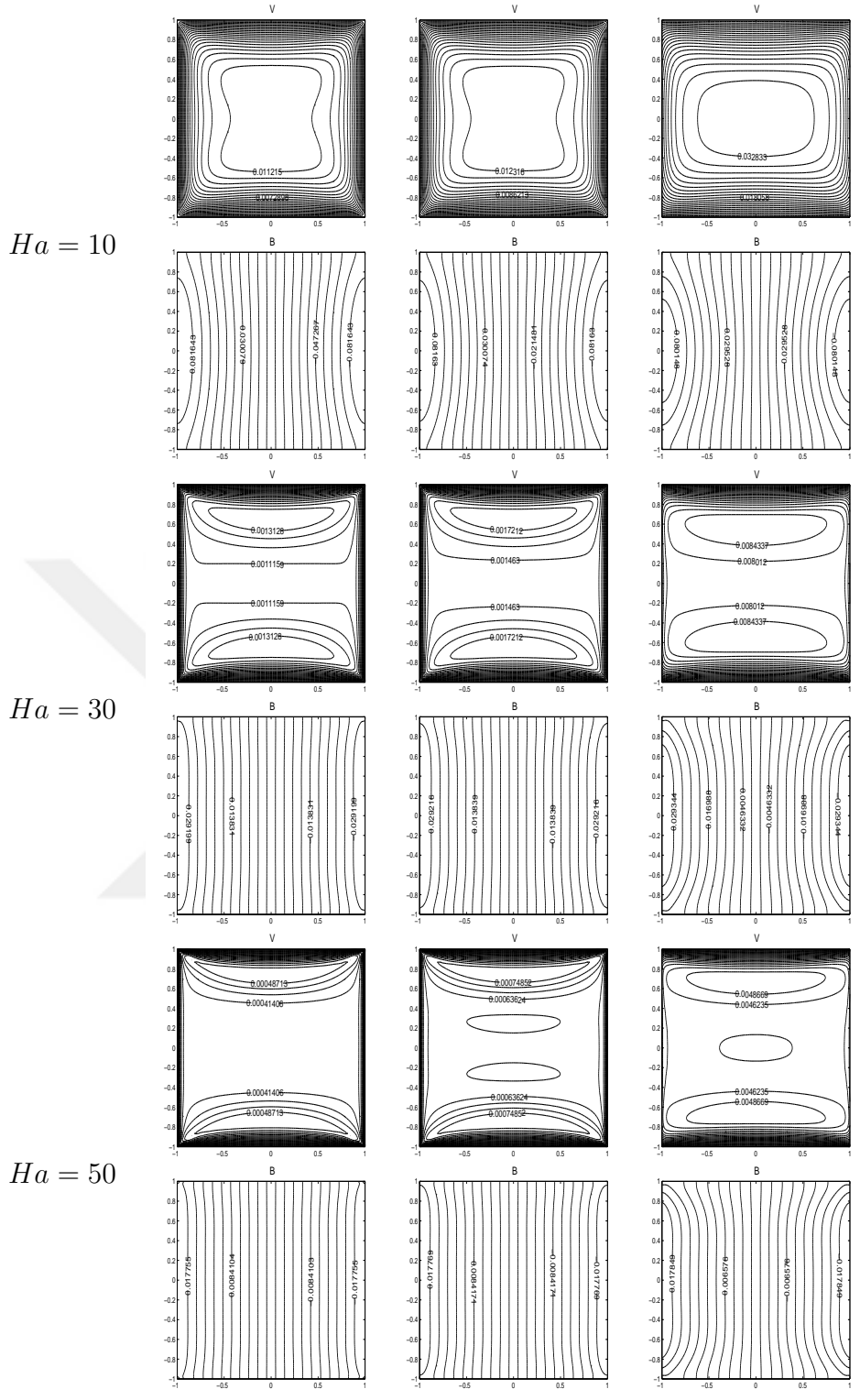


Figure 4.17: Problem 1, $d = 0$ case; velocity and induced magnetic field profiles for $Ha = 10, 30, 50$. $\alpha = 0$ ($s_2 = 0$) left, $\alpha = 0.01$ ($s_2 < 1$) center, $\alpha = 0.2$ ($s_2 > 1$) right.

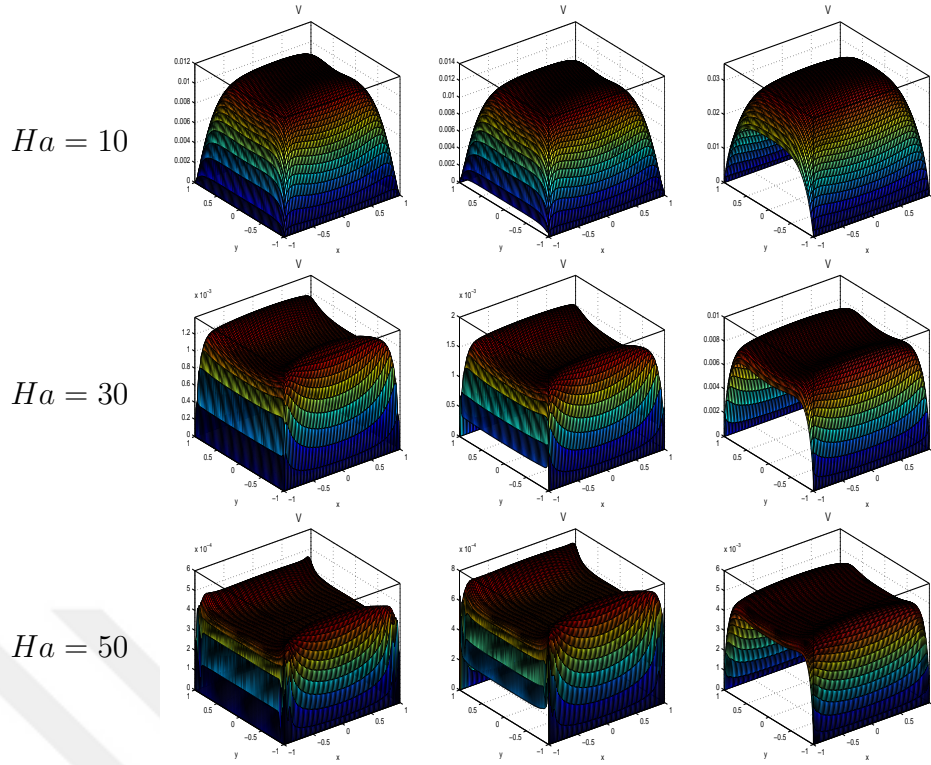


Figure 4.18: Problem 1, $d = 0$ case; velocity level curves for $Ha = 10, 30, 50$. $\alpha = 0$ ($s_2 = 0$) left, $\alpha = 0.01$ ($s_2 < 1$) center, $\alpha = 0.2$ ($s_2 > 1$) right.

4.2.2 Problem 1, $d = 1$ Case

Figure 4.19 show the flow and induced current changes when insulated portions at the center of the vertical walls are present. Slip effect is again significant when $s_2 \geq 1$. As Ha increases, parabolic layers emanating from the conductivity change points are observed and the slip is concentrated in front of the insulated portions especially as Ha increases. However, when Ha is further increased as 30, 50 and $s_2 > 1$, slip is extended to almost whole vertical walls. Induced current isolines are also destroyed from their vertically aligned position making parabola like current lines in front of the conducting portions.

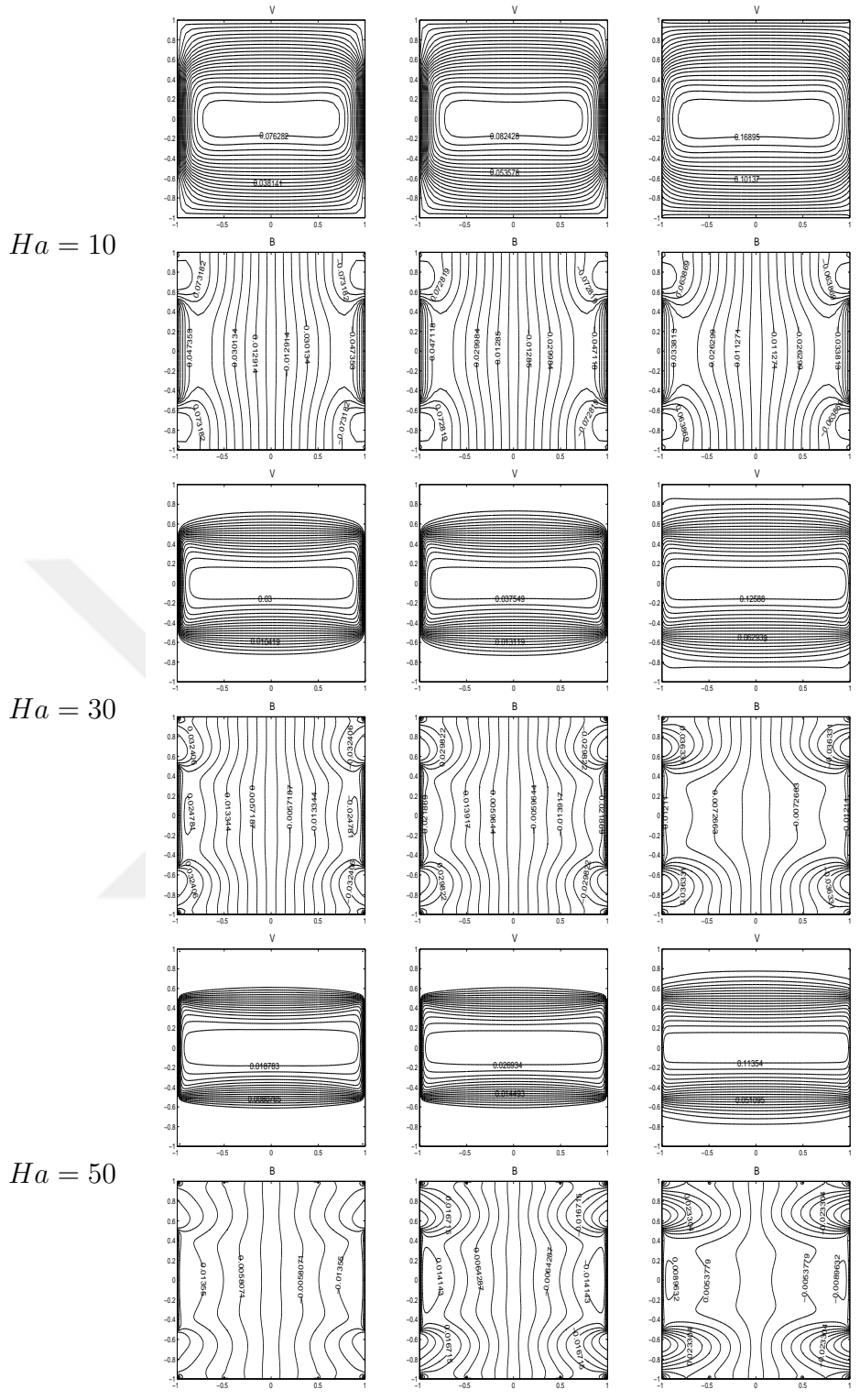


Figure 4.19: Problem 1, $d = 1$ case; velocity and induced magnetic field profiles for $Ha = 10, 30, 50$. $\alpha = 0$ ($s_2 = 0$) left, $\alpha = 0.01$ ($s_2 < 1$) center, $\alpha = 0.2$ ($s_2 > 1$) right.

An increase in the slip ratio accelerates the flow whereas, an increase in the Hartmann number decelerates it as can be observed from Figure 4.20.

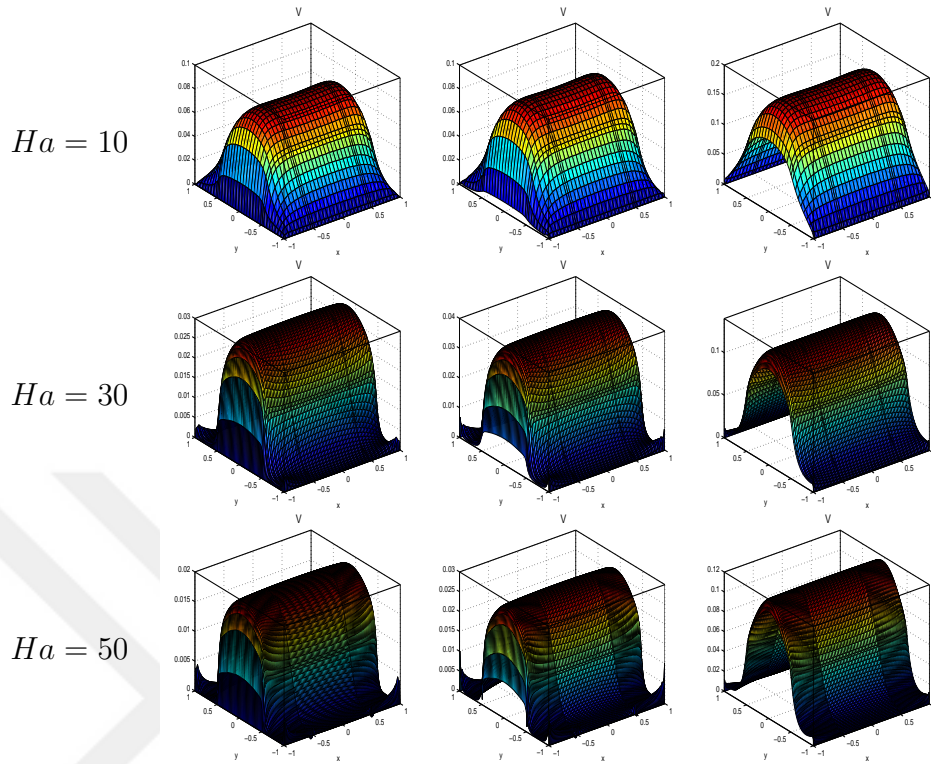


Figure 4.20: Problem 1, $d = 1$ case; velocity level curves for $Ha = 10, 30, 50$. $\alpha = 0$ ($s_2 = 0$) left, $\alpha = 0.01$ ($s_2 < 1$) center, $\alpha = 0.2$ ($s_2 > 1$) right.

4.2.3 Problem 2, $d = 0$ Case

This is the case of, completely insulated vertical walls as a difference from Problem 1, $d = 0$ case where these walls were perfectly conducting. Figures 4.21 and 4.22 display flow profiles and current lines for $Ha = 10, 30, 50$ and $s_2 = 0$, $s_2 < 1$, $s_2 > 1$. In this case, slip effect is observed for slightly smaller values of s_2 for all values of Ha . This shows that, if the slip walls are also insulated the effect of the slip comes for smaller values of the slip ratio s_2 from the case that the slip walls are perfectly conducting. Hartmann layers are diminished as in the other cases and the induced magnetic field decreases when the slip effect is dominant ($s_2 > 1$). Strong slip forces induced current to behave as if all the walls are insulated for $s_2 > 1$ especially when Ha is large.

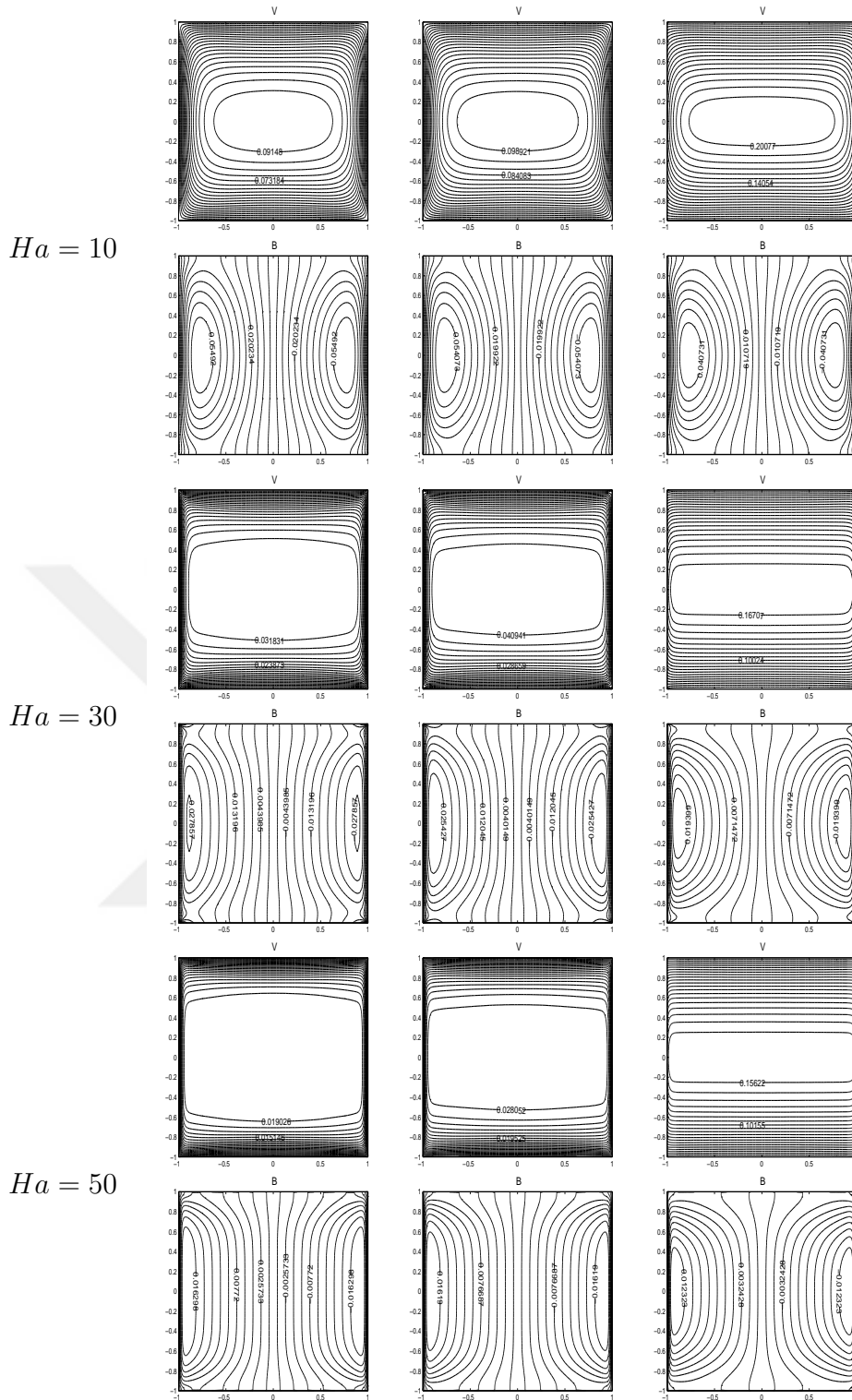


Figure 4.21: Problem 2, $d = 0$ case; velocity and induced magnetic field profiles for $Ha = 10, 30, 50$. $\alpha = 0$ ($s_2 = 0$) left, $\alpha = 0.01$ ($s_2 < 1$) center, $\alpha = 0.2$ ($s_2 > 1$) right.

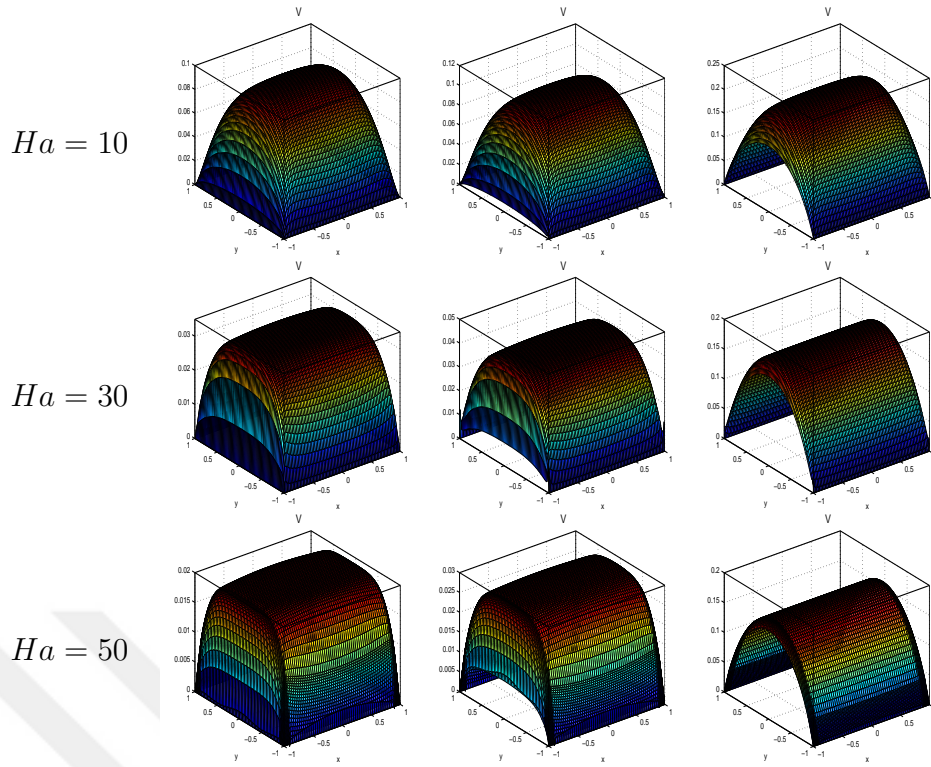


Figure 4.22: Problem 2, $d = 0$ case; velocity level curves for $Ha = 10, 30, 50$. $\alpha = 0$ ($s_2 = 0$) left, $\alpha = 0.01$ ($s_2 < 1$) center, $\alpha = 0.2$ ($s_2 > 1$) right.

4.2.4 Problem 2, $d = 1$ Case

When the vertical slip walls have symmetrically placed electrodes at the centers (Figures 4.23, 4.24), slip is observed on the insulated parts as in the case of Problem 1, $d = 1$. As Ha increases ($Ha \geq 30$) parabolic layers in front of the discontinuity points are developed keeping the side layers whereas in Problem 1, $d = 1$ case, side layers were diminished. As Ha increases together with the slip ratio, slip is extended to almost whole vertical walls. Current lines circulate in front of the electrodes leaving the other parts of the cavity electrically motionless. For large Ha , the flow is concentrated in front of the side layers and connected to the parabolic layers. Thus, the flow action is generally in front of the insulated portions leaving the central part stagnant.

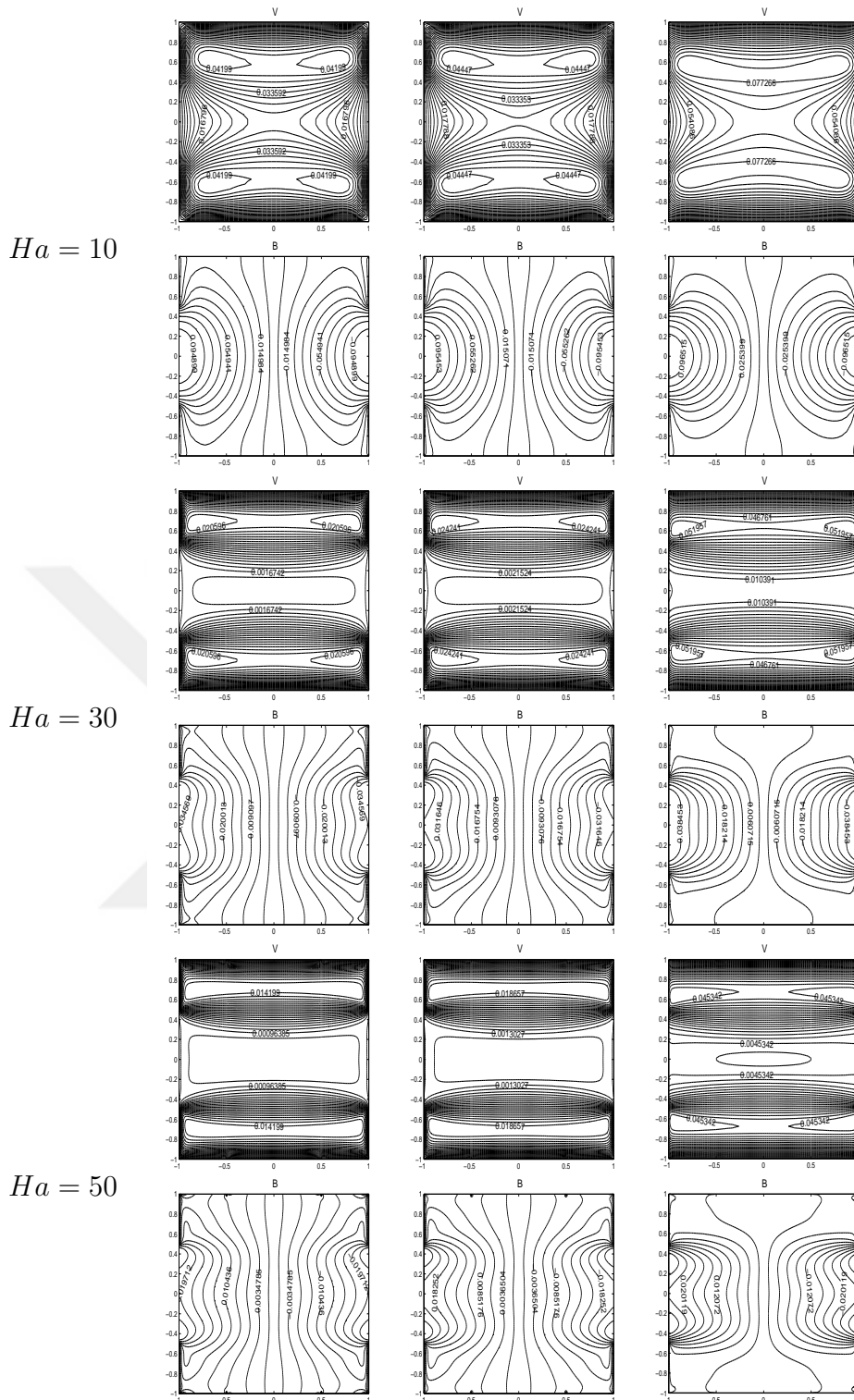


Figure 4.23: Problem 2, $d = 1$ case; velocity and induced magnetic field profiles for $Ha = 10, 30, 50$. $\alpha = 0$ ($s_2 = 0$) left, $\alpha = 0.01$ ($s_2 < 1$) center, $\alpha = 0.2$ ($s_2 > 1$) right.

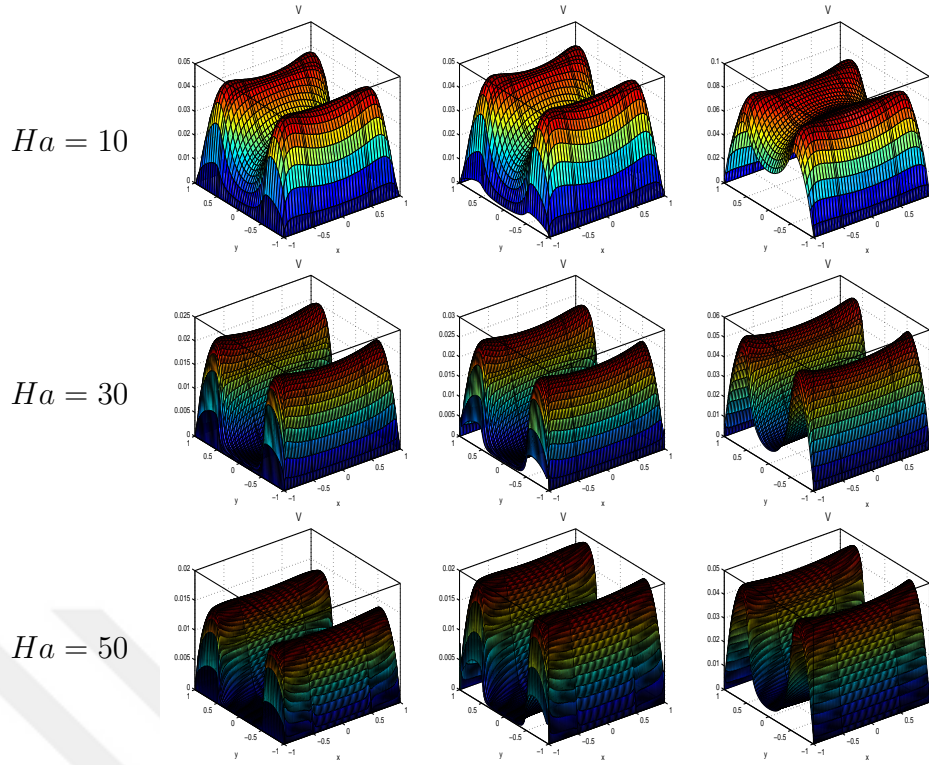


Figure 4.24: Problem 2, $d = 1$ case; velocity level curves for $Ha = 10, 30, 50$. $\alpha = 0$ ($s_2 = 0$) left, $\alpha = 0.01$ ($s_2 < 1$) center, $\alpha = 0.2$ ($s_2 > 1$) right.

4.3 MHD Flow Driven by Electrodes Between Parallel Infinite Slipping Plates

In this section, the MHD flow between two parallel slipping and conducting infinite plates containing symmetrically placed electrodes of length $2l$ is studied. The flow is driven by the current traveling between the electrodes in the plates. An external magnetic field is applied perpendicular to the plates, and an external circuit is connected to the plates at the sides of the electrodes, so a current enters the fluid from one plate and leaves from the other which generates also an electric potential. The fluid starts to move with the interaction of the electric current and the imposed magnetic field. This MHD flow problem can be considered as the MHD rectangular pipe problem in which the horizontal sides are extended up to infinity. Thus, the velocity and the induced magnetic field have only components in the pipe axis direction. Their variations are in the 2D cross-section of the pipe (the duct between infinitely long parallel plates). In this

case, $\nabla \cdot \mathbf{j} = 0$ results in $\nabla^2 \Phi = -\frac{\partial V}{\partial x}$ (Section 1.6).

The coupled DRBEM discretized matrix-vector equations (2.135) and (2.139)

$$\begin{aligned} \mathbf{H}V - \mathbf{G}\frac{\partial V}{\partial n} &= -(\mathbf{H}\hat{\mathbf{U}} - \mathbf{G}\hat{\mathbf{Q}})\mathbf{F}^{-1}\left\{Ha\frac{\partial B}{\partial y}\right\} \\ \mathbf{H}B - \mathbf{G}\frac{\partial B}{\partial n} &= -(\mathbf{H}\hat{\mathbf{U}} - \mathbf{G}\hat{\mathbf{Q}})\mathbf{F}^{-1}\left\{Ha\frac{\partial V}{\partial y}\right\} \\ \mathbf{H}\Phi - \mathbf{G}\frac{\partial \Phi}{\partial n} &= -(\mathbf{H}\hat{\mathbf{U}} - \mathbf{G}\hat{\mathbf{Q}})\mathbf{F}^{-1}\left\{\frac{\partial V}{\partial x}\right\} \end{aligned} \quad (4.6)$$

are solved for the velocity $V(x, y)$ of the fluid and the induced magnetic field $B(x, y)$ as a whole without introducing an iteration. The electric potential computations are carried after the nodal solutions for the velocity and the induced magnetic field are obtained (Section 4.3.5).

The effects of both the slip ratio and the length of the electrodes are discussed on the flow and magnetic field behaviors for increasing values of Hartmann number. Figure 4.25 shows the geometry and the boundary conditions of the problem. The infinite walls behave as the slipping, partly conducting and partly perfectly conducting (due to the electrodes) parallel plates. The solution provides striking examples of the kind of layers which may be produced in a flow by discontinuities in the electrical boundary conditions when a strong magnetic field is applied to the fluid. This problem may be considered as the MHD duct flow in which the sides at $x = \pm 1$ are extended to infinity, and the external magnetic field applies perpendicular to the walls $y = \pm 1$.

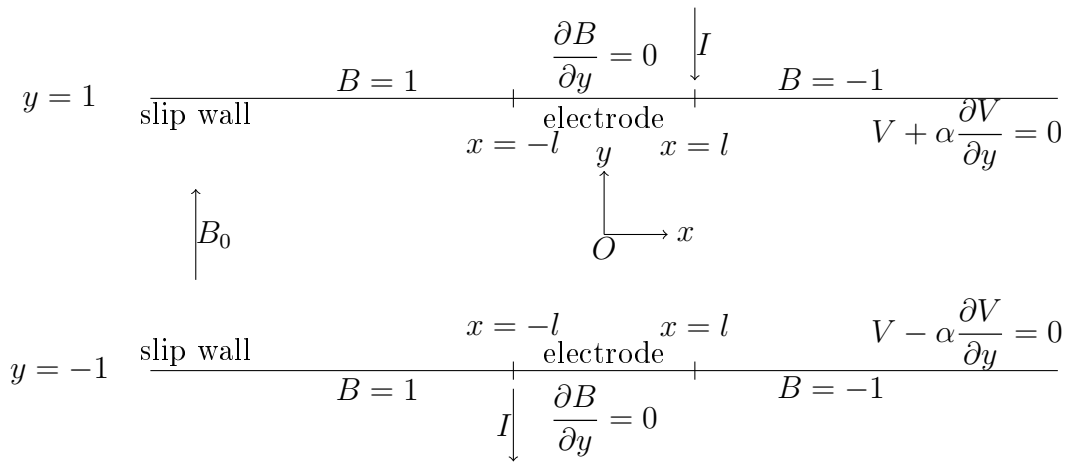


Figure 4.25: Problem geometry and the boundary conditions.

The velocity and the induced magnetic field are computed by using at most $N = 336$ constant boundary elements on the plates, and some interior points for a finite horizontal length $-3 \leq x \leq 3$, $y = \pm 1$. The equivelocity and equivalue induced magnetic field lines (current lines) are plotted for several values of perfectly conducting length l , and for slip ratio values $s_2 < 1$, $s_2 = 1$, $s_2 > 1$ (where $s_2 = \alpha Ha$) when the Hartmann number is increasing as $Ha = 10, 50, 100$.

4.3.1 Case 1: $s_2 = 0$, $l = 0$, Ha increases

When the current is injected by line electrodes set in non-conducting plates at $x = 0$, $y = \pm 1$, current enters the fluid at $(0, 1)$ and leaves at $(0, -1)$ giving conductivities $B = -1$ and $+1$ for $x > 0$ and $x < 0$, respectively, and the plates are no-slip walls. Figures 4.26 and 4.27 show equal velocity and induced magnetic field lines for increasing values of Ha . One can notice from these graphs that although the MHD problem is solved for an infinite strip, the flow is confined to a relatively small region near the $x = 0$ line on which the plates have jump in the values of magnetic field. In the rest of the region the fluid is almost stagnant. This region is reduced when Ha increases. The flow emanates from the line electrodes and spreads into the channel in terms of four reversal velocity loops symmetrically located with respect to x - and y - axes. Current lines travel between the source points of line electrode in terms of closed loops. Also, in most parts of the region the value of induced magnetic field is stationary and equal to its maximum value. The velocity vanishes at the symmetry line $y = 0$ and shows highest values when approaching the plates.

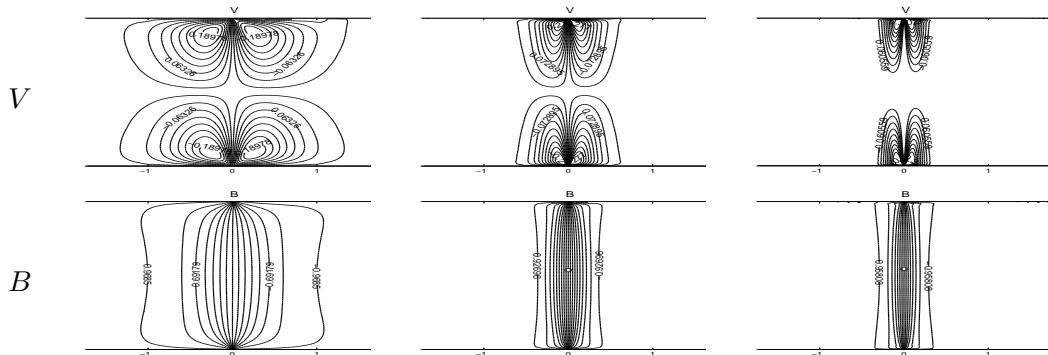


Figure 4.26: $s_2 = 0$, $l = 0$ from left to right $Ha = 10, 50, 100$.

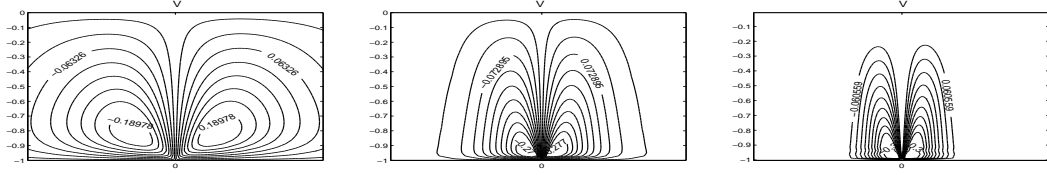


Figure 4.27: $s_2 = 0$, $l = 0$ from left to right $Ha = 10, 50, 100$, velocity profile on the bottom half of the channel.

This special case of the flow induced by line electrodes has been considered by Hunt and Williams [29] and our solution for $l = 0$, $s_2 = 0$ coincides with theirs. They examine asymptotic solution for large Ha in separate regions.

It is noted that as Ha increases boundary layer formation starts for $x > 0$ and $x < 0$ on the plates. These are Hartmann layers of order of thickness $1/Ha$. There is also a thin region near $x = 0$ line where shear layers (parabolic layers) originating from the source points $(0, 1)$ and $(0, -1)$ of order of width $1/\sqrt{Ha}$ spreading along magnetic lines for increasing values of Ha .

4.3.2 Case 2: $l = 0$, $Ha = 10$, s_2 varies as $s_2 < 1$, $s_2 = 1$, $s_2 > 1$

The effect of the slip ratio is examined for a fixed Hartmann number in the absence of perfectly conducting part in the plates.

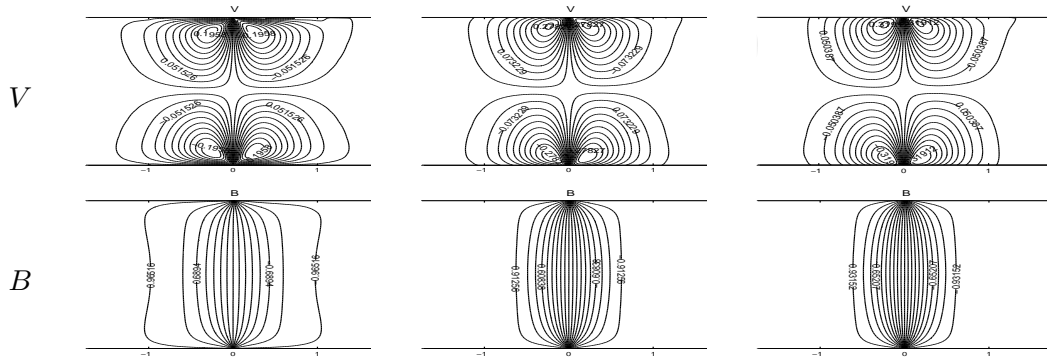


Figure 4.28: $l = 0$, $Ha = 10$ from left to right $s_2 < 1$ ($\alpha = 0.001$), $s_2 = 1$ ($\alpha = 0.1$), $s_2 > 1$ ($\alpha = 0.2$)

When the slip ratio is less than 1 (Figure 4.28), a slight slip is noticed on the

plates, however Hartmann layer formation is visible on each wall. As s_2 is increasing slips on the plates become dominant weakening the Hartmann layers, and the magnitude of the velocity increases. Hartmann layers are diminished especially for $s_2 > 1$. Also, when the slip ratio increases both the flow and induced magnetic field lines (current lines) tend to concentrate to the line electrodes ($x = 0$ line).

4.3.3 Case 3: $s_2 = 0$, $Ha = 50$, l varies as $l = 0.1, 0.3, 0.5$

In this case, two electrodes of length $2l$ are placed symmetrically with respect to the x -axis at the middle of the plates indicating the perfectly conducting parts of the no-slip walls ($\partial B/\partial n = 0$). The length of the electrodes is varied as $l = 0.1, 0.3, 0.5$ for a fixed Hartmann number $Ha = 50$.

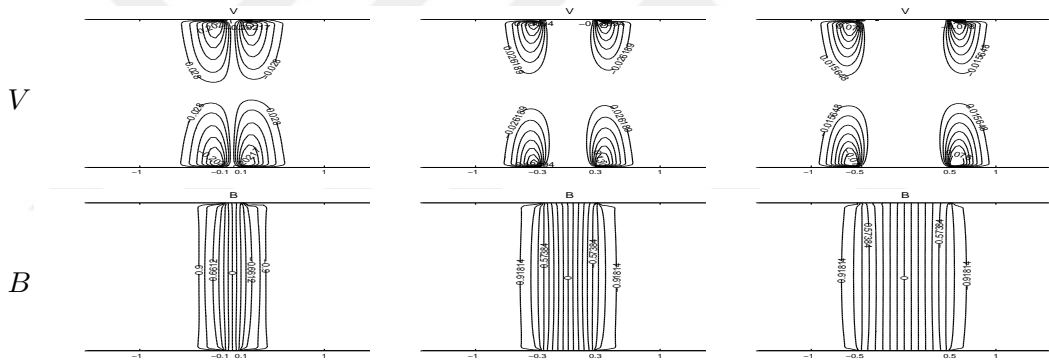


Figure 4.29: $s_2 = 0$, $Ha = 50$ from left to right $l = 0.1$, $l = 0.3$, $l = 0.5$

It is observed from Figure 4.29 that, the increase in l (perfectly conducting portion) causes the formation of a stagnant region for the velocity in front of the electrodes. Induced magnetic field lines are perpendicular to $y = \pm 1$ lines for $-l < x < l$ demonstrating the derivative condition on B ($\partial B/\partial n = 0$). Parabolic layers (shear layers) in induced magnetic field lines originating from $x = l$ and $x = -l$ are connected at $x = 0$ line but are separated as l is increasing. The problem is solved numerically in [80] by using BEM with fundamental solution derived for coupled MHD equations. The present DRBEM solution compares well with their solutions for the electrodes with finite length ($l \neq 0$) cases.

4.3.4 Case 4: $Ha = 10$, s_2 varies as $s_2 < 1$, $s_2 = 1$, $s_2 > 1$ and l varies as $l = 0.3$, $l = 0.5$

Finally, the effects of both the slipping and partly conducting, partly perfectly conducting walls on the behavior of the flow and induced magnetic field are studied for a fixed Hartmann number value ($Ha = 10$).

In Figures 4.30 and 4.31, the length of the conducting part is fixed as $l = 0.3$ and $l = 0.5$, respectively and the slip ratio effect is considered when $s_2 < 1$, $s_2 = 1$, $s_2 > 1$. The slip in the velocity is more observed on the plates as the slip ratio increases. Hartmann layers are only shown for $s_2 < 1$ but start to diminish for $s_2 = 1$ and are completely lost for $s_2 > 1$. That is, the thickness of Hartmann layers and the slip length are comparable for $s_2 = 1$.

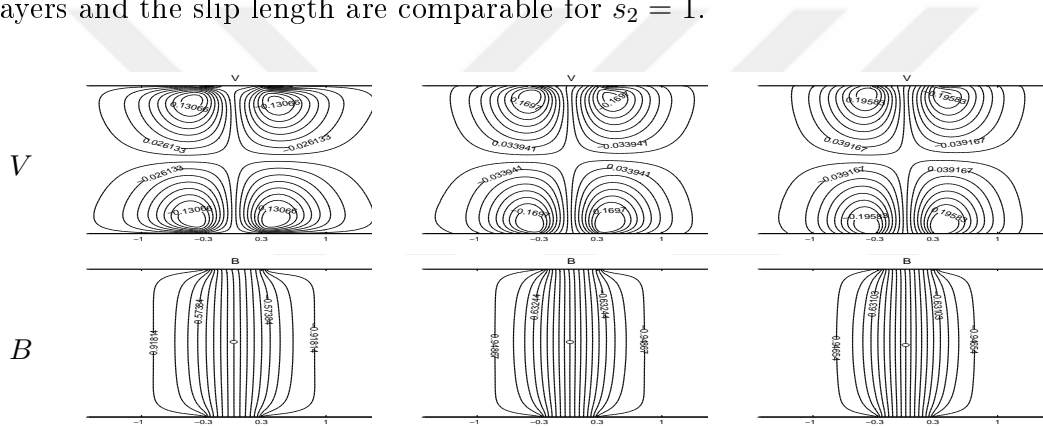


Figure 4.30: $Ha = 10$, $l = 0.3$ from left to right $s_2 < 1$ ($\alpha = 0.001$), $s_2 = 1$ ($\alpha = 0.1$), $s_2 > 1$ ($\alpha = 0.2$)

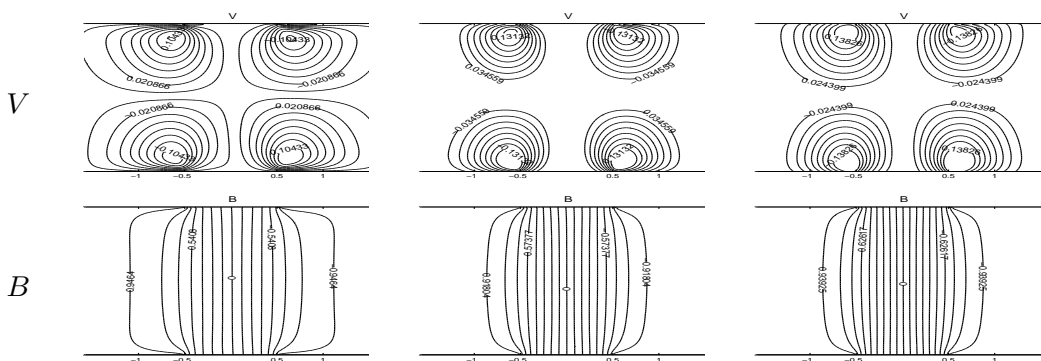


Figure 4.31: $Ha = 10$, $l = 0.5$ from left to right $s_2 < 1$ ($\alpha = 0.001$), $s_2 = 1$ ($\alpha = 0.1$), $s_2 > 1$ ($\alpha = 0.2$)

The increase in the electrodes length retards the weakening effect of slipping on Hartmann layers, that is, the Hartmann layers can still be observed near the plates (i.e. when the electrode length is $l = 0.3$ the slip starts to weaken the Hartmann layer at $s_2 = 1$, but when the electrode length is $l = 0.5$ the slip diminishes Hartmann layers when $s_2 > 1$). Induced magnetic field lines are not affected much with the slip ratio increase, but when the electrodes are getting longer, the currents directly travel from the top electrode to the bottom electrode being perpendicular to the plates.

4.3.5 Electric potential computations

In this section, electric potential distribution between the infinite plates including electrodes is studied together with slip velocity condition. The problem geometry and the boundary conditions are presented in Figure 4.32

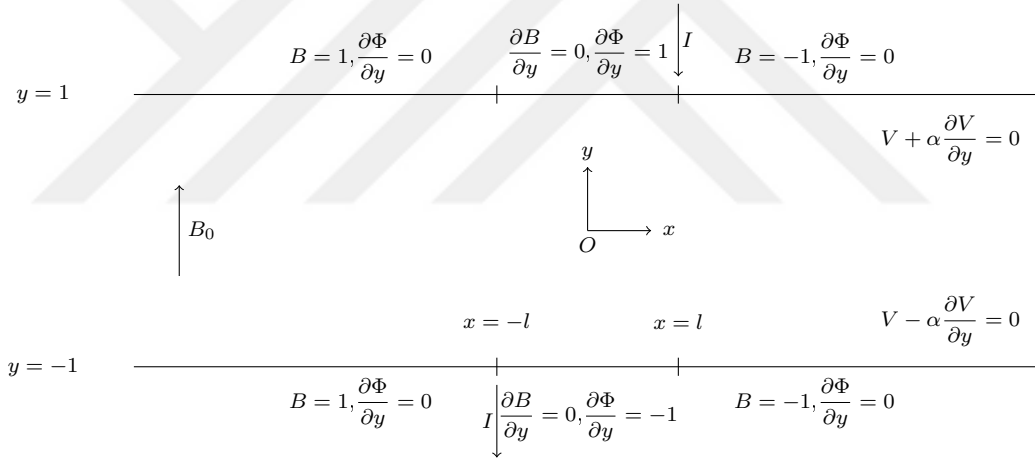


Figure 4.32: Electric potential boundary conditions.

The DRBEM matrix-vector equation for the electric potential (2.139)

$$\mathbf{H}\Phi - \mathbf{G}\frac{\partial\Phi}{\partial n} = -(\mathbf{H}\hat{\mathbf{U}} - \mathbf{G}\hat{\mathbf{Q}})\mathbf{F}^{-1}\left\{\frac{\partial V}{\partial x}\right\} \quad (4.7)$$

is solved after the nodal values for the velocity and induced magnetic field are obtained as discussed in Chapter 2, Section 2.7. Figure 4.33 displays the induced magnetic field and the equipotential lines when there is no external magnetic field (i.e. $Ha = 0$) and the walls are not slipping. In order to compare the numerical results with the ones in [35], the bottom wall is placed on $y = 0$

line and $\Phi = 1$ and $\Phi = -1$ boundary conditions are imposed on the top and bottom electrodes, respectively. In this case, the velocity becomes zero within the domain by the strong maximum principle [83]. Then, a Laplace equation is obtained for the electric potential. Symmetric behaviors are observed both for the induced magnetic field and the electric potential with respect to $x = 0$ and $y = 0$ lines, respectively. The electric potential is high in magnitude near the electrodes and equipotential lines form half ellipses around the electrodes which were also observed in [35].

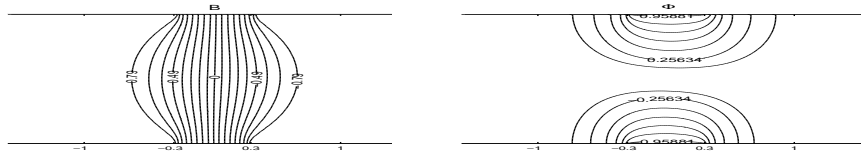


Figure 4.33: Validation case. The bottom wall is on $y = 0$ line, $Ha = 0$, $s_2 = 0$, $l = 0.3$, $\Phi = 1$ on the top and $\Phi = -1$ on the bottom electrodes.

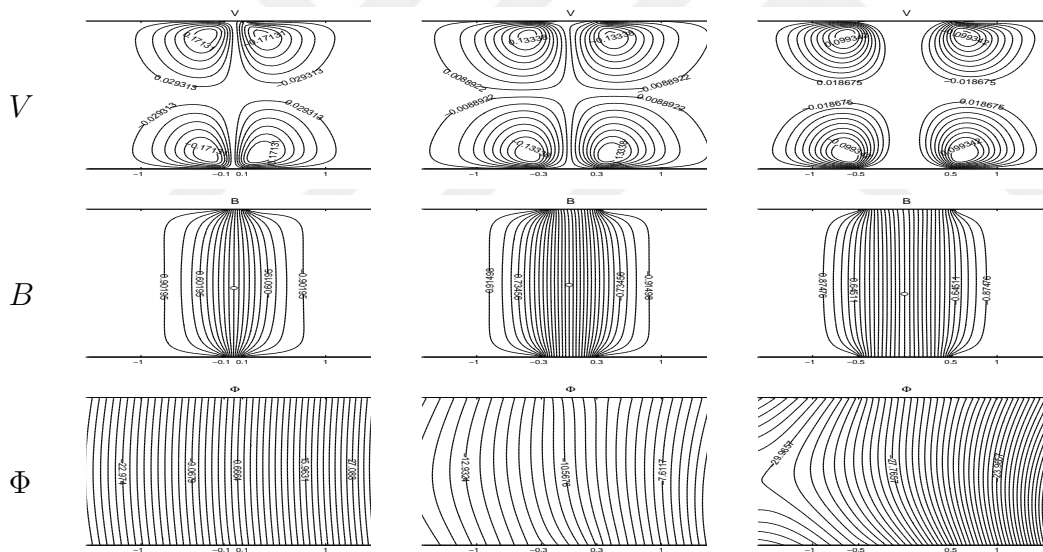


Figure 4.34: $Ha = 10$, $s_2 = 0$ from left to right $l = 0.1, 0.3, 0.5$.

Figures 4.34 and 4.35 display the influence of the vertically applied magnetic field on the equipotential lines for $Ha = 10, 50$ and varying electrode lengths $l = 0.1, 0.3, 0.5$. Electric potential is vertically aligned between the plates when the electrode length is small. An increase in the electrodes length causes the bending of equipotential lines and a deterioration from their profiles through the left and right. The behavior of the electric potential does not alter much as

Ha increases for $l \leq 0.3$. When $l = 0.5$ and $Ha = 50$, the disturbances in the equipotential lines through the left and right disappear.

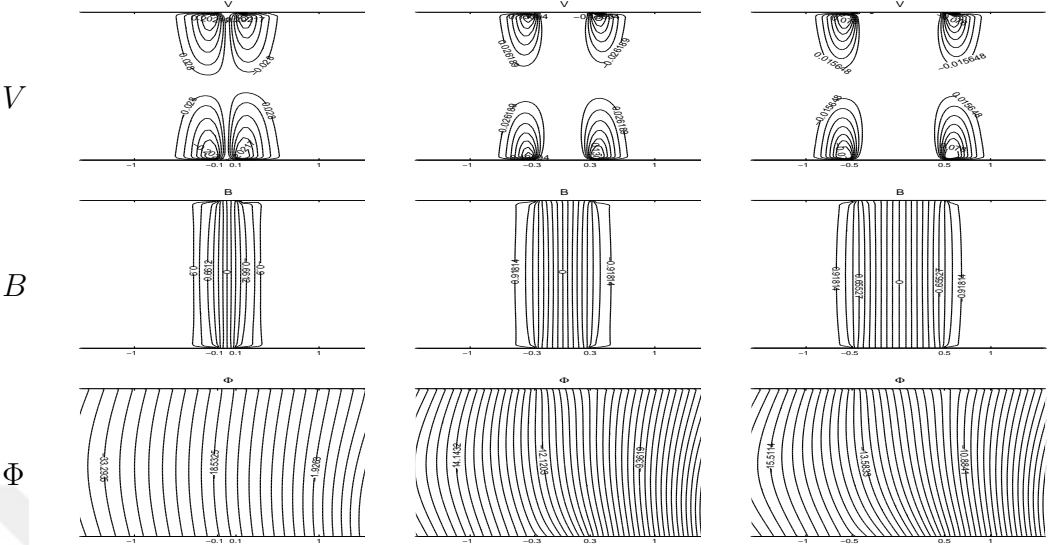


Figure 4.35: $Ha = 50$, $s_2 = 0$ from left to right $l = 0.1, 0.3, 0.5$.

In the strong slip condition $s_2 \geq 1$ (Figure 4.36) bending in equipotential lines between the electrodes becomes more significant even for small $Ha = 10$. An increase in the slip ratio results in a symmetric behavior in electric potential with respect to the origin.

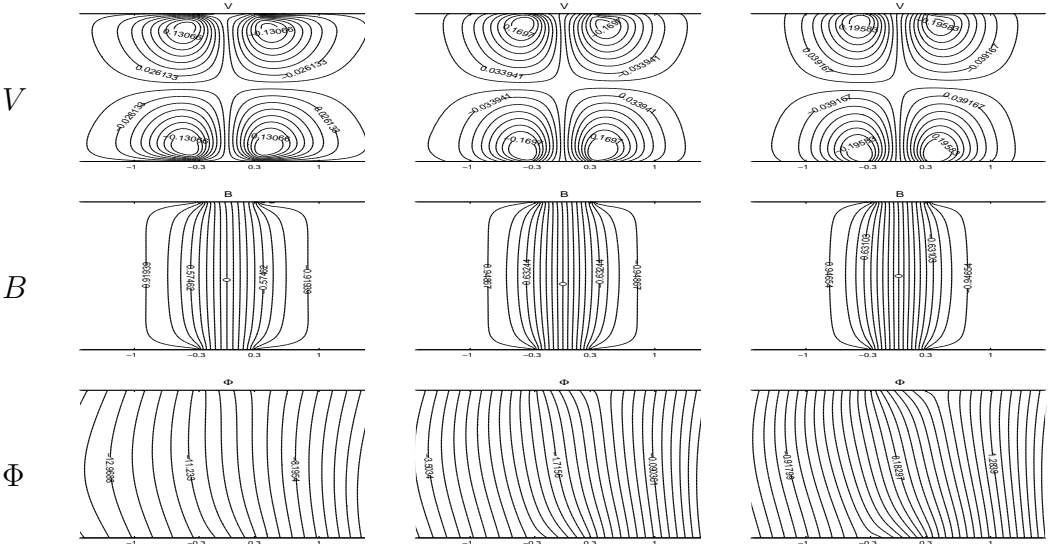


Figure 4.36: $Ha = 10$, $l = 0.3$ from left to right $s_2 < 1$ ($\alpha = 0.001$), $s_2 = 1$ ($\alpha = 0.1$), $s_2 > 1$ ($\alpha = 0.2$).

In Chapter 4, first the DRBEM formulation of the MHD duct flow problem with slip velocity condition is presented. The fluid is driven by a constant pressure gradient in the pipe-axis direction. The coupled system of discretized equations are combined into a larger system and solved once without introducing an iteration. Secondly, the same MHD flow equations without the pressure gradient are solved between parallel plates when the fluid is driven by the electrodes placed symmetrically at the centers of the plates. The results are obtained for wide ranges of wall conductivities and slip conditions for both of the problems.

The influences of slipping and conducting walls are;

1. MHD duct flow:

- As the slip length increases, the flow accelerates.
- The influence of the slip is significant when the slip length is greater than the slipping wall boundary layer thickness.
- When the side walls or the Hartmann walls admit slip, the side layers or the Hartmann layers, respectively, get lost especially when the slip ratio is greater than one.
- When the Hartmann walls exhibit slip, the side layer thickness increases and the induced magnetic field magnitude slightly decreases as the slip length increases.
- In the case of perfectly conducting Hartmann walls, the fluid is in action also at the center of the cavity when the slip is strong ($s_2 > 1$).
- When all of the duct walls admit slip, for small Ha the slip is visible at all of the duct walls. For high Hartmann numbers the flow is controlled completely by the slip at the Hartmann walls due to the thicker boundary layer at the side walls.
- When the Hartmann walls are partly insulated and partly perfectly conducting, the flow is concentrated in front of the insulated portions, forming parabolic layers emanating from the conductivity changes and leaving the rest of the cavity stagnant.
- The slip is more effective on the insulated portions of the vertical walls as Hartmann number increases and extends through the whole

vertical walls as the slip ratio advances.

2. MHD flow between parallel infinite plates:

- As Hartmann number increases Hartmann layers of thickness order $1/Ha$ are formed in front of the conducting parts, and also shear layers of thickness order $1/\sqrt{Ha}$, originating from the end points of the electrodes are observed.
- As the slip ratio is increased ($s_2 > 1$) Hartmann layers are weakened and the slip velocity magnitude increases.
- Increase in the length of the electrodes causes the formation of a stagnant region for the velocity in front of the electrodes, and retards the weakening effect of slipping on the Hartmann layers.
- The effects of the increase in the Hartmann number and the increase in the slip ratio are comparable when the slip ratio is equal to one.
- Bending between the electrodes in equipotential lines becomes significant as the slip ratio advances.

The number of boundary elements in the DRBEM is required to be taken around 320 – 400 for MHD flow in rectangular duct or between infinite plates especially for large values of Hartmann number since the coupled equations are solved together. Thus, the resulting system has a coefficient matrix with larger condition number compared to FHD problems considered in the thesis. However, the systems were able to be solved by using a solver performing Gaussian elimination with pivoting which takes care of the full behavior of the coefficient matrix minimizing the computational time.



CHAPTER 5

CONCLUSION

This thesis provides an extension to the applications of the DRBEM in fluid dynamics problems which are highly nonlinear. The two-dimensional, steady, laminar pipe flow problems that arise in FHD and MHD theory are simulated by the use of the DRBEM. In the FHD pipe flow problems, the governing equations are considered in primitive (velocity-pressure-temperature) variables and the missing pressure equation is derived through momentum and the continuity equations. The no-slip boundary conditions are imposed for the velocity and the Dirichlet type boundary conditions are generated for the pressure with an approximation based on the finite difference scheme and the DRBEM coordinate matrix. This type of model equations enable one to find the nodal solutions of all original problem variables including pressure. An iterative solution procedure is proposed between the flow velocity and pressure equations. Throughout the thesis, the fundamental solution of the Laplace equation is made use of in order to transform the modeling equations containing Laplace operator into the coupled system of boundary integral equations. The inhomogeneity parts are approximated by the linear radial basis functions. The boundary only nature of the method provides the numerical solutions with a low computational cost when compared to other numerical methods requiring domain discretization since the resulting linear systems are small in size. DRBEM also handles the nonlinearities in the convection terms easily with the use of coordinate matrix. In most of the simulations the boundaries of the problem domains are discretized by the constant boundary elements.

The proposed numerical solution procedure is tested by the simulations of many

physical problems ranging from FHD Stokes flow to FHD forced convection flow in pipes. The numerical tests reveal the need of relaxation parameters for the convergence of the pressure and the temperature equations. The effect of the magnetization force generated by a point magnetic source on the Stokes flow is considered first by neglecting the convection terms in the momentum equations. It is found that, constant or linear element discretizations does not bring a significant change in the flow profiles. In the presence of the magnetic field, pressure highly concentrates around the source and increases with the magnetization force. The influence of the magnetization force is high in circular cavities than in square cavities due to the disturbances coming from the corners of the square cavity. Then, convection terms are added to the mathematical model and the change in the flow and pressure profiles due to the magnetization force are investigated. Depending on the convection terms, the equation for the axial velocity is also taken into account. The obtained numerical results show that, an increase in the magnetization force results in a retarded flow around the magnetic source in the axial direction. In order to obtain similar behaviors in Stokes and incompressible flows $M = Mn/Re$ has to be higher for Stokes flow than for the incompressible flow. This may be caused by the high viscosity of the Stokes fluid. Increasing the number of point magnetic sources forms secondary flows and the axial flow retardation in the square cavity occurs for smaller magnetic numbers in two sources case than in the single source case due to the combined effects of multiple sources. As a last case for the FHD flow, energy equation is added to the mathematical model and the connection between the magnetization and buoyancy forces is analyzed together with the viscous dissipation. It is found that, when the point source is below the adiabatic wall the main effect of the point magnetic force is to keep the center of the cavity at nearly a constant temperature whereas when the point magnetic source is placed below the cold wall the main influence of the magnetization and buoyancy forces is the cooling of the channel. The viscous dissipation effect can only be observed when both Mn and Ra are high. The DRBEM is the most effective numerical method in solving Stokes and incompressible fluid flow problems under point magnetic sources since it can deal with the highly nonlinear terms easily which are present in all the equations, with the DRBEM coordinate matrix.

In the second part of the thesis, the influence of the slip velocity wall condition on the MHD pipe flow and MHD flow between parallel infinite plates is simulated by the DRBEM. The discretized system of equations in terms of the axial velocity and the induced magnetic field are combined into a large system and solved in one stroke. This procedure provides the solution on the boundary and at the interior nodes in a short period of time. In the MHD pipe flow, when all of the duct walls admit slip, the slip is visible at all of the walls for small Ha . For high Hartmann numbers the flow is controlled completely by the slip at the Hartmann walls due to the thicker boundary layer at the side walls. The slip is more effective on the insulated portions of the slipping Hartmann walls as Hartmann number increases and extends through the whole vertical walls as the slip ratio advances. In the case of electrically driven flow between two parallel infinite plates, as the slip ratio increases Hartmann layers are weakened and the slip velocity magnitude increases. Increase in the length of the electrodes causes the formation of a stagnant region for the velocity in front of the electrodes, and retards the weakening effect of slipping on the Hartmann layers. Equipotential lines show a significant bending between the electrodes in the strong slip conditions. The DRBEM is the most suitable method for MHD flow problems with slip velocity since it provides both the velocity and its normal derivative at once on the walls which are required in the definition of slip condition.



REFERENCES

- [1] Munson BR, Young DF, Okiishi TH, and Huebsch WW. *Fundamentals of Fluid Mechanics*. Wiley, Asia, 2010.
- [2] Potter M and Wiggert DC. *Schaum's Outline of Fluid Mechanics*. McGraw-Hill, USA, 2008.
- [3] Rosensweig RE. *Ferrohydrodynamics*. Dover Publications, Mineola, New York, 2014.
- [4] Tzirtzilakis EE. A mathematical model for blood flow in a magnetic field. *Physics of Fluids*, 17:077103:1–15, 2005.
- [5] Incropera FP and DeWitt DP. *Introduction to Heat Transfer*. John Wiley and Sons, 1996.
- [6] Muller U and Buhler L. *Magnetofluidynamics in Channels and Containers*. Springer, 2001.
- [7] Krasnopolskaya TS, Meleshko VV, Peters GWM, and Meijer HEH. Mixing in Stokes flow in an annular wedge cavity. *European Journal of Mechanics-B/Fluids*, 18:793–822, 1999.
- [8] Finn MD and Cox SM. Stokes flow in a mixer with changing geometry. *Journal of Engineering Mathematics*, 41:75–99, 2001.
- [9] Fletcher CAJ. *Computational Techniques for Fluid Dynamics 2*. Springer, Berlin, 1991.
- [10] Plansey R and Collin RE. *Principles and Applications of Electromagnetic Fields*. Mc Graw-Hill, NewYork, 1961.
- [11] Higashi T, Yamagishi A, Takeuchi T, Kawaguchi N, Sagawa S, Onishi S, and Date M. Orientation of erythrocytes in a strong magnetic field. *Blood*, 82 (4):1328–1334, 1993.
- [12] Haik Y, Pai V, and Chen CJ. Development of magnetic device for cell separation. *Journal of Magnetism and Magnetic Materials*, 194:254–261, 1999.
- [13] Ruuge EK and Rusetski AN. Magnetic fluids as drug carriers: Targeted transport of drugs by a magnetic field. *Journal of Magnetism and Magnetic Materials*, 122:335–339, 1993.

- [14] Cantillon-Murphy P, Cundy TP, Patel NK, Yang GZ, Darzi A, and Teare JP. Magnets for therapy in the GI tract: a systematic review. *Gastrointestinal Endoscopy*, 82 (2):237–245, 2015.
- [15] Hou CH, Hou SM, Hsueh YS, Lin J, Wu HC, and Lin FH. The in vivo performance of biomagnetic hydroxyapatite nanoparticles in cancer hyperthermia therapy. *Biomaterials*, 30:3956–3960, 2009.
- [16] Lienhard IV JH and Lienhard V JH. *A Heat Transfer Textbook*. Cambridge, Massachusetts, 2000.
- [17] Loukopoulos VC and Tzirtzilakis EE. Biomagnetic channel flow in spatially varying magnetic field. *International Journal of Engineering Science*, 42:571–590, 2004.
- [18] Dragos L. *Magnetofluid Dynamics*. Abacus Press, 1975.
- [19] Atkinson KE. *An Introduction to Numerical Analysis*. John Wiley and Sons, Canada, 1989.
- [20] Demmel JW. *Applied Numerical Linear Algebra*. SIAM, 1996.
- [21] Young DL, Jane SJ, Fan CM, Murugesan K, and Tsai CC. The method of fundamental solutions for 2D and 3D Stokes problems. *Journal of Computational Physics*, 211:1–8, 2006.
- [22] Soleimani Kutanaei S, Roshan N, Vosoughi A, Saghafi S, Barari A, and Soleimani S. Numerical solution of Stokes flow in a circular cavity using mesh-free local RBF-DQ. *Engineering Analysis with Boundary Elements*, 36:633–638, 2012.
- [23] Chen JT, Hsiao CC, and Leu SY. A new method for Stokes problems with circular boundaries using degenerate kernel and Fourier series. *International Journal for Numerical Methods in Engineering*, 74:1955–1987, 2008.
- [24] Bustamante CA, Power H, Sua YH, and Florez WF. A global meshless collocation particular solution method (integrated radial basis function) for two-dimensional Stokes flow problems. *Applied Mathematical Modelling*, 37:4538–4547, 2013.
- [25] Kreeft J and Gerritsma M. Mixed mimetic spectral element method for Stokes flow: A pointwise divergence-free solution. *Journal of Computational Physics*, 240:284–309, 2013.
- [26] Galaktionov OS, Meleshko VV, Peters GWM, and Meijer HEH. Stokes flow in a rectangular cavity with a cylinder. *Fluid Dynamics Research*, 24:81–102, 1999.

- [27] Yosinobu H and Kakutani T. Two-dimensional Stokes flow of an electrically conducting fluid in a uniform magnetic field. *Journal of the Physical Society of Japan*, 14:10:1433–1444, 1959.
- [28] Sellier A, Aydin SH, and Tezer-Sezgin M. Free-space fundamental solution of a 2D steady slow viscous MHD flow. *CMES*, 102:5:393–406, 2014.
- [29] Hunt JCR and Williams WE. Some electrically driven flows in magnetohydrodynamics part 1. Theory. *Journal of Fluid Mechanics*, 31(4):705–722, 1968.
- [30] Sezgin M. Magnetohydrodynamic flow in an infinite channel. *International Journal for Numerical Methods in Fluids*, 6:593–609, 1986.
- [31] Sezgin M. Magnetohydrodynamic flow on a half-plane. *International Journal for Numerical Methods in Fluids*, 8:743–758, 1988.
- [32] James MI, Mittal ML, Gupta GP, and Rohatki VK. Electric potential behavior in segmented Faraday-type MHD generators. *Energy Conversion and Management*, 25:211–215, 1985.
- [33] Hunt JCR and Malcolm DG. Some electrically driven flows in magnetohydrodynamics part 2. Theory and experiment. *Journal of Fluid Mechanics*, 1968:775–801, 1968.
- [34] Chowdhury V, Buhler L, Mistrangelo C, and Brinkmann HJ. Experimental study of instabilities in magnetohydrodynamic boundary layers. *Fusion Engineering and Design*, 98-99:1751–1754, 2015.
- [35] Nerguizian V, Alazzam A, Roman D, Stiharu I, and Burnier M. Analytical solutions and validation of electric field and dielectrophoretic force in a biomicrofluidic channel. *Electrophoresis*, 33:426–435, 2012.
- [36] Aminfar H, Mohammadpourfard M, and Ahangar Zonouzi Z. Numerical study of the ferrofluid flow and heat transfer through a rectangular duct in the presence of a non-uniform transverse magnetic field. *Journal of Magnetism and Magnetic Materials*, 327:31–42, 2013.
- [37] Jue TC. Analysis of combined thermal and magnetic convection ferrofluid flow in a cavity. *International Communications in Heat and Mass Transfer*, 33:846–852, 2006.
- [38] Sheikholeslami M, Ganji DD, and Rashidi MM. Ferrofluid flow and heat transfer in a semi annulus enclosure in the presence of magnetic source considering thermal radiation. *Journal of the Taiwan Institute of Chemical Engineers*, 47:6–17, 2015.

- [39] Kenjeres S. Numerical analysis of blood flow in realistic arteries subjected to strong non-uniform magnetic fields. *International Journal for Heat and Fluid Flow*, 29:752–764, 2008.
- [40] Goharkhah M and Ashjaee M. Effect of an alternating nonuniform magnetic field on ferrofluid flow and heat transfer in a channel. *Journal of Magnetism and Magnetic Materials*, 362:80–89, 2014.
- [41] Sheikholeslami M and Rashidi MM. Effect of space dependent magnetic field on free convection of Fe_3O_4 -water nanofluid. *Journal of the Taiwan Institute of Chemical Engineers*, 56:6–15, 2015.
- [42] Tzirtzilakis EE, Sakalis VD, Kafoussias NG, and Hatzikonstantinou PM. Biomagnetic fluid flow in a 3D rectangular duct. *International Journal for Numerical Methods in Fluids*, 44:1279–1298, 2004.
- [43] Tzirtzilakis EE and Xenos MA. Biomagnetic fluid flow in a driven cavity. *Meccanica*, 48:187–200, 2013.
- [44] Idris NA, Amin N, and Rahmat H. Effect of gravitational acceleration on unsteady biomagnetic fluid flow. *Applied and Computational Mathematics*, 3(6):285–294, 2014.
- [45] Morega A and Faur S. A FEM analysis of biomagnetic fluid flow in a rectangular duct under the influence of a magnetic field. In *Proceedings of the Third Workshop on Mathematical Modelling of Environmental and Life Sciences Problems*, pages 205–218, 2004.
- [46] Khashan SA and Haik Y. Numerical simulation of biomagnetic fluid downstream an eccentric stenotic orifice. *Physics of Fluids*, 18:113601–113610, 2006.
- [47] Bhargava R, Beg OA, Sharma S, and Zueco J. Finite element study of nonlinear two-dimensional deoxygenated biomagnetic micropolar flow. *Communications on Nonlinear Science and Numerical Simulation*, 15:1210–1223, 2010.
- [48] Khashan SA, Elnajjar E, and Haik Y. Numerical simulation of the continuous biomagnetic separation in a two-dimensional channel. *International Journal for Multiphase Flow*, 37:947–955, 2011.
- [49] Tzirakis K, Papaharilaou Y, Giordano D, and Ekaterinaris J. Numerical investigation of biomagnetic fluids in circular ducts. *International Journal for Numerical Methods in Biomedical Engineering*, 30:297–317, 2014.
- [50] Mousavi SM, Farhadi M, and Sedighi K. Effect of non-uniform magnetic field on biomagnetic fluid flow in a 3D channel. *Applied Mathematical Modelling*, 40:7336–7348, 2016.

- [51] Kabeel AE, El-Said EMS, and Dafea SA. A review of magnetic field effects on flow and heat transfer in liquids: Present status and future potential for studies and applications. *Renewable and Sustainable Reviews*, 45:830–837, 2015.
- [52] Islam AW, Sharif MAR, and Carlson ES. Mixed convection in a lid-driven square cavity with an isothermally heated square blockage inside. *International Journal of Heat and Mass Transfer*, 55:5244–5255, 2012.
- [53] Nazari M, Louhghalam L, and Kayhani MH. Lattice Boltzmann simulation of double diffusive natural convection in a square cavity with a hot square obstacle. *Chinese Journal of Chemical Engineering*, 23:22–30, 2015.
- [54] Selimefendigil F and Oztop HF. Natural convection and entropy generation of nanofluid filled cavity having different shaped obstacles under the influence of magnetic field and internal heat generation. *Journal of the Taiwan Institute of Chemical Engineers*, 56:42–56, 2015.
- [55] Chato JC. Heat transfer to blood vessels. *Journal of Biomedical Engineering*, 102:110–118, 1980.
- [56] Tzirtzilakis EE and Kafoussias NG. Biomagnetic fluid flow over a stretching sheet with non linear temperature dependent magnetization. *ZAMP*, 54:551–565, 2003.
- [57] Alimohamadi H, Dehghan-Niri V, and Ashjaee M. Improvement of heat transfer performances of biomagnetic flow in a rectangular duct under different types of magnetic fields. *International Journal of Technology Enhancements and Emerging Engineering Research*, 2:44–48, 2014.
- [58] Rao IJ and Rajagopal KR. The effect of the slip boundary condition on the flow of fluids in a channel. *Acta Mechanica*, 135:113–126, 1999.
- [59] Martini A, Roxin A, Snurr RQ, Wang Q, and Lichter S. Molecular mechanism of liquid slip. *Journal of Fluid Mechanics*, 600:257–269, 2008.
- [60] Priezjev NV, Darhuber AA, and Troian SM. Slip behavior in liquid films on surfaces of patterned wettability: Comparison between continuum and molecular dynamics simulations. *Physical Review E*, 71:041608–041619, 2005.
- [61] Hron J, Roux CL, Malek J, and Rajagopal KR. Flows of incompressible fluids subject to Navier’s slip on the boundary. *Computers and Mathematics with Applications*, 56:2128–2143, 2008.
- [62] Smolentsev S. MHD duct flows under hydrodynamic ‘slip’ condition. *Theoretical and Computational Fluid Dynamics*, 23:557–570, 2009.

- [63] Ligere E, Dzenite I, and Matvejevs A. MHD flow in the duct with perfectly conducting hartmann walls and slip condition on side walls. In *10th PAMIR International Conference-Fundamental and Applied MHD*, pages 279–283, 20-24 June, 2016, Cagliari, Italy.
- [64] Bhatti MM, Abbas MA, and Rashidi MM. Combine effects of Magneto-hydrodynamics (MHD) and partial slip on peristaltic Blood flow of Ree-Eyring fluid with wall properties. *Engineering Science and Technology, an International Journal*, 19:1497–1502, 2016.
- [65] Rivero M and Cuevas S. Analysis of the slip condition in magnetohydrodynamic (MHD) micropumps. *Sensors and Actuators B:Chemical*, 166-167:884–892, 2012.
- [66] Sarma D and Deka PN. Numerical study of liquid metal MHD duct flow under hydrodynamic "slip" condition. *International Journal of Computer Applications*, 81(16):7–10, 2013.
- [67] Rashad AM, Ismael MA, Chamkha AJ, and Mansour MA. MHD mixed convection of localized heat source/sink in a nanofluid-filled lid-driven cavity with partial slip. *Journal of Taiwan Institute of Chemical Engineers*, 68:173–186, 2016.
- [68] Ismael MA, Mansour MA, Chamkha AJ, and Rashad AM. Mixed convection in a nanofluid filled-cavity with partial slip subjected to constant heat flux and inclined magnetic field. *Journal of Magnetism and Magnetic Materials*, 416:25–36, 2016.
- [69] Partridge PW, Brebbia CA, and Wrobel LC. *The Dual Reciprocity Boundary Element Method*. Computational Mechanics Publications, Southampton, Boston, 1992.
- [70] Brebbia CA and Dominguez J. *Boundary Elements and Introductory Course*. WIT Press/Computational Mechanics Publications, 1992.
- [71] Young DL, Tsai CC, Eldho TI, and Cheng AHD. Solution of Stokes flow using an iterative DRBEM based on compactly-supported, positive-definite radial basis function. *Computers and Mathematics with Applications*, 43:607–619, 2002.
- [72] Eldho TI and Young DL. Solution of Stokes flow problem using dual reciprocity boundary element method. *Journal of the Chinese Institute of Engineers*, 24:2:141–150, 2001.
- [73] Tezer-Sezgin M, Bozkaya C, and Turk O. BEM and FEM based numerical simulations for biomagnetic fluid flow. *Engineering Analysis with Boundary Elements*, 37:1127–1135, 2013.

- [74] Tezer-Sezgin M. Boundary element method solution of MHD flow in a rectangular duct. *International Journal for Numerical Methods in Fluids*, 18:937–952, 1994.
- [75] Tezer-Sezgin M and Han Aydin S. Solution of magnetohydrodynamic flow problems using the boundary element method. *Engineering Analysis with Boundary Elements*, 30:411–418, 2006.
- [76] Liu HW and Zhu SP. The dual reciprocity boundary element method for magnetohydrodynamic channel flows. *ANZIAM Journal*, 44:305–322, 2002.
- [77] Bozkaya C and Tezer-Sezgin M. Fundamental solution for coupled magnetohydrodynamic flow equations. *Journal of Computational and Applied Mathematics*, 203:125–144, 2007.
- [78] Nishad CS, Chandra A, and Sekhar GPR. Flows in slip-patterned microchannels using boundary element methods. *Engineering Analysis with Boundary Elements*, 73:95–102, 2016.
- [79] Tezer-Sezgin M and Bozkaya C. The boundary element solution of the magnetohydrodynamic flow in an infinite region. *Journal of Computational and Applied Mathematics*, 225:510–521, 2009.
- [80] Bozkaya C and Tezer-Sezgin M. A numerical solution of the steady MHD flow through infinite strips with BEM. *Engineering Analysis with Boundary Elements*, 36:591–566, 2012.
- [81] Micchelli CA. Interpolation of scattered data: distance matrices and conditionally positive definite functions. *Constructive approximation*, 2:11–22, 1986.
- [82] Zhu SP, Liu HW, and Marchant TR. A perturbation DRBEM model for weakly nonlinear wave run-ups around islands. *Engineering Analysis with Boundary Elements*, 33(1):63–76, 2009.
- [83] Evans LC. *Partial differential equations*. American Mathematical Society, 1998.
- [84] Segal V and Raj K. An investigation of power transformer cooling with magnetic fluids. *Indian Journal of Engineering and Material Sciences*, 5:416–442, 1998.
- [85] Lo DC, Young DL, and Tsai CC. High resolution of 2D natural convection in a cavity by the DQ method. *Journal of Computational and Applied Mathematics*, 203(1):219–236, 2007.
- [86] Pint BA, More KL, Meyer HM, and DiStefano JR. Recent progress addressing compatibility issues relevant to fusion environments. *Fusion Science and Technology*, 47:851–855, 2005.



CURRICULUM VITAE

PERSONAL INFORMATION

Surname, Name: ŞENEL, Pelin

Nationality: Turkish (TC)

Date and Place of Birth: 22 June, Kastamonu

Phone: 0903123646808

Fax: 0903122101105

EDUCATION

Degree	Institution	Term
Ph.D.	Department of Mathematics, Middle East Technical University	2012-2017
M.Sc.	Department of Mathematics, Hacettepe University	2010-2012
B.Sc.	Department of Mathematics, Ankara University	2005-2010
Erasmus Program	Faculty of Mathematics and Computer Science, Jagiellonian University	2009-2010 Fall
Minor Program	Department of Business Administration, Ankara University	2007-2011
High School	Kocatepe Mimar Kemal High School	2001-2005

EMPLOYMENT

Year	Place	Enrollment
2012-Present	Department of Mathematics, Middle East Technical University	Research Assistant

PUBLICATIONS

International Journal Publications

- 1.1 P. Senel, M. Tezer-Sezgin, Pipe flow of a magnetizable fluid in rectangular cavities under magnetic sources, Engineering Analysis with Boundary Elements, vol:83, p. 55-66, 2017, doi: 10.1016/j.enganabound.2017.07.017
- 1.2 P. Senel, M. Tezer-Sezgin, DRBEM solution of biomagnetic fluid flow and heat transfer in cavities-CMMSE2016, Journal of Mathematical Chemistry, vol:55, p.1407-1426, 2017, doi: 10.1007/s10910-016-0721-9
- 1.3 P. Senel, M. Tezer-Sezgin, DRBEM solutions of Stokes and Navier-Stokes equations in cavities under point source magnetic field, Engineering Analysis with Boundary Elements, vol:64, p. 158-175, 2016, doi: 10.1016/j.enganabound.2015.12.007
- 1.4 M. Turkyilmazoglu, P. Senel, Heat and mass transfer of the flow due to a rotating rough and porous disk, International Journal of Thermal Sciences, vol:63, p. 146-158, 2013, doi: 10.1016/j.ijthermalsci.2012.07.013

International Conference Proceedings

- 2.1 M. Tezer-Sezgin, P. Senel, Electrically driven MHD flow between two parallel slipping and partly conducting infinite plates, European Conference on Numerical Mathematics and Advanced Applications-ENUMATH 2017, Voss, Norway, 25-29 September 2017 (Submitted to the book of proceedings)

- 2.2** P. Senel, M. Tezer-Sezgin, MHD duct flow with slipping velocity on the Hartmann and side walls, Engineering Mechanics Institute International Conference- EMI 2017-IC, Rio de Janeiro, Brazil, 19-22 March 2017 (Submitted to post-conference book of proceedings in Trends in Engineering Mechanics Special Publications)
- 2.3** P. Senel, M. Tezer-Sezgin, Convective flow of blood in square and circular cavities, Eleventh Workshop On Mathematical Modeling of Environmental and Life Sciences Problems-MMELSP 2016, Constanta, Romania, 12-16 October 2016 (Accepted for publication in the journal Analele Stiintifice ale Universitatii Ovidius Constanta, Seria Matematica)
- 2.4** Pelin Senel, M. Tezer-Sezgin, Flow in a square cavity with an obstacle under the influence of a non-uniform magnetic field, Advances in Boundary Element & Meshless Techniques XVII-BETEQ 2016, Ankara, Turkey, 11-13 July 2016, p.139-145
- 2.5** P. Senel, M. Tezer-Sezgin, DRBEM solution of biomagnetic fluid flow under a point source magnetic field, Proceedings of the 16th International Conference on Computational and Mathematical Methods in Science and Engineering-CMMSE 2016, Rota, Cadiz, Spain, 4-8 July 2016, p.1172-1183
- 2.6** P. Senel, M. Tezer-Sezgin, Flow in a rectangular duct under the influence of the magnetic field, The Proceedings of the 10th UK Conference on Boundary Integral Methods-UKBIM 2015, University of Brighton, UK, 13-14 July 2015, p.179-188
- 2.7** Pelin Senel, M. Tezer-Sezgin, Stokes flow in a lid-driven rectangular duct under the influence of a point source magnetic field, Advances in Boundary Element & Meshless Techniques XVI-BETEQ 2015, Valencia, Spain, 6-8 July 2015, p.85-90

International Conference Abstracts

- 3.1** P. Senel, M. Tezer-Sezgin, DRBEM solution of MHD flow in pipes with partly insulated partly perfectly conducting slipping walls, 7th International Conference on Advanced Computational Methods in Engineering-ACOMEN 2017, Ghent, Belgium, 18-22 September 2017

National Conference Abstracts

- 4.1** Pelin Senel, M. Turkyilmazoglu, Gözenekli ve pürüzlü disk üzerinde kütle ve ısı transferi, (in English: Heat and mass transfer on the porous and rough disk), 7th Ankara Mathematics Days, Bilkent University, Ankara, Turkey, 31 May-1 June, 2012

Posters presented in National Workshops

- 5.1** P. Senel, M. Tezer-Sezgin, Forced convection flow of biomagnetic fluid in a pipe of square cross-section, 3rd Women Mathematicians Association Workshop, Izmir, Turkey, 27-29 May 2016

NUMERICAL METHODS

Boundary Element Method (BEM), Finite Element Method (FEM), Finite Difference Method (FDM).

TEACHING

- Calculus with Analytic Geometry
- Calculus of Functions of Several Variables
- Calculus for Mathematics Students I
- Calculus for Mathematics Students II
- Partial Differential Equations

FUNDING AND ACADEMIC PROJECTS

- Middle East Technical University, Scientific Research Project, BAP 01-01-2015-004, “Numerical solutions of magnetohydrodynamic (MHD)-Stokes flow using the dual reciprocity boundary element method (DRBEM)”, 2015
- TUBITAK BİDEB 2211 Graduate Scholarship, September 2010- June 2012
- European Union Grant for exchange students, 2009-2010 Academic Year Fall Semester (total of 5 months)
- Ankara University Grants for exchange students, 2009-2010 Academic Year Fall Semester (total of 5 months)

LANGUAGE SKILLS

English (Advanced), Polish (Starter), French (Starter).

COMPUTER SKILLS

Office Programs (Word, Excel, PowerPoint), Latex, Matlab, Mathematica